Measurement of gauge boson joint-polarisation states in WZ production at the LHC with the ATLAS detector

Luka Selem

To cite this version:

Luka Selem. Measurement of gauge boson joint-polarisation states in WZ production at the LHC with the ATLAS detector. High Energy Physics - Experiment [hep-ex]. Université Savoie Mont Blanc, 2022. English. NNT : 2022CHAMA033 . tel-04496037

UNIVERSITÉ
SAVOIE
MONT BLANC

THÈSE

Pour obtenir le grade de

DOCTEUR DE L'UNIVERSITÉ SAVOIE MONT BLANC

Spécialité : **Physique Subatomique et Astroparticules**

Arrêté ministériel : 25 Mai 2016

Présentée par

Luka SELEM

Thèse dirigée par **Emmanuel SAUVAN**

préparée au sein du **Laboratoire d'Annecy de Physique des Particules**
dans **l'École Doctorale de Physique de Grenoble**

Mesure des états de co-polarisation des bosons de jauge en production de paire WZ au LHC avec le détecteur ATLAS

Measurement of gauge boson joint-polarisation states in WZ pair production at the LHC with the ATLAS detector

Thèse soutenue publiquement le **27 septembre 2022**,
devant le jury composé de :
M. Philippe SCHWEMLING
Professeur des universités, Université Paris-Diderot, Rapporteur
M. Vincent TISSERAND
Directeur de recherche, CNRS, Rapporteur, Président du jury
M^{me} Elzbieta RICHTER-WAS
Professeuse, Jagiellonian University, Examinatrice
M. Guillaume UNAL
Directeur de recherche, CERN, Examinateur
M. Gilles MAURIN
Maître de conférences, Université Savoie Mont-Blanc, Examinateur

Ab auroram temporum, homines ad
polarisationem bosonorum cogitant.
Nullius scriptor, numquam

Contents

Introduction

The Standard Model of particle physics provides a very precise and successful description of interactions within matter at the smallest accessible scale.Developed along the second half of the twentieth century, it was met with many experimental successes, the latest being the discovery of the Higgs boson in 2012 [1, 2]. However, built around only three out of the four fundamental interactions of Nature, it leaves aside gravity which is better described by the macroscopic scale theory of general relativity. Not withstanding all its past and continued confirmations by experimental measurements, the Standard Model cannot have the final say on physics laws and would be better described as an effective theory, only valid at the "low" energies presently accessible to human experiments. More philosophical considerations around the strange mass hierarchy of particles,the still large number of free parameters and the fine-tuning of one of them, the Higgs mass, all back up the search for beyond the Standard Model theories. As yet, tentative theories developed to solve these problems have failed to provide any experimental evidence. Similarly, cosmological open questions such as dark matter or dark energy cannot be answered by the present Standard Model and have lead so far to unsuccessful searches.

Another way to approach the problem is through precision measurements. Without experimental evidence, from a particle physics point of view, of deviations from the Standard Model predictions, there is still no clear indication as to where new physics could lie. The goal of precision measurements is to provide such information. The recent measurement by the CDF Collaboration of the $W^{\pm}$ boson mass in significant tension with the Standard Model prediction [3] is an example of what precision measurement can achieve. Precision measurements targeting very rare processes is another handle to discovering potential new physics. The triple and quartic gauge couplings in the electroweak sector provide such rare processes that have yet to be fully tested against Standard Model predictions. Such processes are nowadays studied mainly with the Large Hadron Collider (LHC) operated at CERN providing proton–proton collisions at very high energy with an unprecedented rate. The ATLAS experiment, a detector sat at an interaction point of the LHC, allows a variety of measurements on particles produced at its collision point.

In this thesis, the focus will be on collisions producing $W^{\pm}$ and Z bosons simultaneously, studied with the ATLAS detector. This $W^{\pm}Z$ production is a diboson process, that is a process involving the simultaneous production of two electroweak gauge bosons. Diboson processes became promising channels to probe the Standard Model, as they allow studying the electroweak triple and quartic gauge couplings. They remain nevertheless challenging experimental targets due to their low cross section which translates in low event yields among all the proton–proton collisions. As can be seen in Fig. 1, the total production cross section of various diboson processes WW, ZZ, WZ are of the order of the Higgs boson total production cross section. In addition to the high centre-of-mass energy of the

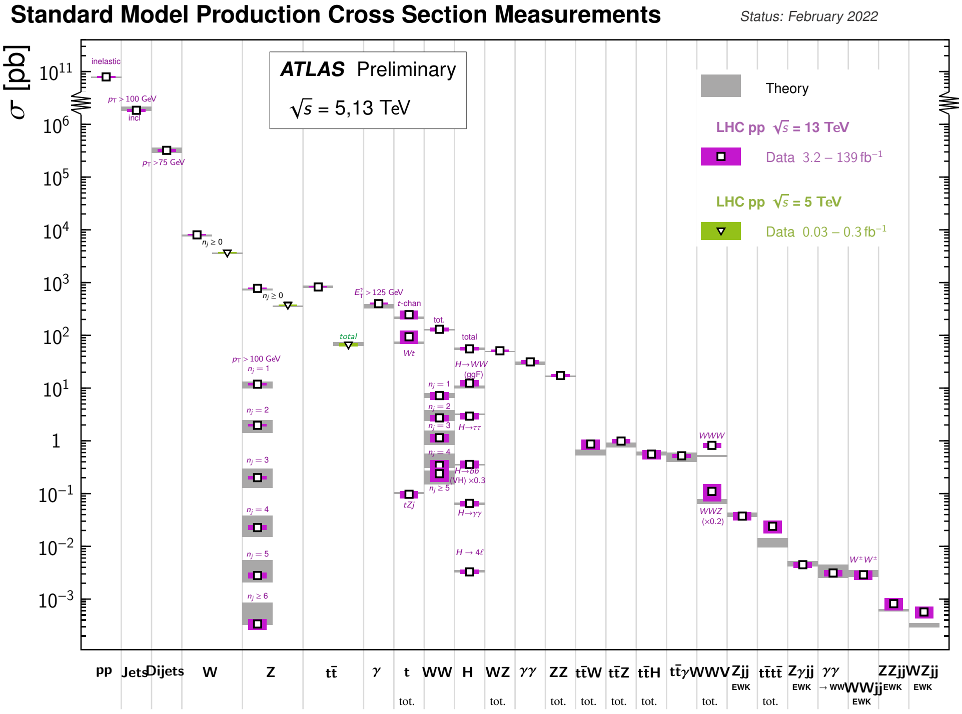

Figure 1 Summary of several Standard Model total and fiducial production cross-section measurements from Run 2 data, corrected for branching fractions, compared to the corresponding theoretical expectations. From Ref. [4].

collision needed to produce both bosons, the collection of very large datasets is therefore required. Among these diboson processes, the $W^\pm Z$ production, detected by its leptonic decay, constitutes an experimental compromise between a high cross section and a clean signature in the detector.

Moreover, the vector bosons of the electroweak sector have an interesting property which sets them apart from the other gauge bosons of the Standard Model: they are massive. This mass is incorporated in the Standard Model by the mechanism of Brout-Englert-Higgs which also postulates the existence of the Higgs boson. On the other hand, this mass allows them to have a third degree of freedom for their polarisation, associated to a longitudinal polarisation on top of the two original transverse ones. It is therefore of interest to study diboson processes through the prism of their polarisation to get a more detailed test of the Standard Model.

The polarisation of the $W^\pm$ boson was first studied at LEP, the predecessor of the LHC, in e^+e^- collisions producing a $W^\pm W^\mp$ pair. The single $W^\pm$ boson polarisation fractions were measured by the OPAL, L3, and DELPHI collaborations [5–7]. It was also measured in ep collisions by the H1 collaboration [8]. In hadronic collisions, it was measured by the CDF and DØ collaborations [9–11] in $p\bar{p}$ at the Tevatron, in the decay of the top quark. In pp collisions at the LHC, the ATLAS and CMS collaborations measured it in single boson production [12, 13]. The Z boson polarisation was also measured in single boson production by CDF, ATLAS and CMS [14–16]. As a next step for hadronic colliders, the polarisation of single bosons independently of each other was studied in diboson processes. It was performed for the first time in $W^\pm Z$ production by the ATLAS Collaboration [17], followed by the CMS Collaboration [18]. Regarding joint-polarisation of a diboson system, the first measurements also date back from LEP. The correlations between polarisations of both $W^\pm$

boson in $W^{\pm}W^{\mp}$ production was studied by L3 [19] while DELPHI and OPAL attempted to measure the joint-polarisation fractions [20, 21]. The DELPHI measurement provided observations of the composite transverse-transverse and mixed joint-polarisation states but failed to have enough precision to observe the longitudinal-longitudinal joint-polarisation state. The OPAL measurement had a similarly low precision on the longitudinal-longitudinal joint-polarisation fractions. The analysis presented in this thesis, studying $W^{\pm}Z$ production with leptonic decay, provides the first measurement of joint-polarisation fractions in hadronic collisions and the first observation ever of a longitudinal-longitudinal joint-polarisation state in a diboson process.

However, the amount of inelastic proton–proton collisions produced at the ATLAS interaction point exceeds by nine orders of magnitude the production of the most frequent processes of interest for physicists, as visible in Fig. 1. The selection of physically interesting events such as diboson processes needs therefore an automatised trigger system. In preparation for the Run 3 of the LHC that started in 2022, the ATLAS detector underwent several upgrades among which the replacement of its calorimeter trigger system. It allowed the increase of the granularity of calorimeter inputs considered at the trigger level improving the trigger performances. This will also allow maintaining the same acceptance rate in degraded conditions due to increased pile-up, as is expected for future runs of the LHC. The complete redesign of the trigger electronic chain required for this new Digital Trigger is presented in this thesis.

Chapter 1 will first present theoretical grounds for the study of the polarisation of vector bosons in proton–proton collisions. Chapter 2 will then describe the LHC and the ATLAS detector which provide the experimental data for the works developed in this thesis. Chapter 3 will focus more specifically on the calorimeter trigger chain and the upgrade it underwent before Run 3. This will allow me in Chapter 4 to describe specifically my personal contribution to this upgrade. Going back to physics analysis, the theoretical description of the studied $W^{\pm}Z$ production, particularly in term of polarisation, is presented in Chapter 5. The selection and reconstruction in data of the inclusive $W^{\pm}Z$ production, along with its associated background estimation, is described in Chapter 6. Finally, Chapter 7 will provide a complete description of the measurement of joint-polarisation fractions in the inclusive $W^{\pm}Z$ selected events, along with single boson polarisation fractions as an extension of Ref. [17] on a larger dataset.

Summary of my personal contributions

As a PhD student, I was confronted to the two main aspects of the work of an experimental particle physicist: detector development and physics data analysis. On the hardware side, I contributed among a wide team of engineers and physicists to the already well advanced project of the liquid Argon calorimeter Phase 1 upgrade, in what started as my ATLAS author qualification task. On the physics analysis I joined a team of ATLAS physicists working on the $W^{\pm}Z$ diboson process, spearheaded by my supervisor Emmanuel Sauvan. My work aiming at joint-polarisation fraction measurement was performed within this team. Additionally, it builds on earlier developments with the inclusive study of the $W^{\pm}Z$ production [22] and the subsequent measurement of single boson polarisation [17] with a fraction of the dataset used here. This latter work was mainly performed by my supervisor's previous PhD student Angela Burger, whose thesis I used as a reference [23].

For the sake of clarity, the experimental and theoretical contexts of the two main subjects treated in this thesis are presented. With increasing precision and complexity, their description aims at making understandable the new developments I produced. In order to clarify for the reader what is of my own work, the list below ordered by chapter summarises my personal contributions:

Chapter 4: This chapter represents the hardware half of my thesis work. The first section describes in detail the main components of what I was responsible for – the configuration of the energy computation in the new Digital Trigger of ATLAS – and how I implemented it. The second section describes the various tests I conducted for the commissioning of this configuration and the energy computation functionality itself, making it ready for data-taking.

Chapter 5: Here, my main contribution lies in Section 5.4. I implemented techniques to extract polarisation fraction from an inclusive Monte Carlo sample. I compared them and used them for various purposes, most prominently to motivate the choice of the frame in which the measurement of polarisation fractions is performed.

Chapter 6: Minor personal contributions in this chapter include the study of the background related to migrating γ^* and the choice of the method for the p_z^ν reconstruction, more detailed in Appendix C.

Chapter 7: This last chapter represents the bulk of my personal work on the analysis side of this thesis.

Section 7.1: I implemented the parametrisation of the fit as described in this section.

Section 7.2: While I did not develop the classification DNN described in this section, I did perform the study justifying its choice as discriminating variable.

Section 7.3: I extended the analytical reweighting method described in this section to adapt it to joint-polarisation measurement. I extensively explored its implicit assumptions to understand its limitations.

Section 7.4: I did not develop myself the alternative methods described in this section to obtain polarisation template sets.

Sections 7.5, 7.6 and 7.7: These last sections are all of my own work.

Chapter 1

Theoretical aspects

This thesis will focus on the study of the polarisation of the $W^{\pm}$ and Z vector bosons. These are fundamental particles of the Standard Model of particle physics which provides a description of three of Nature's four fundamental interactions: electromagnetism, the weak interaction and the strong interaction, leaving aside gravity best described by general relativity. These interactions are modelled by gauge theories each associated to a gauge boson as the interaction mediator. The $W^{\pm}$ and Z vector bosons are gauge bosons of the electroweak theory, itself unifying the electromagnetism and the weak interaction. Differently from other bosons in the Standard Model, they were found to have a mass. To accommodate this particularity without spoiling the founding principles of the Standard Model, the Brout Englert Higgs (BEH) mechanism [24, 25] proposes the spontaneous symmetry breaking mechanism of a scalar field which results in masses for the W^{+}, W^{-} and Z bosons vector bosons along with a new scalar boson. This Higgs boson finally observed in 2012 provides experimental backing for this mechanism. On the other hand, this mass allows these vector bosons to have three degrees of freedom for their polarisation vector, when massless gluons and photons can only have transverse polarisation modes. As a result, the additional longitudinal polarisation state is a quite unique feature of $W^{\pm}$ and Z vector bosons which is ultimately linked to the BEH mechanism. They provide therefore an interesting probe to test this mechanism and look for new physics.

The theoretical grounds for the study of the polarisation of vector bosons at a hadron collider will be described in this chapter. In Section 1.1, the basic principles of quantum field theory and the components of the Standard Model will be described. Then, going into more details, the unified electroweak theory and the BEH mechanism will be presented. A more general purpose description of the Standard Model and the underlying quantum field theory can be found in Ref. [26]. Next, in Section 1.2, polarisation in the context of massive vector bosons and the specificities of the longitudinal polarisation will be described. Finally, how these aspects of the Standard Model can be modelled in proton–proton collisions will be explained in Section 1.3.

1.1 The electroweak theory in the Standard Model

1.1.1 Lagrangian and symmetries

The goal of fundamental physics is to develop a quantitative description of Nature's phenomena with the simplest components and principles. One such principle is the *least action principle* which in classical physics states that the dynamics of a physical system will tend to minimise its *action* $\mathcal{S}$ defined as

$$\mathcal{S} = \int_{t_i}^{t_f} L(x, \dot{x}; t) dt \; , \tag{1.1}$$

where x and $\dot{x}$ denote the three components of position and speed as functions of time t. These functions are the degrees of freedom that are adjusted by the minimisation of $\mathcal{S}$. The physics of the phenomena is thus completely described in the Lagrangian L. This formulation of a physical phenomena in terms of a Lagrangian and other so-called variational principles is in fact a universal and very fruitful approach.

This idea survived the various revolutions in physics at the turn of the twentieth century, namely quantum mechanics and special relativity, at the expense of some generalisation. From special relativity, this principle was modified to treat time and position on an equal footing, with x^μ the contravariant coordinates of the four-vector position of an event in space-time. Combined with quantum mechanics, the physical objects considered are now quantum fields; classical particles as the electron are now seen as localised excitations of such fields. The action is thus redefined as a function of the density of Lagrangian $\mathcal{L}$, that will for simplicity be called Lagrangian from now on:

$$\mathcal{S}[\varphi] = \int \mathcal{L} \left(\varphi, \partial_\mu \varphi; x\right) d^4x \; , \tag{1.2}$$

with φ the fields of the considered quantum field theory. In quantum field theories, the action appears in more complicated formulas, but the principle of encapsulating the rules of the physical theory in the Lagrangian $\mathcal{L}$ persists.

In particle physics, an important application of the theory is the computation of interaction rate of different processes. The starting point is to consider an initial state i and a final state f composed of some combinations of the various fields of the theory. The computation of the probability of the transition $i \to f$ is $\langle i|f\rangle = \langle i|\mathrm{S}|i\rangle$ involving the S-matrix

$$\mathrm{S} = T \, \exp\left(i \int \mathcal{L}_{int} \left(\varphi_{in}, \partial_\mu \varphi_{in}; x\right) d^4x\right) \; . \tag{1.3}$$

Here, $\mathcal{L}_{int}$ is the interaction Lagrangian applied on the free fields of the initial state φ_{in}, and T is the time order operator. This exponential can be developed in a Taylor expansion, leading to a formula in powers of the interaction Lagrangian. From there, complex calculations involving the Lehmann-Symanzik-Zimmermann reduction formula [27] allow the computation of a given transition probability at a given order in the Taylor expansion. If the coupling constant of the interaction Lagrangian $\mathcal{L}_{int}$ is small, the higher orders of the Taylor expansion, which effectively are in powers of this coupling constant, can be neglected. This gives rise to a perturbative approach of the theory, with the lowest order for a given process being called the Leading Order (LO). A much simpler way of computing these transition probabilities is through Feynman diagrams that represent in a graphical way allowed interactions between the fields in the initial and final states at a given order in the perturbative theory. Such diagrams are drawn following so called Feynman rules that are directly derived from the structure of the Lagrangian. They allow the computation of matrix elements $\mathcal{M}_{fi}$ of the S-matrix which are a key part in the computation of processes cross sections.

The problem is now to develop a Lagrangian for the interactions of the most fundamental particles of the universe. A central idea in classical physics is the conservation of certain quantities, the most prominent example of which being the conservation of the energy elevated as the first principle of thermodynamics. In fact, this idea is directly linked to the idea of symmetries of the Lagrangian by the Noether's theorem: any continuous symmetry of the Lagrangian implies the conservation of an associated quantity and conversely any conservation law is a sign of an underlying symmetry. The interplay between experimental and theoretical physics along the twentieth century allowed the development of the Standard Model of particle physics. On one side, experiments discovered particles and conservation laws, sometimes broken. On the other side, theoretical developments tried to accommodate these in Lagrangians built around symmetry groups, in turn postulating the existence of new particles. One such particle, the Higgs boson, was postulated in 1964 [24, 25] and only discovered in 2012 at the Large Hadron Collider [1, 2].

1.1.2 The Standard Model Lagrangian

Particles in the Standard Model belong to two distinct groups, bosons or fermions, as a consequence of the Pauli exclusion principle in quantum mechanics. Bosons act as mediators for fundamental interactions which are the electromagnetic interaction, the weak interaction and the strong interaction – the gravitational interaction is beyond the scope of the Standard Model. On the other hand, fermions act as the matter content to which these interactions apply. From the relativistic equation

$$E^2 - \vec{p}^2 = m^2 \, , \tag{1.4}$$

linking the energy E and momentum $\vec{p}$ of a free matter particle of mass m, a first order differential equation, the Dirac equation, was derived to describe relativistic matter particles in the quantum field formalism. These particles are described by Dirac spinors ψ which obey the free Dirac Lagrangian

$$\mathcal{L}_D = \bar{\psi} \left(i\partial\!\!\!/ - m \right) \psi \, , \tag{1.5}$$

with $\partial\!\!\!/ = \gamma^\mu \partial_\mu$, γ^μ the Dirac matrices, and $\bar{\psi} = \gamma^0 \psi^\dagger$ the adjoint of the field ψ. There are four independent solutions to the Dirac equations, that can be grouped in two categories: particles described by the spinor u and anti-particles described by the spinor v, which are charge conjugate of the particles. Each spinor still lives in a two-dimensional space that can be projected on two *chirality* eigenstates called *left* and *right*. This mathematical feature is exactly equivalent in the massless case to the two helicity states ±1/2, with helicity the projection of the spin 1/2 of the fermion on the momentum $\vec{p}$.

Within the Standard Model, each of the three fundamental interactions considered is associated to a symmetry group, itself linked to a conserved quantum number through the Noether's theorem:

- The strong interaction arises from the $SU(3)$ symmetry group and is associated to the colour charge among *red*, *green* and *blue*, for coloured particles, and *white* for colour neutral particles. The theory built around this $SU(3)$ group is called Quantum Chromodynamics (QCD). It postulates that only particles living in the singlet representation of $SU(3)$, that is *white* particles, can exist freely. This colour confinement principle means that colour charged particles can only exist in bound states.

- The weak interaction arises from the $SU(2)$ symmetry group and is associated to the weak isospin I. It has the particularity of being null for all fermions of right chirality, meaning the weak interaction only applies to fermions of left chirality.
- The electromagnetic interaction arises from the U(1) symmetry group, and is associated to the electric charge Q. In the original formulation, the conserved quantity is the hypercharge Y, and the electromagnetic interaction arises as an unbroken symmetry with $Q = I_3 + Y/2$ after the electroweak spontaneous symmetry breaking described in Section 1.1.3.

Different types of fermions are associated to different quantum numbers of these three symmetry groups. Only sensitive to the weak interaction are the neutrinos of left chirality. Then, charged leptons interact weakly and electromagnetically. The lightest and most common of them is the electron. Together with the neutrinos, they are called leptons. Then come the quarks, sensitive to all fundamental interactions including the strong interaction, and as such components of atomic nuclei. The first generation of fermions is represented in Tab. 1.1 with their associated quantum numbers. With increased masses, this first generation is repeated with the same quantum numbers in a second and third generation, giving all the fermions of the Standard Model as visible in the left part of Fig. 1.1. The corresponding anti-particles are obtained by inverting all quantum numbers.

Table 1.1 Quantum numbers of fermions of the first generation. The L or R index indicates the Left or Right chirality of the fermion. The electric charge Q is linked to the third component of the weak isospin I_3 and the hypercharge Y by $Q = I_3 + Y/2$. The colour charge can be red r, green g or blue b for particles sensitive to the strong interaction and is labelled *colourless* for particle that are colour neutral.

	Weak Isospin I_3	Hypercharge Y	Electric Charge Q	Colour charge
electron e^-_L	-1/2	-1	-1	*colourless*
electron e^-_R	0	-2	-1	*colourless*
electronic neutrino $\nu_{e\,L}$	+1/2	-1	0	*colourless*
electronic neutrino $\nu_{e\,R}$	0	0	0	*colourless*
quark up u_L	+1/2	+1/3	+2/3	*r,g,b*
quark up u_R	0	+4/3	+2/3	*r,g,b*
quark down d_L	-1/2	-1/3	-1/3	*r,g,b*
quark down d_R	0	-2/3	-1/3	*r,g,b*

To summarise, the Standard Model Lagrangian is made invariant under the symmetry groups $SU(3)_C \times SU(2)_L \times U(1)_Y$. For each added symmetry, the fermion Lagrangian of Eq. (1.5) is made invariant under said symmetry by replacing the derivative ∂_μ by the covariant derivative D_μ

$$\partial_\mu \to D_\mu = \partial_\mu - igA^a_\mu t^a \ , \tag{1.6}$$

with A^a_μ the vectorial fields of the gauge bosons associated to the interaction, t^a the generators of the Lie algebra of the symmetry group considered and g the coupling constant of the interaction with the fermion. To complete the Standard Model Lagrangian, a

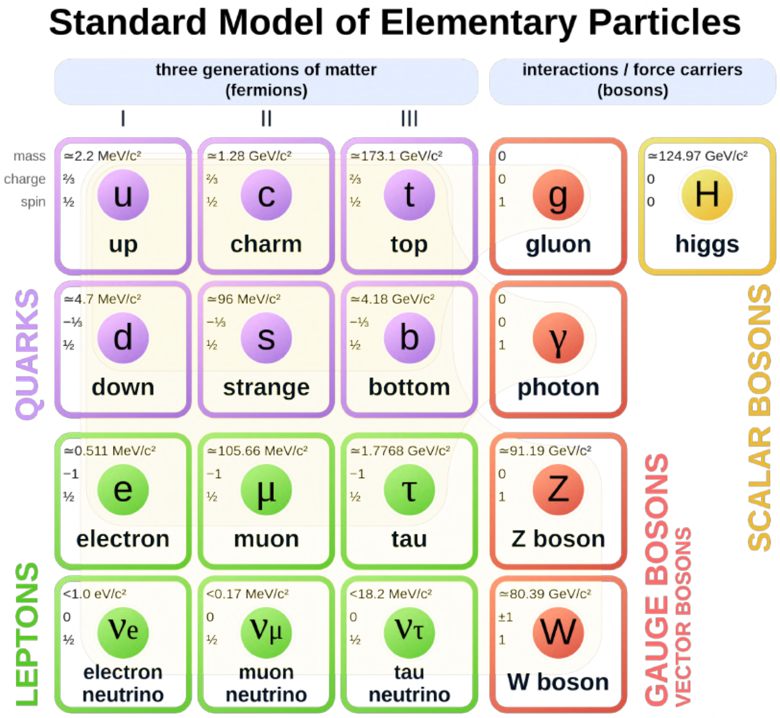

Figure 1.1 The Standard Model particles.

Lagrangian for the newly introduced bosons, called Yang-Mills Lagrangian, is added:

$$\mathcal{L}_{YM} = \frac{1}{4} F^a_{\mu\nu} F^{a\ \mu\nu} \ , \tag{1.7}$$

with $F_{\mu\nu}$ the field strength associated to the gauge bosons A by

$$F_{\mu\nu} = \partial_\mu A_\nu - \partial_\nu A_\mu - ig\left[A_\mu, A_\nu\right] \ , \tag{1.8}$$

with $[.,.]$ the commutator. Nevertheless, this Lagrangian cannot accommodate massive particles without breaking one symmetry. Experimentally, this is in particular a problem for the $W^\pm$ and Z bosons associated to the weak interaction, as we know they have a mass responsible for their finite decay time. This is solved with a mechanism of spontaneous symmetry breaking of the electroweak sector $SU(2)_L \times U(1)_Y$ as detailed in Section 1.1.3. This mechanism uses the spontaneous symmetry breaking of the potential of an additional scalar field ϕ to give a mass to three of the four gauge bosons of $SU(2)_L \times U(1)_Y$. This creates a new massive scalar boson, the Higgs boson, and leaves $U(1)_{EM}$ as an emergent unbroken symmetry associated to the electromagnetism. Consequently, after spontaneous symmetry breaking, the Standard Model Lagrangian is invariant only under $SU(3)_C \times U(1)_{EM}$. For $SU(3)_C$, there are 8 generators yielding eight gauge bosons called *gluons*. For the broken $SU(2)_L$, the 3 generators are associated to the three massive gauge bosons of the weak interaction, namely W^+, W^- and Z. Finally, the boson associated to the $U(1)_{EM}$ symmetry is the photon γ. These bosons are represented on the right part of Fig. 1.1.

To complete the Standard Model Lagrangian, a Lagrangian $\mathcal{L}_\phi$ must be added for the additional scalar field ϕ. This field is also used to give mass to every fermions through Yukawa couplings, bringing a final addition $\mathcal{L}_{Yuk.}$ to the Standard Model Lagrangian. In total, the Standard Model Lagrangian before spontaneous symmetry breaking is

$$\mathcal{L}_{SM} = \mathcal{L}_{YM} + \mathcal{L}_D + \mathcal{L}_\phi + \mathcal{L}_{Yuk.} \ . \tag{1.9}$$

1.1.3 The Electroweak Theory

Weak interactions are described by the $SU(2)_L$ group and, leptons and quarks of left chirality can be arranged in isospin doublets as follow:

$$\begin{pmatrix} \nu_e \\ e^- \end{pmatrix}_L , \quad \begin{pmatrix} \nu_\mu \\ \mu^- \end{pmatrix}_L , \quad \begin{pmatrix} \nu_\tau \\ \tau^- \end{pmatrix}_L , \tag{1.10}$$

$$\begin{pmatrix} u \\ d' \end{pmatrix}_L , \quad \begin{pmatrix} c \\ s' \end{pmatrix}_L , \quad \begin{pmatrix} t \\ b' \end{pmatrix}_L , \tag{1.11}$$

where d', s', and b' are flavour eigenstates related to the mass eigenstates d, s, b by the Cabibbo-Kobayashi-Maskawa (CKM) matrix. Right-handed components stay as singletons under the $SU(2)_L$ symmetry.

The electroweak theory unifies the weak interaction with the electromagnetic interaction of group $U(1)_{EM}$ by considering the new group of symmetry $SU(2)_L \times U(1)_Y$ with Y the hypercharge. This group has four gauge bosons W^1_μ, W^2_μ, W^3_μ from $SU(2)_L$ and B_μ from $U(1)_Y$. The generators of the Lie algebra of $SU(2)_L$ are the Pauli matrices labelled τ^a, multiplied by 1/2. This yields the covariant derivative

$$D_\mu = \partial_\mu - ig\frac{\tau^a}{2}W^a_\mu - ig'\frac{Y}{2}B_\mu , \tag{1.12}$$

where g and g' are respectively the coupling constants of $SU(2)_L$ and $U(1)_Y$.

As such, the four gauge bosons are massless as any mass term in the Lagrangian would break the gauge symmetry. A mechanism is introduced to spontaneously break the symmetries of the group so that after symmetry breaking, mass terms appear for the three bosons of the weak interaction. The simplest of such mechanisms was proposed by Brout, Englert and Higgs in 1964 [24, 25]. It is based on adding a scalar field ϕ represented by the isospin doublet

$$\phi = \begin{pmatrix} \phi^+ \\ \phi^0 \end{pmatrix} = \frac{1}{\sqrt{2}} \begin{pmatrix} \phi_1 + i\,\phi_2 \\ \phi_3 + i\,\phi_4 \end{pmatrix} , \tag{1.13}$$

associated to the potential V

$$V(\phi) = \mu^2|\phi^\dagger\phi| + \lambda|\phi^\dagger\phi|^2, \qquad \mu^2 < 0,\ \lambda > 0 . \tag{1.14}$$

Using the covariant derivative D_μ of Eq. (1.12), the Lagrangian of this scalar field ϕ is thus

$$\mathcal{L}_\phi = (D^\mu\phi)^\dagger(D_\mu\phi) - V(\phi) . \tag{1.15}$$

The potential V has non trivial minima degenerated on the hypersphere of radius $|\phi^\dagger\phi| = v^2/2 = -\mu^2/(2\lambda)$. Analogously in 2 dimensions, the potential would have the shape of the base of a wine bottle (see Fig. 1.2) and the minima are on a circle. The spontaneous symmetry breaking emerges from the choice of one realisation of this minimum on the hypersphere to become the vacuum ground state. This state is chosen arbitrarily, at the expense of a $SO(4)$ rotation, to be

$$\phi_0 = \begin{pmatrix} 0 \\ \frac{v}{\sqrt{2}} \end{pmatrix} . \tag{1.16}$$

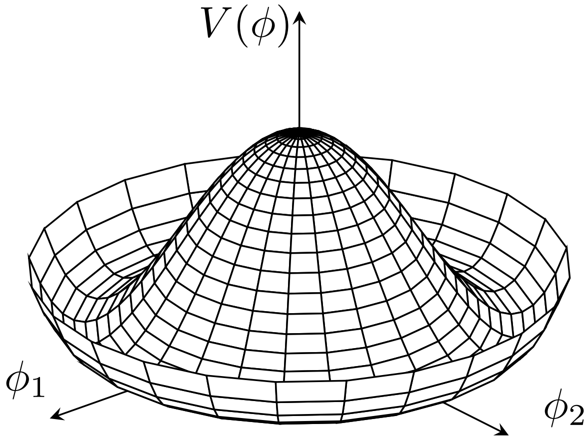

Figure 1.2 The wine bottle base shape of a potential $V(\phi) = \mu^2|\phi|^2 + \lambda|\phi|^4$ for the field $\phi = \phi_1 + i\phi_2$ with $\mu^2 < 0$ and $\lambda > 0$.

The symmetry $SU(2) \times U(1)_Y$ is thus broken, leaving only the unbroken symmetry $U(1)_{EM}$. From the Nambu-Goldstone theorem, this creates three massless bosons w_1, w_2, w_3 that emerge from the unitary parametrisation of ϕ around the ground state:

$$\phi = e^{\frac{i}{v}\sum\limits_a \frac{\tau^a}{2} w^a} \begin{pmatrix} 0 \\ \frac{v+h}{\sqrt{2}} \end{pmatrix} , \tag{1.17}$$

where the $\tau^a/2$ are the generators of the broken symmetry $SU(2)$, and h is the surviving scalar field that will be identified to be the Higgs boson. A gauge transformation

$$\Omega = e^{\frac{-i}{v}\sum\limits_a \frac{\tau^a}{2} w^a} \tag{1.18}$$

of $SU(2)$ will transform the $\mathcal{L}_\phi$ constituents in

$$\phi \to \phi' = \Omega\phi = \begin{pmatrix} 0 \\ \frac{v+h}{\sqrt{2}} \end{pmatrix} , \tag{1.19}$$

$$\tau^a W^a_\mu \to \tau^a W^{a\ \prime}_\mu = \Omega\ \tau^a W^a_\mu\ \Omega^\dagger + \frac{i}{g}\Omega\partial_\mu\Omega^\dagger = \Omega\ \tau^a \left(W^a_\mu - \frac{1}{gv}\partial_\mu w^a\right)\ \Omega^\dagger , \tag{1.20}$$

$$YB_\mu \to YB'_\mu = \Omega\ YB_\mu\ \Omega^\dagger = YB_\mu . \tag{1.21}$$

Through this gauge transformation the goldstone bosons can be made to disappear from $\mathcal{L}_\phi$. For the potential $V(\phi)$ it is straight forward. In the kinetic term derivative $(D^\mu\phi)^\dagger(D_\mu\phi)$, they get absorbed in a mass term for the bosons transformed under this symmetry. Or more precisely, linear combinations of the $W^{a\ \prime}$ and B yield the mass eigenstates W^+, W^- and Z bosons.

$$W^\pm_\mu = \frac{1}{\sqrt{2}}\left((W^1_\mu - \frac{1}{gv}\partial_\mu w^1) \pm i(W^2_\mu - \frac{1}{gv}\partial_\mu w^2)\right) , \tag{1.22}$$

$$Z_\mu = c_w\left(W^3_\mu - \frac{1}{gv}\partial_\mu w^3\right) - s_w B_\mu \qquad \text{with } c_w = \frac{g}{\sqrt{g^2+g'^2}} \text{ et } s_w = \frac{g'}{\sqrt{g^2+g'^2}} . \tag{1.23}$$

A fourth bosons is created by these linear combination, that will not be associated to any mass term: the photon, gauge boson of the residual $U(1)_{EM}$ symmetry

$$A_\mu = s_w W^3_\mu + c_w B_\mu . \tag{1.24}$$

Consequently, this mechanism, by giving a mass to the $W^\pm$ and Z bosons, provides them also with an additional degree of freedom carried by the absorbed Goldstone boson. This will be linked to an additional degree of freedom in the polarisation. Also, this unifying mechanism implies that electromagnetism and the weak interaction are no longer separated interactions and photons and Z bosons are fundamentally mixed.

Finally a complete description of the electroweak sector of the Standard Model Lagrangian can be made. The weak interaction, from a development of the interaction terms in the covariant derivative of $\mathcal{L}_D$ in Eq. (1.5), uses the massive gauge bosons through the charged current Lagrangian $\mathcal{L}_{CC}$ for the $W^\pm$ and the neutral current Lagrangian $\mathcal{L}_{NC}$ for the Z. For the leptonic isospin doublets formed of the charged lepton field ℓ and the neutrino field ν, these are

$$\mathcal{L}_{CC} = \frac{g}{\sqrt{2}} W_\mu^+ \bar{\ell} \gamma^\mu \frac{1-\gamma_5}{2} \nu_\ell + \frac{g}{\sqrt{2}} W_\mu^- \bar{\nu}_\ell \gamma^\mu \frac{1-\gamma_5}{2} \ell \; , \tag{1.25}$$

$$\mathcal{L}_{NC} = \frac{g}{\sqrt{2}\cos\theta_w} Z_\mu \bar{\ell} \gamma^\mu (c_v - c_a\gamma_5)\ell + \frac{g}{\sqrt{2}\cos\theta_w} Z_\mu \bar{\nu} \gamma^\mu (c_v - c_a\gamma_5)\nu \; , \tag{1.26}$$

with $(1-\gamma^5)/2$ acting as a projector on the left chirality state. The mixed nature of the Z appears with the c_v and c_a parameters that drive vectorial and axial vectorial couplings. From Eq. (1.23), a vectorial part from B is added to the pure left chirality part, giving

$$c_v = I_3 - 2Q\sin^2(\theta_\mathrm{w}) \; , \tag{1.27}$$

$$c_a = I_3 \; , \tag{1.28}$$

with θ_w the weak mixing angle appearing from the identification of the parameters c_w and s_w of (1.23) to a sine and a cosine. The interactions between the electroweak gauge bosons arise from the Yang-Mills Lagrangian

$$\mathcal{L}_{YM} = -\frac{1}{4} W_i^{\mu\nu} W_{\mu\nu}^i - \frac{1}{4} B^{\mu\nu} B_{\mu\nu} \; , \tag{1.29}$$

$$\text{with } B_{\mu\nu} = \partial_\mu B_\nu - \partial_\nu B_\mu \; , \tag{1.30}$$

$$\text{and } W_{\mu\nu}^i = \partial_\mu W_\nu^i - \partial_\nu W_\mu^i + g\left(W_\mu \wedge W_\nu\right)^i \; . \tag{1.31}$$

The supplementary term for the $W_{\mu\nu}^a$ arises from the non abelian nature of the $SU(2)_L$ group. Multiplied by itself, this term will yield quartic gauge couplings, and multiplied by a partial derivative term, it yields a triple gauge coupling. Going to mass eigenstates, almost every possible coupling with $W^\pm$ boson, Z boson and photon respecting charge conservation are allowed, as exemplified in Fig. 1.3. A consequence of the orthogonality of the Z boson and the photon is that couplings with only Z bosons and photons are forbidden.

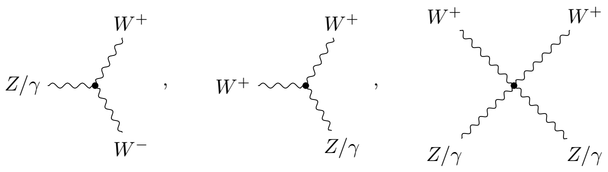

Figure 1.3 Examples of triple and quartic gauge couplings.

1.2 The polarisation of massive vector bosons

1.2.1 Specificities of the longitudinal polarisation

The $W^\pm$ and Z bosons have three degrees of freedom: two from the original massless bosons of the unbroken $SU(2)_L$, and one from the absorbed Goldstone boson. These appear for the massive $W^\pm$ and Z bosons as three different polarisations. Let us consider a vector boson B^μ with momentum four-vector k^μ. Vector bosons being spin 1 particles, three possible spin quantum states exist, each associated to a polarisation vector ε^μ. The boson field can then be decomposed in plane harmonic waves as

$$B^\mu = \varepsilon^\mu e^{\pm ik\cdot x} \ . \tag{1.32}$$

The study of the Lagrangian of a free massive spin 1 boson implies

$$\partial_\mu B^\mu = 0 \Leftrightarrow \varepsilon^\mu k_\mu = 0 \ , \tag{1.33}$$

without any gauge choice. For the photon, such relationship comes at the expense of a gauge choice which in turn destroys one polarisation mode. But for massive gauge bosons, the three polarisations will survive, as hinted by the new degree of freedom gained absorbing a Goldstone boson; the original four dimensions of space-time are reduced to three by Eq. (1.33).

Choosing a frame, such that the four-momentum is expressed $k^\mu = (E, 0, 0, k_z)$, the two transverse polarisation vector can be parametrised as

$$\varepsilon^\mu_\pm = \frac{1}{\sqrt{2}}(0, 1, \pm i, 0) \ , \tag{1.34}$$

which correspond to circular polarisations, left for ε^μ_-, and right for ε^μ_+. It can be shown that they correspond to states of spin along the z-axis $S_z = \pm 1$. In the following, the positive (resp. negative) helicity state will be called *right* polarisation (resp. *left* polarisation). The third polarisation mode, which is going to be longitudinal, is orthogonal to the two transversal polarisations, and to k^μ because of Eq. (1.33). It can thus be written

$$\varepsilon^\mu_0 = \frac{1}{\sqrt{E^2 - k_z^2}}(k_z, 0, 0, E) = \frac{1}{m}(k_z, 0, 0, E) \ , \tag{1.35}$$

where the fore-factor using the mass m of the boson comes from the covariant normalisation $\varepsilon^\mu \varepsilon_\mu = -1$ of the space-like polarisation vectors. It clearly appears from this formula that such polarisation cannot exist for a massless boson.

A fundamental difference arises between longitudinal and transversal polarisations: only the longitudinal polarisation has a dependence with the energy. Consequently, in a Feynman diagram calculation, every longitudinal polarisation increases by a power of one the dependence in the energy of the corresponding matrix element $\mathcal{M}$. This has consequences on the cross section computation that transverse polarisation do not have. At the high energy limit, the mass becomes negligible and $k_z \approx E \gg m$ such that the longitudinal polarisation becomes proportional to the four-momentum

$$\varepsilon^\mu_0 \approx \frac{1}{m} k^\mu \ . \tag{1.36}$$

As a result, from Eq. (1.22) and (1.23), at high energy the longitudinal polarisation corresponds exactly to the $\partial_\mu w$ term, that is the Goldstone boson.

This relates to the Goldstone Equivalence Theorem [28]: a Feynman diagram computation at high energy, that is replacing every longitudinal polarisation vector by the four-momentum as shown in Eq. (1.36), is equal to the computation of the same diagram replacing every longitudinal vector boson by a Goldstone boson. At high energy, the longitudinal polarisation can thus allow probing the BEH mechanism. This is an alternative to probing the Higgs field properties as done in more direct Higgs boson production measurements.

The theoretically distinct nature of the longitudinal polarisation implies that any longitudinal polarisation vector in a matrix element amplitude computation scales with the energy. This effects has striking consequences in the context of vector boson scattering. In such processes, two vector bosons scatter with a quartic gauge coupling. If all bosons in the initial and final states are polarised longitudinally, this results in an amplitude that scales as a power of four of the energy. Such processes have a cross section blowing up at high energy, breaking unitarity. This effect is partly mitigated taking into account, in the amplitude computation, processes involving two triple gauge couplings with an intermediate gauge boson propagator. However, unitarity is only restored considering also processes where the intermediate propagator is a Higgs boson. Any deviation from the Standard Model Higgs boson would therefore spoil the precise cancellations at work in this process. This shows how longitudinal polarisation allows probing processes very sensitive to new physics.

However, vector boson scatterings are very rare processes. The cross section of such process started to be measured only very recently, with the first measurement being performed in $W^{\pm}Z$ production in 2018 [29]. In more accessible cases, it was shown that in diboson inclusive processes with both bosons polarised longitudinally, an amplitude zero effect appears in the angular distribution of both bosons [30]. From an Effective Field Theory point of view, considering polarisation can make visible the impact of interferences of the Standard Model with new physics [31].

1.2.2 The Frame Choice

It should be noted that polarisation is not an intrinsic property of the vector bosons. For example, the longitudinal polarisation is defined as the polarisation along the direction of the boson. Nevertheless, the idea of the direction of a particle is not Lorentz invariant: any boost in another direction than that of the particle in the original frame will change this direction, meaning that the angle between this direction and the boost direction will change. Only a boost in the direction of the particle will preserve this direction.

This can easily be seen, using the same coordinate system as for the polarisation vectors of Eq. (1.34) and (1.35), by defining the projectors P_T on transversal polarisation, and P_L on longitudinal polarisation:

$$
{P_T}^{\mu}{}_{\nu} = \begin{pmatrix} 0 & 0 & 0 & 0 \\ 0 & 1 & 0 & 0 \\ 0 & 0 & 1 & 0 \\ 0 & 0 & 0 & 0 \end{pmatrix} , \qquad {P_L}^{\mu}{}_{\nu} = \begin{pmatrix} 1 & 0 & 0 & 0 \\ 0 & 0 & 0 & 0 \\ 0 & 0 & 0 & 0 \\ 0 & 0 & 0 & 1 \end{pmatrix} . \tag{1.37}
$$

Then, with a boost along the particle direction, here Oz,

$$\Lambda_z{}^{\mu}{}_{\nu}(\beta) = \begin{pmatrix} \gamma & 0 & 0 & \gamma\beta \\ 0 & 1 & 0 & 0 \\ 0 & 0 & 1 & 0 \\ \gamma\beta & 0 & 0 & \gamma \end{pmatrix} , \tag{1.38}$$

one gets

$$[\Lambda_z(\beta), P_L]^{\mu}_{\nu} = 0 \, . \tag{1.39}$$

Whereas along an other direction in the transverse plane, for example Ox,

$$\Lambda_x{}^{\mu}{}_{\nu}(\beta) = \begin{pmatrix} \gamma & \gamma\beta & 0 & 0 \\ \gamma\beta & \gamma & 0 & 0 \\ 0 & 0 & 1 & 0 \\ 0 & 0 & 0 & 1 \end{pmatrix} , \tag{1.40}$$

one gets

$$[\Lambda_x(\beta), P_L]^{\mu}_{\nu} = \gamma\beta \begin{pmatrix} 0 & -1 & 0 & 0 \\ 1 & 0 & 0 & 0 \\ 0 & 0 & 0 & 0 \\ 0 & 0 & 0 & 0 \end{pmatrix} . \tag{1.41}$$

Consequently, the choice of the frame is crucial in any polarisation study. In fact, the choice of the vector boson direction axis, traditionally the z-axis, is what matters. Then, any boost along this axis, for example to go into the boson rest frame, will not change the picture in term of polarisations. In the rest frame of the boson, the polarisation vectors of Eq. (1.34) and (1.35) become

$$\varepsilon^{\mu}_{+} = \frac{1}{\sqrt{2}}(0, 1, +i, 0) , \qquad \varepsilon^{\mu}_{-} = \frac{1}{\sqrt{2}}(0, 1, -i, 0) , \qquad \varepsilon^{\mu}_{0} = (0, 0, 0, 1) \, . \tag{1.42}$$

1.2.3 Spin density matrix

In fact, the polarisation of a vector boson is a frame-dependent intermediary step in calculations. In normal experimental settings, the polarisation state of the colliding particles is not completely known and a statistical description is needed. The most general way of looking at polarisation is through the spin density operator. More details on this section can be found in [32]. In the specific case of an object of spin S in a pure quantum state $|\psi\rangle$, the spin density operator is

$$\hat{\rho} = |\psi\rangle\langle\psi| \, . \tag{1.43}$$

Generically, the density operator allows defining quantum states of which not all quantum numbers are defined as an incoherent sum on pure quantum states. With a basis of the Hilbert space of spin $(|S, m\rangle)_{-S<m<S}$, the spin density operator $\hat{\rho}$ will correspond to the incoherent sum

$$\hat{\rho} = \sum_{m=-S}^{m=+S} \Pi_m |S, m\rangle\langle S, m| \, , \tag{1.44}$$

with $0 < \Pi_m < 1$ the probability of the system to be found in the state $|S, m\rangle$. It thus clearly appears that $\hat{\rho}$ is an Hermitian positive semi-definite operator represented by a spin density matrix ρ of dimension $2S + 1$. It follows from the normalisation principle of quantum mechanics that

$$\mathrm{Tr}\left(\rho\right) = \sum_{m=-S}^{m=+S} \Pi_m = 1 \; . \tag{1.45}$$

Consequently, the spin density matrix is diagonalisable with all eigenvalues positive and with a sum of one. Consequently, the spin density operator described in Eq. (1.43) corresponds to a particular case where one eigenvalue is one and all others are zero. The spin density operator formalism thus generalises the particular case of pure quantum states. In this formalism, the expected value $\langle a \rangle$ of a physical observable $\hat{A}$ is given by

$$\langle a \rangle = \mathrm{Tr}\left(A\rho\right) \; . \tag{1.46}$$

Considering the vectorial spin observable $\hat{\mathbf{S}} = \left(\hat{S}_x, \hat{S}_y, \hat{S}_z\right)$, this allows defining the mean polarisation vector

$$\vec{\mathcal{P}} = \mathrm{Tr}\left(\mathbf{S}\rho\right) \; . \tag{1.47}$$

In classical quantum mechanics, this characterises the spin states of a particle or set of particles. However, relativistically, this picture with spin has to be slightly modified to take into account the additional space time symmetry originating from pure Lorentz boosts. The solution is to consider helicity states of the particles, defined as the projection of the spin along the momentum of the particles $\mathbf{S} \cdot \mathbf{p}/||\mathbf{p}||$. Considering the rest frame of a massive particle – which is the case here – the non-relativistic spin description is still valid. It will correspond to the helicity states description provided that the z-axis of the chosen frame is along the momentum of the particle in the observation frame. This choice is called the *Helicity frame*. Of course, what is the observation frame is dependent on what is being studied experimentally, as will be further discussed in Section 5.4.2.

In the case of a vector boson, the associated spin density matrix can be decomposed in the helicity frame basis of Eq. (1.42) with longitudinal polarisation, noted 0, left polarisation noted L and right polarisation noted R. Studying multiple events where such vector boson is produced, the spin density matrix can be – at least partially – extracted. Thus, the diagonal elements will be called the polarisation fractions and the off-diagonal elements will correspond to interference terms between the pure polarisation states. And from Eq. (1.45) follows the normalisation relation on all three polarisation fractions

$$f_0 + f_\mathrm{L} + f_\mathrm{R} = 1 \; . \tag{1.48}$$

Considering a diboson event, the same formalism can be used, only this time, the spin density matrix will be of dimension nine to represent the system of the two bosons. Similarly as in single boson study, the diagonal elements will be joint-polarisation fractions. For simplicity, the left and right polarised bosons are considered together as in a *transverse* polarisation state noted T. This reduces the nine diagonal elements to four joint-polarisation fractions defined as

$$f_{00} = \rho_{00,00} \; , \tag{1.49}$$

$$f_{0\mathrm{T}} = \rho_{0\mathrm{L},0\mathrm{L}} + \rho_{0\mathrm{R},0\mathrm{R}} \; , \tag{1.50}$$

$$f_{\mathrm{T}0} = \rho_{\mathrm{L}0,\mathrm{L}0} + \rho_{\mathrm{R}0,\mathrm{R}0} \; , \tag{1.51}$$

$$f_{\mathrm{TT}} = \rho_{\mathrm{LL},\mathrm{LL}} + \rho_{\mathrm{LR},\mathrm{LR}} + \rho_{\mathrm{RL},\mathrm{RL}} + \rho_{\mathrm{RR},\mathrm{RR}} \; , \tag{1.52}$$

and the normalisation relationship ensues as before

$$f_{00} + f_{0\mathrm{T}} + f_{\mathrm{T}0} + f_{\mathrm{TT}} = 1 \; . \tag{1.53}$$

In any case, the polarisation fractions or joint-polarisation fractions are only coefficients of the spin density matrix of the vector boson. They have meaning only with the associated basis and corresponding frame chosen for the representation of the matrix.

1.3 Proton–proton collisions at the LHC

The Standard Model processes are studied by a variety of experimental setup. The most versatile one is the use of high energy particle collisions. Fixed target experiments were the first experimental setup used to produce these. Later, particle colliders were considered, allowing to reach higher centre-of-mass energies. In such experiments, two particles are accelerated at high energies and then made to collide together. The high energy interaction can lead to a variety of processes later studied by a detector positioned around the collision point. Historically, the simplest form of such collisions involved electrons and positrons in leptonic colliders. Hadronic colliders, smashing together protons or alternatively protons and anti-protons, make it possible to reach higher collision energy. However, using a composite particle such as the proton introduces complexities that will detailed here.

1.3.1 Parton distribution functions

Because of the confinement of the colour charge at low energy, a consequence of Quantum Chromodynamics (QCD), quarks and gluons, together called partons, cannot exist isolated; they always assemble to form colour neutral object called hadrons. Protons are hadrons classically described as composed of two up quarks and one down quark. Nevertheless, the picture is actually more complex as small and short lived energy fluctuations can create within the proton virtual pions, that is pairs of quark-antiquarks. As opposed to the *uud* valence quarks of the protons, these are called sea quarks. All these quarks are coupled in low energy QCD interaction by gluons which as such are also components of the proton.

In QCD, the strong coupling constant α_s decreases when the energy scale considered increases. This leads to an asymptotic freedom of partons which allows considering protons colliding at high energy as an incoherent sum of partons each carrying a fraction of its momentum. This is described by *Parton Distribution Functions* (PDF) that can be noted

$$f_{q/p}\left(x_q, Q^2\right) \; .$$

They are the probability density function associated to a parton q holding a fraction x_q of the momentum of the hadron. These PDF are determined for a given hadron, here denoted by the index p for protons, and for a specific parton, be it a quark, anti-quark or a gluon, here denoted by the index q. Finally, the PDFs are determined at a certain probing energy scale Q^2. They are obtained experimentally with lepton-proton collider at a given probing energy and can be converted to another energy scale from theoretical considerations.

Because of sea quarks, the normalisation of the PDF of a given parton type is not constant, but by definition of the valence quark, in a proton the following relations hold:

$$\int_0^1 dx\,\Big(f_{u/p}(x) - f_{\bar{u}/p}(x)\Big) = 2\ , \tag{1.54}$$

$$\int_0^1 dx\,\Big(f_{d/p}(x) - f_{\bar{d}/p}(x)\Big) = 1\ . \tag{1.55}$$

Also, the total momentum of the proton is recovered summing incoherently all the partons meaning that

$$\int_0^1 dx \sum_q x\, f_{q/p}(x) = 1\ . \tag{1.56}$$

This gives information on the repartition of the momentum of the proton among different partons. At low energy, most of the momentum is carried by the valence quarks u and d. Nevertheless, at higher energy, gluons take more importance as illustrated in Fig. 1.4 for the CT10 PDF set[1] . The valence quark are still found on average with around a third of the momentum of the proton as the simple uud picture would suggest. Yet at high energy, overall, gluons represents the highest share of the proton momentum. On the other hand, the anti-quarks of the sea always represent a small share of the momentum and hold on average less than 10 % of the momentum.

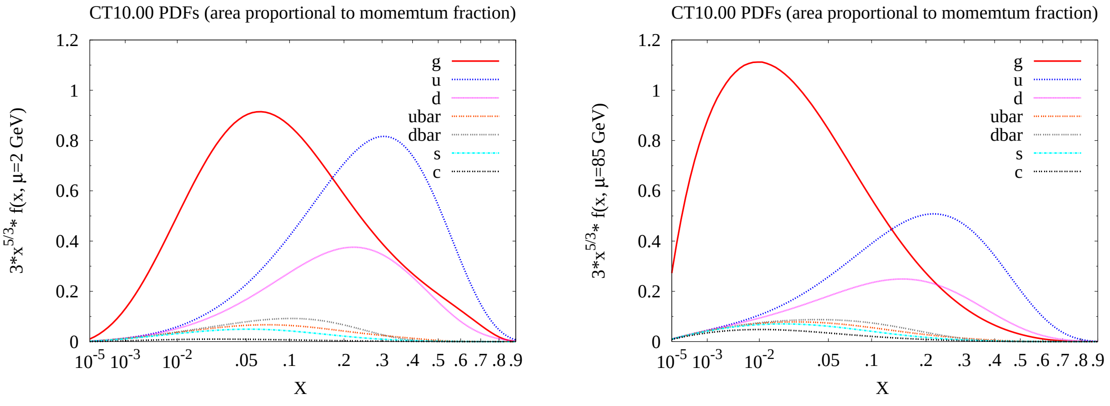

(a) (b)

Figure 1.4 Parton distribution functions of the proton from the CT10 PDF set [33] at an energy scale of 2 GeV (a) and 85 GeV (b). From Ref. [33].

1.3.2 Deep inelastic scattering in proton–proton collisions

In pp collisions, deep inelastic scattering happens when partons within the proton interact directly. Other processes can be elastic scattering – when both protons are left intact and only deviated after the collision – and diffractive collisions – when one are both protons are excited leading to some activity after the collision. Processes studied at hadronic colliders usually originate from deep inelastic scattering.

The description of such processes mixes different energy scale. Their perturbative description rests on the Taylor expansion of Eq. (1.3). The various terms of the Taylor expansion are in powers of the coupling constant of the interaction Lagrangian. The QCD

---

[1] The CT10 PDF set is the main set used in the Powheg Monte Carlo generation described ahead.

coupling constant α_s is typically close to 0.1, and evolves with the energy scale. At high energy, the hard scattering process between the partons can be treated with perturbative QCD calculation. Nevertheless, this usually can only be done up to Next to Leading Order (NLO) because of the complexity of the calculation and cutting the Taylor expansion at a fixed-order leaves some quantities to be divergent. This is treated with a renormalisation procedure that relies on a chosen energy scale μ_R, typically chosen to be the energy scale of the interaction studied. The renormalisation will absorb divergences in physical parameters like the value of a coupling, and the dependence on μ_R of the computed quantity will vanish as more and more orders are taken into account.

This treats well the problem of Ultra-Violet divergences that arise from the fixed-order computation in perturbative theory. In QCD, new difficulties arise from Infra-Red divergences, linked to the high value of the coupling constant at low energy and the invalidity of the perturbative treatment. Another energy scale is used to treat these divergences called the factorisation scale μ_F. Below this scale, in the soft QCD regime, the perturbative description is replaced by other descriptions depending on the context. In the initial state of the collision, PDFs as described in Section 1.3.1, are used to model the soft QCD processes taking place within the proton.

A *pp* collision is thus described with a combination of PDF to model the initial state and perturbative theory cross section calculation to model the hard scattering of two partons in the collision. This is represented by the factorisation formula [34]

$$\sigma_{pp\to X}(s) = \sum_{a,b\in\{q,g\}} \int_0^1 dx_a \int_0^1 dx_b f_{a/p}\left(x_a, \mu_F^2\right) f_{b/p}\left(x_b, \mu_F^2\right) \sigma_{ab\to X}\left(x_a x_b s, \mu_R^2, \mu_F^2\right) \quad (1.57)$$

with $\sigma_{pp\to X}(s)$ the total cross section of the production of X in *pp* collisions at centre-of-mass energy $\sqrt{s}$; $\sigma_{ab\to X}\left(x_a x_b s, \mu_R^2, \mu_F^2\right)$ the computed cross-section of the parton–parton interaction between parton a and b producing X, with x_a and x_b the fraction of momentum carried by the partons and thus $x_a x_b s$ the energy of the cross-section calculation; $f_{a/p}$, $f_{b/p}$ the PDFs of the partons in proton. Typically, the scales μ_R and μ_F are chosen equal.

1.3.3 Modelling of inclusive *pp* collisions

The cross section $\sigma_{pp\to X}$ computed with Eq. (1.57) corresponds to the inclusive production of X in *pp* collisions. It however does not specify anything on X subsequent evolution and possible particles produced alongside. The cross sections of the parton processes $\sigma_{ab\to X}$ are typically computed with Monte Carlo generators. The resulting final state particles are said to be at *Born* or *parton level*, and their subsequent evolution through soft physics processes before detection has to be modelled [34].

Born leptons, through final state radiations, will radiate photons and be reconstructed in a cluster by the detector. This final object, is called a *dressed lepton*. This evolution is even more striking for final state quarks and gluons. They will first evolve through parton showers, with multiple gluon radiations and quark pair productions. When the energy of the showering partons becomes small enough, the QCD colour confinement starts to form colour neutral particles in a process called hadronisation. The formed hadrons, *e.g.* pions, kaons, B-mesons, are usually unstable and will decay in other hadrons. This complex final state is said to be at the *particle level*. The complex structure of these parton showers are grouped in cones named *jets*. These jets are the experimental object considered by the particle detector around the collision point. Additionally, beyond the main process, the other partons in the initial protons can create secondary parton interactions. Along with the beam remnants after the collision, these constitute underlying events. All these soft physics processes around a *pp* collision are summarised in Fig. 1.5.

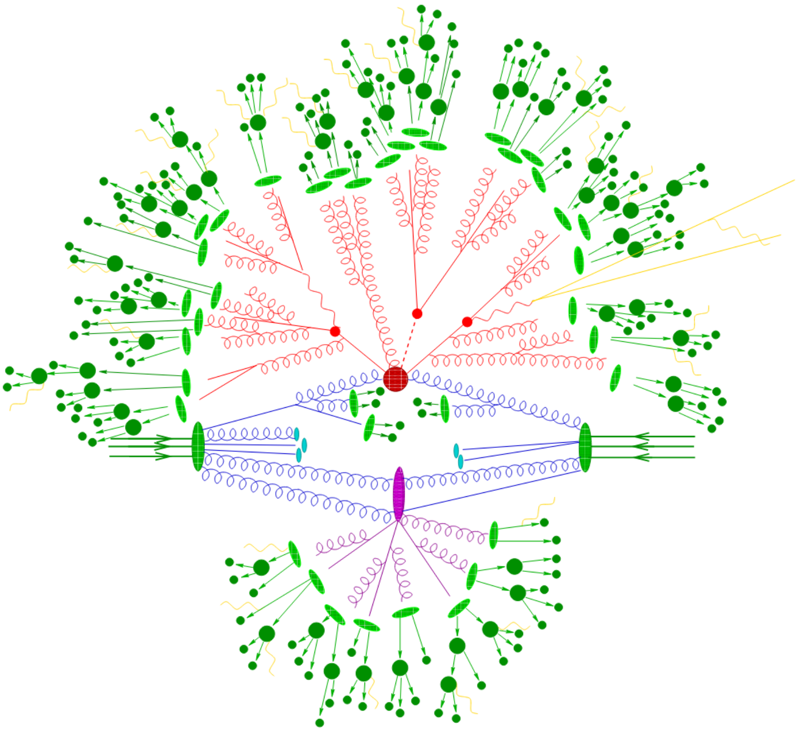

Figure 1.5 Sketch of all the different processes in a *pp* collision as modeled by a Monte Carlo generator. The incoming protons are represented by green blobs in the horizontal direction. The blue lines represent the interacting partons and their initial state radiations. The red blob in the centre represents the hard scattering between two partons. The subsequent parton shower is represented in the tree like structure in red. The following hadronisation is represented in light green, with each small dark green blob denoting a decaying hadron. The radiated photons are represented by yellow lines. A secondary parton interaction is represented in the purple blob. The beam remnants are the light blue blobs. From Ref. [34].

The hard scattering is modelled through a Monte Carlo computation of the matrix elements of the considered process. Monte Carlo generators such as MadGraph [35] or Powheg [36] can usually perform this computation at LO or NLO. Nevertheless, the soft physics processes described earlier are usually not modelled by the main Monte Carlo generator and require a dedicated program abusively called parton shower generator, such as Pythia [37]. From the parton level they will generate parton showers, with each parton having a probability to split in two, be it from gluon radiation or quark pair production. This showering process makes up for higher order QCD left out from the main diagram computation, and are branched on each final state parton. Then, dedicated algorithms of matching and merging are responsible for avoiding double counting with the higher orders computed in the hard scattering matrix elements. This makes it possible to interface the parton shower generator to a main generator [38, 39]. The hadronisation cannot be computed directly and is thus modelled by algorithms based on the string model or the cluster model. The parton shower generator Pythia uses the string model. Another Monte Carlo generator is Sherpa [40]. It internally does everything from the hard scattering matrix element computation to the soft physics, and relies on the cluster model for hadronisation.

Chapter 2

The LHC and the ATLAS detector

The European Organisation for Nuclear Research (CERN) was established in 1954 as a peaceful international organisation promoting fundamental Physics research in second world war devastated Europe. Situated at the French-Swiss border, close to Geneva, the CERN developed, among other experiments, a succession of particle accelerators reaching ever increasing collision energies. After the Synchrocyclotron (1957), the Proton-Synchrotron (1959), and the Super-Proton-Synchrotron (1979), a circular tunnel of 26.7 km was dug for the Large Electron Positron (LEP) collider that started operations in 1989. Finally, this tunnel was reused to give way to the Large Hadron Collider (LHC) [41] in 2008, currently the most powerful particle accelerator in the world, with a design centre-of-mass energy of 14 TeV. The design, operations and future prospects of this particle collider will be described in Section 2.1. The LHC hosts four experiments: ATLAS, ALICE, CMS and LHCb. The work presented in this thesis was performed within the ATLAS Collaboration. The ATLAS experiment [42] will be described in Section 2.2, sub-detector by sub-detector with a focus on the Liquid Argon calorimeters.

2.1 The Large Hadron Collider

2.1.1 Luminosity

A particle collider is characterised by its centre-of-mass energy $\sqrt{s}$, which determines the type of physics processes allowed, and its luminosity which describes the amount of collisions taking place at the interaction point. For a given physical process created in particle collisions, the production rate dN/dt at centre-of-mass energy $\sqrt{s}$ is

$$\frac{dN}{dt}\left(\sqrt{s}\right) = L \cdot \sigma\left(\sqrt{s}\right) \ . \tag{2.1}$$

This is the product of the cross section σ, holding all the underlying physics of this process and directly dependent on the energy, and a parameter depending only on the proton beam characteristics, called the instantaneous luminosity L.

Along with a design centre-of-mass energy in its collision of $\sqrt{s} = 14\,\text{TeV}$, the LHC is also characterised by a high nominal instantaneous luminosity of $1 \times 10^{34}\,\text{cm}^{-2}\,\text{s}^{-1}$. For comparison, this is two orders of magnitude above the peak instantaneous luminosity of the Large Electron Positron collider [43] or the Tevatron, an older $p\bar{p}$ collider located at Fermilab [44]. The instantaneous luminosity at the LHC characterises the proton beams, aggregating the beams parameters in the following way,

$$L = \frac{N_b^2 \cdot n_b \cdot f_{rev}}{4\pi\sigma_x\sigma_y} F \ , \tag{2.2}$$

where

- N_b is the number of protons per bunch. The nominal value at the LHC is 1.15×10^{11}.
- n_b is the number of bunches per beam. The nominal value at the LHC is 2760.
- f_{rev} is the revolution frequency of the LHC, of 11.245 kHz. This parameter is directly linked to the time taken by particles to travel along the length of the LHC ring at the speed of light.
- σ_x and σ_y are the transverse dimension of the beam at the interaction point. They are of the order of 10 ţm.
- F is a geometric reduction factor, between 0.3 and 1, originating from the crossing angle at the interaction point.

This can be rewritten

$$L = \frac{N_b^2 \cdot n_b \cdot f_{rev}\gamma}{4\pi\varepsilon_n\beta^*} F \ , \tag{2.3}$$

with γ the relativistic gamma factor, and introducing parameters governing the shape of the beam which are

- the normalised emittance ε_n, which holds information on the proton density in the beam. It should be the lowest possible; its nominal value at the LHC is 3.75 ţm.
- the beta function β^* at the interaction point. The β function is the envelop of the beam, and the squeezing at interaction point should make it the lowest possible. Its nominal value, dependent on the interaction point considered, is 55 cm for the ATLAS and CMS detectors.

Since the cross section of a physics process is constant in time, one can integrate Eq. (2.1) over the running period of the collider to obtain the so-called integrated luminosity $\mathcal{L}$, as the factor to a cross section to get the event yield of a process.

2.1.2 The LHC machine and operation

The LHC was installed in the pre-existing tunnel of the Large Electron Positron collider, 26.7 km long, 3.8 m wide and situated approximately 100 m under the surface. Differently from its predecessor, the particles collided are of the same sign, and as a result they rotate in two separate opposite direction beams curved by oppositely-poled magnets. Because of a lack of space in the tunnel, both beams are in the same yoke visible in Fig. 2.1(a), with two oppositely poled magnets of around 8 T made of Niobium-Titanium superconducting coils cooled below 2 K in superfluid helium.

Beside the circular parts of the tunnel, there are eight straight sections of a few hundred meter in each of the eight octants of the ring as visible in Fig. 2.1(b). Four such sections host an interaction point with one of the experiment of the LHC: ATLAS in octant 1, ALICE in octant 2, CMS in octant 5 and LHCb in octant 8. ATLAS and CMS are general purpose detectors collecting high luminosity data from proton–proton collisions. ALICE is specialised in heavy ion collisions, happening in special runs of the LHC. LHCb is an asymmetrical detector operating at reduced luminosity and specialised in b-physics and CP violation measurements. The beam is accelerated by radio-frequency cavities of 400 MHz located in octant 4. Finally, a beam dump is installed in octant 6, and octant 3 and 7 host magnets responsible for the cleaning and re-collimating of the beam.

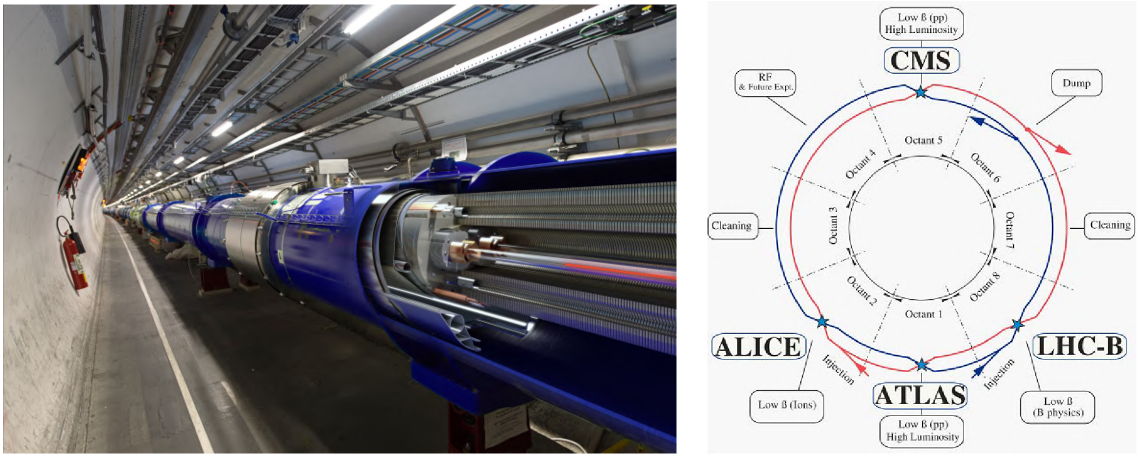

(a) **(b)**

Figure 2.1 (a) A dipole magnet in the LHC tunnel. The two beam pipes are made visible by the 3D cut inside the magnet yoke.
(b) Schematic layout of the LHC and its four experiments ATLAS, ALICE, CMS and LHCb. Figure from Ref. [41].

The magnets of the LHC are unable to cover the full range needed to curve protons from their original energy up to the final LHC beam energy. As a result, the filling of the LHC ring with a proton beam is not done at once. Most CERN previous accelerators are used in a chain shown in Fig. 2.2 to fill the LHC with a proton beam at the design energy. First, the dihydrogen H_2 of the source is ionised to obtain protons H^+, and brought to 50 MeV in the linear accelerator LINAC2[1]. Then the Proton-Synchrotron (PS) together with its four Boosters (PSB) are responsible to bring this proton beam to 26 GeV. Then, the Super-Proton-Synchrotron (SPS) brings it to 450 GeV. Finally this proton beam is split in two and injected in the LHC to create the two opposite direction proton beams.

In all this process, the protons are organised in bunches. The protons arriving from the LINAC are accelerated and grouped by the four PSB in bunches of around 10^{11} protons every 25 ns, that is at a frequency of 40 MHz [41]. Considering that each bunch travels at a speed very close to the speed of light, and the fact that the LHC ring is 26.7 km long, theoretically there are slots for 3560 bunches in the LHC. Nevertheless, the design number of bunches in the LHC ring is of 2760, as stated in Ref. [41]. The first reason for this is a time gap needed by the beam dump. The kicker magnet deviating the beam to the beam dump takes a few microseconds to ramp-up, a time during which there should not be any proton passing through. Another reason is the LHC filling scheme which can be changed and is responsible for variations in the number of bunches over the years.

---

[1] LINAC2 was replaced by LINAC4 as a result of the LHC Injector Upgrade that took place during Long Shutdown 2. LINAC4 accelerates H^- at 160 MeV [45].

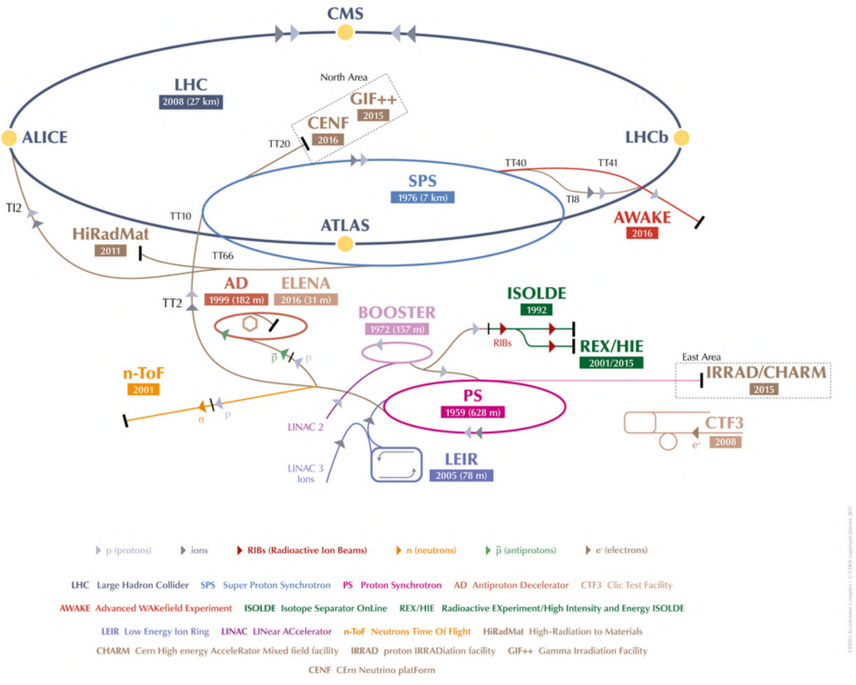

Figure 2.2 The CERN accelerator complex [46].

Not all the proton bunches of the final beam can be sent at once in the LHC. In each of the accelerators of the chain from LINAC2 to the LHC, only a certain number of bunches at speed close to the speed of light can fit given the length of the ring and their time spacing of 25 ns. As a result, once the bunches in one intermediary accelerator have reached the expected energy, they are sent to the next accelerator and stored in loop until this next accelerator is filled. Then this next accelerator starts accelerating all these bunches to the designed energy and the process is repeated (Fig. 2.3). This results in a structure of bunches organised in trains. In the nominal design, the PS injects trains of 72 bunches to the SPS which in turns injects such trains grouped by four in the LHC.

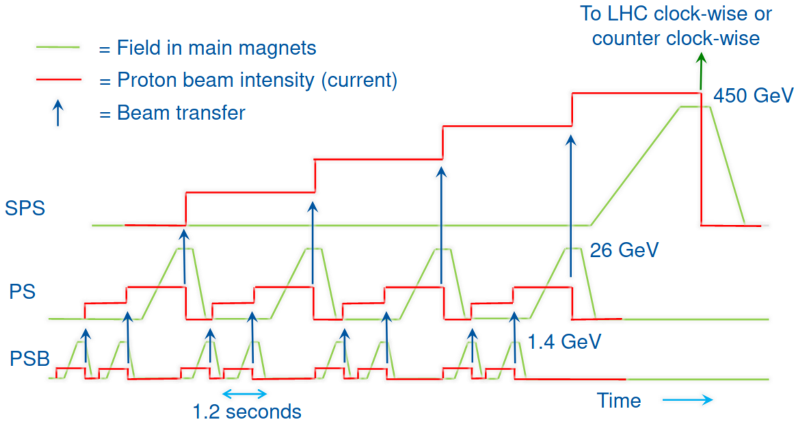

Figure 2.3 Filling and acceleration scheme of the LHC, from the Proton-Synchrotron Boosters (PSB) through the Proton-Synchrotron (PS) and the Super-Proton-Synchrotron (SPS) before sending to the LHC. From Ref. [47].

Once the two proton beams of the LHC have reached their final intensity, the LHC accelerates them to their final energy. The whole process, with some additional time for squeezing and adjusting the beams, takes approximately two hours. Then the two stable beams obtained are used in collisions at the interaction points of the LHC. The beams intensity then goes down as the protons are destroyed in the collisions. This lasts for around twelve hours until the moment when it is more effective luminosity-wise to dump everything and wait for the injection of a new beam.

This LHC cycle is associated in a detector like ATLAS to a continuous period of data taking called a *run*. Events recorded in ATLAS are uniquely defined by their run number, which never resets, and their event number which resets at each run. Yet, along the run, the beam intensity is bound to decrease, and though playing on the beam crossing parameters (called *Luminosity levelling*) can maintain the instantaneous luminosity approximately constant, its exact value along the run has to be measured and recorded. Consequently, a run is subdivided in Luminosity blocks which correspond to a subset of events associated to a known instantaneous luminosity. These Luminosity blocks correspond to around one minute of data taking, that is a few hundred thousands of events.

2.1.3 The LHC timeline

The LHC was first started in 2008. A failure in a dipole magnet forced the LHC to stop and resume in 2010 for Run-1 at a reduced centre-of-mass energy – $\sqrt{s} = 7\,\text{TeV}$ in 2010-2011, 8 TeV in 2012 – and a reduced instantaneous luminosity. After Long Shutdown 1 (LS1) used for consolidation of dipole magnets, the LHC restarted for Run 2 reaching $\sqrt{s} = 13\,\text{TeV}$, close to the design beam energy, and reaching for the first time its nominal luminosity in 2016. Run 2 ended in 2018 with the luminosity reaching the double of its nominal value. Along Run 2, from 2015 to 2018, the data taking in the ATLAS detector provided, as shown in Fig. 2.4, an integrated luminosity of $\mathcal{L} = 139\,\text{fb}^{-1}$ of data considered good for physics analysis. This luminosity is estimated experimentally with the LUCID-2 detector [48] located on both sides of the ATLAS detector around the beam pipe. This measurement is calibrated with a relative uncertainty of 1.7 % [49]. This is the dataset that will be considered in this thesis.

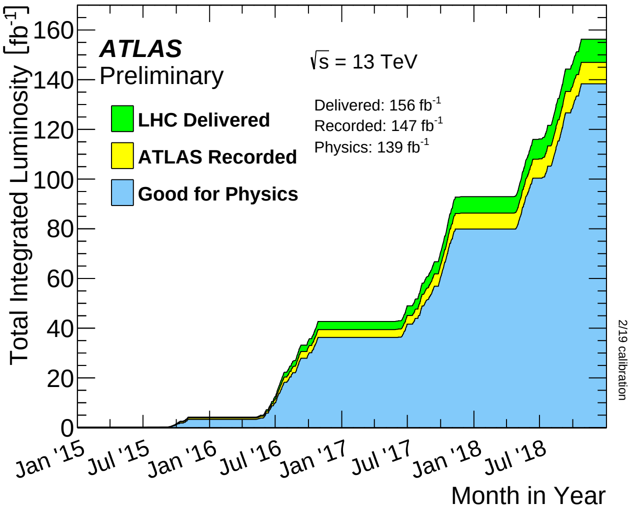

Figure 2.4 Cumulative luminosity versus time delivered to ATLAS (green), recorded by ATLAS (yellow), and certified to be good quality data (blue), during stable beams for *pp* collisions at 13 TeV centre-of-mass energy in 2015-2018. From Ref. [50].

2.1.3.1 Pile-up in the Run 2 data

Collisions in a hadron collider usually do not happen one by one. For one collision of interest, a number of additional collisions happening in its vicinity and within a short time interval create what is called in-time pile-up. Such pile-up can originate from interactions of proton with residual gas in the beam pipe or with a LHC collimator. But the main source of pile-up originates from additional hard scattered proton–proton collisions, as a direct effect of the luminosity. At *bunch-crossings*, happening every 25 ns, bunches of around 10^{11} protons from each beam interact. This usually gives rise to more than one proton–proton collision. The mean number of interaction per bunch-crossing is defined as

$$\mu = \frac{L \cdot \sigma_{inelastic}}{n_b \cdot f_{rev}} , \tag{2.4}$$

where L is the instantaneous luminosity, $\sigma_{inelastic}$ the proton–proton inelastic scattering cross section, taken to be 80 mb at 13 TeV, n_b the number of bunches and f_{rev} the LHC revolution frequency. Out-of time pile-up on the other hand arises from the time response of the detector to an interaction with particles that can last during several bunch crossings. As a result, with more in-time pile-up comes more out-of-time pile-up.

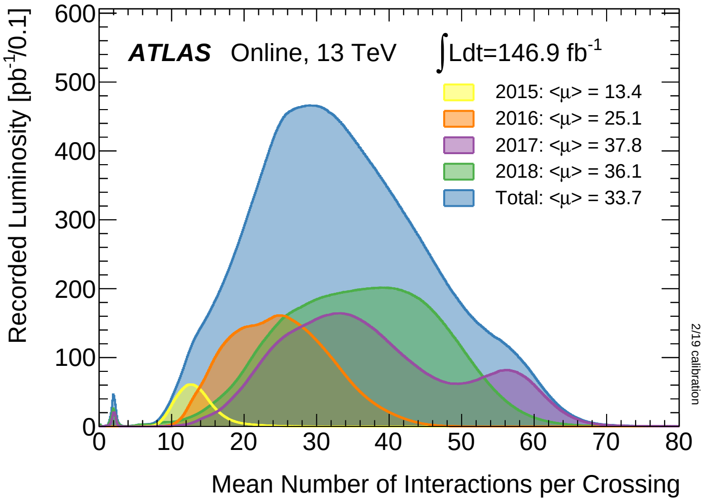

Figure 2.5 Shown is the luminosity-weighted distribution of the mean number of interactions per crossing μ for pp collision data at 13 TeV centre-of-mass energy, for the full Run 2 data taking period (blue) and per year: 2015 (yellow), 2016 (orange), 2017 (violet) and 2018 (green). The overall mean number of collisions $\langle\mu\rangle$ is given per period in the legend. From Ref. [50].

The evolution of this μ is visible on Fig. 2.5 along the four years of Run 2. After 2015, a year dedicated to machine operations for the restart of the LHC, the nominal setup was reached in 2016: with $L = 10^{34}\,\mathrm{cm}^{-2}\,\mathrm{s}^{-1}$ and 2760 bunches, μ is around 25. Yet, it was found possible to decrease the β^* parameter from 55 cm to 30 cm in 2017 and up to 25 cm in 2018, because of better performances than expected from the triplet magnets responsible for the focusing of the beam. Together with an optimised formation of bunch from the PSB to the PS, emittance was also reduced, allowing the luminosity to reach the double of its nominal value. As a result, μ reached almost the double of its nominal value during 2017. Increased use of luminosity levelling at the interaction points allowed reducing it to more manageable values in 2018, around 30–40. This resulted in higher than expected integrated luminosity, with a record of $\mathcal{L} = 65.1\,\mathrm{fb}^{-1}$ in 2018.

An increased luminosity allows the detectors to gather evermore data and study rarer events. But high pile-up is the price to pay, significantly interfering with the reconstruction of events in the detectors. Another consequence of high luminosity is the degradation of the components of the detectors because of high levels of radiations. Both effects require the detectors to go through upgrades to cope with an increasing luminosity.

2.1.3.2 Future runs of the LHC

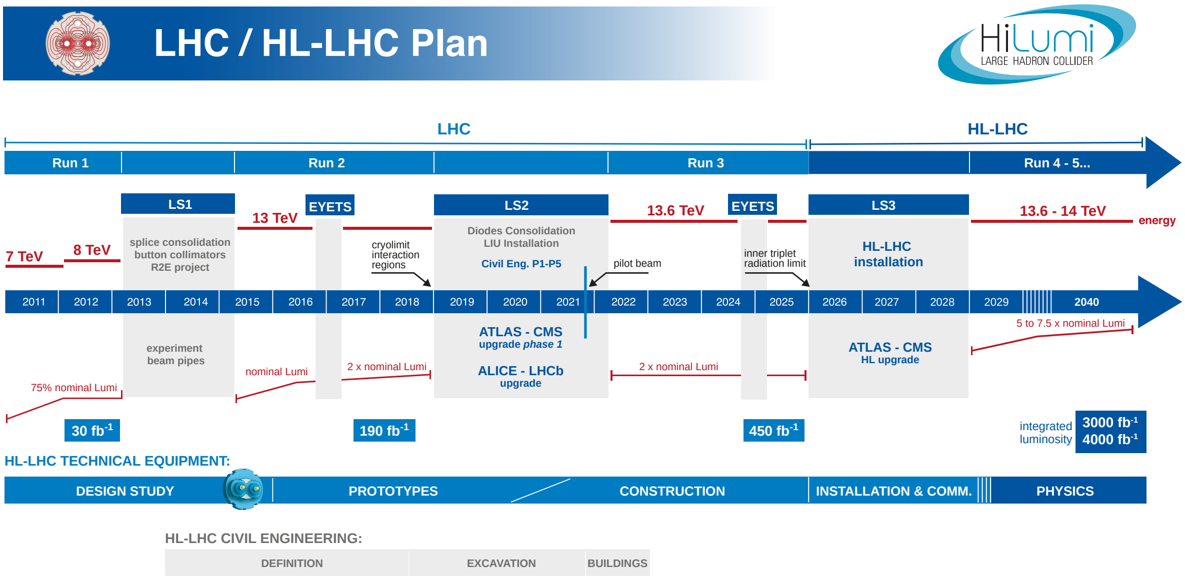

Figure 2.6 LHC baseline plan for the next decade and beyond showing the collision energy (upper line) and instantaneous luminosity (lower line). Plan as taken from Ref. [51] last updated in February 2022.

As is visible in Fig. 2.6, the LHC is forecast to enter a High-Luminosity phase (HL-LHC) in 2029 with the instantaneous luminosity reaching five times its nominal value[2], with hopes of pushing it up to $7.5 \times 10^{34}\,\mathrm{cm}^{-2}\,\mathrm{s}^{-1}$. In the following twelve years or so of HL-LHC, the data collected could reach from $3000\,\mathrm{fb}^{-1}$ up to $4000\,\mathrm{fb}^{-1}$, around ten times what will have been collected previously. In order to reach such high luminosity, on one hand the injection system will be upgraded to increase the beam intensity [45], and on the other hand various systems of the LHC will have to be adapted to cope with this more intense beam [52] (focusing triplet magnets at the interaction region, cryogenics, beam dump, etc.). The four LHC experiments will also need to adapt to the increased pile-up ensuing from such high luminosity, with a μ as high as 200. Additionally, many LHC systems and sub-detectors of the LHC experiments that suffered from high radiations along the LHC runs need replacements.

---

[2] The value of the instantaneous luminosity is given with levelling at the interaction point. Otherwise, at the start of the run, it could be much higher.

The upgrades needed for HL-LHC make use of two Long Shutdowns to be installed. From 2019 to 2021, Long Shutdown 2 (LS2)[3] allowed the installation of the LHC Injector Upgrade and the Phase 1 upgrades of the ATLAS and CMS detectors. Long-Shutdown 3 (LS3) will in turn allow the installation of HL-LHC new equipments and the Phase 2 upgrades of ATLAS and CMS.

In between, Run 3 will make use of the results from the LHC Injector Upgrade [45] together with the improvement that allowed doubling the luminosity in the previous run. The goal is to use this Run as a full scale demonstrator of some features of High Luminosity LHC. One such consequence is an increased brightness of the beam with a number of proton per bunch that should reach 1.8×10^{11} [53]. Improvements from the Phase 1 upgrade of the ATLAS experiment could as a result be used already in Run 3 to cope with a μ that could reach 80. On the energy side, because of some failures in dipole magnets, the nominal energy is still out of reach; the centre-of-mass energy for this run was decided to be 13.6 TeV [54]. The value of the different beam parameters through Run 2 and forecasted for Run 3 are summarised in Table 2.1.

Table 2.1 Parameters of the proton beam at the LHC and ensuing luminosity and pile-up. First column give LHC design values. The second column gives the parameter for Run 2 on average (or maximum if stated). The third column gives prospect values for the Run 3. Values are from Ref. [55], except Run 3 beam energy from final decision value [54].

	Design	Run 2	Run 3
Beam energy [TeV]	7.0	6.5	6.8
Protons per bunch (at start of run), $\times 10^{11}$	1.15	1.2	$1.2 \rightarrow 1.8$
Number of bunches	2800	2500	2800
Normalised Emittance [ţm]	3.75	2.2	2.5
Minimum β^* [cm]	55	$30 \rightarrow 25$	25
Peak Luminosity, [$10^{34}\,\mathrm{cm}^{-2}\,\mathrm{s}^{-1}$]	1.0	2.0	2.0
Peak Pile-up	25	60	55
Total integrated luminosity (LHC delivered) [fb^{-1}]	-	156	350

2.2 The ATLAS experiment

The ATLAS experiment is a general-purpose experiment. It aims at collecting as much information as possible from the particles produced by the high energy inelastic proton–proton collisions provided by the LHC at interaction point 1. Such informations are the energy, momentum, and charge of leptons, photons and hadronic jets. The nature of the particle is also determined combining informations from various sub-detectors. Particles that leave the experiment undetected, such as neutrino or exotic invisible particles, can also be reconstructed using the conservation of momenta in the plane transverse to the beam axis. All these informations allow reconstructing the physics process that took place at the collision and study fundamental phenomena.

---

[3] LS2 was extended by one year to cope with the delay induced in the upgrades mainly by the Covid-19 pandemic. Run 3 was also extended by 18 months with an extended year-end technical stop (EYETS) at the end of 2023.

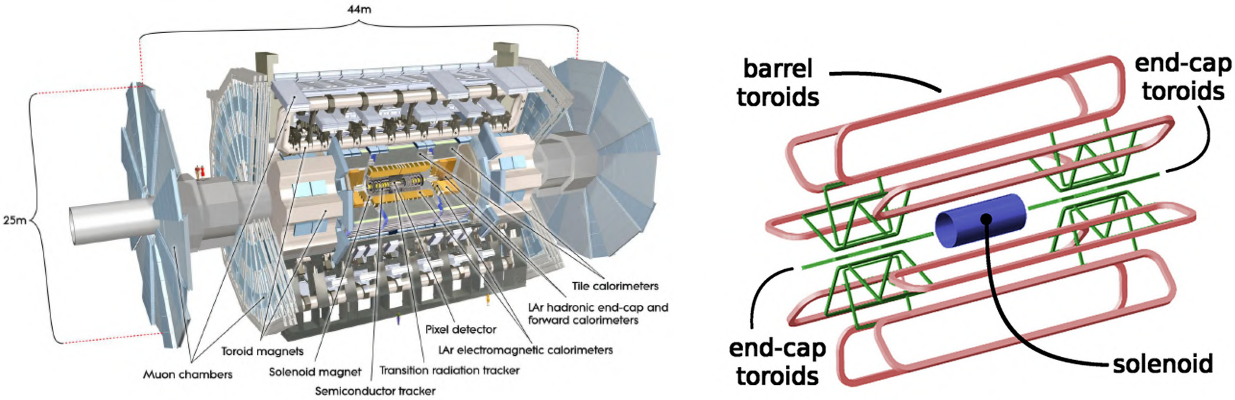

(a) **(b)**

Figure 2.7 The ATLAS detector (a) and the magnet system (b). Taken from Ref. [42].

The ATLAS detector can be roughly described as a 7000 t cylinder 25 m high, 44 m long and located 80 m underground along the beam axis, with the collisions taking place at the centre of the structure. The goal is to cover as much of the solid angle around the collision point as possible. Consequently, ATLAS can be sub-divided in a barrel oriented along the beam axis and two symmetrical end-caps closing the barrel on each side.

Inside the barrel, closest to the beam axis is the Inner Detector (see Section 2.2.2) responsible for detecting the tracks of charged particles, based on two technologies: pixel and micro-strip semiconductors, and Transition Radiation Trackers (TRT). A thin superconducting solenoid surrounding it is responsible for the creation of an axial 2 T magnetic field inside the Inner Detector to curve the tracks and extract their momentum. Then, an electromagnetic calorimeter based on Liquid Argon (LAr) technology is responsible for the measurement of the energy of electrons and photons (see Section 2.2.3.1), stopping them in the process. Heavier particles are stopped in the following layer, a hadronic calorimeter. In the end-caps, it is based on LAr technology; in the barrel it is based on scintillating Tiles (see Section 2.2.3.2). Finally, to detect the tracks of muons, the last charged particle able to cross all the calorimeters, Muon Chambers (see Section 2.2.4) surround the whole. To curve the muons tracks, the chambers are bathed in a toroidal 0.5–1.0 T magnetic field around the calorimeters barrel, generated by three eightfold magnets, one large in the barrel and two smaller ones in each end-caps. These give its name to the detector ATLAS, *A Toroidal LHC ApparatuS*.

The general structure of the ATLAS detector is illustrated in Fig. 2.7(a) along with its magnet system in Fig. 2.7(b). Most of the information in the following sections are taken from Ref. [42].

2.2.1 ATLAS coordinates

In order to locate its different components, an ATLAS coordinate system is defined in Fig. 2.8(a). The origin of this coordinate system is the interaction point. The x-axis points from the collision point to the centre of the LHC ring and the y-axis points upward. This results in a Cartesian right-handed coordinate system with the z-axis along the beam, in the counter-clockwise direction as seen from above. The positive z side of ATLAS is labelled side A; the negative z side is labelled side C. Spherical coordinates are used around the

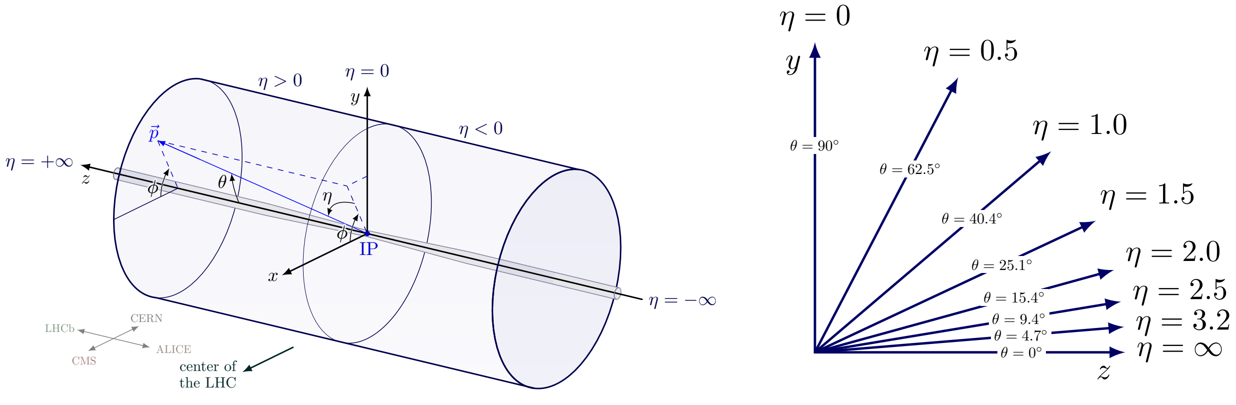

(a) **(b)**

Figure 2.8 (a) The ATLAS coordinate system. (b) Correspondence between the pseudo-rapidity η and the angle θ.

collision point, with ϕ the azimuthal angle around the z-axis and θ the angle with the z-axis. The ϕ angle fits well with the barrel geometry of the detector while the θ angle gives an idea of how transverse or forward/backward a particle is.

An object in the detector, a particle or group of particles, can be characterised by its energy E and its momentum $\vec{p}$. These physical quantities are linked in the four-vector $\mathbf{p} = (E, \vec{p})$ which is normalised to the invariant mass squared m^2_{inv} of the object with the relation

$$\mathbf{p} \cdot \mathbf{p} = E^2 - \vec{p}^{\,2} = m^2_{inv} \ .$$

The *transverse* momentum p_{T} corresponds to the component of the momentum in the (x, y) plane, $p_{\mathrm{T}} = \sqrt{p_x^2 + p_y^2}$. The *longitudinal* momentum is thus p_z. With this, we can define the rapidity

$$y = \ln\left(\frac{E + p_z}{E - p_z}\right) \ .$$

This quantity has the property of being an additive quantity under a boost along the z-axis. Differences of rapidity are thus Lorentz invariant quantities under such boosts.

In the context of high energy collisions at the LHC, most particles can be considered light, with masses orders of magnitude below their typical energy of a few GeV. In the limit of $m_{inv} << E$, the rapidity becomes equivalent to a pseudo-rapidity η defined as

$$\eta = -\ln\left(\tan\frac{\theta}{2}\right) \ .$$

In practice, this quantity is used instead of the polar angle θ. As a result, a position in the barrel can be described in the (η, ϕ) plane. The correspondence between the pseudo-rapidity η and the angle θ is visible in Fig. 2.8(b). It follows that distances between objects in this plane, used to define their isolation, can be expressed as $\Delta R = \sqrt{\Delta\eta^2 + \Delta\phi^2}$.

Finally, the transverse energy E_{T} defined as the energy in the transverse plane can be expressed as $E_{\mathrm{T}} = \sqrt{m^2 + p_{\mathrm{T}}^2}$. This can be rewritten $E_{\mathrm{T}} = E/\cosh(y)$, becoming in the low mass approximation,

$$E_{\mathrm{T}} = E/\cosh(\eta) \ . \tag{2.5}$$

2.2.2 The Inner Detector

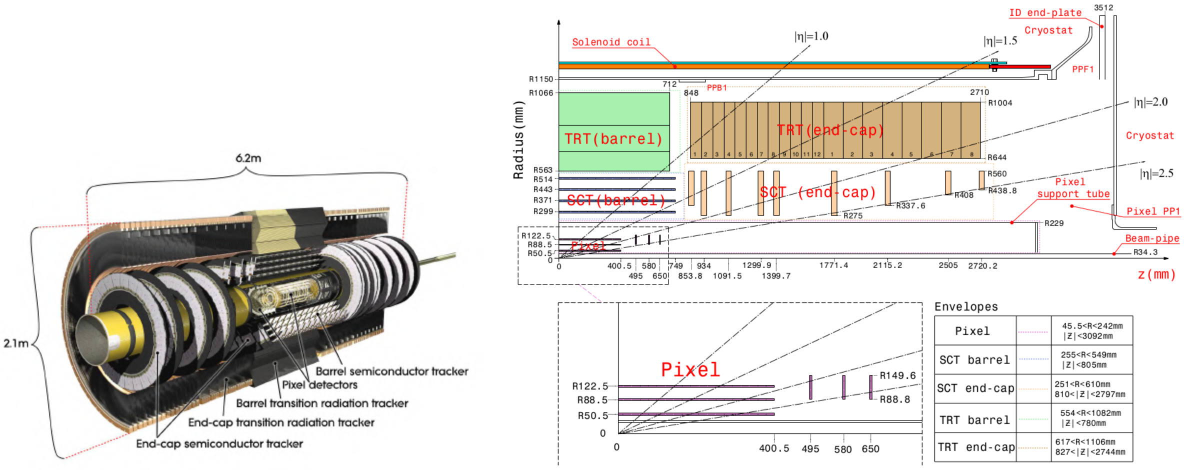

Figure 2.9 The Inner Detector. From Ref. [42].

With nominal luminosity of the LHC, it is expected that approximately 1000 particles will emerge from the multiple collisions happening at each bunch crossing. Closest to the beam pipe, these particles cross first the Inner Detector described in Fig. 2.9. It is immersed in a 2 T magnetic field parallel to the beam axis created by the solenoid surrounding it. This magnetic field curves the track of particles with radius inversely proportional to their transverse momentum p_{T}. Consequently, the Inner detector has two main goals: it must distinguish the tracks closer to the beam pipe in order to reconstruct all the different primary and secondary vertices, and it must reconstruct tracks with a good enough resolution to be able to extract the curvature radius and thus measure the p_{T}. The Inner Detector is a cylinder, 7 m long and with a radius of approximately 1 m allowing it to cover a pseudo-rapidity range of $|\eta| < 2.5$. It is made of three sub-modules with, from the beam pipe outward, the Pixel detector, the Semi-Conductor Tracker (SCT) and the Transition Radiation Tracker (TRT).

The first two modules, made of silicon pixels and strips, are based on the semi-conductor detector technology. When a particle crosses a semi-conductor detector, it excites electrons within, creating electron-holes pairs. These mobile carriers travel in the junction electric field generating an electric current recorded in a readout channel. The high geometrical precision and low energy needed to create a hit in such detectors allow good vertex reconstruction, at the expense of a lower number of hits. The Pixel detector allows good geometrical resolution for vertex reconstruction, being segmented in R, ϕ and z. It comprises in the centre barrel region three layers arranged in concentric cylinders, and as end-caps three disks on each side. During Long Shutdown 1, a fourth layer named Insertable B-layer, closer to the beam pipe, was added in order to improve vertex reconstruction and specifically b-jets secondary vertex reconstruction. With this layer added, Pixels cover radii from 33.25 mm to 122.5 mm with 80.4 million readout channel. Then silicon micro-strips arranged in four cylindrical layers in barrel and nine disks per end-cap from SCT cover up to radii around 600 mm with 6.3 million readout channels.

Further away from the beam pipe is the TRT based on a different technology. Straw tubes with a wire at the centre are filled with a gas that will ionise at the passage of a particle. A field is maintained between the wire and the walls of the tube to collect the signal and record a hit. Such tubes arranged longitudinally in the barrel and radially in the end-caps, provide $R-\phi$ and $\phi-z$ information respectively, and cover the outer part of the Inner Detector for a pseudo-rapidity range of $|\eta|<2$. Though less precise than silicon detectors, they provide a much bigger number of hits, typically 30 per track, and up to 36, with 351 000 readout channels.

The combination of Pixels and SCT with TRT allows good pattern recognition and precise p_{T} measurement. The nominal resolution for p_{T} is

$$\sigma_{p_{\mathrm{T}}}/p_{\mathrm{T}} = 0.05\,\% p_{\mathrm{T}}[\mathrm{GeV}] \oplus 1\,\% \,, \tag{2.6}$$

with $\oplus$ denoting addition in quadrature. However, degradation from high radiations and the expected high increase of tracks at HL-LHC will make it obsolete. It will be replaced by the Internal Tracker (ITk), an ATLAS Phase 2 upgrade, with planned installation during Long Shutdown 3 before the start of HL-LHC.

2.2.3 Calorimeters

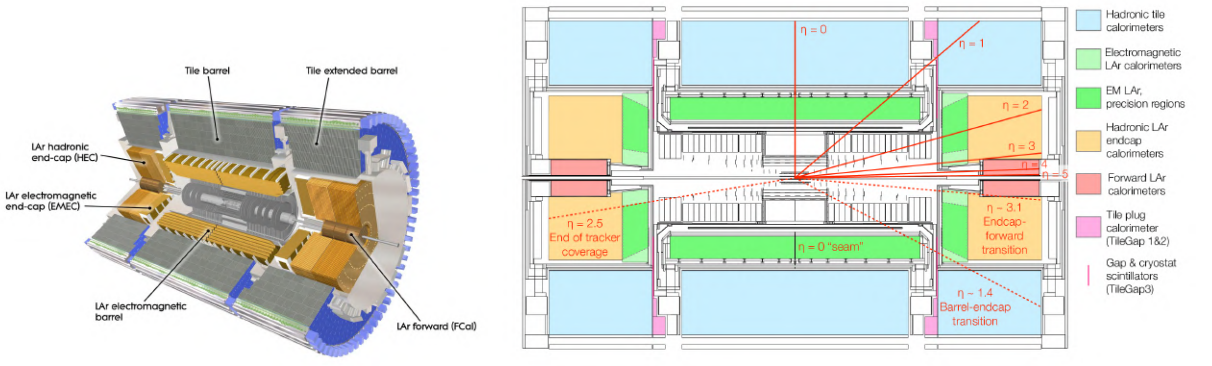

Figure 2.10 Calorimeters in ATLAS. From Ref. [42].

Right after the Inner Detector, calorimeters are responsible for the measurement of the energy of all particles emerging from the collisions, with the exception of muons and neutrinos. This is achieved using highly absorbent material to stop them and make them deposit their energy in an active material. Alternating layers of absorbent and active material create calorimeter cells each measuring a part of the energy deposited by the original particle. These sampling calorimeters allow extracting topological information on the energy deposit of particles, at the expense of a lower resolution. Typically, there are two types of calorimeters: electromagnetic calorimeters able with good energy resolution to stop light particles[4], that is electrons and photons, and hadronic calorimeters stopping all other particles, mainly hadrons from jets. There are five different calorimeter systems in ATLAS, as shown in Fig. 2.10: two are electromagnetic calorimeters, and three are hadronic calorimeters.

2.2.3.1 Liquid Argon electromagnetic calorimeters

When entering the electromagnetic calorimeter, electrons and photons develop an electromagnetic shower. Electrons and positrons loose energy mainly through bremsstrahlung,

---

[4] Developing electromagnetic showers, for example from a pion decay, can also be stopped in the electromagnetic calorimeter.

that is radiating a photon γ, as long as their energy is above a critical energy E_c. Below this energy, the radiation rate becomes lower than the ionisation rate and the shower stops developing. On the other hand, photons will interact with matter in pair production, $\gamma \rightarrow e^- e^+$ producing electrons e^- and positrons e^+ as long as their energy is above the mass energy of the electron-positron pair. These two processes can be seen as happening alternatively, the energy of the initial particle being split in all the branches of the daughter particles, as is visible in the very simplified sketch of Fig. 2.11(a). The typical length for such electromagnetic showers is called the radiation length X_0 and depends on the material used as absorber. When the daughter particles have energies below the critical energy, they start mainly depositing their energy through ionisation. In ATLAS electromagnetic calorimeters, the development of the shower happens in the lead plates, while the ionisation happens in the liquid Argon (LAr) in between. The ionisation creates free electrons that drift toward the readout electrode in the middle of the liquid Argon, as represented in Fig. 2.11(b). This creates an electric signal that is extracted from the electrode and treated in LAr electronics to compute the energy deposited (see Section 3.1).

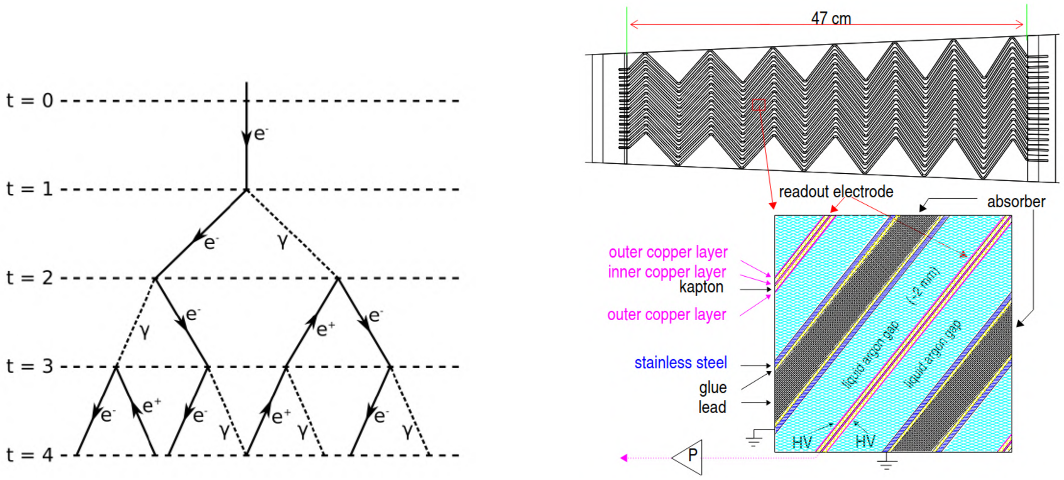

(a) (b)

Figure 2.11 (a) Sketch of an electromagnetic shower. (b) Internal structure of the LAr Electromagnetic Barrel accordion shape with alternate layers of active material (liquid Argon, in blue), absorber (lead plates, in grey) and readout electrode (copper, in pink). From Ref. [56].

The electromagnetic calorimeter is split in the Electro-Magnetic Barrel (EMB), covering pseudo-rapidity range $|\eta| < 1.475$ in the barrel, and the Electro-Magnetic End-Caps (EMEC), covering pseudo-rapidity range $1.375 < |\eta| < 3.2$ with wheels in each end-cap. Layers of the lead absorber alternate with layers of the liquid Argon active material in an accordion geometry in the barrel and end-caps. Such a geometry allows a complete ϕ coverage without any cracks. In the barrel, the accordion waves are axial and run along ϕ around the barrel. In the end-caps, the wave run along the axial z in planes that radiate from the beam axis. The barrel is at least $22X_0$ thick (at $\eta = 0$) and the end-caps at least $24X_0$ thick. Considering lead as absorber and a 100 GeV electron, the maximum of the shower will happen at approximately $10X_0$, with an additional $16X_0$ to contain 95 % of the shower. The LAr electromagnetic calorimeter does thus a good job at containing electromagnetic showers in the relevant energy range.

Each calorimeter is split in cells with a high granularity, in the (η, ϕ) plane and in depth. In the barrel, there are three layers in depth: front, middle and back. They are preceded by the presampler, a layer of cells with only the active material. It is designed to take into account electromagnetic showers that could have started developing in the dead material between the interaction point and the calorimeter. A precise representation of LAr cells in all depths of the barrel is shown in Fig. 2.12. Having such a sampling calorimeter degrades slightly the resolution on energy, as the energy deposited in between cells has to be estimated. However, it provides a handle to study electromagnetic showers topologies. Proper understanding of the development of electromagnetic showers allows then the precise calibration of the deposited energy and estimation of the nature of the initial particle, using shower shape variables. Such variables based on combinations of energy deposit in cells of the shower, include R_η and $w_{\eta,2}$, estimating the transversal spread of the shower in the middle layer of the calorimeter, and f_3 estimating the relative contribution of the back layer in the longitudinal development of the shower. The complete description of these shower shape variables can be found in Ref. [57] along with an assessment of their separation power between different physics signatures.

The nominal resolution for the energy E in the electromagnetic calorimeter is

$$\sigma_E/E = 10\,\%/\sqrt{E[\mathrm{GeV}]} \oplus 0.7\,\% \,. \tag{2.7}$$

The pseudo-rapidity range for the high granularity of the electromagnetic calorimeter matches also that of the Inner Detector allowing for very good combined reconstruction of electrons. Combining Eq. (2.6) and (2.7), this complementarity appears, with the calorimeter more precise at high energy, and the tracker better at low energy.

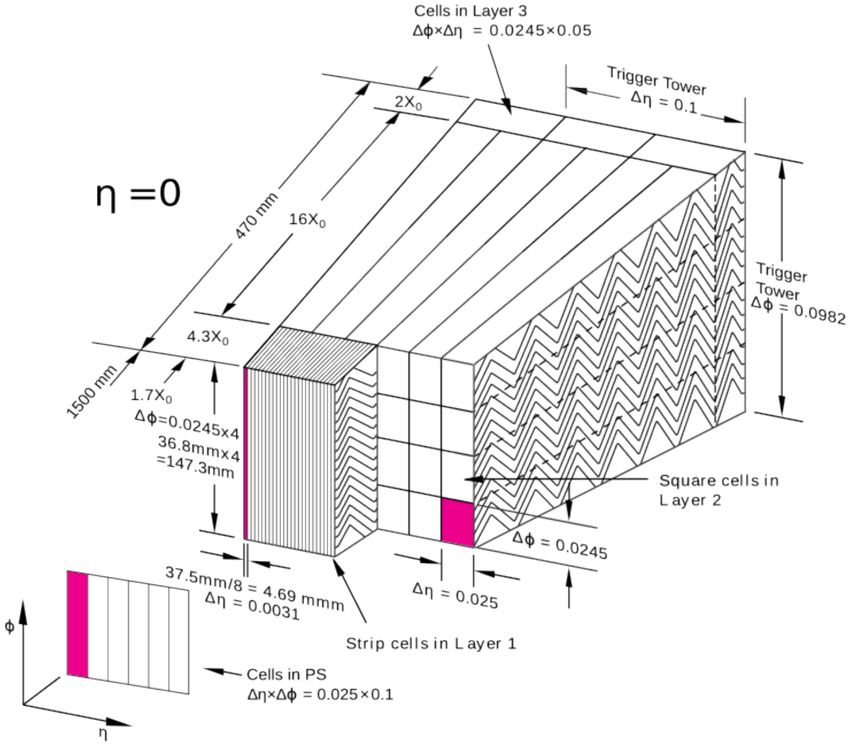

Figure 2.12 Sketch of LAr cells in the barrel. The innermost layer PS denotes the presampler used to correct for energy loss before the calorimeter. Then layer 1 (front), layer 2 (middle) and layer 3 (back) are visible in a $\Delta\eta \times \Delta\phi = 0.1 \times 0.1$ module called Trigger Tower. From Ref. [58].

2.2.3.2 Hadronic calorimeters

After the electromagnetic calorimeters, hadronic calorimeters are responsible for stopping much heavier particles, such as protons and neutrons. The shower of such particles in the calorimeter are much messier, involving a variety of nuclear reactions. These systems responsible for jet energy measurement are as a result less precise. The nominal resolution for the energy E in ATLAS hadronic calorimeters is

$$\sigma_E/E = 50\,\%/\sqrt{E[\mathrm{GeV}]} \oplus 3\,\% \,. \tag{2.8}$$

Nevertheless, beside the energy measurement, they are thick enough to contain hadronic shower particles and prevent them to enter the muon detectors surrounding the whole. This combined with a high pseudo-rapidity range, allows for missing transverse energy $E_{\mathrm{T}}^{\mathrm{miss}}$ computation, used for neutrino reconstruction or in exotic particle searches.

In ATLAS, the hadronic calorimeter comprises the Tile calorimeter, the Hadronic End-Caps (HEC) and the Forward Calorimeter (FCal). The first relies on scintillating tiles as active material, with steel plates as absorbent. It is located in the barrel and in two extensions of the barrel in the end-caps, covering respectively pseudo-rapidity ranges $|\eta| < 1.0$ and $0.8 < |\eta| < 1.7$. The HEC and FCal on the other hand use liquid Argon as active material as in the electromagnetic calorimeter, but with a different geometry. The HEC uses copper as absorbent and covers pseudo-rapidity range $1.5 < |\eta| < 3.2$. The FCal located in the end-caps extends the pseudo rapidity range covered by calorimeters, covering $3.1 < |\eta| < 4.9$. It is split in each end-caps in three layers: the first using copper as absorbent material aims at electromagnetic measurement, the two latter use the denser tungsten and aim at hadronic jet measurements.

2.2.4 The Muon System

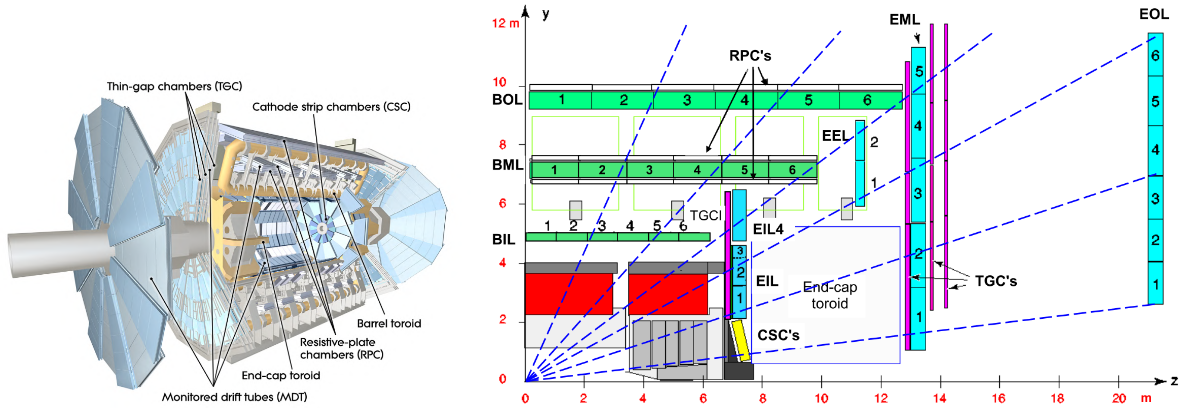

Figure 2.13 Muon detectors in ATLAS. Taken from Ref. [42].

The Muon System constitutes the outermost part of ATLAS, and aims at providing measurements on muons, the last detectable particles left after crossing the other inner sub-detectors. It comprises four different sub-detectors described in Fig. 2.13: Monitored Drift Tubes (MDT) and Cathode Strip Chambers (CSC) used for precision tracking, and Resistive Plate Chambers (RPC) and Thin Gap Chambers (TGC) used for triggering and complementary to the first two. All these detectors are based on similar principles, with a gaseous chamber that will ionise at the passing of a particle; the ionisation electron then drift to the cathode creating an electric signal. The bending of the muon tracks is performed by toroid magnets in the barrel and the end-caps (Fig. 2.7(b)). This bending happens mostly in the plane containing the beam axis at constant ϕ, in a non trivial way as the intensity of the magnetic field is not constant, specifically in the transition region between barrel and end-caps toroids.

The MDT, the main component of the Muon System, is made of Ar/CO$_2$ filled tubes with a wire at the centre collecting the ionisation electron. This gives the coordinate of a hit in the bending plane (η, z) with a precision of 35 ʮm. It is located in three layers around the barrel at 5 m, 7.5 m and 10 m from the beam axis and in four wheels in each end-caps at $|z| \approx 7.4$ m, 10.8 m, 14 m and 21.5 m; this shows the Muon System is the main driver for the ATLAS detector gigantic dimensions. This covers a pseudo-rapidity range of $|\eta| < 2.7$. Nevertheless, the innermost wheel in the end-caps has to cope with more demanding conditions, being in the forward region $(2.0 < |\eta| < 2.7)$ were most produced particles are found, and relatively close to the interaction point. There, the MDT is replaced by the CSC, which instead of tubes has chambers filled with multiple wires and a cathode segmented in strips. They have a higher rate capability and are able to get a rough estimate of the position in the non-bending plane, giving access to the ϕ coordinate.

The trigger chambers RPC and TGC, the first one in the barrel, the second one in the end-caps, serve three purposes. First, with an excellent intrinsic time resolution below 5 ns, they can provide bunch crossing identification. They also provide very fast estimation of the crossing of certain muon p_T thresholds. This is used in the Level-1 trigger (see Section 2.2.5). Finally, they provide a measurement of the ϕ coordinate to complement the MDT precision measurement. This is achieved, for RPC with resistive plates as electrodes kept very close to each other, 2 mm apart. The high electric field in between provides an avalanche of electrons at each ionisation ensuring good time resolution, at the expense of a geometrically less precise measurement. The TGC relies on similar principles, only replacing the anode by multiple wires.

In the end, the Muon System in ATLAS allows precision measurement of muons tracks in all three coordinates, allowing a stand-alone p_T resolution of 10 % for a 1 TeV muon. Due to the intense radiation degradations and the expected even more challenging luminosity condition, the innermost wheel in each the end-cap was replaced as a Phase 1 upgrade by the New Small Wheels.

2.2.5 The trigger system

The high luminosity of collisions in the ATLAS detector entails a high number of events to be recorded. This represents an amount of data impossible to manage. Only considering the 182 468 cells of LAr calorimeters, and encoding the output of their corresponding readout channel on 12 bits at the 40 MHz frequency of bunch crossings, almost 100 Terabits are produced per second. On the other hand, looking back at Fig. 1, it appears that the cross section for pp inelastic scattering at $\sqrt{s} = 13$ TeV is approximately seven orders of magnitude higher than that of most common electroweak processes, and nine orders of magnitude higher than that of the $W^{\pm}Z$ pair production process studied here. As a result, only very few events among all those produced are interesting for the physics program of the ATLAS experiment, and this allows dumping all the others, reducing greatly the problem of the data storage. The selection of physically interesting events is done by a variety of systems called Triggers.

The trigger in ATLAS is separated in two levels: a Level 1 (L1) trigger responsible for reducing the event rate from 40 MHz to 100 kHz, and a High Level Trigger (HLT) reducing it further to 1 kHz [59]. The L1 trigger uses custom electronics to perform fast computations on information from specific ATLAS sub-detectors. For muons, the RPC and TGC described in Section 2.2.4 are used to trigger on high p_{T}. In the calorimeter, a reduced granularity is used grouping cells in modules typically of $\Delta\eta \times \Delta\phi = 0.1 \times 0.1$ called Trigger Tower, as visible in Fig. 2.12, allowing for the selection of high energy clusters as signs of electrons, photons, tau, jets, and $E_{\mathrm{T}}^{\mathrm{miss}}$. With these information combined, the L1 trigger determines if a L1 accept should be delivered or not. This decision should occur within 2.2 µs after the considered bunch crossing, to avoid an overflow of the buffer where standard readout data is stored meanwhile. After a L1 accept, the data from the main readout is sent to the HLT along with the L1 trigger data. The HLT uses a computer farm to perform higher level algorithms on data and reduce the event rate to 1 kHz. Differently to the L1 trigger limited by the speed at which data can be written on disk, the HLT is actually limited by the amount of offline computing resources, such as disk storage space, available. Ultimately, the HLT output rate, already five times higher than first expected, cannot be increased for lack of computing resources, and can only be reduced at the expense of physics performances.

With the planned increase in luminosity and the ensuing increase in pile-up, the L1 accept and HLT rate would increase dramatically. To keep the same rates without increasing energy or p_{T} thresholds at the expense of physics performance, both triggers have to improve their rejection rate. This is done in the ATLAS Phase 1 upgrade mainly by improving the L1 Calorimeter trigger (L1Calo) and crucially its input data as will be described in Chapter 3.

Chapter 3

Phase 1 upgrade of the Liquid Argon calorimeter

The primary motivation of the ATLAS Phase 1 upgrade is to improve the Level-1 trigger and maintain similar acceptance rates in degraded conditions due to a higher pile-up. On the calorimeter side, the driving idea is to improve the input data in the trigger processor by replacing the coarse grouping of cells in Trigger Towers by a finer grouping in Super Cells. This increased granularity visible in Fig. 3.1, improves the energy resolution measured and allows the use of shower shape variables at the trigger level. For further improvement, the signal coming from the detector cells is digitised in a new trigger processing chain called Digital Trigger. The ensuing improvement in L1 trigger efficiency and background rejection should allow it to keep the same rate at 100 kHz with similar low p_{T} thresholds, around 25 GeV, for a luminosity at $L = 3 \times 10^{34}\,\mathrm{cm}^{-2}\,\mathrm{s}^{-1}$ and average number of interactions per bunch crossing at $\langle \mu \rangle = 80$ [57].

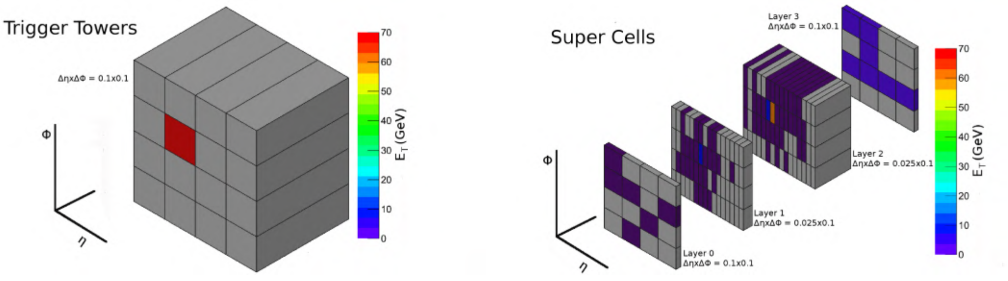

(a) **(b)**

Figure 3.1 An electron with $E_{\mathrm{T}} = 70\,\mathrm{GeV}$ as seen by the Level-1 Calorimeter electronics with inputs from Trigger Tower (a) and from SuperCells (b). From Ref. [57].

However, replacing Trigger Towers by Super Cells will increase roughly by one order of magnitude the amount of cells to be managed by the trigger electronics. This requires a wide upgrade of the LAr calorimeter electronics from the front-end to back-end, incorporating the Digital Trigger electronics. The LAr electronics is responsible for the computation of all energies recorded in all LAr cells at every bunch crossing, with as input the analogical ionisation signal of each cell. After a description of LAr electronics and the energy computation process in Section 3.1, based on Ref. [57, 58], the components of the Phase 1 upgrade new Digital Trigger will be described in Section 3.2.

3.1 Energy computation in LAr electronics

3.1.1 Overview of the LAr electronics

The pulses from the 182 468 cells of all the LAr calorimeter sub-detectors EMB, EMEC, HEC and FCal are treated in a readout electronics described in Fig. 3.2. This architecture can be split in front-end and back-end parts that have different locations. The front-end is located on detector, in 58 Front-End Crates right outside the LAr cryostat, in the gap between the barrel and end-caps, and on the outer face of the end-caps. This electronics has limited access and must be radiation tolerant. The back-end electronics is housed in the USA15 counting room, off detector but still in the ATLAS cavern.

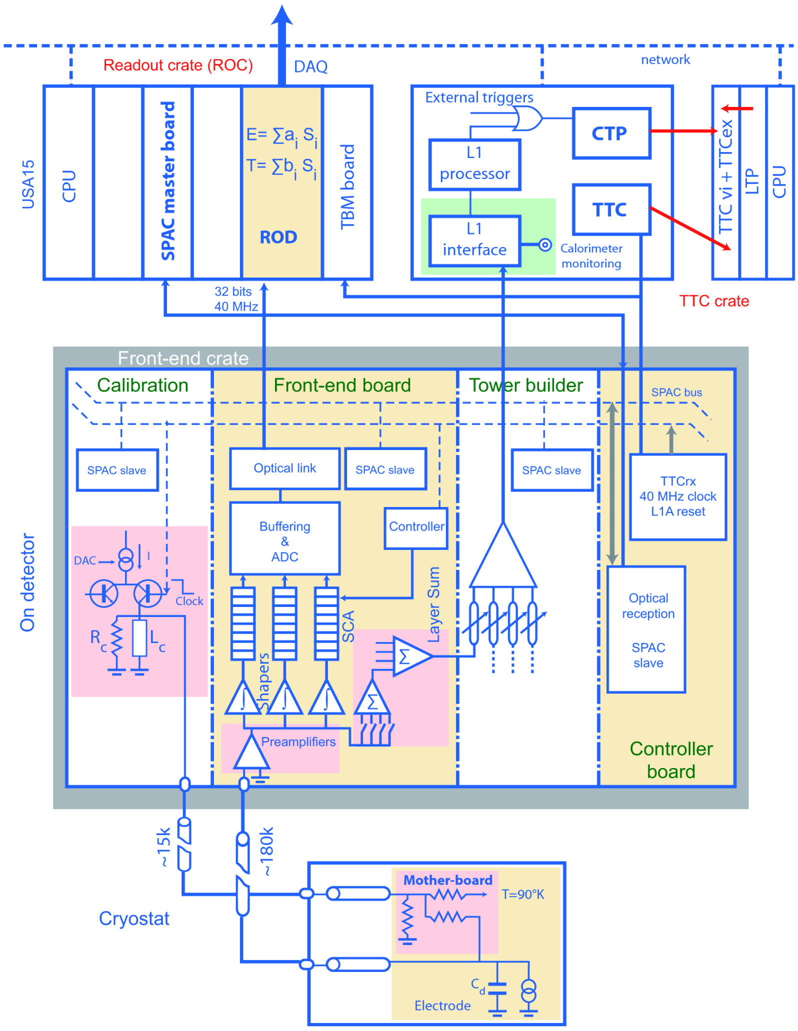

Figure 3.2 Schematic block diagram of the original LAr readout electronics. The ionisation signal proceeds from the cryostat to the on-detector Front-End Crate and finally to the back-end electronics in the USA15 counting room. This diagram is valid for EMB and EMEC calorimeters, slight changes would be needed for HEC and FCal. From Ref. [57].

A Front-End Crate (FEC) houses around 20 boards of four main different types: Front-End Boards (FEB), Tower Builder Boards (TBB), Calibration boards and Controller boards. The majority of boards in Front-End Crates are FEBs, responsible for the amplification, shaping and buffering of the analog signal of 128 LAr cells from a specific transversal layer of the calorimeter. Upon a L1 accept, the signal is then digitised and sent to the back-end.

A component of the FEBs, the Layer Sum Board (LSB) sums the analog signal in one layer as an input for the TBB. It in turn sums the analog signal from different layers to form Trigger Tower signals. The Calibration board delivers pulses similar to the ionisation signal in order to calibrate the readout-electronics. Finally, the Controller board receives and distributes the LHC 40 MHz clock and other configuration or control signals. For completeness, some FEC host Monitoring boards that are used to read out various monitors such as temperature or mechanical constraints.

The back-end houses mainly Read Out Drivers (ROD) in VME crates[1]. The RODs are mainly for the computation of energy from the stream of signal samples released from the front-end and corresponding to a L1 accept (see Section 3.1.2). There are also various boards used for communication with the VME crates (labelled CPU board) or Front-End Crates (labelled SPAC master board), and Trigger Busy Modules responsible for Trigger, Timing and Control (TTC) signals (such as the LHC clock) in their own VME crate. The L1Calo trigger system receives analog signals from the TBB and equivalent signals from the Tiles calorimeter to make the L1 accept decision. The L1Calo system achieves this through several computations: the pulse is sampled at 40 MHz, the bunch crossing is identified using the pulse shape and the transverse energy is computed using a look-up table.

3.1.2 Energy computation with Optimal Filtering Coefficients

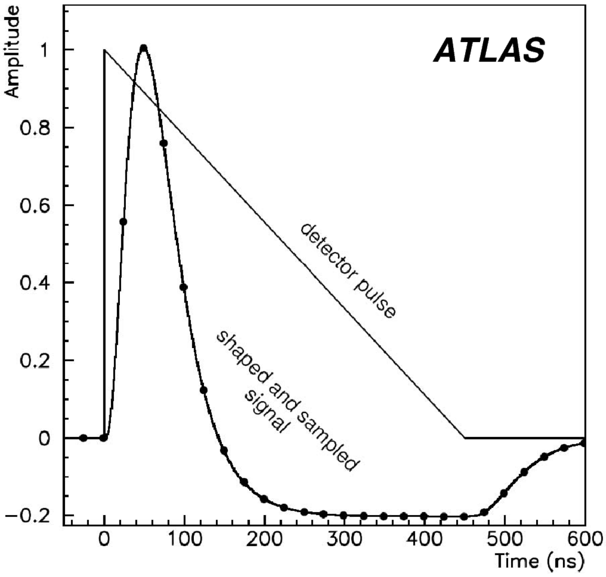

Figure 3.3 Signal shape from the ionisation pulse (triangle) and after the shaping in the Front-End Board (curve with dots). The time scale origin is the bunch crossing when the energy was deposited. The dots represent the successive bunch crossings. The vertical axis represents the normalised amplitude of the signal. From Ref. [58].

The ionisation signal coming from the LAr cells is typically a triangle, as shown in Fig. 3.3, decreasing steadily during 400 ns in the EMB[2]. However, with a bunch crossing every 25 ns, this long tail is a problem. It creates what is called *out-of-time pile-up*, meaning

---

[1] The Versa Module Eurocard (VME) crate is a type of modular crate electronics. It is a box open at its front end, and with the back end containing power and data connectors. Rails on the side allow various electronic modules to be inserted.

[2] The drift time varies with η in the EMEC.

the calorimeters still record energy deposited from previous bunch-crossing in addition to other *in-time* pile-up events happening at the same bunch crossing. One has to imagine the electrical signal as the superposition of such triangles distributed randomly depending on if a particle deposited energy at a specific bunch crossing or not. With tails lasting almost 20 bunch crossings, a lot of out-of-time pile-up is created. To reduce this, the signal goes through a shaper becoming more peaked right after the energy deposit and diving to negative values subsequently in order to have a net null area, as visible in Fig. 3.3. A consequence of this bipolar shape is that the average output value of a cell is zero, effectively subtracting the out-of-time pile-up baseline. This is only valid for long bunch trains as the pile-up contribution is then on average constant; around bunch trains start or end some corrections are required. The shaping characteristic time is chosen as an optimum between pile-up noise minimisation and electronic noise minimisation [58]. This shaped signal is then sampled at the bunch crossing frequency by an Analog-to-Digital Converter (ADC) in 12 bits values called ADC counts. This sampling however degrades slightly the cancellation of the out-of-time pile-up by the bipolar shape.

The signal after going through the shaper is characterised by three important parameters: its pedestal, its amplitude and its time delay. The pedestal corresponds to an overall offset of the signal allowing for the negative part in the tail used to cancel out-of-time pile-up. The amplitude of the signal – minus the pedestal – is proportional to the amount of energy deposited. The time delay corresponds to the time between the recorded peak and the correct associated bunch crossing. This delay arises mainly from the shaping as a systematic effect of around 50 ns, the shaping time. For better precision, the phase τ is defined as the instant when the peak is found within the 25 ns of a bunch crossing.

Upon a L1 accept, five samples are sent to the RODs where the energy deposited E and the phase τ are computed using a method from signal processing theory named optimal filtering [60]. The normalised bipolar shape of the signal is known and labelled $g(t)$. With a time origin at the assumed crossing time, the signal $S(t)$ can be parametrised with the amplitude A and the phase τ, as

$$S(t) = A\ g\left(t - \tau\right)\ .$$

The signal is sampled at every bunch crossing t_i in ADC counts S_i, that is only positive values. The bipolar shape and its negative value tail is recovered by subtracting the pedestal p, and $S(t)$ should be replaced by $S_i - p$. With a first order Taylor expansion around $\tau = 0$, noting g_i and g'_i the values of $g(t_i)$ and its first derivative $g'(t_i)$ at the sampling time t_i, the signal samples become

$$S_i - p = A\ g_i - A\tau\ g'_i + n_i\ ,$$

the additional term n_i being a random noise term. From there, two random variables u and v are defined,

$$u = \sum_i^N a_i\left(S_i - p\right)\ ,$$
$$v = \sum_i^N b_i\left(S_i - p\right)\ .$$

With N an arbitrary number of samples, the sets $(a_i)_{0<i<N}$ and $(b_i)_{0<i<N}$ are coefficients to be determined with a constrained minimisation. The following requirements are imposed,

$$\langle u \rangle = A = \sum_i^N a_i A\ g_i - a_i A\tau\ g'_i\ ,$$

$$\langle v \rangle = A\tau = \sum_i^N b_i A\ g_i - b_i A\tau\ g'_i\ ,$$

the noise term average $\langle n_i \rangle = 0$ disappearing. This yields the constraint terms

$$\sum_i^N a_i\ g_i = 1\ , \quad \sum_i^N a_i\ g'_i = 0\ , \tag{3.1}$$

$$\sum_i^N b_i\ g_i = 0\ , \quad \sum_i^N b_i\ g'_i = -1\ , \tag{3.2}$$

for the minimisation of the variances

$$\mathrm{Var}(u) = \sum_i^N \sum_j^N a_i a_j R_{ij}\ , \tag{3.3}$$

$$\mathrm{Var}(v) = \sum_i^N \sum_j^N b_i b_j R_{ij}\ , \tag{3.4}$$

with $R_{ij} = \langle n_i n_j \rangle$ the noise autocorrelation function at time $t_j - t_i$. From there, with Lagrange multipliers, it is possible to extract the two unique sets $(a_i)_{0<i<N}$ and $(b_i)_{0<i<N}$ of Optimal Filtering Coefficients (OFC) [60]. In the end, the amplitude in ADC counts A and the phase τ are expressed with OFCs as

$$A = \sum_i^{N_{samples}} a_i \left(S_i - p\right)\ , \tag{3.5}$$

$$\tau = \frac{1}{A} \sum_i^{N_{samples}} b_i \left(S_i - p\right)\ . \tag{3.6}$$

In physics runs since Run 2, for each triggered event, four ADC count samples are sent to the RODs. In this case, four OFCs a_i and b_i are needed and in Eq. (3.5) and (3.6), $N_{samples} = 4$.

3.1.3 Calibration coefficients

In the LAr readout electronics, the amplitude of the signal is proportional to the energy deposited in the calorimeter cell. This proportionality factor is a combination of different effects [61] and as such the energy can be expressed as

$$E = F_{DAC\rightarrow\mu\mathrm{A}} \cdot F_{\mu\mathrm{A}\rightarrow\mathrm{MeV}} \cdot \left(\frac{M_{phys}}{M_{cal}}\right)^{-1} \cdot C_{\mathrm{HV}} \cdot \sum_m^{N_{ramps}} R_m\ \left(A_{ADC}\right)^m . \tag{3.7}$$

From right to left,

- A_{ADC} is the signal amplitude in ADC count as computed with OFCs as in Eq. (3.5).

- R_m are the coefficients of a polynomial of degree N_{ramps} in powers of A_{ADC} at the degree m. This polynomial fits the conversion from unit current (DAC) to ADC counts accounting for possible non-linearities. In the RODs, a simple linear fit is used.
- C_{HV} is a correction factor applied when the high voltage is not nominal. This correction originates from the η dependence of the high-voltage needed in the cells of the EMEC which is not fully achieved for practical reasons, or more generally because of occasional leakage current. Its estimation is described in Ref. [62].
- M_{phys}/M_{cal} is a correction factor used to take into account the difference between the pulse height in calibration runs and in physics runs.
- $F_{\text{ţA}\to\text{MeV}} = (I/E \cdot f_{sampling})^{-1}$ is a conversion factor from the current in ţA to the energy deposited in the active and passive part of the calorimeter cell. It depends on the energy to current ratio I/E coming from the characteristics of the copper electrode and the ionisation potential of liquid Argon, and of the sampling fraction $f_{sampling}$ linking the total energy deposited to the energy deposited in the liquid Argon active phase. Both are estimated from test beam data for LAr cells [61].
- $F_{DAC\to\text{ţA}}$ is a conversion factor from the current in DAC units to ţA. It is defined by the calibration board specificities, and the cell motherboard injection resistor.

Some so-called calibration coefficients need regular updating for all LAr cells. These coefficients are the pedestal p, the OFCs a_i and b_i, the ramp coefficients R_m and the M_{phys}/M_{cal} coefficient. Three types of calibration runs are used to obtain them:

Pedestal run: In such runs, no calibration pulse is sent to the calorimeter cells. For each cell, typically $N_{ev} \approx 1000$ events are recorded with typically $N_{samples} \approx 7$ samples for each. With no signal injected, the distribution of the $N_{events} \times N_{samples}$ samples is used as visible in Fig. 3.4. The mean will give the pedestal p and the standard deviation will give the noise σ. This noise is fully incoherent, coherent noise sources having been identified and corrected in the past [63]. From there, the normalised noise autocorrelation matrix is computed as $R_{ij}/\sigma^2 = \langle (s_i - p) \times (s_j - p) \rangle / \sigma^2$, with $\langle . \rangle$ noting the average on N_{ev} events. This will be used for the OFC computation in the minimisation of Eq. (3.3)–(3.2).

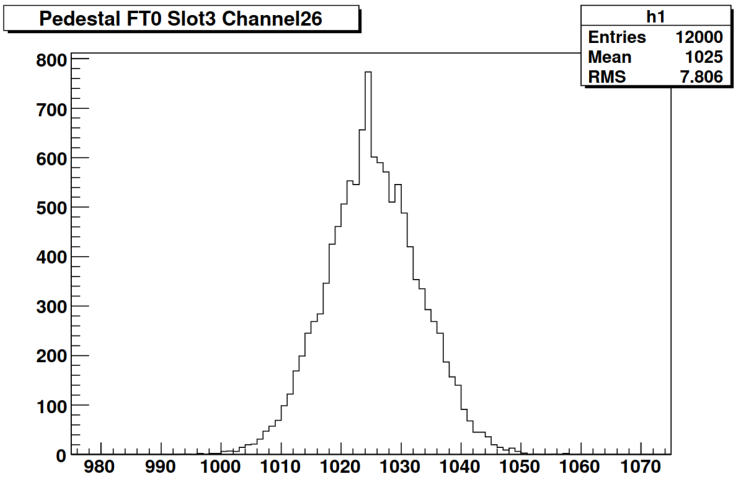

Figure 3.4 Pedestal distribution in ADC count for one LAr cell over 2000 events with 6 samples recorded. From Ref. [61].

Delay runs: These runs aim at obtaining the shape of the signal of known amplitude after amplification and shaping. A fixed amplitude pulse is sent to LAr cells and 32 samples are recorded. This is reproduced 24 times with a time delay of 1.04 ns in order to cover the time difference of 25 ns between two bunch crossing. All the recorded samples are reordered in time, thus reconstructing the calibration signal pulse with a 1.04 ns sampling time. Then the pedestal p is subtracted in order to recover an estimate of the normalised shape $g(t)$ of the signal. The cells are pulsed in various patterns in order to mitigate cross-talks[3]. The obtained shape $g_{cal}(t)$ is visible for one cell in Fig. 3.5(a).

The noise autocorrelation matrix R_{ij} – obtained in pedestal runs – and the normalised shape of the calibration pulse $g_{cal}(t)$ are the elements of Eq. (3.1)–(3.4) needed to extract the OFC sets for amplitude and phase calculation of a given LAr cell[4]. Yet, the calibration pulse is only an approximation of the triangular physics pulse using exponentials. With differences in the injection point of the current and parasitic inductances in the calibration cables this creates shape differences with the physical ionisation signal. Electrical models simulating the detector and the electronics chain are used to deconvolve these differences and obtain the ionisation pulse shape $g_{phys}(t)$. This reshaping modifies the amplitude of the signal as visible in Fig. 3.5(b). A factor M_{phys}/M_{cal} is used to account for this change in amplitude, and propagated to Eq. (3.7). As a result, for each cell, two sets of OFCs can be extracted: calibration OFCs use the shape $g_{cal}(t)$ and physics OFCs use the derived shape $g_{phys}(t)$. The latter will be used by the RODs in physics run.

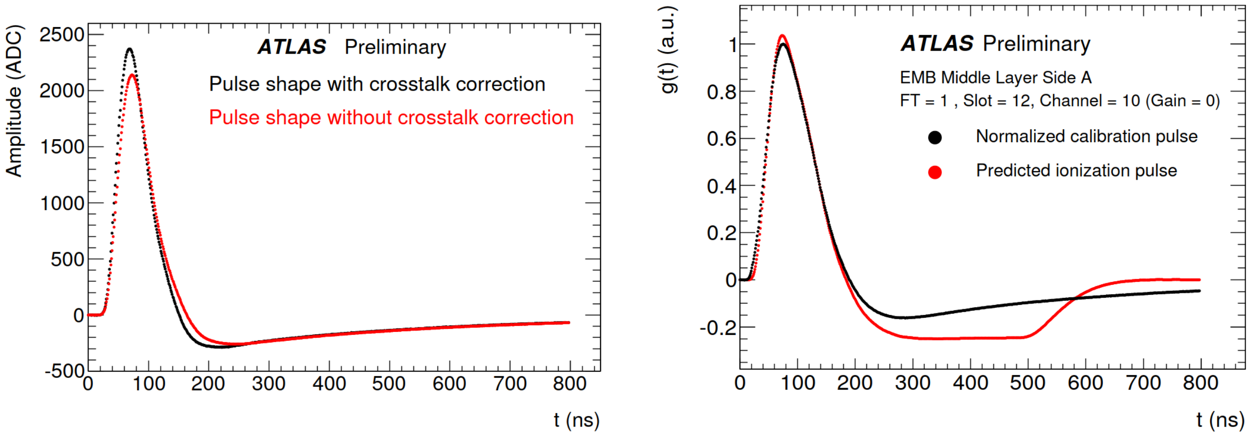

(a) (b)

Figure 3.5 (a) Pulse shape from a LAr front layer cell reconstructed in delay runs with (black) and without (red) cross-talk correction. (b) Comparison of normalised calibration pulse shape (black) and derived normalised physics pulse shape (red) for one middle layer EMB LAr cell. Both from Ref. [63].

Ramp runs: In ramp runs, calibration pulse with currents DAC values spanning the full range allowed, from 0 to 65 500, are sent to the cells. For each DAC value, 200 events are recorded with five samples sent to the RODs. There, the peak amplitude in ADC counts A_{ADC} is reconstructed with optimal filtering using the calibration OFCs.

---

[3] These cross-talks arise from leakage of the calibration pulse current in neighbouring cells. This is responsible for about 8 % loss in the injected current.

[4] The derivative of the shape $g'(t)$ is numerically computed from the normalised shape $g(t)$.

Finally, the peak amplitudes are fitted by a linear relation DAC $= R_0 + R_1\, A_{ADC}$. The R_0 ramp coefficient is only used for EMB cells to keep non-linearities low enough [63]. Consequently, in Eq. (3.7), $N_{ramps} = 1$, and most of the time only the R_1 value is non zero. This value is obtained with a ratio as displayed in Fig. 3.6 for LAr cells in various layers.

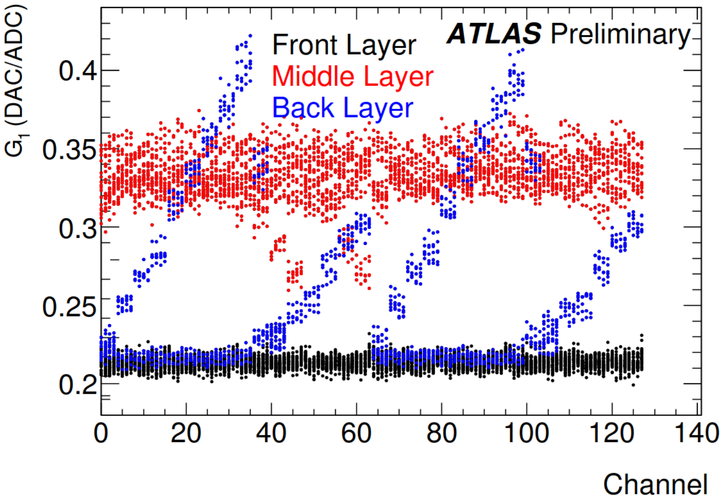

Figure 3.6 Slope term R_1 (labelled G_1 in the figure) obtained from ramp runs for front, middle and back layers of 128 EMB LAr cells of a FEB. From Ref. [63].

3.2 The Digital Trigger upgrade

3.2.1 Expected improvements

The Phase 1 upgrade for the LAr calorimeters consists mostly in the replacement of the Trigger Tower based trigger system as described in Section 3.1.1, by a new Digital Trigger. Its main feature is the use of a higher granularity at the trigger level with Super Cells. A Trigger Tower in the barrel is, as shown in Fig. 3.7, replaced by 10 Super Cells. In other regions of the LAr calorimeters, the improvement in the geometry can be different (for example, in the HEC and FCal, the Super Cells correspond exactly to the Trigger Towers), but globally, the 5248 Trigger Towers are replaced by 34 048 Super Cells. At each bunch crossing, the energy of each Super Cell is computed by the Digital Trigger readout electronics with an improved precision thanks to the higher granularity and smaller quantisation scale of the digitised signal. Crucially, for Super Cells, the transverse granularity of the calorimeter is recovered, allowing for the observation of the electromagnetic shower development along the calorimeter's depth. The legacy trigger system only used a threshold on the deposited energy. Thanks to Super Cells, the use of shower shape variables at the L1 trigger level with improved filtering algorithms allows for a better background rejection.

Simulations using LAr cells results to recompute the Super Cells output were performed to assess the expected improvement in Ref. [57]. The increased precision is visible in Fig. 3.8(a) for electrons energy computation: both the energy resolution and the bias are greatly reduced using Super Cells. This should translate in an improved efficiency of the trigger: signal events with an E_{T} just above the trigger threshold, and thus that should be

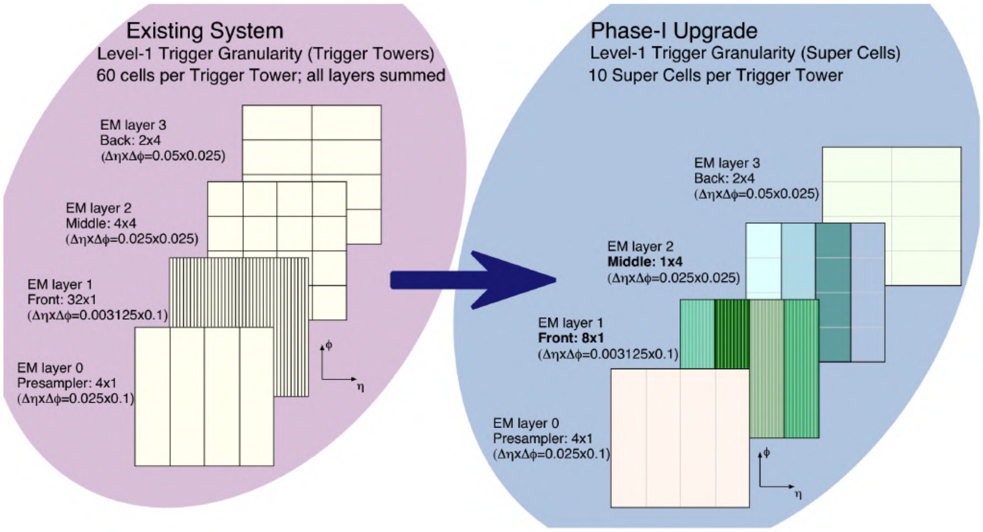

Figure 3.7 Representation in the (η, ϕ) plane and in the four transversal layers of an EMB Trigger Tower (left) and the 10 Super Cells within (right). From Ref. [57].

selected, have a higher chance of having a reconstructed E_{T} effectively above this threshold. This translates in a sharper trigger efficiency turn-on curve as exemplified in Fig. 3.8(b) in the case of jets. Moreover, the use of shower shape variables in addition to the E_{T} threshold allows for a greater background rejection: for a given efficiency the L1 trigger acceptance rate is lowered. In Fig. 3.9, triggering for electrons, this improvement happens for E_{T} thresholds up to 50 GeV. Similarly, for a given rate of electron trigger around 20 kHz[5], the threshold can be lowered by a few GeV.

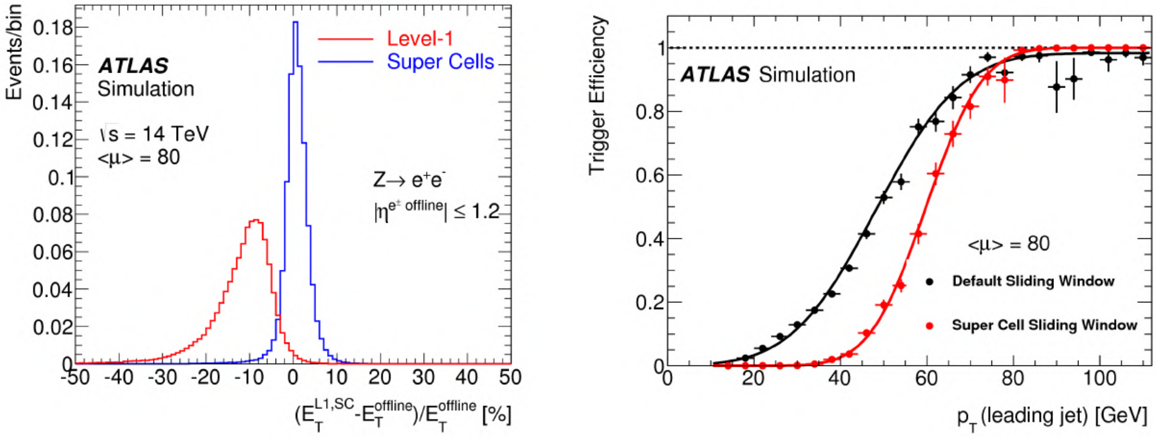

(a) (b)

Figure 3.8 (a) Energy resolution on electrons from $Z \to ee$ computed with Trigger Towers (labelled Level-1, in red) and with Super Cells (in blue) as simulated with Run 3 pile-up conditions $\langle\mu\rangle = 80$. (b) Trigger efficiency turn-on curve as a function of the highest p_{T} offline jet for $\langle\mu\rangle = 80$ in simulated QCD dijet events. For jets within $|\eta| < 2.5$, the performance of the default sliding window algorithm (black points) is compared to that of the sliding window algorithm based on Super Cells (red points). Both from Ref. [57].

However, these improvements come with many challenges. First, the performance requirements are high: the energy computation precision should be below 250 MeV and

---

[5] The 100 kHz L1 trigger bandwidth is split for triggering on different physics objects: electrons & photons, muons, τ, jets & $E_{\mathrm{T}}^{\mathrm{miss}}$.

stay unbiased even under high pile-up conditions. Additionally, while in the main readout, the RODs compute the cell energies at the L1 accept rate – up to 100 kHz – the Digital Trigger electronic chain must compute the Super Cells transverse energies E_T and signal phase τ at the bunch crossing rate of 40 MHz. Yet, the granularity of Super Cells is not as reduced as that of Trigger Towers implying that a massive amount of data has to be managed at a very high rate. Consequently, a complete overhaul of the electronic chain is required. This in part is only possible thanks to progresses in electronic components since the 1990's when the original LAr readout electronics was first designed.

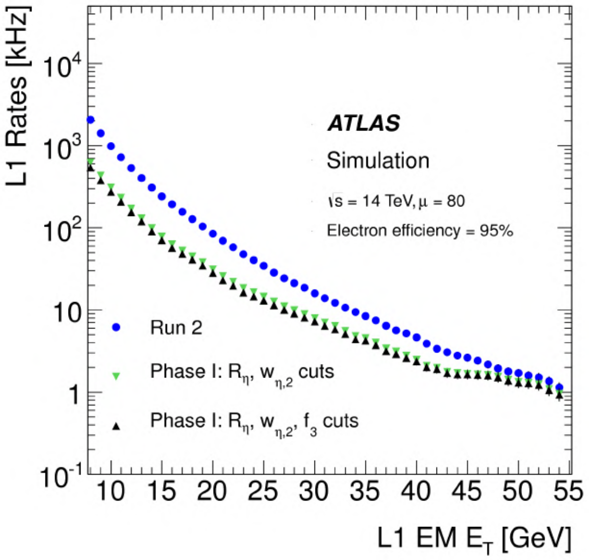

Figure 3.9 L1 trigger rate for a 95 % electron efficiency as a function of the E_T threshold as in Run 2 (blue) and with Run 3 conditions (green and black) but with different requirements on the shower shape variables R_η, $w_{\eta,2}$ and f_3 (see Section 2.2.3). From Ref. [57].

3.2.2 Digital Trigger electronic components

All the elements affected by the Phase 1 upgrade of the LAr electronics are visible in Fig. 3.10 with red arrows or a red outline. Starting in the FEB, a new LSB will send Super Cell analog signal to the new Digital Trigger electronic chain. In the front-end, the LAr Trigger Digitiser Boards (LTDB) are responsible of the sampling and digitisation of the analog signal at the bunch crossing frequency. It is also responsible for the reconstruction of Trigger Tower analog signals that are then sent to the TBBs. This allows maintaining the legacy trigger chain functional for at least the initial phase of the Run 3. Then, the digitised samples are sent through 77 m optical links to the back-end crates in the USA15 counting room. There, the LAr Digital Processing System (LDPS) is responsible for the computation of the transverse energy E_T and the signal phase τ. The LDPS then sends E_T for each cell at its associated bunch crossing to the three new Feature EXtractors (FEX) in L1Calo, targeting electromagnetic (eFEX), jet (jFEX) and global (gFEX) features. During all this process, the individual LAr cells signals are stored in buffers of the FEBs for a maximum of 2200 ns. From the *pp* collision time to the reception of E_T in the FEXs, the latency budget of the Digital Trigger chain is of 1275 ns. Effectively, only 1095 ns are needed, corresponding to 43.8 bunch crossings [64].

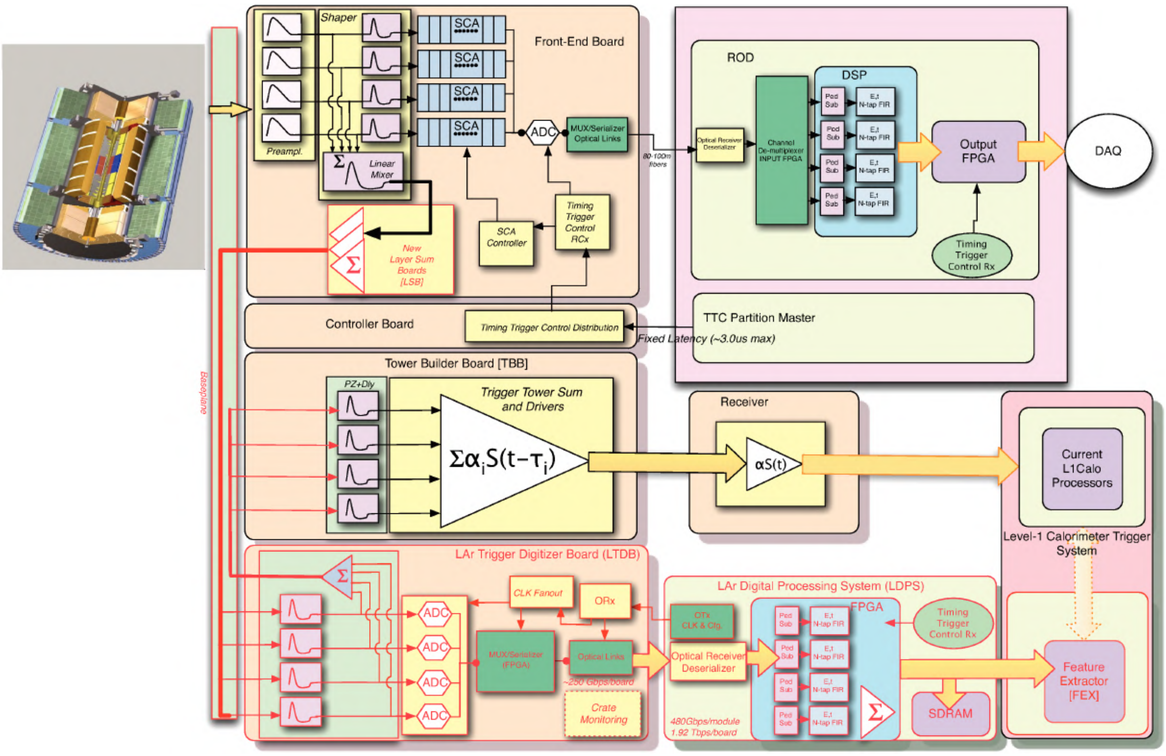

Figure 3.10 Schematic block diagram of the LAr electronics after the Phase 1 upgrade. The first line of blocks corresponds to the standard readout electronic chain. The second line of blocks corresponds to the legacy trigger system based on Trigger Towers. Finally, the last line of blocks corresponds to the new Digital Trigger electronics. Elements affected by the Phase 1 upgrade are marked by red outlines and arrows. From Ref. [57].

On the detector side, the upgrade required to open the FECs and empty them of all their boards. This allowed to completely change their baseplane which is responsible for the various connections and the powering of the boards in the FEC. Room was made to accommodate 124 LTDBs in 114 FECs with a new baseplane. This new baseplane allows the new connections of the LTDB to the TBB, providing the legacy trigger system with Trigger Tower signals, and the connection of the new LSB to the LTDB. The LSB being a mezzanine board mounted on the FEBs, its replacement required to bring all FEBs to a surface laboratory. The new LSB now sums the analog signal of cells to form Super Cells. This can be done directly as opposed to Trigger Towers because Super Cells geometry aligns with FEBs management of LAr cells in only one given calorimeter layer.

Each LTDB processes in parallel the signals from 320 Super Cells (channels) with 80 Analog-to-Digital Converter chips, each processing 4 channels. Each channel signal is sampled at 40 MHz and digitised to 12 bits values called ADC counts. As a result, at every bunch crossing for each channel, it outputs one ADC count of the original signal among the $2^{12} = 4096$ available values. Typically, the pedestal is around 1000 ADC counts, leaving a range around 3000 counts for the energy resolution. These values are then prepared for transmission on 5.12 Gb/s optical fibers, with eight channels per fiber. In total, up to 40 optical fibers transmit to the LDPS at 40 MHz the serialised ADC counts from eight channels each.

The LDPS comprises 30 LAr Digital Processing Boards (LDPB) installed in three crates of the USA15 counting room as visible in Fig. 3.11(a). It should manage in total close to 30 Tb/s as compared to around 2 Tb/s with the legacy Trigger Tower. This requires the use

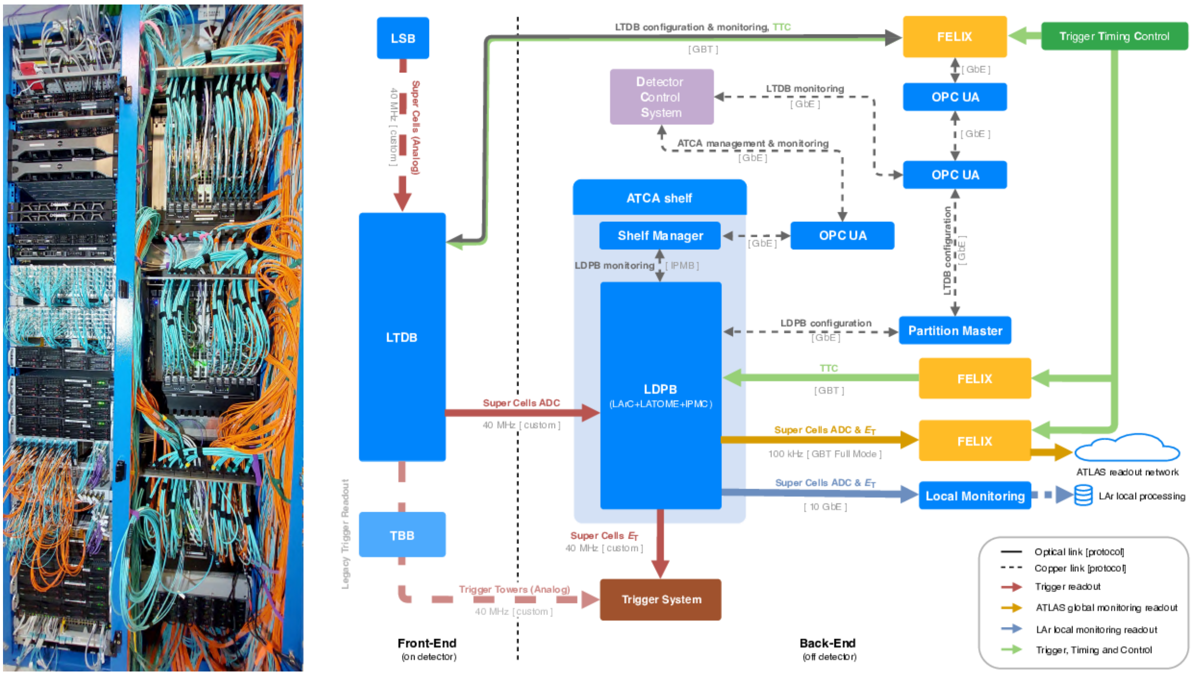

(a) **(b)**

Figure 3.11 (a) Picture of the Digital Trigger rack in the USA15 counting room. In the left rack are the Run Control, Detector Control System, Local Monitoring and FELIX systems. The three ATCA crates are visible on the right rack.
(b) Data paths of the Digital Trigger. From Ref. [57].

of ATCA (Advanced Telecommunications Computing Architecture) crates superior to the VME crates in cooling, power or bandwidth. Each LDPB is a LAr Carrier (LArC) blade hosting mezzanine cards called LAr Trigger prOcessing MEzzanine (LATOME). There are up to four LATOMEs per LArC for a total of 116 LATOMEs. As an intermediary with the ATCA shelf manager, an Intelligent Platform Management Controller (IPMC) is plugged on each LArC. Each LATOME has mainly one FPGA (Firmware Programmable Gate Array) and a Modular Management Chip (MMC) managing the onboard sensors (temperature, voltage, etc.) and the connection to the IPMC.

The various Digital Trigger data paths around the LDPS are illustrated in Fig. 3.11(b). With the main readout paths (red arrows) the LDPBs receive ADC counts from the LTDBs and send E_{T} to the FEXs at 40 MHz. Monitoring paths sending E_{T} and the corresponding four ADC counts for offline energy recomputation are split between a global path to the main data acquisition system for every L1 accept trough the FELIX system[6](yellow arrow) and a more flexible local monitoring path (blue arrow). The TTC information and its various counters used for synchronisation are sent to the LDPBs through the FELIX system (green arrows). In addition to these five main data paths, the Detector and Control System, connected through the IPMC and ATCA shelf manager to the LDPB, monitors the hardware and ensures safety mechanism in case of failure. Finally, the *Partition Master* computer manages the configuration and operation of all LTDBs and LDPBs.

---

[6] The Front-End LInk eXchange is a detector agnostic readout architecture providing access to the Trigger and Data Acquisition system to front-end ATLAS subsystems.

3.2.3 The LATOME board

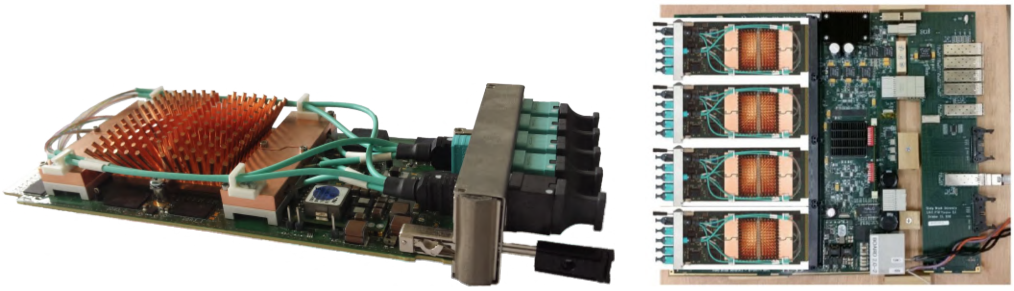

(a) (b)

Figure 3.12 Picture of a LATOME board equipped with optical fibers and a copper heatsink (a), and picture of a LAr Carrier equipped with four LATOME boards (b).

The bulk of the processing of Super Cells raw data happens in the LATOME, visible in Fig. 3.12, for a very challenging total latency of 415 ns. This latency, still a third of the total latency of the Digital Trigger electronics, allows for the delivery of transverse energy and associated bunch crossing identifier (BCID) for up to 320 Super Cells at 40 MHz to the FEXs. It manages up to 48 optical fibers at 5.12 Gb/s of input data (blue front connectors on the picture) and outputs to the FEX in 48 optical fibers at 11.2 Gb/s (black front connector on the picture). The LArC hosting the LATOMEs manages the monitoring and TTC paths as well as the powering of all LATOMEs.

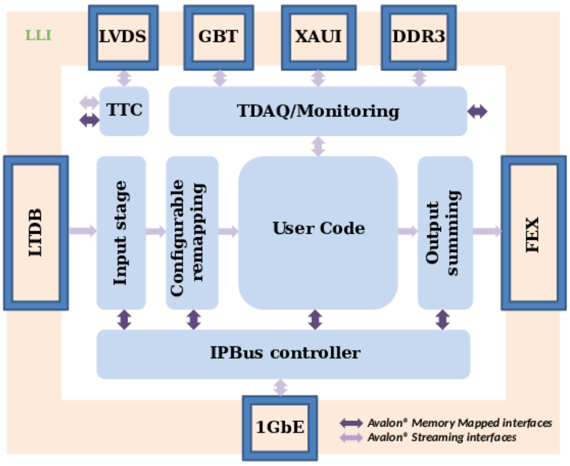

Figure 3.13 Block diagram of the LATOME Firmware. The pale brown frame represents the interface with the hardware. The inner pale blue boxes are functional blocks of the firmware. From Ref. [64].

The firmware of the LATOME, the low level software responsible for the realisation of its assigned tasks, is embedded in its FPGA. The Low Level Interface (LLI) controls the hardware components of the LATOME. In particular, it is responsible for the interface with the various data paths described in Fig. 3.11(b) and the FPGA core layers. The main data path illustrated in Fig. 3.13 is split in a few blocks:

- The input ADC counts from the LTDB first go through the **Input Stage** block. There, the data from all input optical fibers is de-serialised. Additionally, the data coming from the on-detector FECs 77 m away have some fiber dependent time delays. This blocks realigns all the data of the same Bunch Crossing Identifier (BCID).

- In the **Configurable Remapping** block, the data from different Super Cells is rearranged in order to group Super Cells from a same Trigger Tower together, as Trigger Tower output is needed by some FEXs. Also, the 48 parallel input streams are rearranged into 62 input streams. As a result, each stream goes from managing 8 Super Cells per 25 ns to only 6, lowering the electronic clock from $8 \times 40 = 320$ MHz to $6 \times 40 = 240$ MHz. This allows to ease the computation of E_{T} and BCID assignment in the User Code block that follows.
- The **User Code** computes the transverse energy E_{T} and pulse phase τ at every bunch crossing using Optimal filtering in the same fashion as in Section 3.1.2. For a given BCID, if the phase is short enough, a pulse is believed to have been detected and the computed E_{T} is sent forward to the following block; else no energy deposit is considered and 0 is sent. This block will be described more in depth in Section 4.1.
- The **Output Summing** block sums the E_{T} in different (η, ϕ) regions depending on the granularity required by the FEXs. The eFEX, targeting electromagnetic objects, keeps the Super Cell granularity, and no extra summing is needed. Nevertheless, the jFEX, targeting jets and $E_{\mathrm{T}}^{\mathrm{miss}}$, and the gFEX, targeting large jets and ΣE_{T}, need respectively the data to be summed on $\Delta\eta \times \Delta\phi = 0.1 \times 0.1$ (Trigger Tower) and $\Delta\eta \times \Delta\phi = 0.2 \times 0.2$. The data can thus be duplicated depending on the different FEX receivers and the output data flow rate increases. In total, slightly more than 40 Tb/s are sent to the FEX systems.

Chapter 4

From calibration to computation

I joined the LAr Phase 1 upgrade group of LAPP in 2019 as part of my ATLAS author qualification task. Within the LAr Phase 1 upgrade, LAPP was primarily responsible for the production and qualification of all the LATOME boards[1], hence the Savoyard cheese name they received. When I started working on the Phase 1 upgrade, the production of LATOME boards was almost complete and efforts were put into the validation of their integration on the LArC. In parallel, developments of their firmware were ongoing to make all the required functionalities fit on the finite amount of logic elements available on the FPGA within the specified latency. Finally, developments on the software side aimed at being able to configure and monitor the LATOMEs using the LAr Online interface. This interface manages data acquisition in LAr and is used by shifters in the ATLAS Control Room during LHC operations. I worked specifically on the configuration of the User Code block of the LATOME firmware, and later in the commissioning of the functionalities it introduced.

I will present first in detail the User Code block and the problematic of its configuration before each run in Section 4.1. The User Code requires for its various tasks a set of coefficients taken externally from a database. At each configuration, they are loaded in their reserved registers in the LATOME's FPGA. These coefficients and their use in the User Code will first be described in Section 4.1.1. The database side holding originally the coefficients is described in Section 4.1.2. From the database, they are made ready for the loading in the LATOME (Section 4.1.3) and filled in the appropriate register (Section 4.1.4).

Then, in Section 4.2, the commissioning of the User Code will be described. As first tests, the proper loading of the User Code registers was checked (Section 4.2.1). Then more advanced tests allowed to check the computation performed in the User Code and compare it to offline reconstruction (Section 4.2.2). This allowed to improve alternatively the code or the documentation to obtain in the end, a User Code fully validated. In addition to this validation, the degradation entailed by the finite numerical precision of the LATOME computation was assessed and shown to be negligible compared to the total energy resolution of the Digital Trigger (Section 4.2.3).

---

[1] The LAPP was in addition responsible for the IPMC board and its interface with the MMC and the ATCA Shelf Manager.

4.1 User Code coefficients

4.1.1 User Code operation

The User Code completes the main task of the LATOME: computing E_T from ADC counts. It has a complex architecture split in various blocks represented in Fig. 4.1. First, a **Pedestal correction** block removes an offset from the incoming ADC counts to recover a sampling of the original bipolar pulse shape. First, the Super Cell specific pedestal is subtracted from the input ADC counts. However, the negative tail of the LAr pulse shape (Fig. 3.3) is not able to properly cancel in-time pile-up at the beginning of a bunch train in an LHC run. Consequently, an additional BCID-dependent *Baseline Correction* is subtracted from the ADC counts. This correction depending on the LHC bunch scheme, it is directly calculated on the LATOME for each Super Cell at each of the 3564 bunch crossings of an LHC cycle. The ADC counts, corrected by the Super Cell pedestal, are averaged for the given bunch crossing on 1024 cycles. Because the luminosity decreases along an LHC run, this correction is updated every 10 s. This block outputs at every bunch crossing m the sampled signal minus the fixed Super Cell pedestal and its BCID dependent correction $S_m - p_m$.

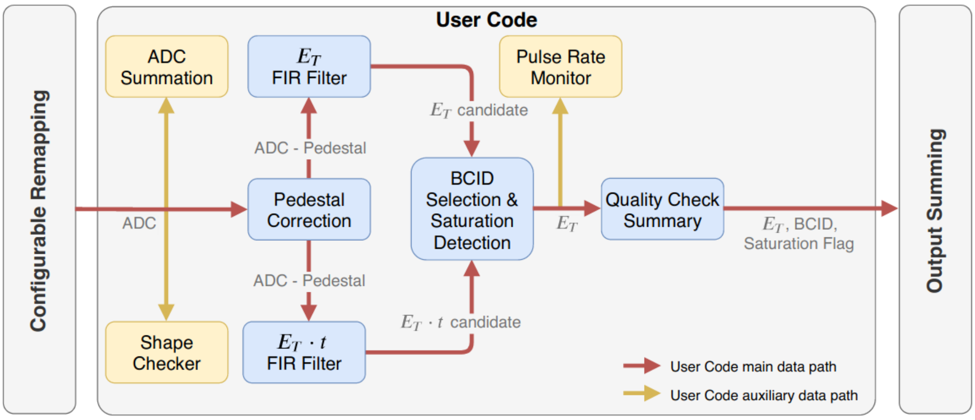

Figure 4.1 Block diagram of the User Code. From Ref. [64].

Then two **FIR Filters** (Finite Impulse Response) are responsible for the calculation of respectively E_T and $\xi = E_\mathrm{T} \cdot \tau$, using OFCs as described in Section 3.1.2. For every bunch crossing m, E_T and ξ are computed using the ADC count received and the three following ones:

$$E_\mathrm{T}(m) = \sum_{i=0}^{4} a_i \left(S_{m+i} - p_{m+i}\right) \ , \tag{4.1}$$

$$\xi(m) = E_\mathrm{T}(m) \cdot \tau(m) = \sum_{i=0}^{4} b_i \left(S_{m+i} - p_{m+i}\right) \ , \tag{4.2}$$

with a_i and b_i the two sets of OFCs. The amplitude – which is directly E_T – and the phase τ, the parameters of the pulse as in Fig. 4.2(a), are computed continuously for every BCID, using the ADC counts from the three following BCIDs. This introduces a minimal latency of three bunch crossings. An FPGA manipulates numbers in binary form. As a result additions, subtractions and bit shifts are straight forward to implement but high speed multiplications require a special block called a DSP. Clever arrangement of these

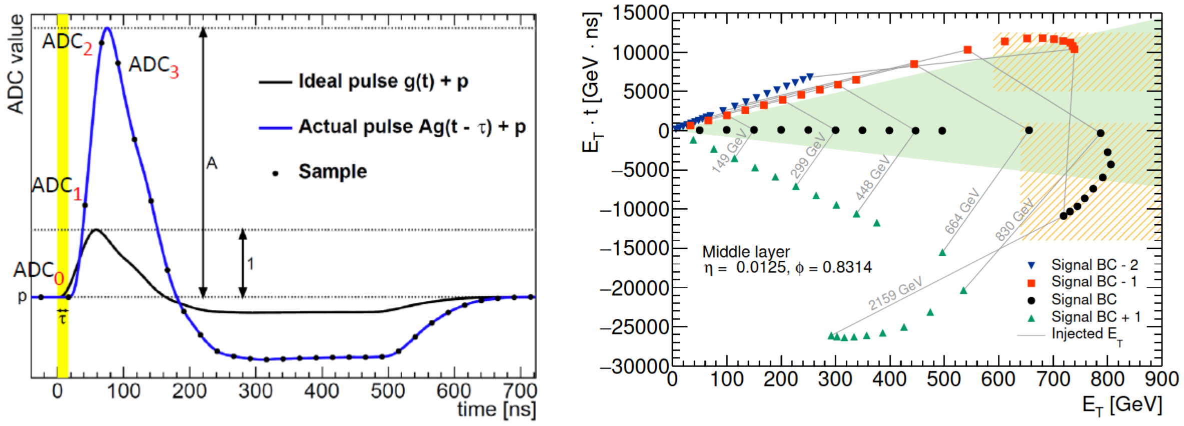

(a) **(b)**

Figure 4.2 (a) Parameters of a pulse in a LATOME. (b) $\xi = E_\mathrm{T} \cdot \tau$ as a function of E_T measured in calibration runs with injected pulses of known E_T and bunch crossing. For various injected E_T, the computed point obtained with the correct set of four ADC count, starting at BCID m, is displayed in black. The same computation is performed starting with BCID $m+1$ (green), $m-1$ (red) and $m-2$ (blue). Points obtained with the same injected E_T are linked by grey lines. The selection criterion is represented by the green area. The orange hatched regions represent the saturation regions. From Ref. [64].

DSP blocks allow to parallelise computation for a limited additional latency of 0.5 bunch crossing.

For a given Super Cell, one E_T and ξ is computed at every BCID, independently of whether there was a pulse in the Super Cell or not. The **BCID Selection** block compares the E_T and ξ results from the two filters to determine if the phase τ is small enough to be associated to a pulse happening at the considered BCID, as in the situation of Fig. 4.2(a). This is indirectly assessed by comparing E_T and ξ. A pair of E_T and BCID is considered correct if

$$\begin{cases} 8E_\mathrm{T} < \xi < -8E_\mathrm{T} & \text{if} \quad -1 < E_\mathrm{T} \leq 0\,\mathrm{GeV}\,, \\ -8E_\mathrm{T} < \xi < 8E_\mathrm{T} & \text{if} \quad 0 < E_\mathrm{T} \leq 10\,\mathrm{GeV}\,, \\ -8E_\mathrm{T} < \xi < 16E_\mathrm{T} & \text{if} \quad E_\mathrm{T} > 10\,\mathrm{GeV}\,. \end{cases} \tag{4.3}$$

Among the 25 ns between two BCIDs, a window of ±8 ns is thus used. For high energy particles, this window is extended asymmetrically up to 16 ns to avoid a wrong BCID assignment of hypothetical long-lived particles. Finally, conditions for negative energy events are used to take into account resolution effects. The comparisons make use of powers of two easily implemented with bit shifts in the FPGA. At BCID m, if this criterion is failed, the User Code will output $E_\mathrm{T} = 0$; else the computed E_T is sent.

Finally, this selection can be biased by saturation effects: large energy deposits can lead to saturated pulses in the front-end electronics, leading to shorter rise time of the pulse and ultimately a wrong E_T and BCID assignment. A **Saturation Detection** block is used to detect such events. Pulses with known E_T and BCID are injected in calibration runs to a Super Cell and the computed E_T and ξ are plotted in Fig. 4.2(b). This is done using four ADC counts starting from the correct BCID m, but also at $m-1$, $m-2$ and $m+1$. The green triangular area corresponds to the selection condition of Eq. (4.3). The phase of such calibration pulses is always the same and thus, the relation between E_T and ξ should be linear, with the slope τ negative for BCID $m+1$, and increasingly positive for BCID $m-1$ and $m-2$. This linear behaviour is observed in Fig. 4.2(b) up to high energies when saturation starts appearing. Then, the shorter rise time of saturated pulses makes all the curves go down. Two orange hatched regions on this E_T against ξ plot are used to detect saturated pulses, the upper rectangle detecting saturated pulses with computations at BCID $m-1$, the lower one with computations at the correct BCID m. These rectangles correspond to the conditions

$$E_\mathrm{T}(m-1) < E_\mathrm{T}^{\text{threshold, BCID}-1} \quad \text{and} \quad \xi^{\text{min, BCID}-1} < \xi(m-1) < \xi^{\text{max, BCID}-1}, \tag{4.4}$$

$$E_\mathrm{T}(m) < E_\mathrm{T}^{\text{threshold}} \quad \text{and} \quad \xi^{\text{min}} < \xi(m) < \xi^{\text{max}}, \tag{4.5}$$

where the six saturation detection parameters $E_\mathrm{T}^{\text{threshold, BCID}-1}$, $\xi^{\text{min, BCID}-1}$, $\xi^{\text{max, BCID}-1}$, $E_\mathrm{T}^{\text{threshold}}$, ξ^{min}, ξ^{max}, are introduced. These parameters are determined for each Super Cell. Upon fulfilling one or both of these conditions, the pulse is considered saturated and the selection block decision is not considered anymore. If both conditions of Eq. (4.4)–(4.5) are passed, the pulse is still considered to have valid timing and $E_\mathrm{T}^{\text{threshold}}$ is sent; else the output at the considered BCID is 0. For completeness, three auxiliary modules in Fig. 4.1 (yellow blocks) compute monitoring data, but are not part of the main data flow.

4.1.2 The COOL database

Three out of four blocks of the User Code use configurable parameters: four OFCs and one pedestal for each FIR Filter, and six parameters for saturation detection. These parameters are each loaded in a register of the FPGA during the configuration of the LATOME. For each Super Cell, a total of 16 parameters have to be loaded. Each LATOME managing up to 320 Super Cells, up to 5120 registers must be filled by parameters from the correct corresponding Super Cell. These constitute non-event data that can be stored by ATLAS computing tools in two types of databases: configuration databases and condition databases.

In the TDAQ environment of the LAr Digital Trigger, the configuration database used, based on the OKS (Object Kernel Support) object manager [65, 66], stores software and hardware configuration data *e.g.* which LATOME is on which LArC, what version of the firmware is used, etc. Nevertheless, the User Code parameters are characterised by a limited validity in time. For instance, the OFCs and pedestals come from calibration runs and, during stable running conditions, they are updated approximately once per month. Only the most recent set of parameters is loaded in the registers of the LATOMEs during the configuration before each run. Yet, it must be possible to recover the complete configuration in use at any time in the past. This should allow in particular offline reconstruction of each step of the Digital Trigger computation for any specific event. To meet this requirement, the User Code parameters are stored in a database, called condition database, that organises data objects by Interval of Validity (IoV). In ATLAS, the condition databases are based on `COOL` [67, 68], a product developed by the LHC Computing Grid team.

In the `COOL` database, the data is stored in folders themself part of a structure of folders. Within each folder, data object of the same type are stored, each with a corresponding IoV. The User Code parameters for all Super Cells are stored in new dedicated folders within data object of the BLOB (Binary Large OBject) type. A BLOB is a raw data structure arranging the binary encoding of the values for each Super Cell one after the other. Custom code from ATLAS computing framework is responsible for the decoding of these vectors. When accessing the database, a validity key combining the run number and the luminosity block allows to extract all the BLOBs corresponding to the requested time. `COOL` is only responsible for the management of IoVs, and as such, condition databases can use different underlying database technologies. The main ATLAS `COOL` database, based on Oracle DB, contained among others calibration coefficients for LAr cells. New folders for the Super Cell parameters in the User Code folders were added as a result of the Phase 1 upgrade. For tests, it was possible to create more flexible dummy `COOL` databases on a SQLite back-end.

In the main readout, the energy is obtained from the ADC counts with Eq. (3.7). The Digital Trigger outputs transverse energy instead of energy, thus a factor $1/\cosh(\eta)$ from Eq. (2.5), must be applied to make the conversion. Additionally, the DSP in the User Code outputs the energy as a signed integer with a precision associated to its least significant bit of 12.5 MeV. This implies that an additional coefficient $\mathrm{LSB} = 12.5$ should divide the energy from Eq. (3.7) that is otherwise expressed in MeV. Finally, similarly to the general case in the main readout, only the coefficient R_1 survives as the ramp run is a linear fit and R_0 is not used. Consequently, Eq. (3.7) must be modified to

$$E_{\mathrm{T}} = F_{DAC\to\text{ţA}} \cdot F_{\text{ţA}\to\mathrm{MeV}} \cdot \left(\frac{M_{phys}}{M_{cal}}\right)^{-1} \cdot C_{\mathrm{HV}} \cdot R_1 \cdot \frac{1}{\mathrm{LSB}} \cdot \frac{1}{\cosh(\eta)} \cdot \sum_{i=0}^{3} a_i \left(ADC_i - p\right). \tag{4.6}$$

The computation of ξ uses exactly the same formula, only replacing the a_i by b_i. The LSB coefficient is not modified, meaning the precision on E_{T} within the product $\xi = E_{\mathrm{T}} \cdot \tau$ is kept the same.

To allow the complete offline reconstruction of the LATOME output, factors $F_{DAC\to\text{ţA}}$, $F_{\text{ţA}\to\mathrm{MeV}}$, M_{phys}/M_{cal}, C_{HV}, R_1 and LSB are stored as floats in the `COOL` database each in a dedicated folder. The factor $1/\cosh(\eta)$ is directly applied to the OFCs a_i in the calibration runs output. These modified a_i are all stored in one BLOB of floats, along with the similarly modified b_i BLOB, inside the OFC folder of the `COOL` database. The pedestal p is also stored in a BLOB of floats inside its own `COOL` folder. Finally, the six saturation detection parameters of Eq. (4.4)–(4.5) are stored in `COOL`, directly as integers ready to be used in the User Code.

4.1.3 Coefficients in LATOME registers

Nevertheless, the LATOME only uses pedestals and OFCs, as in Eq. (4.1)–(4.2). As a result, all the coefficients from Eq. (4.6) are taken from the database and multiplied by each OFC to create LATOME-ready OFCs $\tilde{a}_i$:

$$\tilde{a}_i = f \cdot a_i \qquad \text{with} \quad f = F_{DAC\to\text{ţA}} \cdot F_{\text{ţA}\to\mathrm{MeV}} \cdot \left(\frac{M_{phys}}{M_{cal}}\right)^{-1} \cdot C_{\mathrm{HV}} \cdot R_1 \cdot \frac{1}{\mathrm{LSB}} \cdot \frac{1}{\cosh(\eta)}. \tag{4.7}$$

The same factor is applied to the b_i. The pedestals p are left unaffected.

A last step is to convert these pedestals and modified OFCs in float to signed integers with hard points fitting in the 18 bits[2] available in their register. Rounding, signs and hard points have direct consequences on the implementation of this conversion. For a signed integer of N bits, the range covered is $[-2^{N-1}; 2^{N-1} - 1]$. For positive integers k in this

---

[2] The original 14 bits size was found during commissioning to be too small for the range covered by the OFCs.

range, it is represented in binary as `0b0kN−1...k2k1k0` where `0b` is a prefix to indicate a binary representation and each $\mathtt{k_i}$ is 1 or 0 from the following decomposition of k:

$$k = \mathtt{k_{N-1}} \cdot 2^{N-1} + ... + \mathtt{k_2} \cdot 2^2 + \mathtt{k_1} \cdot 2^1 + \mathtt{k_0} \cdot 2^0. \tag{4.8}$$

As such, only half of the allowed range, from 0 to $2^{N-1} - 1$, is used and the number could also fit in $N - 1$ bits. The positive integers from $2^{N-1} =$ `0b10...000` to the maximum value on N bits $2^N - 1 =$ `0b11...111` are used to represent negative integers, going backward from the maximum value to the middle value. For example, -1 will be represented by the positive integer $2^N - 1 =$ `0b11...111` and the minimum value -2^{N-1} is represented by `0b10...000`. In general, a negative integer k will be represented by the positive integer $\tilde{k}$ such that

$$\tilde{k} = 2^N - k. \tag{4.9}$$

Consequently, the most significant bit – the most to the left – is 0 for positive integers and 1 for negative integers. This bit is called a sign bit. Finally, the hard point is a way to introduce a representation of decimals in binary. For example, a hard point set to 3 bits amounts to using the integer k to represent the number with a decimal part $\hat{k} = k/2^3$ transforming Eq. (4.8) in

$$\hat{k} = \mathtt{k_{N-1}} \cdot 2^{N-1-3} + ... + \mathtt{k_2} \cdot 2^{-1} + \mathtt{k_1} \cdot 2^{-2} + \mathtt{k_0} \cdot 2^{-3}. \tag{4.10}$$

As a result, the three least significant bits – the most at the right – represent decimals, from left to right 0.5, 0.25 and 0.125.

This representation of signed numbers with a decimal part is visible in Fig. 4.3 for numbers used in computations of the Pedestal Correction block of the User Code. The ADC count arriving in the User Code are 12 bits positive integers. The pedestal that is subtracted is a positive 14 bits integer with a hard point set to 3 bits for precise subtraction. The Baseline Correction can be negative and has the same precision as the pedestal: it is thus stored on 9 bits, with 1 sign bits and 3 decimal bits. As a result, the so-called Pure ADC count that will be used in the FIR Filter blocks has 16 bits with 1 sign bit and 3 decimal bits.

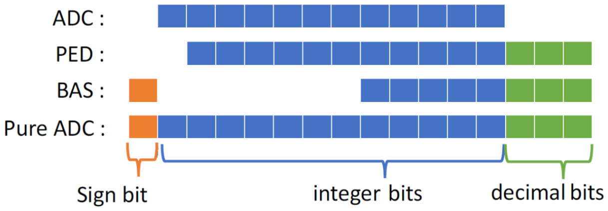

Figure 4.3 Binary representation of numbers used in the Pedestal Correction block of the User Code. Each coloured square represents a slot for one bit.

The OFCs a_i are stored in 18 bits registers as signed integers with a hard point set at 5 bits. They thus cover the range $[-4096; 4095]$ with a precision of $1/2^5 = 0.03125$. To convert them from their float value, they are first multiplied by 2^5 and then rounded to accommodate the hard point in the integer representation. Then as a check, the absolute value is taken and it is checked if it fits on the 17 bits available. If so, this 17 bits positive integers is given back its original sign and transformed in a 18 bits signed integer with Eq. (4.9). A similar procedure is applied to the OFCs b_i but with a hard point set at 3 bits, because the b_i being typically larger, more of the 18 bits are used for the range at the expense of the decimal precision. The pedestals also have this same treatment, with hard point set at 3 bits as already described in Fig. 4.3.

In the DSPs of the FIR Filters, the OFCs are multiplied by the Pure ADCs. For E_T computation, that is a 18 bits number with 1 sign bit, 12 integer bits and 5 decimal bits multiplying a 16 bits number with 1 sign bit, 12 integer bits and 3 decimal bits. The result will thus be a 33 bits number, with 1 sign bit, $12+12=24$ integer bits and $5+3=8$ decimal bits. The DSP anyway outputs the result of multiplications on 44 bits signed integers. The 8 decimal bits are dropped as an irrelevant precision, leaving a signed integer with its least significant bit corresponding to a precision of 12.5 MeV as fixed in Section 4.1.2. To lower the amount of data in the output, only the 17 lower bits are kept, giving an E_T encoded on a 18 bits signed integer. The corresponding allowed range of energy is thus of $\pm 2^{17} \cdot 12.5\mathrm{MeV} = \pm 1.64\,\mathrm{TeV}$, which is enough for most events. In case of overflow (underflow), the maximum (minimum) value in the range is sent.

From the selection criterion in Eq. (4.3), the phase τ should range from -8 to 16. This requires a 5 bits signed integer. To keep the same E_T range and precision requires a 17 bits integers. The FIR filter output for ξ is thus encoded on a 22 bits signed integer. Similarly as for E_T computation, the $3+3=6$ decimal bits of the DSP output are dropped and then, the 21 lower bits are kept with in addition the sign bit. All the ranges of the DSP output kept depending on the computation are summarised in Fig. 4.4.

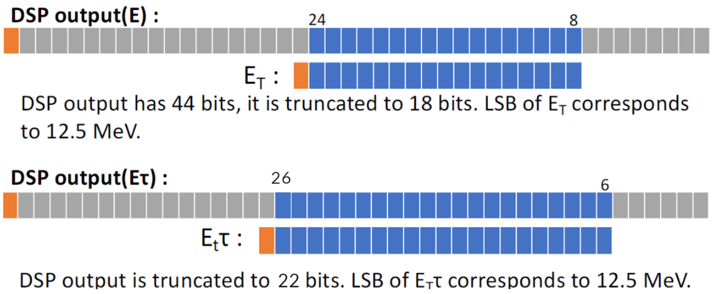

Figure 4.4 Binary representation of the DSP outputs and bit selection. Each square represents a slot for one bit.

4.1.4 Filling registers

The LATOME configuration in the LAr Online framework makes use mainly of two software packages named `LDPB` and `OnlineLatomeDB`. At the start of the configuration of LATOMEs, the package `OnlineLatomeDB` is in charge of retrieving all the needed coefficients from the `COOL` database, using a validity key created combining the current run number and first luminosity block. In particular, the OFCs and pedestals go through the treatment described in Section 4.1.3 to obtain coefficients ready to be loaded in the LATOMEs' registers. All these coefficients are stored for all Super Cells in an `OnlineLatomeDB` API[3] that will be accessed at the configuration of each LATOME. This configuration is managed by the `LDPB` package LATOME by LATOME. At the time of the configuration of the User Code, the API holding all the coefficients is accessed. Then, the code is responsible to find the coefficients corresponding to the registers present in the LATOME being configured.

---

[3] An Application Programming Interface (API) is a type of software interface that acts as a connection between pieces of softwares, as opposed to a user interface that would connect a software to a user.

As was described in Section 3.2.3, the data from the different Super Cells arrives in the User Code arranged in 62 streams of 6 Super Cells. A Super Cell is uniquely identified by its stream number and place in that stream; to this are associated the 16 registers of User Code coefficients to be filled. Mapping files within the firmware release provide the Offline ID of a Super Cell, given its stream and position in the stream. The Offline ID is a number that uniquely identifies a physical Super Cell within the detector. A Super Cell can also be identified by an Online ID, which is linked to its cabling in the LAr electronics. The LATOME firmware uses Offline ID as the geometrical information is more important, as exemplified by the Configurable Remapping block. The Online ID on the other hand is used to organise the coefficients in the `COOL` database as most of them arise from calibration runs within the LAr electronics. Both IDs are different and the one to one correspondence could change during the many years of operation of the Digital Trigger, during Run 3 and HL-LHC. For book-keeping reasons, a folder in the `COOL` database allows the conversion from Offline to Online ID.

To summarise, the Offline ID taken from the LATOME firmware is first converted to the Online ID using the `COOL` database conversion folder that was dumped in the `OnlineLatomeDB` API. This Online ID is then used as a key to obtain the 16 parameters of the Super Cell considered. These coefficients are then written to the corresponding registers of the FPGA.

4.2 Commissioning

4.2.1 Register Loading commissioning

In projects of such complexity, it is important to thoroughly assess the proper implementation of each functionality, separately first, and in increasingly aggregated form later, in what is called *commissioning*. In this spirit, the structure detailed in Section 4.1 was slightly modified to test each step separately. First, custom `COOL` databases on a SQLite back-end allowed testing specifically the loading of the different registers of a Super Cell, holding coefficients as integers directly in the LATOME register format. A first such database had, for every Super Cell, the same set of dummy values of User Code coefficients. It allowed to check that every coefficient was indeed loaded in the registers of each connected Super Cell.

A second test `COOL` database had its OFCs chosen to check the computation was going as expected in the LATOME firmware. With pedestals chosen to be zero, and OFCs of both FIR Filters to be $a_i = b_i = (1; 0; 0; 0)$ for every Super Cell. Having the exact same set of OFCs for the E_T and ξ calculation ensures that the computed E_T and ξ will be the same, and that the selection criterion from Eq. (4.3) will always be passed. From Eq. (4.1) the E_T output should be exactly the ADC sent at the BCID considered. Conversely, choosing $a_i = b_i = (0; 0; 0; 1)$, the E_T output is the ADC three bunch crossing later. These configurations and similar ones were tested in special runs in which the ADC counts sent to each channel were set at each bunch crossing to the associated BCID, allowing to explicitly check the expected ADC is indeed selected by the filters. Playing with these different databases allowed checking the expected database was indeed filled in the registers. This allowed also checking the OFCs were filled in the right order.

4.2.2 Energy offline re-computation

The energy computation formula being validated, the next step was to check with real OFCs coming from calibration. They would thus all be different for each Super Cell. Additionally, the conversion from floats to signed integers of Section 4.1.3 had to be implemented and could thus be checked. Comparing the LATOME output to an offline computation allowed indirectly to check that all the coefficients were filled in the correct register and in the correct format. The initial 14 bits reserved for the OFCs registers proved not to be enough and were extended to 18 bits. The final structure of the `COOL` database coming from calibration was devised and the configuration of the LATOME was operated as in Section 4.1.1, with in addition the Baseline Correction, Saturation and Selection blocks disabled. Pulses were sent on every Super Cell at a given BCID m and 20 samples were recorded from BCID $m-2$ to $m+18$. The E_{T} output of the LATOME was also recorded for BCID $m-1$, m and $m+1$. Ten such events were recorded for every Super Cell. Using the recorded samples, it was possible to reproduce offline the computation in the LATOME as described by the firmware documentation. After adjustments, this offline computation was shown to agree perfectly with the recorded E_{T}, as visible in Fig. 4.5(a). The difference between the LATOME and the offline re-computed energy is shown to be exactly 0 for all Super Cells, in all events, and for all three energies recorded per event. This validates the FIR filter for E_{T} computation in the User Code and thus the proper loading of all associated pedestals and OFCs of all Super Cells.

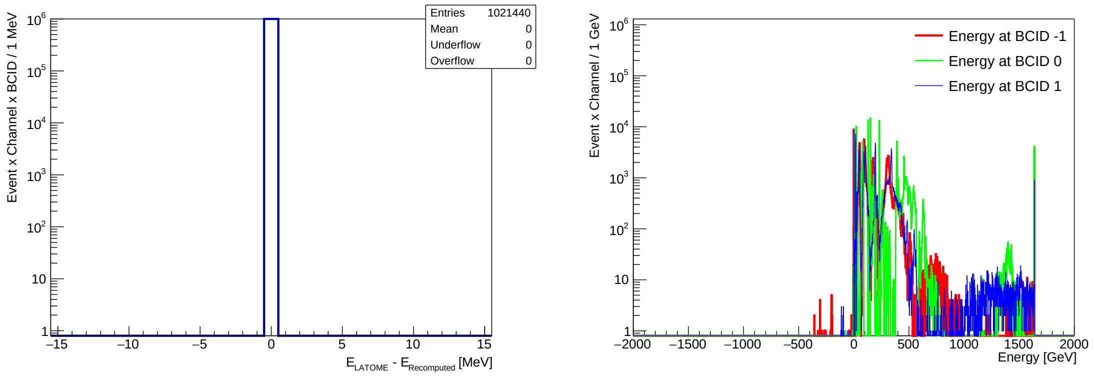

(a) **(b)**

Figure 4.5 (a) Histogram of the difference between $\mathrm{E}_{\mathrm{LATOME}}$ the E_{T} output of the LATOME and $\mathrm{E}_{\mathrm{Recomputed}}$ from the offline computation. The bins width is 1 MeV, well below the computational resolution at 12.5 MeV, and the bins height is in log scale. (b) Histogram of the distribution of the energies from the LATOME at BCID $m-1$, m and $m+1$. The bins width is 1 GeV, and the bins height is in log scale.

The LATOME output energy distribution is shown in Fig. 4.5(b). The overflow bin is clearly visible at 1638.4 GeV. It is also visible that some energies computed by the LATOME are negative. This is because the Selection block is disabled, and as a result the FIR Filter result for computations started well before or after the actual peak can yield unphysical results. No underflow bin at −1638.4 GeV is visible not because the case does not happen, but rather because in this case, the LATOME outputs 0, which is an abnormal behaviour found in this study.

The same study enabling the Selection block was performed pulsing similarly all Super Cells and recording ten events. However, here the LATOME E_{T} output is after the selection block and will thus be 0 if the selection criterion is not passed. In case of overflow (underflow) of the computed ξ, the maximum (minimum) value on the 22 bits available is kept. Interestingly, this means that in this case, the selection criterion will never pass, as

$$\xi^{22\text{bits max}} = 2^{21} - 1 > 16 \times (2^{17} - 1) = 16E_{\mathrm{T}}^{18\text{bits max}} \, ,$$
$$\xi^{22\text{bits min}} = -2^{21} < -8 \times 2^{17} = 8E_{\mathrm{T}}^{18\text{bits min}} \, .$$

Again, the offline computation, including the selection criterion, agrees perfectly with the LATOME output for all Super Cells, in all events, and for all three energies recorded per event, as visible in Fig. 4.6(a). The selected energy distribution is shown in Fig. 4.6(b). The calibration pulse is supposed to have been sent at BCID m which is reflected in the figure as most of the energies kept are indeed kept at BCID m. The energy at BCID $m-1$ or BCID $m+1$ is sometimes selected as the OFCs used in this study do not have perfect timing adjustment. The overflow bin is clearly visible, as well as the bin at 0 that now contains all the rejected energies.

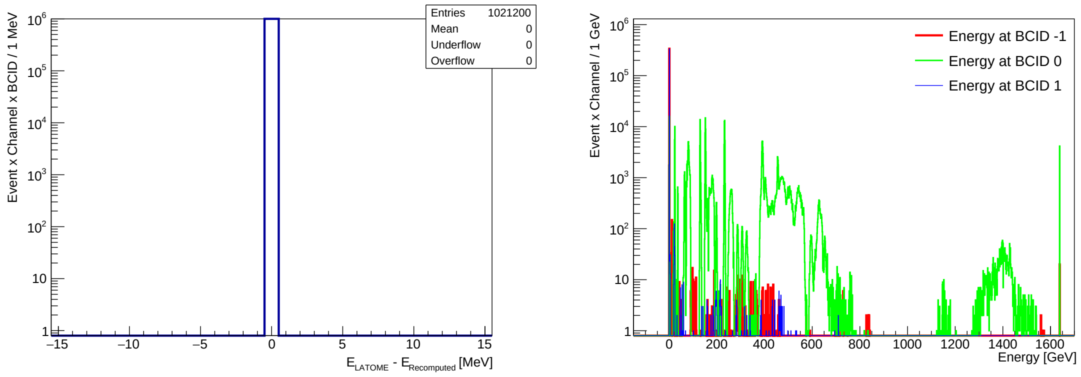

(a) **(b)**

Figure 4.6 (a) Histogram of the difference between $\mathrm{E}_{\mathrm{LATOME}}$ the E_{T} output of the LATOME after selection block and $\mathrm{E}_{\mathrm{Recomputed}}$ from the offline computation. The bins width is 1 MeV, well below the computational resolution at 12.5 MeV, and the bins height is in log scale. (b) Histogram of the distribution of the energies from the LATOME after selection, at BCID $m-1$, m and $m+1$ with $m=0$, the BCID at which the calibration pulse is supposed to happen. The bins width is 1 GeV, and the bins height is in log scale.

4.2.3 Performances of the E_{T} computation

A similar offline computation of the energy can be done using this time the full float precision of the OFCs. The direct comparison of the full float precision energy to the LATOME output gives the energy resolution. Representing the difference between both results, a distribution centred on zero is obtained, with standard deviation of 100 MeV, and large tails, as visible in Fig. 4.7(a). This is approximately the precision of the fourth least significant bit of the LATOME output – the least significant bit representing 12.5 MeV. This numerical precision choice in the LATOME output is thus very conservative. Still, this resolution is small compared to the typical values of the energy computed. Besides, the energy resolution, defined as the relative difference of the LATOME output with the full float precision energy obtained offline, is found to be very small as visible in Fig. 4.7(b). The obtained distribution is centred on zero and very peaked, with a standard deviation at the per mil level.

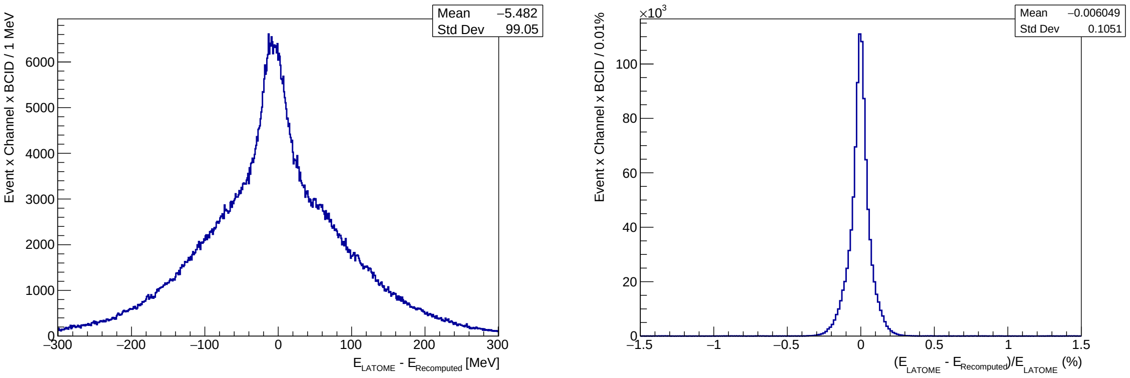

(a) **(b)**

Figure 4.7 (a) Histogram of the difference between $\mathrm{E}_{\mathrm{LATOME}}$ the E_{T} output of the LATOME and $\mathrm{E}_{\mathrm{Recomputed}}$ from the offline computation with the full float precision for the OFCs. The bins width is 1 MeV, well below the computational resolution at 12.5 MeV. (b) Histogram of the energy resolution of $\mathrm{E}_{\mathrm{LATOME}}$ the E_{T} output of the LATOME compared to $\mathrm{E}_{\mathrm{Recomputed}}$ from the offline computation with the full float precision for the OFCs.

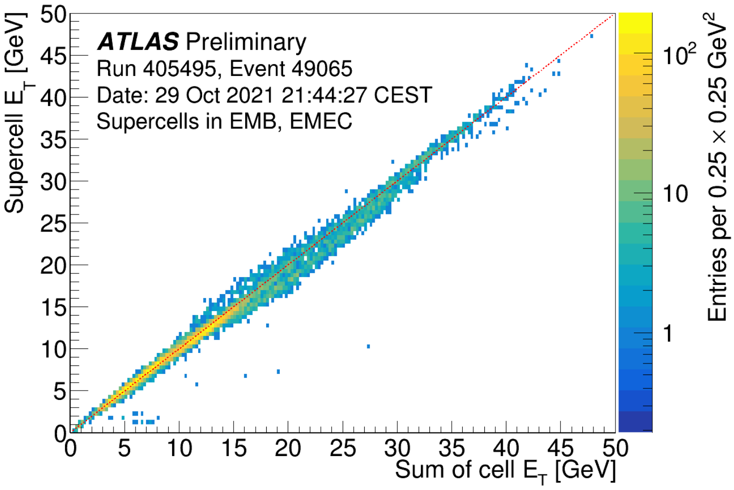

Figure 4.8 Measured E_{T} in Super Cells from all layers of the LAr EMB and EMEC computed offline, compared to the summed E_{T} from their constituent LAr cells obtained through the main readout path. The data are from a single event of a beam splash run. The red line of equation $y = x$ marks the agreement of both values. From Ref. [69].

The E_{T} computed on the LATOME for the Super Cells can be compared to the energy obtained with the LAr cell geometrical resolution in the main readout. Of course the coarser granularity of the Super Cells creates a disagreement. Data recorded during October 2021 Pilot Beam run, preliminary to Run 3, allows assessing this agreement. In Fig. 4.8, the E_{T} of Super Cells recorded with the main readout LAr cells granularity is compared to the E_{T} reconstructed in the Super Cell. This reconstruction is made offline with preliminary calibration coefficients of the corresponding Super Cells as the full chain of the Digital Trigger was not ready at the time. Both readouts – LAr cells and Super Cells– are well correlated as the excellent agreement along the $y = x$ line shows. The disagreement along this line yields a resolution of the order of one GeV. This resolution, an effect of the coarser geometrical granularity of Super Cells, is one order of magnitude above the resolution observed from the finite precision of OFCs in the LATOMEs computation. The precision chosen for the OFCs in the LATOME firmware thus creates no significant degradation of the performance of the Digital Trigger.

Chapter 5

Theoretical modelling of $W^{\pm}Z$ production

Using the wealth of data collected by the ATLAS detector during the Run 2 of the LHC, it is possible to study a variety of phenomena. In this thesis, we focus more specifically on diboson processes, of which the ultimate goal is to measure the joint-polarisation state fractions. However, the $W^{\pm}$ and Z bosons are detected only by their decay products in the detector. The choice is made to study among WW, $W^{\pm}Z$ and ZZ processes, the $W^{\pm}Z$ production with leptonic decay as an experimental compromise

In diboson processes, each boson can decay in quarks or leptons. On the one hand, each final state quark will give a jet in the detector. On the other hand, among leptons, muons and electrons will be precisely measured with their tracks and calorimeter deposit. The τ leptons will decay shortly after the primary vertex and are more complicated to reconstruct. Therefore, the leptonic decay, not considering the τ, will give the cleanest signature in the detector. In leptonic decay, the ZZ production has a clean four-lepton signature, associated to very low background. Nevertheless, the cross section of this process is the lowest of all diboson processes. The WW production has the highest cross section, but each $W^{\pm}$ boson will decay in one lepton and one neutrino that will only be detected in ATLAS indirectly by $E_{\mathrm{T}}^{\mathrm{miss}}$. In WW production, the reconstruction of two neutrinos degrades the experimental signature which is spoiled by many two-lepton backgrounds. As a result, $W^{\pm}Z$ production constitutes a good experimental compromise, with an expected intermediate event yield and a rather clean three-lepton signature associated to low background. The experimental signature considered in this thesis is thus

$$pp \to \ell\nu\ell'\bar{\ell}' + X \ , \tag{5.1}$$

with each lepton ℓ being either an electron or a muon. With no further requirements, the inclusive selection will have in in addition jets and photon from initial and final state radiations represented by the "X".

This chapter will focus on the theoretical descriptions behind this experimental signature. How polarisation emerges in such events and the ensuing theoretical predictions for single boson polarisation fractions and joint-polarisation fractions, defined in Section 1.2, will be particularly detailed. First, in Section 5.1, fixed-order theoretical calculations will provide a more quantitative theoretical prediction for the inclusive cross section along with the definition of the fiducial phase space in which the measurement is performed. Then, in Section 5.2, the study of the topology of $W^{\pm}Z$ events will allow the identification of variables sensitive to polarisation. Angular momentum conservation considerations will justify this connection. Finally, direct polarised fixed-ordered theoretical calculations will provide predictions for joint-polarisation fractions. However, such theoretical calculations do not allow the full simulation of the $W^{\pm}Z$ inclusive or polarised production used to tune the analysis and compare to data. This is made possible with Monte Carlo samples described in Section 5.3. Finally, in Section 5.4, theoretical predictions on polarisation fractions are extracted from an inclusive Monte Carlo sample using the aforementioned angular momentum conservation considerations. The main use of this is to get an idea of what to expect from the theory concerning the polarisation of the bosons, their correlations between each other, their dependence with kinematic variables, etc. I particularly worked on this analytical description of polarisation and the extraction of polarisation fractions.

5.1 Inclusive theoretical calculation

As a first step, the theoretical description of the inclusive $W^{\pm}Z$ production is described in this section. This will allow discussing the inclusive production cross section prediction and describing the fiducial phase space in which the measurement is performed.

5.1.1 Inclusive $W^{\pm}Z$ production

The three lepton signature of the $W^{\pm}Z$ inclusive process can be split in four configurations, depending on the flavour of the bosons decay: eee, μee, $e\mu\mu$, $\mu\mu\mu$. At the typical energy scale of diboson production, the mass of the lepton is negligible such that theoretical predictions will not distinguish between eee and $\mu\mu\mu$ production on the one hand, and μee and $e\mu\mu$ on the other hand. The main difference between single flavour and double flavour configurations arises from the additional diagrams created by exchanging the roles of identical final state leptons. Nevertheless, these supplementary diagrams only change the theoretical prediction at the per mil level. This effect will therefore be neglected in the following and the cross sections for all leptonic flavour combinations will be assumed to be all equal and generically labelled $\sigma_{pp\to\ell^{\pm}\nu\ell'\bar{\ell}'}$. For simplicity, one double flavour configuration will be considered,

$$pp \to e^{+}\nu_e\ \mu^{+}\mu^{-}\ +\ X. \tag{5.2}$$

There are ten Feynman diagrams associated to such process at the leading order in perturbation theory. To easily visualise this, let us consider the s-channel diagram of $qq' \to e^{+}\nu_e$ with a W^{+} boson as propagator:

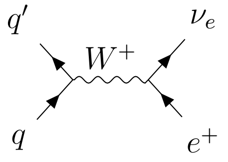

.

Starting with this diagram, a Z boson can radiate from one of the five branches. This creates five diagrams for the considered final state (5.2), to which four diagrams can be added by replacing the Z boson by a photon γ – the neutrino cannot radiate a photon for lack of electrical charge:

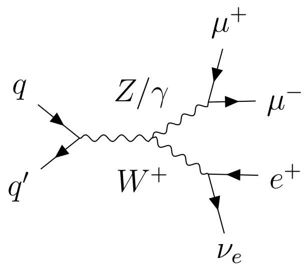

,

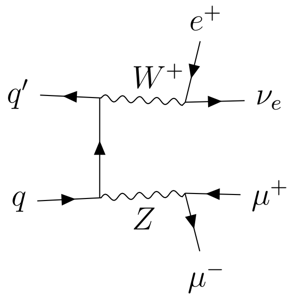

,

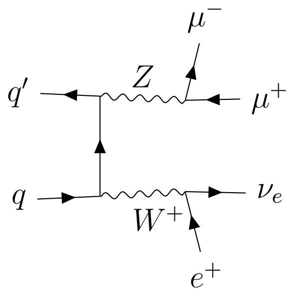

, (5.3)

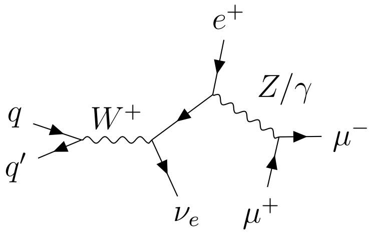

,

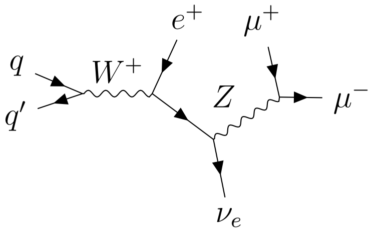

. (5.4)

The three first of these diagrams (5.3) are the only ones such that the W^+ boson and the Z boson can simultaneously be on-shell. These resonant diagrams are the main diagrams in the cross section computation. Within the Double Pole Approximation (DPA), only the three resonant diagrams are considered. Finally, a last non resonant diagram without any Z boson exists:

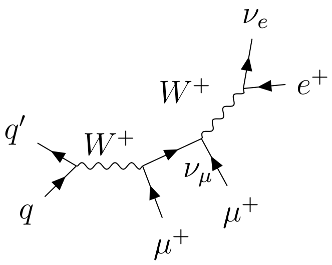

. (5.5)

With these ten diagrams – or three within the DPA – the LO amplitude of the process (5.2) can be obtained. Every diagram corresponds to a term $\mathcal{M}_i$ and the total amplitude is the module of the sum of all these terms

$$\mathcal{A} = |\sum_i \mathcal{M}_i|^2 \ .$$

Because of the electroweak unification, every weak coupling is ultimately proportional to the square root of the fine structure constant α_{EW}, and thus the amplitude taking the square of all this will scale as one α_{EW} per electroweak coupling. The same can be said of the strong coupling constant α_{s}. At LO, the amplitude is thus of the order $\mathcal{O}(\alpha_{\text{EW}}^4\alpha_{\text{s}}^0)$. The computation of the amplitude at Next to Leading Order (NLO) is obtained by adding higher order diagrams. There are the NLO QCD terms of the order $\mathcal{O}(\alpha_{\text{EW}}^4\alpha_{\text{s}}^1)$, and the NLO EW terms of the order $\mathcal{O}(\alpha_{\text{EW}}^5\alpha_{\text{s}}^0)$. Both contributions are computed similarly, with the difference that NLO EW corrections use much more diagrams than NLO QCD corrections, as the latter ones can only add QCD couplings on the initial state two quark branches.

Besides, the NLO EW corrections are expected to be small comparatively to NLO QCD corrections because α_{s} is higher than α_{EW} at the energy scale of the process [70] :

$$\alpha_{\mathrm{s}}(m_Z^2) = 0.11800 \pm 0.0010 \; , \tag{5.6}$$

$$\alpha_{\mathrm{EW}}(m_Z^2) = 0.0078154 \pm 0.0000005 \; . \tag{5.7}$$

Therefore, the NLO QCD corrections must be computed in priority, while the NLO EW can be computed later for additional precision, and still then considering only the three DPA diagrams. Two types of NLO corrections can be added for a given diagram: virtual and real corrections. The virtual corrections arise from the addition of a loop to diagrams. Yet, considering loop diagrams would add two coupling constants, so that the virtual correction terms are only the interference terms of a loop diagram with a tree-level diagram. For example in NLO QCD such term can be

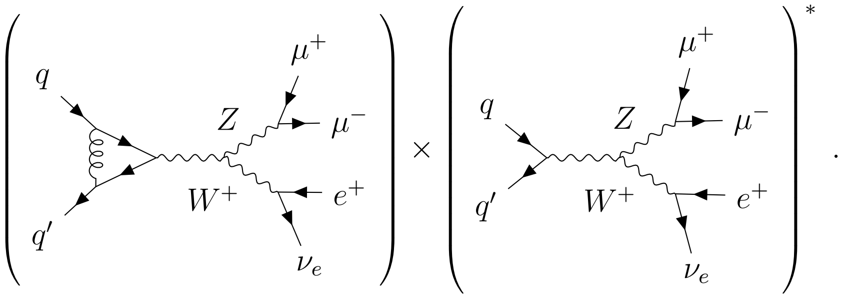

The real corrections amount to the radiation of a gluon or photon from a branch of the diagram, corresponding mostly to initial or final state radiations. In NLO QCD, such terms can be

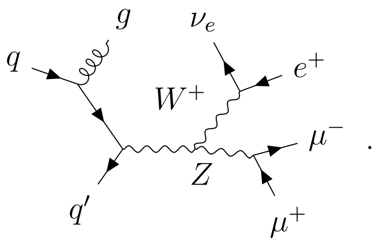

This diagram computation gives rise to UV and IR divergences. These are treated as described in Section 1.3 with renormalisation scale μ_R, and factorisation scale μ_F, typically chosen as $\mu_R = \mu_F = (M_W + M_Z)/2$. Finally the computed parton level cross section is incorporated with PDFs in the factorisation formula of Eq. (1.57). One last ingredient when targeting $W^{\pm}Z$ production is to define a mass window for the Z boson, effectively reducing the phase space of the final state particles. The electroweak (EW) mixing of the Z boson and the photon, as in Eq. (1.23-1.24), imply that they can never be meaningfully separated. However, without a mass window, non-resonant contributions from low energy photons would significantly change the cross section of the process because W production with a virtual photon γ^* is dominant at low m_Z, the invariant mass of the two decay leptons reconstructed as the mass of the Z boson. Since the first ATLAS Z boson production measurement [71], and still for the present study on $W^{\pm}Z$ production, the total phase space is defined with the mass window

$$66\,\mathrm{GeV} < m_Z < 116\,\mathrm{GeV} \; . \tag{5.8}$$

The cross section of inclusive $W^{\pm}Z$ production was computed in Ref. [72] in the total phase space defined by Eq. (5.8), at centre-of-mass energy of Run 2 $\sqrt{s} = 13\,\mathrm{TeV}$ at

LO (5.9), NLO QCD+EW (5.10) and at NNLO QCD + NLO EW (5.11), using the automated MATRIX framework:

$$\sigma^{\text{Tot,th LO}}_{pp\to W^{\pm}Z} = 24.79^{+4.2\,\%}_{-5.2\,\%}\ \text{pb}\ , \tag{5.9}$$
$$\sigma^{\text{Tot,th NLO}}_{pp\to W^{\pm}Z} = 44.67^{+4.9\,\%}_{-3.9\,\%}\ \text{pb}\ , \tag{5.10}$$
$$\sigma^{\text{Tot,th NNLO}}_{pp\to W^{\pm}Z} = 49.62^{+2.2\,\%}_{-2.0\,\%}\ \text{pb}\ . \tag{5.11}$$

The relative uncertainty quoted come from the 7-point scale variation, that is varying independently μ_R and μ_F at half or double of their nominal value with the constraint $0.5 \leq \mu_R/\mu_F \leq 2$. The importance of considering higher order is clear as NLO corrections increase by 80 % the cross section. Yet, in most process, NLO corrections are sufficient for an accurate estimation. It is not the case for $W^{\pm}Z$ production as NNLO corrections still increase the NLO prediction by 11 %, more than the scale uncertainty quoted. This shows the importance of considering higher order corrections when studying $W^{\pm}Z$ production.

5.1.2 Fiducial phase space predictions

Theoretical predictions in the total phase space, defined with only the cut of Eq. (5.8), take into account all events of a specific process produced. While describing the theory in the most general way, such predictions are usually not very practical: detectors limited geometrical acceptance means that they will never be able to catch every events produced. For example, from ATLAS sub-detector descriptions (Section 2.2), obtaining the tracks of a particle in the Inner Detector with $|\eta| > 2.5$ is simply impossible. More generally, as described ahead in Section 6.1, specific event selection requirements imply that only events in a certain fraction of the total phase space can be reconstructed. A fiducial phase space is thus defined to represent the region in which a particle can and should be reconstructed. The fiducial cuts defined in Table 5.1 reflect the selection criteria of Table 6.3. This phase space is associated to an acceptance of around 40 %, meaning that the rest of the generated $W^{\pm}Z$ events produced do not fall within the fiducial phase space for geometrical reasons. Generator level events in the fiducial phase space are used as the reference, *i.e.* what would be observed if the detector was perfect. Of course this is not the case and effects of the reconstruction in the detector will alter this picture, mainly reducing the number of events selected.

Table 5.1 Definitions of the total phase space and the fiducial phase space used for the study of $W^{\pm}Z$ production. The cone ΔR is defined in Section 2.2.1.

Variable	Total Phase Space	Fiducial Phase Space
Lepton $\lvert\eta\rvert$	—	< 2.5
p_{T} of ℓ_Z, p_{T} of ℓ_W [GeV]	—	> 15, > 20
M_Z range [GeV]	$66 - 116$	$\lvert M_Z - M_Z^{\text{PDG}}\rvert < 10$
m_{T}^{W} [GeV]	—	> 30
$\Delta R(\ell_Z^-, \ell_Z^+)$, $\Delta R(\ell_Z, \ell_W)$	—	> 0.2, > 0.3

Theoretical predictions in the fiducial phase space can be more directly compared to an experimental measurement as the only differences lie in the imperfect reconstruction in the detector. Comparing a measurement to the total phase space theoretical predictions is a more far fetched extrapolation. Uncertainties on this extrapolation can only be assessed through Monte Carlo generation thus introducing a strong dependence on the theory. Calculations for the cross section in inclusive $W^{\pm}Z$ production with leptonic decay in the fiducial phase space defined in Table 5.1 at NNLO QCD was performed with MATRIX [73] yielding the cross section in Eq. (5.12). This cross section concerns only one leptonic decay channel; assuming leptonic universality the cross section in all leptonic decay channels as defined in Eq. (5.1) is four time bigger. The cross sections splitting by the charge of the $W^{\pm}$ boson is presented for $W^{+}Z$ and $W^{-}Z$ production in respectively Eq. (5.13) and Eq. (5.14):

$$\sigma^{\text{Fid.,th NNLO}}_{W^{\pm}Z\to\ell^{\pm}\nu\ell'\bar{\ell}'} = 64.01^{+2.3\,\%}_{-2.1\,\%}\ \text{fb}, \tag{5.12}$$
$$\sigma^{\text{Fid.,th NNLO}}_{W^{+}Z\to\ell^{+}\nu\ell'\bar{\ell}'} = 37.80^{+2.2\,\%}_{-2.0\,\%}\ \text{fb}, \tag{5.13}$$
$$\sigma^{\text{Fid.,th NNLO}}_{W^{-}Z\to\ell^{-}\nu\ell'\bar{\ell}'} = 26.22^{+2.3\,\%}_{-2.1\,\%}\ \text{fb}. \tag{5.14}$$

It is visible that $W^{-}Z$ production has a lower cross section than $W^{+}Z$ production. This is because $W^{+}Z$ events originate from $u\bar{d}$ quark interactions while $W^{-}Z$ events originate from $\bar{u}d$ quark interactions. The anti-quarks are found as sea quarks in the proton and thus have similar PDF. However, the u valence quark has a PDF normalisation roughly twice higher than that of the d valence quark, meaning it is roughly involved in twice as much pp collisions.

5.2 Polarisation impact on angular variables

Practically, polarisation manifests itself in the angular topology of physics processes. This is ultimately linked to angular momentum conservation in the studied physics process. Studying the topology of $W^{\pm}Z$ events, it is thus possible to identify angular variables sensitive to polarisation. The frame dependence of polarisation arises then from the fact that these angular variables can only be defined with respect to a given frame. A more general approach with the spin-density matrix will provide a more quantitative description of the link between polarisation and these angular variables. Finally, a direct calculation of polarised cross sections will provide a description of joint-polarisation fractions which are otherwise more complicated to describe with the spin-density matrix.

5.2.1 Angular observables

There are two types of variables to describe a $W^{\pm}Z$ event: bosonic variables and fermionic variables.

- Bosonic variables characterise the bosons and the process that produced them *e.g.* the p_{T} or the pseudo-rapidity $|\eta|$ of each boson. The choice of the frame in which they are evaluated will be discussed later.
- Fermionic variables are related to the decay leptons of each boson. To avoid mixing with bosonic variables, they are evaluated in the rest frame of the decaying boson.

Fermionic variables are mostly independent of bosonic variables, being ultimately only correlated to intrinsic properties of the boson which are its mass and its polarisation. The geometrical decay of a vector boson, labelled V for generality, in its rest frame and the

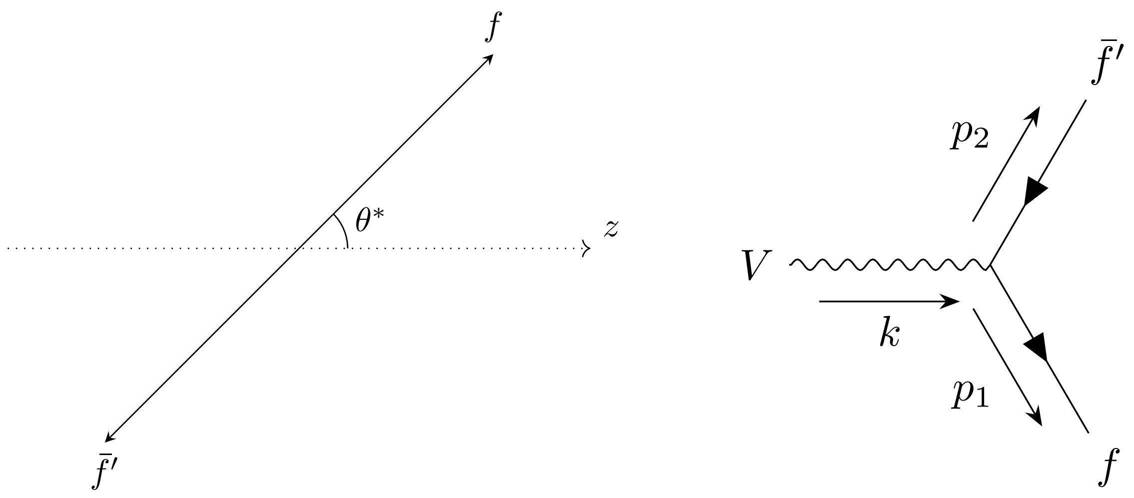

(a) **(b)**

Figure 5.1 Decay of a vector boson V in its rest frame (a), and the Feynman diagram associated to this process (b).

associated Feynman diagram are represented in Fig 5.1. The z-axis is chosen arbitrarily and for now does not play any role. The variables describing the leptons are their mass (and thus the flavour at which V decayed) and their four-vector $\mathbf{p_1}$ and $\mathbf{p_2}$ which are in the boson rest frame

$$\mathbf{p_1} = (E_1^*, p^* \sin\theta^*, 0, p^* \cos\theta^*) \ , \qquad \mathbf{p_2} = (E_2^*, -p^* \sin\theta^*, 0, -p^* \cos\theta^*) \ ,$$

with E^* and p^* the energy and momentum of the decay lepton in the boson rest frame and θ^* the polar angle with respect to a chosen z-axis. The energy momentum conservation implies that E^* and p^* are completely constrained by the masses of the leptons and the boson. Neglecting the relatively low mass of the leptons, E^* and p^* are in fact equal to $m_V/2$, half the mass of the boson. There are thus only two interesting fermionic degrees of freedom,

- their flavour which manifest itself only in the negligible mass of the fermions.
- the $\cos\theta^*_\ell$ which traduces the anisotropy of the decay.

The observable $\cos\theta^*_\ell$ ultimately has a distribution that is only linked to the polarisation of the decaying boson. In $W^\pm Z$ events, this creates two polarisation observables $\cos\theta^*_{\ell W}$ and $\cos\theta^*_{\ell Z}$ each evaluated in the rest frame of respectively the $W^\pm$ boson and the Z boson. These variables are defined as the cosine of the decay angle θ^* of the negatively charged lepton produced in the decay of the $W^\pm$ or Z boson, as visible in Fig. 5.1(a), except for the W^+ boson where only the positively charged lepton is observed and thus used. To unify the treatment of W^+ and W^- bosons, the variable $q_W \cdot \cos\theta^*_{\ell W}$ is considered, multiplying $\cos\theta^*_{\ell W}$ by q_W the charge of the $W^\pm$ boson.

However, in Fig. 5.1(a), the choice of the z-axis is not determined beforehand. This is directly linked to the fact that the polarisation of a boson is not a Lorentz invariant quantity and thus, all variables used later on will be defined in a specific reference frame. Two main frames can be chosen, of which schematic representations are given in Fig. 5.2. Following are the descriptions of the two main frames and how $\cos\theta^*_\ell$ is computed in each case.

Helicity frame: This frame uses the direction of the boson in the laboratory frame (Fig. 5.2(a)) to define the z-axis in the boson rest frame. To compute it, first the Lorentz vectors of the boson and the decay leptons are reconstructed with the kinematic variables of the decay leptons found in the detector, that is in the laboratory frame. Then, the Lorentz vectors of the decay leptons are boosted in the rest frame of the boson. One lepton Lorentz vector is chosen following the prescription above, and the cosine of its angle with the boson's Lorentz vector is $\cos\theta^*_\ell$.

Modified Helicity frame: This frame uses the direction of the boson in the $W^\pm Z$ rest frame (Fig. 5.2(b)) to define the z-axis in the boson rest frame. As a result the Lorentz vector of the boson and the leptons reconstructed from detector information in the laboratory frame are first boosted in this $W^\pm Z$ rest frame. The leptons Lorentz vectors are then boosted a second time from this frame to the boson rest frame. Again, the cosine of the angle between the chosen lepton Lorentz vector and the boson Lorentz vector is $\cos\theta^*_\ell$.

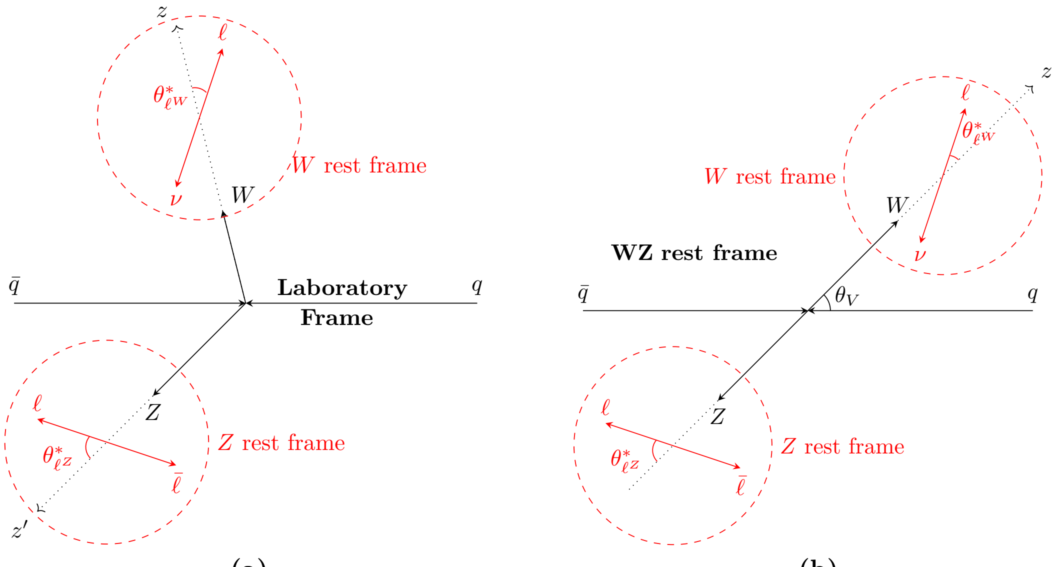

(a) **(b)**

Figure 5.2 Definition of $\cos\theta^*_\ell$ in the Helicity frame (a) and in the Modified Helicity frame (b).

In a similar reasoning as for the decay of a single boson, one can consider the $W^\pm$ and Z bosons as decay products of the two-parton system in the pp collision. In the rest frame of such collision, which is symmetrically the $W^\pm Z$ rest frame, a polar angle θ_V can be defined as visible in Fig. 5.2(b). This observable would be linked to the global spin of the two-parton system and ultimately the joint-polarisation of the two produced bosons. Taking into account reasons of symmetry, the variable considered for this purpose is $|\cos\theta_V|$. It however can only be defined in the *Modified Helicity* frame.

In this study, the *Modified Helicity* frame will be used. This choice will be discussed in Section 5.4.2. At generator level, the Born kinematics of generated leptons is used (see Section 1.3.3), and the assignment of these leptons to the generated mother boson is done using the built-in algorithm of the Monte Carlo generator. The generator-level neutrino coming from the $W^\pm$ boson decay is used. This allows reconstructing at particle level in the total phase space all the kinematic variables of the W and Z bosons and the polarisation observables $\cos\theta^*_{\ell W}$, $\cos\theta^*_{\ell Z}$ and $|\cos\theta_V|$.

Yet, the computation of this angle is complicated in data by the impossibility to measure the longitudinal momentum p_z^ν of the neutrino four-vector at the reconstructed level. This affects strongly the reconstruction of $\cos\theta^*_{\ell W}$, and in the *Modified Helicity* frame, $\cos\theta^*_{\ell Z}$ as well, because of the boost in the $W^{\pm}Z$ rest frame. Different methods to reconstruct from data this p_z^ν, and with it the four-vector of the $W^{\pm}$ boson, are described ahead in Section 6.2. Still, this will imply a worse resolution on $\cos\theta^*_{\ell W}$ than on $\cos\theta^*_{\ell Z}$.

5.2.2 Spin Density Matrix

Using general considerations on spin conservation [74], the differential cross-sections along some angular variables can be described only from the helicity information of the initial and final states considered, independently of the process taking place. For the initial state, the spin configuration is best defined by the spin density matrix ρ described in Section 1.2. For now, the spin density matrix of a single vector boson V will be considered. With Ref. [75, 76], this is used to derive the angular dependence of the decay of one vector boson V.

The boson V has spin 1 and thus its spin density matrix ρ is a 3×3 matrix Hermitian positive semi-definite with trace equal to one. There are thus eight free real parameters in ρ. Such a matrix can be decomposed in the sum of irreducible order two tensors [32] classified by their rank[1]. The order zero tensor is proportional to the identity and being the only one not traceless, it is normalised by 1/3 to give a unit trace to ρ. Then, there are three order one tensors which are proportional to the spin operator in all three directions, and five order two tensors built from the spin operators.

$$\rho = \frac{1}{3}\mathbf{1} + \frac{1}{2}\sum_{k=-1}^{1}\langle S_k\rangle \mathbf{S_k} + \sum_{k=-2}^{2}\langle T_k\rangle \mathbf{T_k}\ , \tag{5.15}$$

with $S_{\pm1} = \frac{1}{\sqrt{2}}(S_x \pm iS_y)$ and $S_0 = S_z$, yielding in the dimension three fundamental representation, using the spin quantum state basis, $\{|j=1,m=+1\rangle, |j=1,m=0\rangle, |j=1,m=-1\rangle\}$ with m the eigenvalue of S_z,

$$S_0 = \begin{pmatrix}1 & 0 & 0\\ 0 & 0 & 0\\ 0 & 0 & -1\end{pmatrix}\ ,\quad S_+ = \begin{pmatrix}0 & 1 & 0\\ 0 & 0 & 1\\ 0 & 0 & 0\end{pmatrix}\ ,\quad S_- = \begin{pmatrix}0 & 0 & 0\\ 1 & 0 & 0\\ 0 & 1 & 0\end{pmatrix}\ , \tag{5.16}$$

and the five rank two irreducible tensors T_k built from the S_k:

$$\begin{aligned} T_{\pm2} &= S_{\pm1}^2\ , \qquad T_{\pm1} = \frac{\mp1}{\sqrt{2}}\left[S_{\pm1}S_0 + S_0S_{\pm1}\right]\ ,\\ T_0 &= \frac{1}{\sqrt{6}}\left[2S_0^2 - S_{+1}S_{-1} - S_{+1}S_{-1}\right]\ . \end{aligned}$$

In this parametrisation, the components of the mean polarisation vector $\vec{\mathcal{P}}$ are the mean values of the spin operators $\langle S_k\rangle$, and the mean values $\langle T_k\rangle$ are the alignment components. In order to obtain physical observables, these tensors are rearranged in order to obtain

---

[1] The rank of an order two tensor is the dimension of the largest non-zero determinant that can be made with its rows or columns.

Hermitian operators. These are the cartesian components of the spin S_x, S_y and S_z and the Hermitian operators,

$$\begin{aligned} A_1 &= \frac{1}{2}\left(T_{+1} - T_{-1}\right) \ , \quad A_2 = \frac{1}{2i}\left(T_{+1} + T_{-1}\right) \ , \\ B_1 &= \frac{1}{2}\left(T_{+2} + T_{-2}\right) \ , \quad B_2 = \frac{1}{2i}\left(T_{+2} - T_{-2}\right) \ , \end{aligned}$$

and T_0 which was initially Hermitian. Consequently, in the basis of (5.16), the spin density matrix is parametrised as:

$$\rho = \begin{pmatrix} \frac{1}{3} + \frac{\langle S_z\rangle}{2} + \frac{1}{\sqrt{6}}\langle T_0\rangle & \frac{\frac{\langle S_x\rangle}{2} - \langle A_1\rangle - i\left(\frac{\langle S_y\rangle}{2} - \langle A_2\rangle\right)}{\sqrt{2}} & \langle B_1\rangle - i\langle B_2\rangle \\ \frac{\frac{\langle S_x\rangle}{2} - \langle A_1\rangle + i\left(\frac{\langle S_y\rangle}{2} - \langle A_2\rangle\right)}{\sqrt{2}} & \frac{1}{3} - \frac{2}{\sqrt{6}}\langle T_0\rangle & \frac{\frac{\langle S_x\rangle}{2} + \langle A_1\rangle - i\left(\frac{\langle S_y\rangle}{2} + \langle A_2\rangle\right)}{\sqrt{2}} \\ \langle B_1\rangle + i\langle B_2\rangle & \frac{\frac{\langle S_x\rangle}{2} + \langle A_1\rangle + i\left(\frac{\langle S_y\rangle}{2} + \langle A_2\rangle\right)}{\sqrt{2}} & \frac{1}{3} - \frac{\langle S_z\rangle}{2} + \frac{1}{\sqrt{6}}\langle T_0\rangle \end{pmatrix} . \tag{5.17}$$

From this representation, the usual polarisation fractions are related to the spin observable along the z-axis and the alignment observable T_0 by

$$f_{\mathrm{L}} - f_{\mathrm{R}} = -\langle S_z\rangle \ , \tag{5.18}$$

$$f_0 = \frac{1}{3} - \frac{2}{\sqrt{6}}\langle T_0\rangle \ . \tag{5.19}$$

Then, in the formalism of Ref. [74] the matrix element of the decay of a vector boson in the quantum state $|1, m\rangle$ in two leptons with helicity λ_1, λ_2 is

$$\mathcal{M}_{m,\lambda_1,\lambda_2} = a_{\lambda_1,\lambda_2} D^1_{m,\lambda_1-\lambda_2}\left(\phi^*, \theta^*, 0\right) \ , \tag{5.20}$$

with θ^* the decay angle defined in Fig. 5.1(a) and analogously ϕ^* the azimuthal angle defined with respect to an arbitrarily chosen x-axis. The parameter $a_{\lambda_1\lambda_2}$ is a constant with respect to the angular parameters. This will allow to derive the differential cross section of the vector boson decay with respect to θ^* and ϕ^*. This angular information is held by the Wigner D-functions which are the $2j+1$ unitary representations of rotations characterised by the three Euler angles α, β and γ. It can be decomposed as $D^j_{m'm}(\alpha,\beta,\gamma) = e^{-i\alpha m}e^{-i\gamma m}d^j_{m'm}(\beta)$ with the Wigner d-matrix being real.

The decay leptons have such a low mass compared to the typical energy of the decay that they will be considered massless, allowing to consider the conservation of helicity. The initial helicity in the decay is 0, the boson being in its rest frame, and thus only two possibilities arise: $(\lambda_1, \lambda_2) = (\pm\frac{1}{2}, \mp\frac{1}{2})$. Writing $\lambda = \lambda_1 - \lambda_2$ the only possibility is $\lambda = \pm 1$. The transition probability from the mixed state described by the spin density matrix ρ to the two leptons decaying with angles θ^* and ϕ^* is

$$\frac{d\Gamma}{d\cos\theta^* d\phi^*} \propto \sum_{\lambda=\pm1}\sum_{m,m'} \rho_{mm'} \mathcal{M}_{m\frac{+\lambda}{2}\frac{-\lambda}{2}} \mathcal{M}^*_{m'\frac{+\lambda}{2}\frac{-\lambda}{2}} \ , \tag{5.21}$$

$$\frac{d\Gamma}{d\cos\theta^* d\phi^*} \propto \sum_{\lambda=\pm1}\sum_{m,m'} \rho_{mm'} |a_{\frac{+\lambda}{2}\frac{-\lambda}{2}}|^2 e^{i(m-m')\phi^*} d^1_{m\lambda}(\theta^*) d^1_{m'\lambda}(\theta^*) \ . \tag{5.22}$$

The a constant can be factorised noticing that in the massless lepton approximation, the helicity corresponds to the chirality of the lepton and thus

$$\frac{a_{\frac{+1}{2}\frac{-1}{2}}}{a_{\frac{-1}{2}\frac{+1}{2}}} = \frac{g_R^2}{g_L^2} \ , \tag{5.23}$$

with g_R and g_L being the coupling constant of the vector boson to respectively the right and left chirality of the leptons. For a $W^{\pm}$ boson, coupling exclusively to left-handed particles, g_R is zero and g_L is one, meaning only the configuration with a left-handed fermion is allowed. However since the angle θ^* is redefined for W^+ boson to be with respect to the anti-fermion of the decay, the only λ allowed changes with the charge, being $+1$ for W^+ boson and -1 for W^- boson. Using the explicit functions $d^1_{mm'}(\theta^*)$ and the spin density matrix ρ of Eq. (5.17), one gets for the $W^{\pm}$ boson:

$$\begin{aligned}\frac{d\sigma_{W^{\pm}\to\nu\ell^{\pm}}}{d\cos\theta^* d\phi^*} \propto \frac{1}{2\pi}\frac{3}{8}\Big[1+\cos^2\theta^* \pm 2\langle S_z\rangle\cos\theta^* + 2\left(\frac{1}{6}-\frac{1}{\sqrt{6}}\langle T_0\rangle\right)\left(1-3\cos^2\theta^*\right) \\ \pm 2\langle S_x\rangle\cos\phi^*\sin\theta^* \pm 2\langle S_y\rangle\sin\phi^*\sin\theta^* - 2\langle A_1\rangle\cos\phi^*\sin 2\theta^* \\ -2\langle A_2\rangle\sin\phi^*\sin 2\theta^* + 2\langle B_1\rangle\cos 2\phi^*\sin^2\theta^* + 2\langle B_2\rangle\sin 2\phi^*\sin^2\theta^*\Big] .\end{aligned} \tag{5.24}$$

For the Z boson, the formula is slightly more complex as both λ values exist. However, one a constant can be factorised and the importance of each helicity configuration term is weighted by $g_R^2/(g_R^2+g_L^2)$ for $\lambda=+1$ and $g_L^2/(g_R^2+g_L^2)$ for $\lambda=-1$. The terms of $d^1_{m\lambda}(\theta^*)$ left unchanged by a change of λ will not have any fore-factor while those with a sign change will have a fore-factor $(g_R^2-g_L^2)/(g_R^2+g_L^2)$. This factor will in the following be labelled C_{w}, and can be expressed in term of the c_v and c_a as

$$C_{\mathrm{w}} = \frac{2c_a c_v}{c_a^2+c_v^2} = \frac{1/2-2\sin^2(\theta_{\mathrm{w}})}{1/4+\left(-1/2+2\sin^2(\theta_{\mathrm{w}})\right)^2} \approx 0.15 . \tag{5.25}$$

This C_{w} factor only appears in front of terms proportional to the spin expected value for all space directions:

$$\begin{aligned}\frac{d\sigma_{Z\to\ell^+\ell^-}}{d\cos\theta^* d\phi^*} \propto \frac{1}{2\pi}\frac{3}{8}\Big[1+\cos^2\theta^* - 2C_{\mathrm{w}}\langle S_z\rangle\cos\theta^* + 2\left(\frac{1}{6}-\frac{1}{\sqrt{6}}\langle T_0\rangle\right)\left(1-3\cos^2\theta^*\right) \\ -2C_{\mathrm{w}}\langle S_x\rangle\cos\phi^*\sin\theta^* - 2C_{\mathrm{w}}\langle S_y\rangle\sin\phi^*\sin\theta^* - 2\langle A_1\rangle\cos\phi^*\sin 2\theta^* \\ -2\langle A_2\rangle\sin\phi^*\sin 2\theta^* + 2\langle B_1\rangle\cos 2\phi^*\sin^2\theta^* + 2\langle B_2\rangle\sin 2\phi^*\sin^2\theta^*\Big] .\end{aligned} \tag{5.26}$$

These full differential cross sections hold all the information on the spin density matrix parametrisation. This is greatly simplified by integrating over ϕ^* yielding

$$\frac{d\sigma_{Z\to\ell^+\ell^-}}{d\cos\theta^*} \propto \frac{3}{8}\Big[1+\cos^2\theta^* + 2C_{\mathrm{w}}(f_{\mathrm{L}}-f_{\mathrm{R}})\cos\theta^* + f_0\left(1-3\cos^2\theta^*\right)\Big] . \tag{5.27}$$

Similar formulas are found for W^+ boson (resp. W^- boson) replacing C_{w} by -1 (resp. $+1$). Also, rearranging the formula, terms corresponding to the three polarisation fractions can be made to appear. Using $q_W\cdot\cos\theta^*_{\ell W}$, one single formula appears for the $W^{\pm}$ boson:

$$\frac{d\sigma_{W^{\pm}\to\nu\ell^{\pm}}}{d\cos\theta^*_{\ell W}} \propto \frac{3}{8}\left[f_{\mathrm{R}}\left(1+q_W\cdot\cos\theta^*_{\ell W}\right)^2 + f_{\mathrm{L}}\left(1-q_W\cdot\cos\theta^*_{\ell W}\right)^2 + 2f_0\left(1-\left(q_W\cdot\cos\theta^*_{\ell W}\right)^2\right)\right] , \tag{5.28}$$

$$\frac{d\sigma_{Z\to\ell^+\ell^-}}{d\cos\theta^*_{\ell Z}} \propto \frac{3}{8}\left[f_{\mathrm{R}}(1+\cos^2\theta^*_{\ell Z} - 2C_{\mathrm{w}}\cos\theta^*_{\ell Z}) + f_{\mathrm{L}}(1+\cos^2\theta^*_{\ell Z} + 2C_{\mathrm{w}}\cos\theta^*_{\ell Z}) + 2f_0\left(1-\cos^2\theta^*_{\ell Z}\right)\right] . \tag{5.29}$$

It is interesting to note here that each term corresponds exactly to the direct differential cross section computation of a boson with a given polarisation presented in Appendix A. Effectively, these formulas thus amount to the incoherent sum of all three pure polarisation states, weighted by an associated polarisation fraction.

5.2.3 Fixed-order joint-polarisation calculation

The angular description of $W^{\pm}Z$ events does not give any numerical prediction on what the polarisation fractions should be. Moreover, a similar description with spin-density matrix of the $W^{\pm}Z$ system and its joint-polarisation fractions is not available, being mathematically much more complex. These fractions can nevertheless be directly obtained from theoretical calculations based on Feynman diagrams at a fixed-order in perturbative QCD. Interpreting Eq. (5.28) and (5.29), the polarisation fractions can be seen as the ratio of each polarised cross section on the total inclusive cross section.

The $W^{\pm}Z$ production cross section from a pure polarisation configuration is computed with diagrams in the same fashion as in Section 5.1.1, only this time using bosons with a specific polarisation. As described in Section 1.2, these are really pseudo cross sections, the concept of polarisation being frame dependent. However, the ratio to the inclusive cross section will provide the polarisation fractions and joint-polarisation fractions in the frame used for the calculation. In the following, the frame used will be the $W^{\pm}Z$ centre-of-mass frame, associated to the modified helicity frame for single boson polarisation.

Such calculation was performed at NLO in QCD for $W^{\pm}Z$ production in Ref. [77] following a method developed first for WW production [78] and using the MoCaNLO program. The main challenge when computing polarised cross section is the proper definition of what is a polarised signal. While it is well defined for on-shell particles, for the unstable $W^{\pm}$ and Z bosons there is some ambiguity.

First, it only makes sense to talk of polarised $W^{\pm}$ and Z bosons if the corresponding Feynman diagram involves simultaneously two intermediate vector bosons, each separately decaying to leptons. In Section 5.1.1, only the doubly resonant diagrams (5.3) with a Z boson can be considered for this purpose. The other diagrams (5.4) and (5.5) are considered as non-resonant background in this study. Of course restricting to the doubly resonant diagrams does not solve completely the issue as the $W^{\pm}$ and Z bosons should be also on-shell. Within the Double Pole Approximation (DPA), in addition to considering only the doubly resonant diagrams, the $W^{\pm}$ and Z bosons are considered on-shell in the numerators of the amplitude while recovering off-shell effects in the Breit-Wigner denominator of the propagator. As such, diagram amplitudes singling out one boson V of mass M_V and width Γ_V with momentum k and decaying in two leptons of momentum l and $k-l$ takes the form

$$\mathcal{A}_{\mathrm{DPA}} = \mathcal{P}_{\mu}(k)\frac{-g^{\mu\nu}}{k^2 - M_V^2 + i\Gamma_V M_V}\mathcal{D}_{\nu}(l, k-l) \ , \tag{5.30}$$

with $\mathcal{P}_{\mu}$ and $\mathcal{D}_{\nu}$ subamplitudes respectively for the production of the boson V and its decay in leptons. Using the identity

$$g^{\mu\nu} = \left(\sum_{\lambda=0,\pm} \varepsilon_{\lambda}^{\mu\,*}(k)\varepsilon_{\lambda}^{\nu}(k)\right) - \frac{k^{\mu}k^{\nu}}{M_V^2} \ , \tag{5.31}$$

the frame dependent polarisation vectors $\varepsilon_{\lambda}^{\mu}$ defined in Section 1.2 can be made to appear. The amplitude can thus be rewritten

$$\mathcal{A}_{\mathrm{DPA}} = \frac{\sum\limits_{\lambda=0,\pm} \mathcal{P}_{\mu}(k)\varepsilon_{\lambda}^{\mu\,*}(k)\varepsilon_{\lambda}^{\nu}(k)\mathcal{D}_{\nu}(l, k-l)}{k^2 - M_V^2 + i\Gamma_V M_V} = \sum_{\lambda=0,\pm} \mathcal{A}_{\lambda} \ , \tag{5.32}$$

the contraction of the momentum k^ν with the massless lepton decay tensor $\mathcal{D}_\nu$ vanishing[2]. As a result, polarised amplitudes $\mathcal{A}_\lambda$ can be defined. This, sketched for a single boson polarisation, is easily generalised to pure joint-polarisation amplitudes.

To obtain polarised cross sections, the square of the amplitude must be used, which will of course not be the sum of the squares of the polarised amplitudes as interference terms will arise:

$$|\mathcal{A}_{\mathrm{DPA}}|^2 = \sum_{\lambda=0,\pm} |\mathcal{A}_\lambda|^2 + \sum_{\lambda,\lambda'=0,\pm} \mathcal{A}_\lambda \mathcal{A}_{\lambda'} \, . \tag{5.33}$$

In the total phase space, the interference terms should vanish in a similar way as how in Eq. (5.28) and (5.29) integrating on the ϕ^* azimuthal angle brings equations that amount to the sum of polarised cross sections.

In Ref. [77], theorists Ansgar Denner and Giovanni Pelliccioli computed polarised cross section as the square of polarised amplitudes along with the inclusive DPA cross section and the full inclusive cross section. The ratio of the polarised cross section to the DPA inclusive cross section provides an NLO QCD prediction of the polarisation fraction, while the difference between the sum of the polarised cross section and the inclusive cross section allows the estimation of the interference contribution. These were all computed in the fiducial phase space defined in Table 5.1, in the centre-of-mass frame of the $W^\pm Z$ system. Overall, the effect of NLO corrections is found to be important, increasing the polarised cross sections by factors from +31 % to +168 %. This affects joint-polarisation fractions, with f_{00} and f_{TT} decreasing respectively by 30 % and 10 % while the mixed states fractions $f_{0\mathrm{T}}$ and $f_{\mathrm{T}0}$ increase by 50 %. The non-resonant $W^\pm Z$ events amount to 1.8 % at NLO. The interference contribution in the total phase space represents 0.6 % of the events, and will be neglected in the following. The non-resonant $W^\pm Z$ events amount to 1.8 % at NLO.

In a similar way, NLO EW effects where taken into account in Ref. [79]. The addition of this correction to the NLO QCD prediction, however, only lowers the inclusive cross section by 2.3 %. For the polarised cross sections, the effect is roughly of the same order in all pure joint-polarisation, with at most a decrease by 3.3 %. Consequently, the effect on joint-polarisation fractions is negligible.

5.3 Monte Carlo generation of $W^\pm Z$ events

Direct theoretical computations as done in [72, 73] for inclusive production with the automated MATRIX framework, or in [77, 79] for the polarised case with the MoCaNLO framework, allow to obtain total $W^\pm Z$ cross sections and differential cross sections as a function of some chosen variable. However, they only provide theoretical predictions at the parton level and thus miss soft physics effects from parton showers and hadronisation described in Section 1.3.3. Even more problematic, they do not hold information on the correlation between all the physics variables, making it impossible to assess the effect of a cut on one variable on the distribution of another. This issue can only be cured by a complete kinematical description, event by event, of the physics process. Therefore, samples of simulated events are needed to tune a physics analysis *e.g.* to test the effect of cuts on certain variables in the definition of the selection.

---

[2] From Dirac equation for a massless spinor, $\gamma_\nu \partial^\nu \psi = 0$.

5.3.1 Inclusive Monte Carlo samples

Samples of simulated events can be produced by Monte Carlo generators. As described in Section 1.3.3, the hard scattering matrix element computation is usually interfaced with a parton shower generator, allowing the simulation of events at the particle level. These events, to which the m_Z cut of Eq. (5.8) is applied, provide the Monte Carlo theoretical predictions in the total phase space. Similarly, generated events passing the fiducial phase space cuts of Table 5.1 provide the Monte Carlo prediction in the fiducial phase space. In parallel, all the generated events are passed through the ATLAS detector simulation [80] based on GEANT4 [81] to simulate the expected signature in the detector. Then, the same event reconstruction procedure as defined for data (described ahead in Chapter 6) is used to obtain detector-level Monte Carlo events that are fully comparable to data.

For the purpose of this analysis, samples from several Monte Carlo generators are used. The main generator, deemed to be representing best the data in $W^{\pm}Z$ inclusive production, is generated with Powheg-Box v2 [36, 82] at NLO in QCD, including the non-resonant diagrams of Section 5.1.1, the Z/γ^{*} interference, and the decay in τ subsequently decaying to electrons or muons, thus faking the experimental signature. It is interfaced to Pythia 8.210 [37–39] for parton shower, hadronisation and underlying events simulation. To match the MATRIX NNLO QCD cross-section prediction, this Powheg+Pythia sample is rescaled by an overall scale factor of 1.18 in the fiducial phase space.

Two alternative samples were generated at NLO in QCD. First, the Monte Carlo generator MadGraph5_aMC@NLO [35] computes all the matrix elements associated with the experimental signature (5.1) at NLO in QCD with up to two jets. It does not include the Z/γ^{*} interference and the non-resonant background. It is merged with parton shower with Pythia 8.210 [37] using the `FxFx` scheme [83] and will be referred in the following as MadGraph@NLO. Finally, to provide an alternative to Pythia for parton showers, an additional sample from the general purpose Sherpa 2.2.2 [40] Monte Carlo generator is created. Matrix elements for the signature (5.1) with up to one jets at NLO in QCD and with up to three jets at LO are computed with respectively OpenLoops [84] and Comix [85]. They are then merged with the internal Sherpa parton shower [86] following the `MEPS@NLO` prescription [87].

5.3.2 Polarised Monte Carlo samples

Recent developments in Monte Carlo generation now allow the production of polarised samples. It is possible with the recent version 2.7.3 of MadGraph5_aMC@NLO [88] to generate polarised $W^{\pm}$ and Z bosons with their leptonic decay, with nevertheless a few limitations. Mainly, the polarised generation is only available at LO. This is a serious limitation, as NLO effect were shown in Section 5.1.1 to be very important in the inclusive $W^{\pm}Z$ production. The generation is performed in two steps. First the production of polarised $W^{\pm}$ and Z bosons is generated. Then, the electronic or muonic decay of these bosons is generated in the Narrow Width Approximation (NWA[3]) but preserving off-shell effects and spin-correlations using the MadSpin method [89]. However, only the decay of

---

[3] The NWA assumes intermediate particles are on-shell, and their subsequent decay is added in the computation simply as their branching ratio to the required final state. This spoils off-shell effects and spin correlations.

longitudinal 0 or transverse T bosons can be generated. As a result, these polarised samples cannot be used to measure f_{L} or f_{R} in single boson polarisation measurement. To emulate real corrections from NLO in QCD, polarised $W^{\pm}Z$ events are generated in association with zero and one jet. These are merged with parton shower from Pythia 8.244 with the `CKKW-L` scheme [90, 91]. As a result, NLO virtual corrections, non-resonant contributions and $Z/\gamma*$ interferences are not modelled by this MadGraph0,1j@LO generation procedure.

Nonetheless, it was used to generate samples of $W^{\pm}Z$ events up to detector level for a given joint-polarisation state. Four pure joint-polarisation samples W_0Z_0, W_0Z_{T}, $W_{\mathrm{T}}Z_0$, $W_{\mathrm{T}}Z_{\mathrm{T}}$ are generated with this MadGraph0,1j@LO procedure and then merged two by two to create single boson polarised samples $W_0, W_{\mathrm{T}}, Z_0, Z_{\mathrm{T}}$. The polarised samples obtained this way will in the following be collectively labelled `MGgen` samples. The summation of all polarised MadGraph0,1j@LO samples provides an inclusive sample which is found to be in reasonable agreement with the NLO inclusive Powheg+Pythia sample as can be seen in the distributions of polarisation sensitive variables in Fig. 5.3.

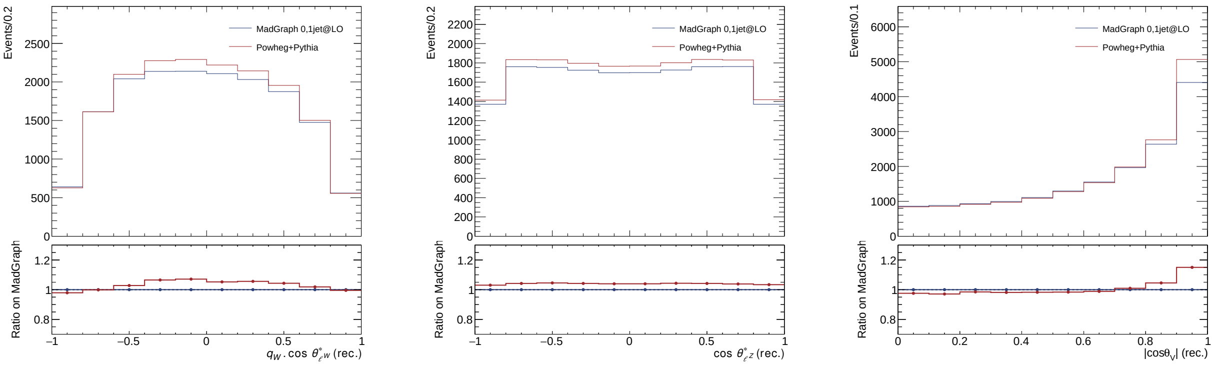

(a) $q_W \cdot \cos\theta^*_{\ell W}$ **(b)** $\cos\theta^*_{\ell Z}$ **(c)** $|\cos\theta_V|$

Figure 5.3 Comparison between distributions of $q_W \cdot \cos\theta^*_{\ell W}$ (a), $\cos\theta^*_{\ell Z}$ (b) and $|\cos\theta_V|$ (c) of inclusive Monte Carlo samples MadGraph0,1j@LO and Powheg+Pythia at detector level for $W^{\pm}Z$ events.

5.4 Polarisation in inclusive Monte Carlo

It is possible to extract polarisation fractions directly from polarised theoretical calculations and simulations. However, these methods rely on strong theory approximations such as the DPA or the NWA. A more general method is to use the differential distributions of Eq. (5.28) and (5.29) that solely originates from angular momentum conservation considerations as detailed in Section 5.2.2. This will provide an insight on the behaviour of polarisation fractions depending on the frame, justifying the choice of the *Modified Helicity* frame. It is then possible to generalise these single boson polarisation formulas to extract joint-polarisation fractions as well.

5.4.1 Single boson polarisation fractions

At truth level in the total phase space, Eq. (5.28) and (5.29) describe the distribution of the variables $q_W \cdot \cos\theta^*_{\ell W}$ and $\cos\theta^*_{\ell Z}$ respectively, in the inclusive NLO in QCD Powheg+Py-

THIA Monte Carlo sample. Being directly linked to angular momentum conservation, these formulas are valid at all orders in perturbation theory and can only be spoiled by:

- final state radiations.
- boson exchanges from initial to final states or between the $W^{\pm}$ boson and Z boson decay leptons.

The first effect is eliminated by considering the Born decay leptons in POWHEG+PYTHIA. The second effect was considered in [15] to be extremely negligible. Consequently, the three polarisation fractions of the $W^{\pm}$ boson (resp. Z boson) can be extracted through a fit of the $q_W \cdot \cos\theta^*_{\ell W}$ (resp. $\cos\theta^*_{\ell Z}$, both indistinctly labeled $\cos\theta^*_{\ell}$) distribution of generated Monte Carlo events by the analytical formula of Eq. (5.28) (resp. Eq. (5.29)). This is a fit with three parameters, each being a polarisation fraction. The fitting function is globally scaled by the integral of the $\cos\theta^*_{\ell}$ distribution. With such parametrisation, the normalisation relation of the fractions (1.48) is not guaranteed. The fitting function can be rewritten to have this relation built in, with this time only two parameters:

$$\frac{1}{\sigma}\frac{d\sigma}{d\cos\theta^*_{\ell}} = \frac{3}{8}\left[1+\cos^2\theta^*_{\ell} + A_4\cos\theta^*_{\ell} + A_0\frac{1}{2}\left(1-3\cos^2\theta^*_{\ell}\right)\right] , \tag{5.34}$$

$$\text{where} \quad A_0 = 2f_0 , \qquad A_4 = \left\{ \begin{array}{ll} \mp 2\left(f_{\mathrm{L}}-f_{\mathrm{R}}\right) & \text{for } W^{\pm} \\ 2C_{\mathrm{w}}\left(f_{\mathrm{L}}-f_{\mathrm{R}}\right) & \text{for } Z \end{array} \right. . \tag{5.35}$$

The fit using this theoretical function is thus a fit with two parameters which is expected to give slightly reduced uncertainties with respect to the fit with three parameters, while enforcing the normalisation relation (1.48). The result of these two analytical fits is shown in Fig. 5.4.

Finally, a last method to extract these fractions is the moments method [15]. One can rewrite the formula (5.34) this way:

$$\frac{1}{\sigma}\frac{d\sigma}{d\cos\theta^*_{\ell}} = \frac{3}{8}\left[\frac{4}{3} + \left(A_0 - \frac{2}{3}\right)\frac{1}{2}\left(1-3\cos^2\theta^*_{\ell}\right) + A_4\cos\theta^*_{\ell}\right] . \tag{5.36}$$

By defining the scalar product

$$\langle f, g\rangle = \int_{\Omega} f\cdot g \, d\Omega ,$$

with $\Omega = \{\cos\theta^*_{\ell} \in [-1;1]\}$, then the following set of functions

$$m(\cos\theta^*_{\ell}) \ : \ \left\{1 \ , \ \frac{1}{2}\left(1-3\cos^2\theta^*_{\ell}\right) \ , \ \cos\theta^*_{\ell}\right\} , \tag{5.37}$$

is orthogonal for this scalar product. Rewriting functions of this set $\{m_i\}_{i\in\{0,1,2\}}$ the distribution becomes

$$\frac{1}{\sigma}\frac{d\sigma}{d\cos\theta^*_{\ell}} = \frac{3}{8}\sum_{i=0}^{2}\alpha_i m_i . \tag{5.38}$$

By defining the moment of a function $m(\cos\theta^*_{\ell})$ the following way:

$$\langle m\rangle = \frac{\int \frac{d\sigma}{d\cos\theta^*_{\ell}} \ m(\cos\theta^*_{\ell}) \ d\cos\theta^*_{\ell}}{\int \frac{d\sigma}{d\cos\theta^*_{\ell}} \ d\cos\theta^*_{\ell}} , \tag{5.39}$$

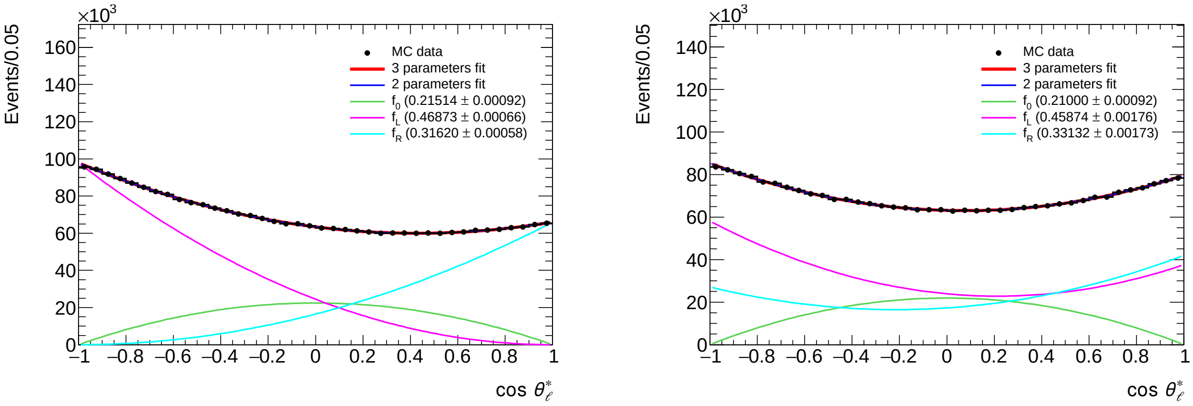

(a) Fit on $\cos\theta^*_{\ell W}$ in W^+Z **(b)** Fit on $\cos\theta^*_{\ell Z}$ in W^+Z

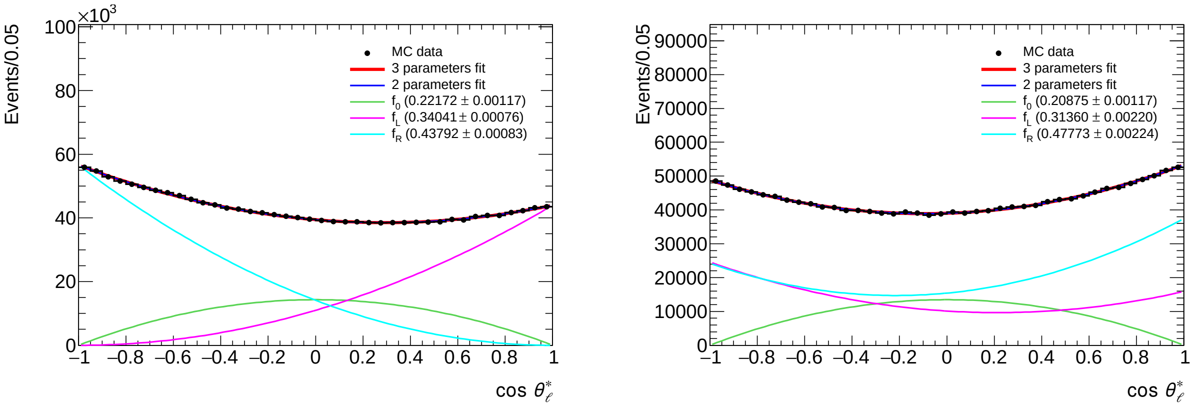

(c) Fit on $\cos\theta^*_{\ell W}$ in W^-Z **(d)** Fit on $\cos\theta^*_{\ell Z}$ in W^-Z

Figure 5.4 Polarisation fractions of $W^{\pm}$ boson (left) and Z boson (right) in W^+Z (top) and W^-Z (bottom) events, extracted from the $\cos\theta^*_\ell$ distributions in the total phase space of the inclusive POWHEG+PYTHIA Monte Carlo sample through analytical fits with three or two parameters.

replacing with (5.38) and adding orthogonality, one gets:

$$\langle m_{i_0}\rangle = \frac{\sum_{i=0}^{2}\alpha_i\langle m_i, m_{i_0}\rangle}{\sum_{i=0}^{2}\alpha_i\langle m_i, 1\rangle}\,, \tag{5.40}$$

$$= \frac{\alpha_{i_0}\|m_{i_0}\|^2}{\alpha_0\|1\|^2}\,, \tag{5.41}$$

$$= \frac{3}{8}\alpha_{i_0}\|m_{i_0}\|^2 \quad \text{because} \quad \|1\|^2 = 2 \quad \text{and} \quad \alpha_0 = \frac{4}{3}\,. \tag{5.42}$$

Thus, computing the norm of each m_i and replacing the α_i by the expressions of Eq. (5.36) gives

$$\begin{aligned} \langle \tfrac{1}{2}(1-3\cos^2\theta^*_\ell)\rangle &= \tfrac{3}{20}\left(A_0-\tfrac{2}{3}\right)\,, \\ \langle\cos\theta^*_\ell\rangle &= \tfrac{1}{4}A_4\,. \end{aligned} \tag{5.43}$$

allowing to extract the parameters A_0 and A_4 linked to the kinematics of the decay of the boson, and with this its polarisation. Extracting fractions from the two A_0 and A_4 parameters implies that they will follow the normalisation relation (1.48) as well.

The fit with three-parameter, the fit with two-parameter and the moments method were compared and found to provide very comparable results, as detailed in Appendix B. Still, the three-parameter fit was found to extract fractions with uncertainties slightly larger. In the following, the moments method is chosen to extract the polarisation fractions of a single boson. In Table 5.2, the total phase space fractions are represented. It shows that the statistical uncertainties from the extraction of fractions are reasonable, at the percent level. A difference in theory from the sign of the $W^{\pm}$ boson is visible. It is very small when considering f_0, but for f_{L} and f_{R}, there is an inversion of the roles when inverting the charge. Additionally, $f_{\mathrm{L}} - f_{\mathrm{R}}$ is also different, being smaller in $W^{+}Z$ events.

Table 5.2 Single boson polarisation fractions at particle level in the total phase space extracted from Powheg+Pythia, distinguishing events with a W^{+} and events with a W^{-}. The uncertainties are statistical only, arising from the moments method used to obtain the fractions.

$W^{\pm}$ boson polarisation

	in $W^{+}Z$	in $W^{-}Z$
f_0	0.1821 ± 0.0009	0.1901 ± 0.0011
f_{L}	0.5006 ± 0.0006	0.3652 ± 0.0007
f_{R}	0.3172 ± 0.0005	0.4447 ± 0.0008

Z boson polarisation

	in $W^{+}Z$	in $W^{-}Z$
f_0	0.1807 ± 0.0009	0.1822 ± 0.0012
f_{L}	0.3612 ± 0.0017	0.5053 ± 0.0022
f_{R}	0.4580 ± 0.0018	0.3125 ± 0.0022

5.4.2 Polarisation correlations and reference frame

As was described in Fig. 5.2, two different frames exist to define the $\cos\theta^{*}_{\ell}$ variable. This choice of frame for $\cos\theta^{*}_{\ell}$ is really the choice of the frame in which the single boson polarisation fractions are measured later on in the analysis. The main difference between the *Helicity* frame and the *Modified Helicity* frame is the direction of the z-axis used to define the direction of the vector boson, and thus the resulting longitudinal polarisation. For a single boson polarisation analysis, any frame would work, as long as the analysis consistently uses everywhere the same frame.

Nevertheless, to talk meaningfully of joint-polarisations, a common frame for the diboson system is needed, when there are actually two *Helicity* frames, one per boson. Analogously to the single boson case, the diboson system rest frame allows assimilating helicity states to spin quantum states making more visible angular effects originating from the spin. The *Modified Helicity* frames originate from this diboson rest frame used for joint-polarisation measurement and provide a common z-axis for both boson along their momentum. It will thus allow comparing joint-polarisation and single boson polarisations and evaluate the correlations between polarisations.

To test this idea, it is possible to represent the evolution of the polarisation fractions of one boson with respect to the $\cos\theta^{*}_{\ell}$ of the other boson. This is obtained extracting the polarisation fractions of one boson with the moments method (Section 5.4.1) in bins of the $\cos\theta^*_\ell$ of the other boson. The underlying idea is that the boson of which the $\cos\theta^*_\ell$ is used will have a favoured polarisation depending on the value of $\cos\theta^*_\ell$, as can be seen on Fig. 5.4. For example, a W^+ boson will be mainly polarised Right for $\cos\theta^*_{\ell W}$ close to $+1$, Left for $\cos\theta^*_{\ell W}$ close to -1, and with a significant amount of longitudinal polarisation for $\cos\theta^*_{\ell W}$ around 0. Then representing the polarisation fractions of the Z boson along $\cos\theta^*_{\ell W}$ will give a first idea of how correlations work.

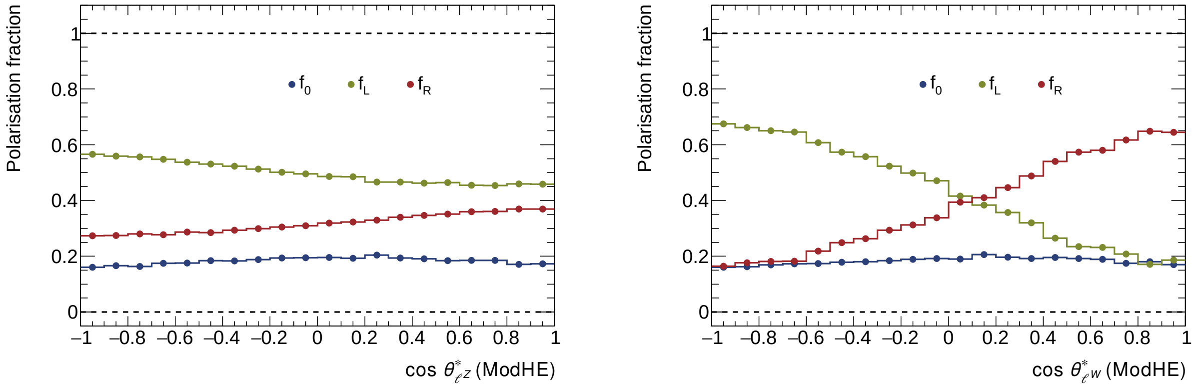

(a) W^+ in `ModHE` **(b)** Z of W^+Z in `ModHE`

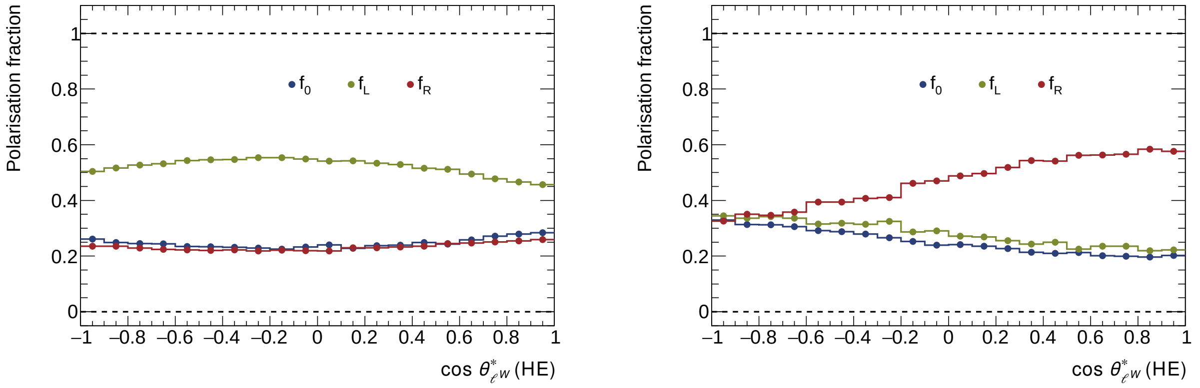

(c) W^+ in `HE` **(d)** Z of W^+Z in `HE`

Figure 5.5 Polarisation fractions of $W^{\pm}$ boson (left) and Z boson (right) in W^+Z events in bins of the $\cos\theta^*_\ell$ of the other boson ($\cos\theta^*_{\ell Z}$ left, $\cos\theta^*_{\ell W}$ right) extracted from POWHEG+PYTHIA at the particle level in the total phase space. The top plot have the $\cos\theta^*_\ell$ defined in the *Modified Helicity* frame (`ModHE`), the bottom plot have the $\cos\theta^*_\ell$ defined in the *Helicity* frame (`HE`).

The two frames show very different behaviour as visible in Fig. 5.5 for W^+Z events (similar results are obtained with W^-Z events). In the *Modified Helicity* frame, the longitudinal fraction and the transverse fractions are almost completely decoupled and the Left and Right fractions have crossed behaviours. For example in Fig. 5.5(b), for a W^+ boson mostly Left ($\cos\theta^*_{\ell W}$ around -1), the Z boson is mostly Left, while for a W^+ mostly Right ($\cos\theta^*_{\ell W}$ around 1), the Z boson is mostly Right. This indicates strong correlations between the transverse polarisations. This behaviour is easy to understand from helicity conservation[4]. A less obvious result is the visible decoupling of the longitudinal polarisation from the transverse polarisations: the longitudinal polarisation fraction of the two bosons are much less correlated. This decoupling is still there though less visible in Fig. 5.5(a) as

---

[4] Note that the z-axis used for the $W^{\pm}$ boson polarisation has opposite direction compared to the z-axis used for the Z boson polarisation.

the $\cos\theta^{*}_{\ell Z}$ is less discriminating between the Left and Right polarisations. However, for the *Helicity* frame, the fractions are mixed and the crossed behaviour is now split between the longitudinal and one transverse polarisation. Using the *Helicity* frame reshuffles the polarisations of the bosons, making less clear the different correlations that appear in the *Modified Helicity* frame. In the end, the *Modified Helicity* frame is the most interesting frame as correlations of single boson polarisations appear clearly.

For joint-polarisation study, the $W^{\pm}$ and Z bosons must be described in their rest frame. This is for example what is done in the MadGraph0,1j@LO polarised Monte Carlo generation detailed in Section 5.3.2. Using such Monte Carlo sample also for single boson polarisation forces to use the *Modified Helicity* frame.

5.4.3 Diboson joint-polarisation fractions

To extract the joint-polarisation fractions, a first idea is to simply multiply single boson polarisation fractions. However, this can only be done under the assumption that the polarisation of both boson are independent. With three polarisations for each boson, one gets thus nine joint-polarisation fractions. As a first step and for simplicity, this number is reduced to four by merging Left and Right polarisations in what will be called the *Transverse* polarisation labeled T. The joint-polarisation fractions f_{00}, $f_{0\mathrm{T}}$, $f_{\mathrm{T}0}$ and f_{TT} are expressed as functions of the longitudinal polarisation of both the $W^{\pm}$ and the Z bosons under the independence assumption:

$$f_{00} = f_0^W f_0^Z \,, \tag{5.44}$$

$$f_{0\mathrm{T}} = f_0^W \left(1 - f_0^Z\right) \,, \tag{5.45}$$

$$f_{\mathrm{T}0} = \left(1 - f_0^W\right) f_0^Z \,, \tag{5.46}$$

$$f_{\mathrm{TT}} = \left(1 - f_0^W\right)\left(1 - f_0^Z\right) \,. \tag{5.47}$$

Yet, mere considerations of angular momentum conservation indicate that the polarisations of both bosons are probably not independent. For example, Fig. 5.5 shows an indirect effect of such correlations, as the polarisation of one given boson is influenced by the kinematic variable value of the other boson. Extracting joint-polarisation fractions under the independence assumption is expected to give a wrong result. As a result, a 2D fit of the 2D histogram of ($\cos\theta^{*}_{\ell W}$,$\cos\theta^{*}_{\ell Z}$) was developed. For this, Eq. (5.28) and (5.29) are multiplied to get the 2D fitting function of Eq. (5.48).

$$\begin{aligned}
\frac{d\sigma}{d\cos\theta^{*}_{\ell W}\, d\cos\theta^{*}_{\ell Z}} = \sigma \Big[& (1 - f_{0L} - f_{0R} - f_{L0} - f_{LL} - f_{LR} - f_{R0} - f_{RL} - f_{RR})\frac{3}{4}\,(1 - \cos\theta^{*}_{\ell W}{}^{2}) \times \frac{3}{4}(1 - \cos\theta^{*}_{\ell Z}{}^{2}) \\
& + f_{0L}\frac{3}{4}(1 - \cos\theta^{*}_{\ell W}{}^{2}) \times \frac{3}{8}(1 + 2 * C_{\mathrm{w}}\cos\theta^{*}_{\ell Z} + \cos\theta^{*}_{\ell Z}{}^{2}) \\
& + f_{0R}\frac{3}{4}(1 - \cos\theta^{*}_{\ell W}{}^{2}) \times \frac{3}{8}(1 - 2 * C_{\mathrm{w}}\cos\theta^{*}_{\ell Z} + \cos\theta^{*}_{\ell Z}{}^{2}) \\
& + f_{L0}\frac{3}{8}(1 \mp \cos\theta^{*}_{\ell W})^{2} \times \frac{3}{4}(1 - \cos\theta^{*}_{\ell Z}{}^{2}) \\
& + f_{LL}\frac{3}{8}(1 \mp \cos\theta^{*}_{\ell W})^{2} \times \frac{3}{8}(1 + 2 * C_{\mathrm{w}}\cos\theta^{*}_{\ell Z} + \cos\theta^{*}_{\ell Z}{}^{2}) \\
& + f_{LR}\frac{3}{8}(1 \mp \cos\theta^{*}_{\ell W})^{2} \times \frac{3}{8}(1 - 2 * C_{\mathrm{w}}\cos\theta^{*}_{\ell Z} + \cos\theta^{*}_{\ell Z}{}^{2}) \\
& + f_{R0}\frac{3}{8}(1 \pm \cos\theta^{*}_{\ell W})^{2} \times \frac{3}{4}(1 - \cos\theta^{*}_{\ell Z}{}^{2}) \\
& + f_{RL}\frac{3}{8}(1 \pm \cos\theta^{*}_{\ell W})^{2} \times \frac{3}{8}(1 + 2 * C_{\mathrm{w}}\cos\theta^{*}_{\ell Z} + \cos\theta^{*}_{\ell Z}{}^{2}) \\
& + f_{RR}\frac{3}{8}(1 \pm \cos\theta^{*}_{\ell W})^{2} \times \frac{3}{8}(1 - 2 * C_{\mathrm{w}}\cos\theta^{*}_{\ell Z} + \cos\theta^{*}_{\ell Z}{}^{2})\Big] \,.
\end{aligned} \tag{5.48}$$

In this equation, there would be $3 \times 3 = 9$ fractions and one normalisation parameter, the overall cross section σ. This normalisation factor could have been taken from the integral of the 2D histogram as was done in single boson polarisation, but the fit is found to perform much better without this assumption. Additionally with the normalisation relationship of the fractions, the sum of the fractions should be equal to 1, bringing the equation back to 9 free floating parameters by redefining one fraction as 1 minus all the others. Here, the chosen redefined fraction is f_{00}.

This method of considering the product of angular variables to extract diboson polarisation was also used for the WW channel at LEP [21]. It provides at once all the joint-polarisation fractions, retaining thus the information on polarisation correlations. All joint-polarisation fractions are extracted from the inclusive Powheg+Pythia Monte Carlo in the total phase space this way and, through additions, brought back to the four f_{00}, $f_{0\mathrm{T}}$, $f_{\mathrm{T}0}$ and f_{TT} fractions. In Fig. 5.6, we can see that the fitted 2D function reproduces well the initial 2D histogram. Fractions extracted with this method are shown in Table 5.3.

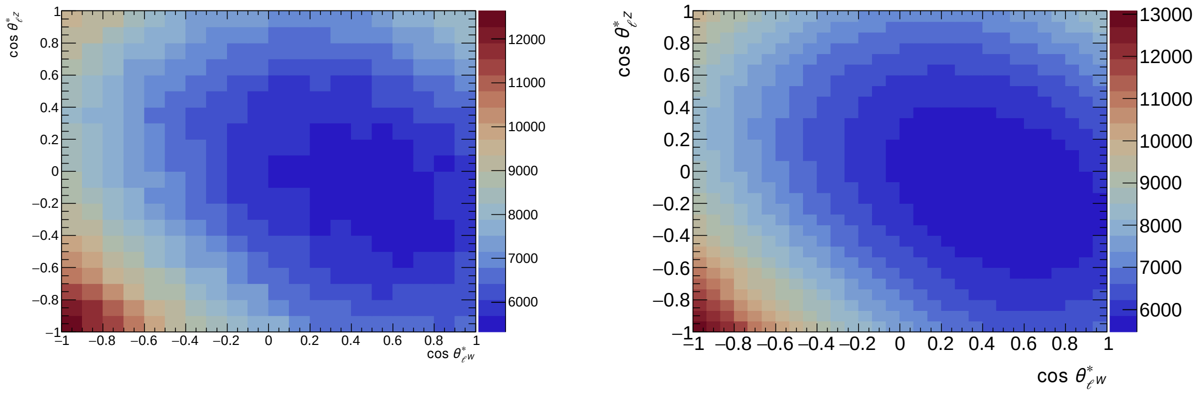

(a) 2D histogram in W^+Z **(b)** 2D fitted function in W^+Z

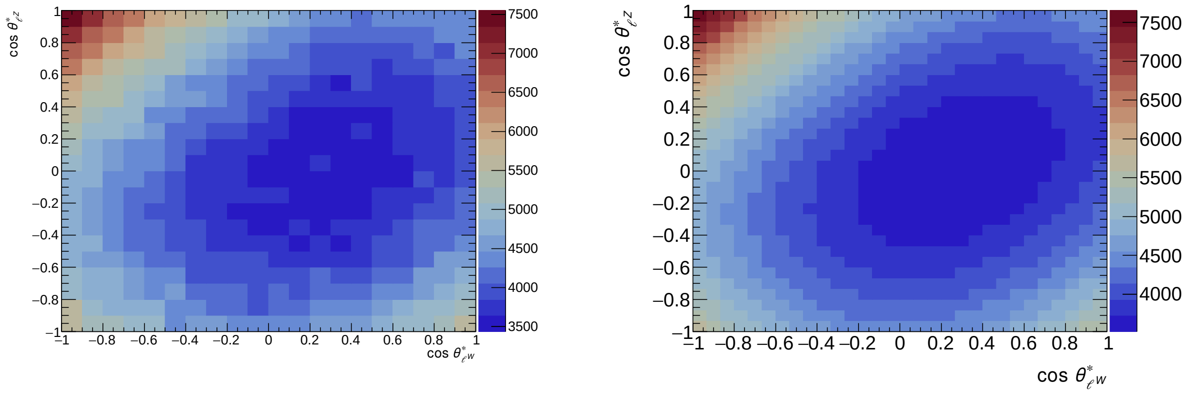

(c) 2D histogram in W^-Z **(d)** 2D fitted function in W^-Z

Figure 5.6 Result of the 2 dimension fit of an inclusive Powheg+Pythia sample in the total phase space. Left are the original 2D histogram of ($\cos\theta^*_{\ell W}$,$\cos\theta^*_{\ell Z}$), right are the fitted 2D functions. On top are W^+Z events, bottom are W^-Z events. The z-axis represented with a color palette corresponds to the number of events.

5.4.4 Link between joint and single boson polarisation

Finally, it is possible to modify the formulas of Eq. (5.44)–(5.47) to make the dependence between each boson polarisation appear. According to NLO calculations in [77], the interferences between polarisations are negligible as they only amount to 0.6 % of the events. Consequently as a first approximation, the spin density matrix of the diboson system can be considered diagonal, and joint-polarisation fractions are really the probability to find the system in a given joint-polarisation state. Basic properties of a probability yield

$$\mathbb{P}\left(W_0\right) = \mathbb{P}\left(W_0 \cap \left(Z_0 \cup Z_T\right)\right) = \mathbb{P}\left(W_0 \cap Z_0\right) + \mathbb{P}\left(W_0 \cap Z_T\right), \tag{5.49}$$

which becomes for fractions

$$f_0^W = f_{00} + f_{0\mathrm{T}}\ , \tag{5.50}$$

$$f_0^Z = f_{00} + f_{\mathrm{T}0}\ . \tag{5.51}$$

In the end by getting f_{00} from a 2D fit and f_0^W and f_0^Z from a 1D fit, one gets the remaining joint-polarisation fractions with

$$f_{0\mathrm{T}} = f_0^W - f_{00}, \tag{5.52}$$

$$f_{\mathrm{T}0} = f_0^Z - f_{00}, \tag{5.53}$$

$$f_{\mathrm{TT}} = 1 + f_{00} - f_0^W - f_0^Z. \tag{5.54}$$

In Table 5.3, the four joint-polarisation fractions extracted from Monte Carlo events in the total phase space are presented using three different methods:

- Using the independence assumption from Eq. (5.44)–(5.47), single boson polarisation fractions extracted with a 1D fit provide joint-polarisation fractions.
- Joint-polarisation fractions are directly extracted with the 2D fit using the analytical formula (5.48).
- Using the reparametrisation from Eq. (5.52)–(5.54) to the (f_{00}, f_0^W, f_0^Z) basis, single boson polarisation fractions extracted with a 1D fit are combined with the f_{00} joint-polarisation fraction extracted with the 2D fit to provide joint-polarisation fractions.

From the independence assumption to the 2D fit, it appears that the results are very close, but still slightly different. The difference is well above the uncertainties, implying that the 2D fit does capture some correlation in the polarisation of the two bosons that the independence assumption would miss.

From the 2D fit to the (f_{00}, f_0^W, f_0^Z) basis, as expected, there are almost no differences in $f_{0\mathrm{T}}$, $f_{\mathrm{T}0}$ and f_{TT}, showing that the 1D and 2D fits are consistent at particle level in the total phase space. This conversely implies that extracting the f_0 fraction of a boson directly with a 1D fit or indirectly with a 2D fit gives coherent results.

In fact, it is possible to go further and extract a parameter directly linked to the dependence of the longitudinal polarisation of both bosons. Such parameter, called R_c, is defined using Bayes formula as

$$R_c = \frac{f_{00}}{f_0^W f_0^Z} = \frac{f_0^{W|Z_0}}{f_0^W} = \frac{f_0^{Z|W_0}}{f_0^Z}\ , \tag{5.55}$$

Table 5.3 Joint-polarisation fractions at particle level in the total phase space obtained by three methods from the POWHEG+PYTHIA sample. The first column shows the results obtained under the independence assumption, that is by multiplying single boson polarisation fractions. The second column shows the result with the 2D fit. Finally, the third column shows the results using f_{00} from the 2D fit and single boson polarisation fractions f_0^W, f_0^Z combined to get $f_{0\mathrm{T}}$, $f_{\mathrm{T}0}$ and f_{TT} (note that the first line is by design exactly the same from the second to the third column). The uncertainties are statistical only, arising from the fits.

W^+Z

Method	Independence	2D fit	(f_{00}, f_0^W, f_0^Z) basis
f_{00}	0.0329 ± 0.0002	0.0485 ± 0.0014	0.0485 ± 0.0014
$f_{0\mathrm{T}}$	0.1492 ± 0.0008	0.1333 ± 0.0016	0.1336 ± 0.0017
$f_{\mathrm{T}0}$	0.1478 ± 0.0008	0.1320 ± 0.0016	0.1322 ± 0.0017
f_{TT}	0.6700 ± 0.0011	0.6862 ± 0.0016	0.6856 ± 0.0019

W^-Z

Method	Independence	2D fit	(f_{00}, f_0^W, f_0^Z) basis
f_{00}	0.0346 ± 0.0003	0.0485 ± 0.0018	0.0485 ± 0.0018
$f_{0\mathrm{T}}$	0.1555 ± 0.0010	0.1411 ± 0.0020	0.1416 ± 0.0022
$f_{\mathrm{T}0}$	0.1476 ± 0.0010	0.1334 ± 0.0020	0.1337 ± 0.0022
f_{TT}	0.6623 ± 0.0013	0.6770 ± 0.0022	0.6762 ± 0.0024

where $f_0^{W|Z_0}$ (resp. $f_0^{W|Z_0}$) is the fraction of W boson (resp. Z boson) polarised longitudinally if the Z boson (resp. W boson) polarisation is already selected longitudinal. It thus represents a test of the independence of the polarisation fraction of both bosons. In case of independence, R_c is expected to be one. The four original joint-polarisation fractions transform with this new set of parameters as

$$f_{00} = R_c f_0^W f_0^Z \tag{5.56}$$

$$f_{0\mathrm{T}} = f_0^W \left(1 - R_c f_0^Z\right), \tag{5.57}$$

$$f_{\mathrm{T}0} = \left(1 - R_c f_0^W\right) f_0^Z, \tag{5.58}$$

$$f_{\mathrm{TT}} = \left(1 - f_0^W\right)\left(1 - f_0^Z\right) + (R_c - 1) f_0^W f_0^Z. \tag{5.59}$$

The link of R_c with the independence hypothesis is clear comparing with the joint-polarisation fractions under the independence hypothesis in Eq. (5.44)–(5.47).

Chapter 6

Inclusive $W^{\pm}Z$ production

The data collected during the Run 2 of the LHC by the ATLAS detector amounts to $139\,\mathrm{fb}^{-1}$ of integrated luminosity. This represents roughly 10^{16} inelastic pp collisions[1]. From Fig. 1, the inclusive cross section for $W^{\pm}Z$ production in all decay channels is roughly two milliards lower. More precisely, considering the total phase space cross section for $W^{\pm}Z$ production in Eq. (5.11), approximately 7 000 000 events with simultaneously a $W^{\pm}$ boson and a Z boson were produced over the course of Run 2. Out of these, we only consider in this analysis events were both bosons decayed in leptons of the first or second generation. With roughly 21 % of $W^{\pm}$ bosons and 7 % of Z boson decaying this way [70], we expect only a bit more than 1 % of $W^{\pm}Z$ inclusive production in our decay channel, for a total of 98 000 events.

This dramatic decrease in the number of available events only reflects the choice to study the $W^{\pm}Z$ diboson process with a clean signature in the detector. As a result, selecting these rare events within the gigantic amount of pp collisions recorded during Run 2 is a crucial step. Furthermore, it is important to define a signal region with a limited number of events from background processes among selected events to be able to isolate the $W^{\pm}Z$ production process. This means the efficiency of the selection has to be balanced by its purity. The reconstruction and selection of $W^{\pm}Z$ events described in Section 6.1 manages to optimise this. For further polarisation studies, the reconstruction of the full topology of these events is needed. This includes the neutrino originating from the $W^{\pm}$ boson, which does not leave any direct footprint in the ATLAS detector. Methods to completely reconstruct this final particle are detailed in Section 6.2. Finally, it is impossible to completely avoid background contamination in the selected events. Accounting for all background processes and developing methods to properly estimate their contributions in the signal region, as detailed in Section 6.3, will allow isolating the contribution from $W^{\pm}Z$ signal events.

The selection criteria will define a fiducial phase space were the measurement is performed, as already described in Table 5.1. The fiducial cross section of Eq. (5.12) predicts 36 000 $W^{\pm}Z$ events in our fiducial phase space. Then, the actual performance of the ATLAS detector for the event reconstruction will further decrease the number of available events. Nonetheless, the signal over background ratio of this very rare process is still good, as shown in Section 6.4. This will then allow studying fainter signals, such as the fraction of such events for different polarisation configurations.

---

[1] The proton–proton inelastic collision cross section is of 80 mb.

6.1 $W^{\pm}Z$ events reconstruction and selection

6.1.1 Particles reconstruction with the ATLAS detector

The ATLAS detector extensively described in Section 2.2 is composed of many sub-detectors each targeting certain aspects of the footprint of collisions in ATLAS. Each collision that passed the two levels of trigger is recorded as an event and goes through reconstruction on the LHC Computing Grid. Combining information from various sub-detectors allows reconstructing physics object candidates. These physics objects are used to characterise the hard scattering physics process happening in the main pp collision. The reconstruction of such objects combining sub-detectors informations is designed centrally in ATLAS by dedicated combined detector performance (CP) groups. The CP groups develop in Athena, the ATLAS reconstruction and analysis software suite [92]. They provide algorithmic tools to define identification quality criteria and final calibration of the particles, along with the estimation of the associated systematic uncertainties. In the context of $W^{\pm}Z$ production, as described by Eq. (5.1), physics objects of interest are primarily electrons and muons. The neutrino goes undetected in the detector, but can be partially reconstructed using missing transverse energy $E_{\mathrm{T}}^{\mathrm{miss}}$. The computation of $E_{\mathrm{T}}^{\mathrm{miss}}$ requires to keep track of every transverse energy produced in the collision. This is eased reconstructing jets inclusively produced in $W^{\pm}Z$ production (see Section 1.3.3). Electrons, muons, jets and $E_{\mathrm{T}}^{\mathrm{miss}}$ are reconstructed and calibrated following the prescriptions from their dedicated CP group:

Electrons [93, 94]: Electrons are reconstructed on one side from the identification of electromagnetic clusters in the LAr electromagnetic calorimeter (Section 2.2.3.1), and in parallel by the reconstruction of tracks in the Inner Detector (Section 2.2.2). Tracks and clusters are matched to create an electron candidate. At this stage, the reconstructed candidates contain a sizeable amount of particles wrongly identified as electrons *e.g.* a light jet or a photon converting to an electron-positron pair by interacting with the material in the tracker.

On top of the reconstruction, a multivariate discriminant combining information from different sub-detectors is created to assess the quality of the identification of the electron candidate. From this discriminant, four working points of increasing background rejection levels are designed, called `Loose`, `Medium` and `Tight`. Candidates selected at a certain level of purity are strictly contained in the looser selection criteria. This entails a decreasing efficiency of the selection for working points of increasing tightness.

Furthermore, electrons can be produced inside a jet. These are non-prompt electrons, that is not produced in the primary vertex, but rather produced as secondary particles. The selection of prompt electrons requires the use of isolation criteria assessing the activity in the vicinity of the electron candidate. The isolation can be evaluated from the calorimeter perspective using an isolation cone $\Delta R = 0.2$ as defined in Section 2.2.1, or from the track perspective, using this time a p_{T}-dependent cone with maximum size $\Delta R = 0.2$ as well. As for identification, isolation working points are defined, either targeting a fixed isolation efficiency uniform η wise but with E_{T} dependence (`Gradient`) or using fixed requirements on the isolation variables from track and calorimeter (`Loose, Tight`) or calorimeter only (`HighPtCaloOnly`).

Muons [95]**:** Muons are primarily reconstructed using hits in the Muon System (Section 2.2.4). The muon candidates are then matched to charged particles reconstructed in the Inner Detector, yielding combined muon candidates. Other muon candidates can be reconstructed matching an Inner Detector track to an isolated segment in the Muon System, or conversely extrapolating a muon candidate of the Muon System not matched by any track in the Inner Detector. Finally, some muon candidates can be reconstructed matching an Inner Detector track to minimum ionising particle energy deposits in the calorimeter. Identification working points are defined similarly as for the electrons. Isolation variables are also defined to reject non-prompt muons using isolation cone of $\Delta R = 0.2$ in calorimeter and p_{T}-dependent cone of up to $\Delta R = 0.3$ in Inner Detector tracks[2]. Many different working points are defined, either using cuts on track isolation variable only (`HighPtTrackOnly, TightTrackOnly`), cuts on both track and calorimeter variables (`Loose, Tight`) and cuts on *particle flow* variables which are a weighted sum of track and calorimeter variables (`PflowLoose, PflowTight`).

Jets [96]**:** Jet reconstruction is primarily based on the anti-k_t algorithm [97] which builds jets from reconstructed objects four-vectors. It uses as parameter the typical radius of the jet, usually set at $R = 0.4$ but tunable for different analysis needs. The input four-vectors can be reconstructed from energy deposit topological clusters in the calorimeters, creating `EMTopo` jets, or with the more advanced *particle flow* algorithm [98] that combines track and calorimeter information, creating `PFlow` jets. Because of the composite nature of jets, problematics of background contamination are treated by carefully calibrating the jet energy scale (JES). This is done applying pile-up corrections and taking into account inefficiencies of the sub-detectors. Additionally, the jet energy resolution (JER) is determined. To further reject pile-up contributions, Jet Vertex Tagger (JVT) algorithms [99] are used in order to keep only jets that match the primary vertex.

$\boldsymbol{E_{\mathrm{T}}^{\mathrm{miss}}}$ [100] The missing transverse momentum, traditionally labelled $E_{\mathrm{T}}^{\mathrm{miss}}$, is obtained from the transverse momentum imbalance. The partons colliding in the hard scattering process have negligible initial transverse momentum. Therefore, from momentum conservation, a missing transverse momentum vector can be reconstructed

$$\vec{E}_{\mathrm{T}}^{\mathrm{miss}} = -\left(\sum_{i\in\{\text{hard objects}\}} \vec{p}_{\mathrm{T},i} + \sum_{j\in\{\text{soft objects}\}} \vec{p}_{\mathrm{T},j} \right), \tag{6.1}$$

with the hard objects being any other objects among leptons or jets reconstructed, and soft objects being any tracks originating from the primary vertex and not matched to any hard objects.

6.1.2 $W^{\pm}Z$ event selection

Events from inclusive $W^{\pm}Z$ production are reconstructed from Run 2 data that passed quality criteria, recorded from 2015 to 2018. These events labelled *Good for Physics* in Fig. 2.4, correspond to 139 fb^{-1} of integrated luminosity. The selection starts among events

---

[2] In the inner detector, fixed radius $\Delta R = 0.2$ can also be used. In that case, the isolation working point variant is tagged by the suffix `_FixedRad`.

recorded by at least one of five single lepton (electron or muon) triggers. The triggering lepton is required to have $p_\mathrm{T} > 27\,\mathrm{GeV}$, one GeV above the trigger threshold[3], to ensure being on the plateau of the trigger efficiency turn-on curve (such curves are illustrated by Fig. 3.8(b)). Events that are incomplete, corresponding to corrupted data from one of the sub-detectors or contain a fake jet from non-collision background[4], are discarded. Furthermore, events are required to have a primary vertex with at least two tracks.

Events with three leptons corresponding to a Z boson and a $W^\pm$ boson are selected. For this purpose, three levels of lepton selection criteria of increasing tightness are defined: baseline, Z-lepton and W-lepton. To each level corresponds specific criteria depending on the lepton flavour. They are summarised in Table 6.1 for muons and Table 6.2 for electrons.

- For all levels, the leptons should be associated to the primary vertex of the collision with criteria on the impact parameters of their track d_0 and z_0. The tracks transverse impact parameter must have a significance $|d_0/\sigma(d_0)|$ better than 3.0 for muons, 5.0 for electrons. The longitudinal impact parameter z_0, defined as the distance on the beam axis between the primary vertex and the projection of d_0, is required to satisfy $|z_0 \cdot \sin\theta| < 0.5\,\mathrm{mm}$.

- A cut on $|\eta|$ allows to control the sub-detector regions used for the reconstruction. For muons, the $|\eta|$ cut goes from the acceptance of the Muons System for baseline leptons down to the acceptance of the Inner Detector for Z and W-leptons. For electrons, the acceptance of the Inner Detector and the precision region of the LAr electromagnetic calorimeter is selected for all levels, excluding the crack region between barrel and end-caps only for Z and W-leptons.

- Fake leptons usually have lower p_T than prompt signal leptons. Cuts on p_T, higher for selections of increasing tightness, allow rejecting these fakes.

- Identification and Isolation working points, as defined in Section 6.1.1 are selected for each case. For the baseline electrons, the working points `Loose+BLayer` makes use of the Insertable B-Layer.

- Different physics object are reconstructed in parallel from the same tracks or energy deposit. An overlap removal procedure allows to correct this and avoid double counting:
  - Muons, being detected with the Muon System, can only overlap with a jet that would have emitted a non-prompt muon. The μ–jets overlap procedure first removes jets with less than three tracks and within $\Delta R < 0.2$ of a muon, then removes muons found within $\Delta R < 0.4$ of a jets with at least three tracks.
  - Two electron candidates can be reconstructed sharing a track. The e–e overlap procedure removes the sub-leading p_T electron in this case.
  - An electron and a muon can be reconstructed sharing a track. In this case, the e–μ overlap procedure removes the electron.

---

[3] For data from the year 2015, it is $p_\mathrm{T} > 25\,\mathrm{GeV}$, because a lower trigger threshold was allowed by lower pile-up conditions.

[4] Non-collision backgrounds can originate from cosmic rays or a proton escaping the beam before the interaction point.

- Electrons can overlap with jets for the same reason as muons. The e–jets overlap procedure first removes jets within $\Delta R < 0.3$ of an electron, then removes electrons found within $\Delta R < 0.4$ of a jet that survived the previous step.
- Due to photon conversion, some calorimeter clusters can be assigned to an electron or a photon. An ambiguity resolution procedure [94] manages to decide between both most of the time, but some candidate remain ambiguous in which case they can be considered as electron or photon depending on what is selected. The e–γ overlap removal removes any electron of ambiguous nature.

Table 6.1 Muon candidate selection criteria for the three levels of selection.

	Baseline selection	Z-lepton selection	W-lepton selection
Vertex Association	$\lvert d_0/\sigma(d_0)\rvert < 3$ (for $\lvert\eta\rvert < 2.5$ only) $\lvert\Delta z_0 \sin\theta\rvert < 0.5\,\text{mm}$ (for $\lvert\eta\rvert < 2.5$ only)		
$\lvert\eta\rvert$ cut	$\lvert\eta\rvert < 2.7$	$\lvert\eta\rvert < 2.5$	$\lvert\eta\rvert < 2.5$
p_{T} cut	$p_{\mathrm{T}} > 5\,\text{GeV}$	$p_{\mathrm{T}} > 15\,\text{GeV}$	$p_{\mathrm{T}} > 20\,\text{GeV}$
Identification	`Loose`	`Medium`	`Tight`
Isolation	`PflowLoose_FixedRad`	`PflowLoose_FixedRad`	`PflowTight_FixedRad`
Overlap Removal	-	μ–jet	μ–jet

Table 6.2 Electron candidate selection criteria for the three levels of selection.

	Baseline selection	Z-lepton selection	W-lepton selection
Vertex Association	$\lvert d_0/\sigma(d_0)\rvert < 5$ $\lvert\Delta z_0 \sin\theta\rvert < 0.5$ mm		
$\lvert\eta\rvert$ cut	$\lvert\eta\rvert < 2.5^*$	$\lvert\eta\rvert < 2.5^*$ Exclude $1.37 < \lvert\eta^{\text{cluster}}\rvert < 1.52$	$\lvert\eta\rvert < 2.5^*$ Exclude $1.37 < \lvert\eta^{\text{cluster}}\rvert < 1.52$
p_{T} cut	$p_{\mathrm{T}} > 5\,\text{GeV}$	$p_{\mathrm{T}} > 15\,\text{GeV}$	$p_{\mathrm{T}} > 20\,\text{GeV}$
Identification	`Loose+Blayer`	`Medium`	`Tight`
Isolation	`Loose`	`HighPtCalo`	`Tight`
Overlap Removal	e–e , e–μ	e–e , e–μ e–jets	e–e , e–μ e–jets , e–γ

* In the calorimeter, $|\eta^{cluster}| < 2.47$

The baseline selection is rather loose in order to select leptons with high efficiency. As it will be described in Section 6.3, the main background to $W^{\pm}Z$ production comes from ZZ events decaying to four leptons. The baseline selection is thus optimised to detect a fourth lepton, providing a veto against ZZ. Then, with a tighter selection, exactly three Z-leptons are requested. Among these, two Z-leptons oppositely charged and of same flavour are required to reconstruct a Z boson. This pair is required to have an invariant mass $m_{\ell\ell}$ within a $\pm 10\,\text{GeV}$ window around the resonant mass of the Z boson $M_Z = 91.1876\,\text{GeV}$ [70]. In case several combinations of leptons could match this requirement, as can happen in the eee or $\mu\mu\mu$ decay channel, the pair with $m_{\ell\ell}$ closest to M_Z is selected. The remaining Z-lepton is then required to pass the W-lepton selection criteria. Finally, to associate this W-lepton to an actual $W^{\pm}$ boson, a cut on the transverse mass of the $W^{\pm}$ boson $m_{\mathrm{T}}^{W} > 30\,\text{GeV}$ should be passed. This transverse mass is a variable designed to account for the fact that in the reconstruction of a $W^{\pm}$ boson, only the transverse momentum of the decay neutrino is known by means of $E_{\mathrm{T}}^{\mathrm{miss}}$. It is defined using the p_{T} of the W-lepton and $E_{\mathrm{T}}^{\mathrm{miss}}$ as

$$m_{\mathrm{T}}^{W} = \sqrt{2p_{\mathrm{T}}^{\ell}E_{\mathrm{T}}^{\mathrm{miss}}\left(1-\cos\Delta\phi\right)}\,, \tag{6.2}$$

with $\Delta\phi$ the azimuthal angle difference in the transverse plane between the W-lepton and the missing transverse momentum. In order to compute the $E_{\mathrm{T}}^{\mathrm{miss}}$, jets are reconstructed before hand as `PFlow` jets. Only jets with $|\eta| < 4.5$ and $p_{\mathrm{T}} > 25\,\mathrm{GeV}$ are considered. Pile-up jets are removed using the jet vertex tagger (JVT) algorithm. All these inclusive event selection criteria are summarised in Table 6.3.

Table 6.3 Overview of the inclusive event selection.

Trigger	At least one of five single lepton triggers fired
Leading lepton p_{T}	$p_{\mathrm{T}}^{\mathrm{lead}} > 27\,\mathrm{GeV}$
Event cleaning	Reject corrupted or incomplete events and events with non-collision background jets
Primary vertex	Hard scattering vertex with at least two tracks
ZZ veto	Strictly less than 4 baseline leptons
N leptons	Exactly 3 leptons passing the Z-lepton selection
Z leptons	2 same flavor oppositely charged leptons passing the Z-lepton selection
Mass window	$\lvert m_{\ell\ell} - M_Z\rvert < 10\,\mathrm{GeV}$
W lepton	Remaining lepton passes the W-lepton selection
W transverse mass	$m_{\mathrm{T}}^{W} > 30\,\mathrm{GeV}$

6.2 Kinematic reconstruction of $W^{\pm}Z$ events

In the event selected in data, the four-momentum of the decay leptons can be reconstructed in the laboratory frame. The hard-scattering neutrino is deemed to be the main contributor to missing transverse momentum and so, p_{T}^{ν} is assumed to be equal to $E_{\mathrm{T}}^{\mathrm{miss}}$. Nevertheless, the conservation of the momentum does not allow to reconstruct its longitudinal momentum p_z^{ν}, as the incoming parton longitudinal momentum is only known statistically through the PDF. Knowing the full kinematic information on all decay leptons would make it possible to completely reconstruct the four-momentum of the $W^{\pm}$ and Z bosons allowing to study specifically their kinematic variables. Besides, this would allow boosting all the particles four-momenta from the laboratory frame to the rest frame of one boson or of the $W^{\pm}Z$ system. This will be very useful for polarisation studies as described in Chapter 7.

6.2.1 Analytical p_z^{ν} reconstruction

As a first idea the $W^{\pm}$ boson pole mass M_W can be used as a constraint. The $W^{\pm}$ boson four-momentum $\mathbf{P}_W$, which is also the sum of the four-momenta of the W-lepton $\mathbf{P}_{\ell W}$ and the neutrino $\mathbf{P}_{\nu}$, is normalised by M_W. This yields an equation of which ultimately, the only unknown is p_z^{ν}:

$$\mathbf{P}_W^2 = M_W^2 = \left(\mathbf{P}_{\ell W} + \mathbf{P}_{\nu}\right)^2 \ . \tag{6.3}$$

Neglecting the mass of the leptons, and expressing Eq. (6.3), as a function of energies E, transverse momenta p_{T} and longitudinal momenta p_z, it transforms as

$$\frac{M_W^2}{2} = E^{\ell}E^{\nu} - \mathbf{p}_T^{\ell}\cdot\mathbf{p}_T^{\nu} - p_z^{\ell}p_z^{\nu} \tag{6.4}$$

$$\Leftrightarrow \left(\xi - p_z^{\ell}p_z^{\nu}\right)^2 = E^{\ell 2}E^{\nu 2} = E^{\ell 2}\left({p_T^{\nu}}^2 + {p_z^{\nu}}^2\right) \quad \text{with} \quad \xi = \frac{M_W^2}{2} + \mathbf{p}_T^{\ell}\cdot\mathbf{p}_T^{\nu}\ . \tag{6.5}$$

Simplifying and solving the previous equation brings:

$$p_z^{\nu} = \frac{p_z^{\ell}\xi \pm \sqrt{\Delta}}{{p_T^{\ell}}^2}\ , \tag{6.6}$$

where:

$$\Delta = {p_z^{\ell}}^2\xi^2 - {p_T^{\ell}}^2\left[E^{\ell 2}{p_T^{\nu}}^2 - \xi^2\right]\ . \tag{6.7}$$

If the discriminant Δ is positive, there are two real solutions to this equation and a procedure must be determined to choose the retained p_z^{ν}. In the cases where Δ is negative, no real solution exist, only a complex one. This corresponds to events with an off-shell $W^{\pm}$ boson, having a transverse mass larger than the pole mass $M_W = 80.385\,\text{GeV}$ [70]. The fraction of such events is about 33 %. Several procedures for both cases are described in Ref. [101]. Here, the following procedure is chosen:

- $\Delta > 0$: Take the smallest solution in absolute value.
- $\Delta < 0$: Take the real part of the complex solution.

This *analytical* method for p_z^{ν} reconstruction is characterised by a rather poor resolution for various reasons. First, p_{T} and $E_{\mathrm{T}}^{\mathrm{miss}}$ can be subject to misreconstruction. Moreover, other particles can contribute to $E_{\mathrm{T}}^{\mathrm{miss}}$ beside the hard-scattering neutrino, rendering the approximation $p_{\mathrm{T}}^{\nu} \approx E_{\mathrm{T}}^{\mathrm{miss}}$ less valid. Finally, off-shell $W^{\pm}$ bosons and the procedure for the choice of a p_z^{ν} solution bring further misreconstructions. The previous single boson polarisation measurement [17] used this analytical method for p_z^{ν} reconstruction.

6.2.2 DNN-based p_z^{ν} reconstruction

Another idea is to use a Deep Neural Network (DNN) fed with various kinematic variable of a $W^{\pm}Z$ event to estimate p_z^{ν}. Such DNN was developed to estimate p_z^{ν} using Tensorflow v1.3 [102] with Keras v2.2.4-tf [103] back-end. The DNN was trained on the POWHEG+PYTHIA Monte Carlo sample (see Section 5.3.1) to reconstruct p_z^{ν} using as inputs:

- p_{T} of the W-lepton.
- p_z of the W-lepton.
- the $E_{\mathrm{T}}^{\mathrm{miss}}$ component along the direction of the W-lepton.
- the $E_{\mathrm{T}}^{\mathrm{miss}}$ component perpendicular to the direction of the W-lepton.
- the p_z^{ν} reconstructed with the analytical method described above.

Such input selection encodes the ϕ-rotational symmetry in the detector, leading to a reduction of the number of inputs (five instead of six), a faster training and therefore an overall better performance.

The architecture of the DNN is designed to take into account the $W^{\pm}$ boson mass constraint. This mass m_W is reconstructed with no trainable parameter directly from the input variables and the p_z^{ν} obtained. Then, the loss function used to train the DNN is the sum of the mean squared errors on the neutrino momentum components and the mean squared error on m_W. The target to compute these errors are taken from the true value in the Monte Carlo, including for m_W, making the DNN aware of the natural width of the $W^{\pm}$ boson. This is an advantage compared to the analytical reconstruction method which only knows of the pole mass M_W.

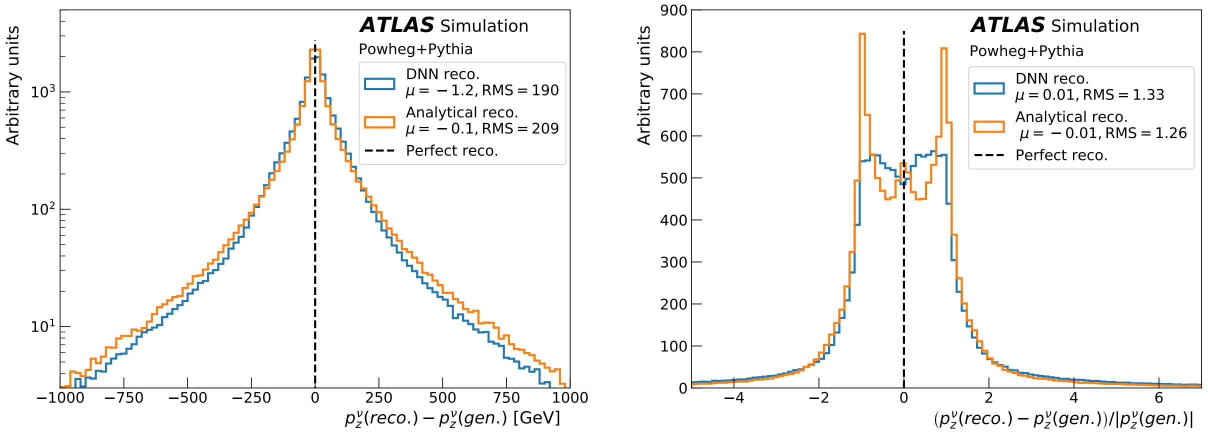

(a) Error **(b)** Resolution

Figure 6.1 Error on p_z^{ν} (a) and the associated resolution (b), as reconstructed by the regression DNN (blue) and analytical method (orange). In the legend, μ notes the mean value and RMS (Root Mean Square) is the standard deviation.

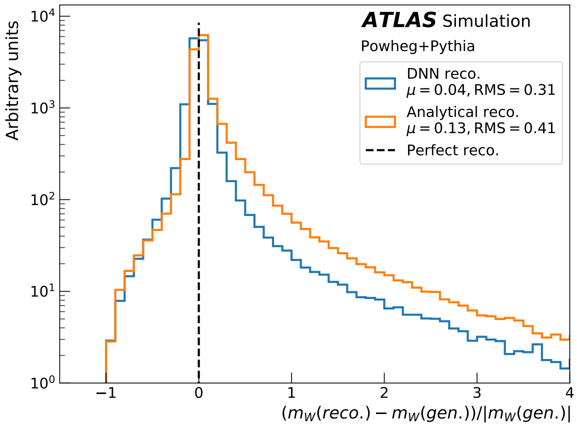

Figure 6.2 Resolution of m_W as reconstructed by the regression DNN (blue) and analytical method (orange). In the legend, μ notes the mean value and RMS (Root Mean Square) is the standard deviation.

The analytical and DNN-based methods applied on the Powheg+Pythia Monte Carlo sample are compared looking at the error and resolution on p_z^{ν} in Fig. 6.1. The DNN regression method is able to give a reasonable estimate of p_z^{ν} for events on which the analytical method fails and provides a 10% decrease of the p_z^{ν} error standard deviation thanks to an improved resolution at high p_z^{ν}. Additionally, the regression method improves the m_W resolution from the value of 41 % obtained with the analytical method to 31 %, as visible in Fig. 6.2. Both methods show no bias.

The polarisation measurement described in Chapter 7 was performed at the reconstructed level on signal only Monte Carlo samples using both methods. As detailed in Appendix C, the central values for the polarisation fractions measured are found to be very similar, but the associated uncertainty is reduced with the DNN-based method. In the following, the baseline p_z^{ν} reconstruction will use this DNN.

6.3 Background estimation

The experimental signature of $W^{\pm}Z$ production in Eq. (5.1) is not unique to this process and some background processes can mimic it. These backgrounds exist in two categories: reducible and irreducible backgrounds. Reducible background processes have a different experimental signature, that is strictly less than three real leptons, but still pass the selection criteria due to fake leptons being reconstructed in the detector. They are reducible in the sense that improvement on the detector understanding or selection criteria can be used to reduce them. Irreducible background processes on the other hand generate three or more leptons. Because of the limited acceptance of the detector, even with perfect reconstruction, some leptons can always be missed. In this sense, these background processes, even with a final state containing more than three charged leptons, can never be fully reduced, hence their name.

6.3.1 Irreducible background estimation

The main irreducible background comes from ZZ production with one lepton escaping detection. This background is reduced by the ZZ veto criteria rejecting events with more than three leptons from the loose *baseline lepton* selection as described in Section 6.1.2. Though greatly reduced, it still constitutes the main background of this analysis. Another important background comes from $t\bar{t}+V$, the production of a top anti-top quark pair along with one electroweak boson V among $W^{\pm}$ and Z bosons. Subdominant backgrounds come from tZ, the production of a top quark with a Z boson, and from VVV, the triple electroweak boson production. Finally, $WZjj-$EW, the $W^{\pm}Z$ production in vector boson scattering is treated as a background as well, mainly because this process is not taken into account in our signal sample for polarisation studies. These backgrounds are estimated through Monte Carlo simulations of which the validity is checked.

The ZZ process is simulated by SHERPA at NLO QCD with up to one additional QCD jet, and at LO with two or three QCD jets. The electroweak vector boson scattering $ZZjj-$EW process is also simulated by SHERPA at LO and added to this ZZ background. A ZZ control region is created with the same selection as the signal region (Table 6.3) only inverting the ZZ veto criteria: four or more baseline leptons are required. The control distributions of m_{T}^{W} in this ZZ control region is shown in Fig. 6.3(a). In this case, a fake $W^{\pm}$ boson candidate is reconstructed from one of the ZZ decay leptons. In this region, the reducible backgrounds are estimated as well with Monte Carlo samples: $t\bar{t}$ and Z+jets with POWHEG+PYTHIA, $Z\gamma$ and $W\gamma$ with SHERPA. The ZZ events represent 88 % of all events in this region and there is agreement of the sum of all Monte Carlo with data within 10 %. As will be described in Section 7.6.3, this control region is incorporated in the polarisation measurement fit, providing an adjustment of the normalisation of this ZZ background.

The $t\bar{t}+V$ background is simulated by merging MADGRAPH samples of $t\bar{t}W$ and $t\bar{t}Z$ processes simulated at NLO in QCD and interfaced to PYTHIA. The validity of this simulation is estimated in a validation region defined adding to the signal region selection of Table 6.3 the requirement of two jets originating from a b-quark[5]. As in the ZZ control

---

[5] The b-quark in B-hadrons does not decay instantaneously and thus b-jets will appear to be created from a secondary vertex a few centimeters away from the primary vertex. This feature is used by algorithms to tag such b-jets.

region, reducible backgrounds are estimated by Monte Carlo samples. In this validation region, the $t\bar{t}+V$ background represents 83 % of all events according to Monte Carlo predictions. After an overall rescale of the $t\bar{t}+V$ background by 1.4, the MC sample sum is found to agree with data. A 15 % overall uncertainty is considered for the total yield of this rescaled sample. This uncertainty allows covering data to Monte Carlo disagreements. This is visible in Fig. 6.3(b) presenting the control distributions of m_{T}^{W}, reconstructed from a possibly fake $W^{\pm}$ boson candidate, in this $t\bar{t}+V$ validation region.

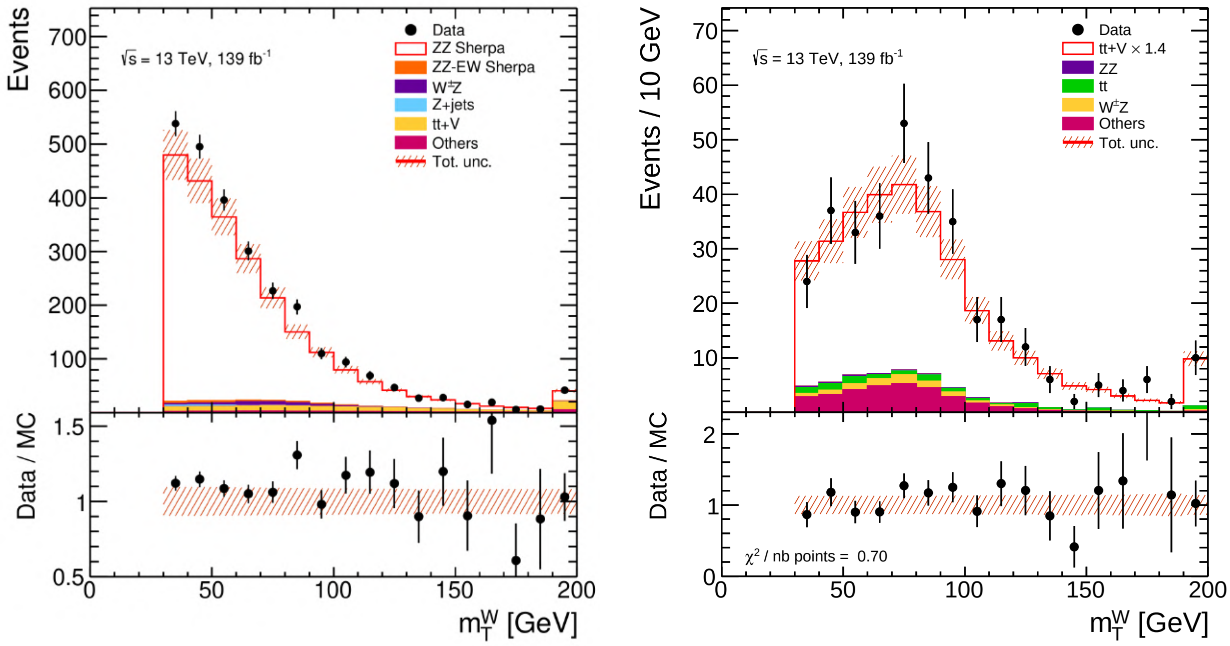

(a) **(b)**

Figure 6.3 Control distribution of m_{T}^{W} in the ZZ control region (a) and in the $t\bar{t}+V$ validation region (b). The composition of both regions are estimated by Monte Carlo scaled to the expected luminosity in Run 2. The dashed red band incorporates a 1.7 % systematic uncertainty on the luminosity [49] and an overall normalisation uncertainty of 10 % for the ZZ sample in (a) and 15 % for the rescaled $t\bar{t}+V$ sample in (b).

The tZ irreducible background is estimated with MadGraph +Pythia and associated to an overall uncertainty of 15 % [104]. The triboson VVV background is simulated with Sherpa and associated to an overall conservative uncertainty of 30 %. The $WZjj-$EW background is simulated by MadGraph+Pythia at LO and associated to an overall uncertainty of 25 %. Also, events from off-shell photons passing the total phase space selection from Eq. (5.8) are treated as signal events. Such events outside of the m_Z mass window can still migrate to the fiducial phase space during reconstruction and thus constitute background. This migrating γ^* background is estimated using the truth information from the Powheg+Pythia inclusive $W^{\pm}Z$ signal sample and associated to a conservative overall uncertainty of 20 %. Finally, some $W^{\pm}Z$ production channel are treated as background as well. These can be from one of the electroweak bosons decaying to a τ lepton, which can in turn decay into an electron or a muon. This background is estimated also with the Powheg+Pythia signal sample truth information removing the cut on the decay lepton flavour. The magnitude of this background is directly linked to the cross section of the $W^{\pm}Z$ production and is therefore subject to a special treatment that will be described in Section 7.1.3.

6.3.2 Reducible background estimation

Reducible backgrounds originate primarily from top quark pair $t\bar{t}$ (with each top quark decaying through a $W^{\pm}$ boson to a b-quark jet and a lepton), $Z\gamma$, $W\gamma$ and Z+jets processes, the jets or photon produced along creating a fake third lepton in the detector. Other reducible backgrounds are arising from Wt and WW processes. Interactions of real leptons in the detector can be simulated, allowing to determine its reconstruction efficiency using a Monte Carlo simulation. The remaining biases in the simulation are then corrected by calibrating the simulation on data using well known physics processes. However, estimating the probability to reconstruct a fake lepton is badly simulated. Thus, data driven methods are needed to estimate reducible backgrounds from misidentified leptons. In this analysis, a method called the Matrix Method [17, 105, 106] is used.

6.3.2.1 Principle of the Matrix Method

Signal events are characterised by three lepton candidates. In the following they are ordered in subscripts: first the $W^{\pm}$ boson decay lepton, second the Z boson decay lepton of leading p_{T} and third the Z boson decay lepton of sub-leading p_{T}. The starting point of the Matrix Method is to consider each lepton candidate as created either by:

- a real lepton (R): any lepton produced by the decay of a $W^{\pm}$ or a Z boson.
- a fake lepton (F): leptons within a hadronic jet, light jets or leptons from photon conversion faking a lepton in the detector.

Of course, the true nature of a candidate is inaccessible from the experimental side. A selection of so-called Matrix Method leptons is defined in Table 6.4. On the one hand, this selection is a bit tighter than the baseline lepton selection for p_{T} cut, $|\eta|$ region and identification working point. On the other hand, no isolation criteria or overlap removal is considered to enrich the selection in fake leptons. It should be noted as well that the W-lepton or Z-lepton criteria are strictly contained within this Matrix Method selection. As such, leptons are classified in two selection levels:

- Tight leptons (T): signal leptons selected as W-lepton for the first one, Z-leptons for the second and third, as described in Tables 6.2 and 6.1.
- Loose leptons (L): leptons passing the Matrix Method selection summarised in Table 6.4 and failing the tight selection.

Eight disjoint regions of three lepton events are created with corresponding yields N_{TTT}, N_{TTL}, N_{TLT}, N_{LTT}, N_{TLL}, N_{LTL}, N_{LLT}, and N_{LLL}. On an event-by-event basis, the selection criteria for electron or muon is used for both L and T selections.

Similarly, events can be split in eight truth categories depending on the true nature of the lepton candidate: N_{RRR} events correspond to $W^{\pm}Z$ signal events or irreducible backgrounds as described in Section 6.3.1, N_{FRR} events have the W-lepton from fake origin but real Z-leptons, and so on. To relate selection categories and truth categories two probabilities are defined:

- $e = \mathbb{P}(T|R)$ the probability for a real lepton to pass the tight selection, also known as the efficiency of the selection.
- $f = \mathbb{P}(T|F)$ the probability for a fake lepton to pass the tight selection.

Table 6.4 Selection of Matrix Method leptons. These are fundamental requirements on all leptons considered in the Matrix Method. Loose leptons pass this selection but fail the signal requirements, tight leptons pass in addition the signal lepton selection cuts.

Electrons	Muons
$\lvert d_0/\sigma(d_0)\rvert < 5$	$\lvert d_0/\sigma(d_0)\rvert < 3$
$\lvert \Delta z_0 \sin\theta\rvert < 0.5$ mm	$\lvert \Delta z_0 \sin\theta\rvert < 0.5$ mm
$\lvert\eta\rvert < 2.47$	$\lvert\eta\rvert < 2.7$
Exclude $1.37 < \lvert\eta\rvert < 1.52$	-
$p_{\mathrm{T}} > 15\,\mathrm{GeV}$	$p_{\mathrm{T}} > 15\,\mathrm{GeV}$
`Loose` Identification	`Medium` Identification

The complementary probability $1-e$ (resp. $1-f$) is noted $\bar{e}$ (resp. $\bar{f}$). These probabilities depend on the lepton type and thus will be tagged in the following with an index associated to the position of the lepton in the order defined above. The category with three fake leptons is expected to have a negligible yield N_{FFF}, and is not considered in the following. Symmetrically, the LLL selection category is not used. Selection categories and truth categories are thus related by the 7×7 matrix

$$\begin{pmatrix} N_{TTT} \\ N_{TTL} \\ N_{TLT} \\ N_{LTT} \\ N_{TLL} \\ N_{LTL} \\ N_{LLT} \end{pmatrix} = \begin{pmatrix} e_1e_2e_3 & e_1e_2f_3 & e_1f_2e_3 & f_1e_2e_3 & e_1f_2f_3 & f_1e_2f_3 & f_1f_2e_3 \\ e_1e_2\bar{e}_3 & e_1e_2\bar{f}_3 & e_1f_2\bar{e}_3 & f_1e_2\bar{e}_3 & e_1f_2\bar{f}_3 & f_1e_2\bar{f}_3 & f_1f_2\bar{e}_3 \\ e_1\bar{e}_2e_3 & e_1\bar{e}_2f_3 & e_1\bar{f}_2e_3 & f_1\bar{e}_2e_3 & e_1\bar{f}_2f_3 & f_1\bar{e}_2f_3 & f_1\bar{f}_2e_3 \\ \bar{e}_1e_2e_3 & \bar{e}_1e_2f_3 & \bar{e}_1f_2e_3 & \bar{f}_1e_2e_3 & \bar{e}_1f_2f_3 & \bar{f}_1e_2f_3 & \bar{f}_1f_2e_3 \\ e_1\bar{e}_2\bar{e}_3 & e_1\bar{e}_2\bar{f}_3 & e_1\bar{f}_2\bar{e}_3 & f_1\bar{e}_2\bar{e}_3 & e_1\bar{f}_2\bar{f}_3 & f_1\bar{e}_2\bar{f}_3 & f_1\bar{f}_2\bar{e}_3 \\ \bar{e}_1e_2\bar{e}_3 & \bar{e}_1e_2\bar{f}_3 & \bar{e}_1f_2\bar{e}_3 & \bar{f}_1e_2\bar{e}_3 & \bar{e}_1f_2\bar{f}_3 & \bar{f}_1e_2\bar{f}_3 & \bar{f}_1f_2\bar{e}_3 \\ \bar{e}_1\bar{e}_2e_3 & \bar{e}_1\bar{e}_2f_3 & \bar{e}_1\bar{f}_2e_3 & \bar{f}_1\bar{e}_2e_3 & \bar{e}_1\bar{f}_2f_3 & \bar{f}_1\bar{e}_2f_3 & \bar{f}_1\bar{f}_2e_3 \end{pmatrix} \begin{pmatrix} N_{RRR} \\ N_{RRF} \\ N_{RFR} \\ N_{FRR} \\ N_{RFF} \\ N_{FRF} \\ N_{FFR} \end{pmatrix} . \tag{6.8}$$

This is a system of seven equations with seven unknowns as the truth categories yields. The goal is to estimate events in the TTT category that are not from real leptons

$$N_{fakes} = N_{TTT} - e_1e_2e_3N_{RRR} \,. \tag{6.9}$$

The system can be solved for this N_{fakes}, applying to the first equation of the system a linear combination of the others and rearranging the terms:

$$\begin{aligned} N_{fakes} = {} & [N_{TTL} - e_1e_2\bar{e}_3N_{RRR}]\frac{f_3}{\bar{f}_3} + [N_{TLT} - e_1\bar{e}_2e_3N_{RRR}]\frac{f_2}{\bar{f}_2} + [N_{LTT} - \bar{e}_1e_2e_3N_{RRR}]\frac{f_1}{\bar{f}_1} \\ & -[N_{TLL} - e_1\bar{e}_2\bar{e}_3N_{RRR}]\frac{f_2}{\bar{f}_2}\frac{f_3}{\bar{f}_3} - [N_{LTL} - \bar{e}_1e_2\bar{e}_3N_{RRR}]\frac{f_1}{\bar{f}_1}\frac{f_3}{\bar{f}_3} - [N_{LLT} - \bar{e}_1\bar{e}_2e_3N_{RRR}]\frac{f_1}{\bar{f}_1}\frac{f_2}{\bar{f}_2} + \mathcal{O}\left(f^3\right) . \end{aligned} \tag{6.10}$$

A term like $e_1e_2\bar{e}_3N_{RRR}$ corresponds in fact to events with real leptons in the TTL loose selection category. Thus $N_{TLL} - e_1\bar{e}_2\bar{e}_3N_{RRR} = N^{red.}_{TLL}$ is the number of events from fake lepton origin in the TTL category. All other similar terms can be rewritten the same way. Additionally, the factors with index 2 and 3 both correspond to Z-lepton and should be the same as they correspond to the same selection criteria, while index 1 corresponds to W-leptons. Fake Factors are defined as

$$F_W = \frac{f_1}{\bar{f}_1} \,, \tag{6.11}$$

$$F_Z = \frac{f_2}{\bar{f}_2} = \frac{f_3}{\bar{f}_3} \,, \tag{6.12}$$

and thus Eq. (6.10) can be rewritten:

$$N_{fake} = N^{red.}_{TTL}F_Z + N^{red.}_{TLT}F_Z + N^{red.}_{LTT}F_W - N^{red.}_{TLL}F_ZF_Z - N^{red.}_{LTL}F_WF_Z - N^{red.}_{LLT}F_WF_Z. \tag{6.13}$$

The yields in the loose selection categories are easily accessible in data. Consequently, the last ingredient left to determine are the Fake Factors.

6.3.2.2 Estimation of the Fake Factors

The Fake Factors are estimated in control regions orthogonal to the signal region and designed to select one fake lepton. The probability f is then the fraction of these events that pass the tight selection and the fake factor is simply the ratio of event passing the tight selection to events failing it.

Three control regions are designed each targeting one type of reducible background: the Z+jets region, the $t\bar{t}$ region and the $V+\gamma$ region. First, all signal region selection criteria of Table 6.3 are followed, up to the ZZ veto criteria which is replaced by the requirement for at least three Matrix Method leptons. A Z-lepton pair is selected with certain criteria on charge, flavour and invariant mass and the third lepton ℓ_F selected is the highest p_{T} Matrix Method lepton. The control regions are designed so that ℓ_F is from fake origin. The selection criteria for each control region are summarised in Table 6.5. These control regions are orthogonal to the signal region thanks to the reversed m_{T}^{W} cut or the charge and flavour selection of the leptons. They are also disjoint between each other.

Z+jets		$V+\gamma$	$t\bar{t}$
e^+e^-, $\mu^+\mu^-$ Z-lepton		$\mu^+\mu^-$ Z-lepton	$e^+\mu^-$, $e^-\mu^+$ Z-lepton
ℓ_F is a e $m_{\mathrm{T}}^{W} < 30\,\mathrm{GeV}$ $85\,\mathrm{GeV} < m_{\ell_Z\ell_Z} < 106\,\mathrm{GeV}$ $E_{\mathrm{T}}^{\mathrm{miss}} < 30\,\mathrm{GeV}$	ℓ_F is a μ $m_{\mathrm{T}}^{W} < 30\,\mathrm{GeV}$ $76\,\mathrm{GeV} < m_{\ell_Z\ell_Z} < 106\,\mathrm{GeV}$ -	ℓ_F is a e $m_{\mathrm{T}}^{W} < 30\,\mathrm{GeV}$ $55\,\mathrm{GeV} < m_{\ell_Z\ell_Z} < 85\,\mathrm{GeV}$ $E_{\mathrm{T}}^{\mathrm{miss}} < 30\,\mathrm{GeV}$ $m_{3\ell} < 105\,\mathrm{GeV}$	ℓ_F is same flavour same charge of an ℓ_Z ℓ_Z opposite flavour opposite charge of ℓ_F passes W-lepton selection

Table 6.5 Selection criteria in the three control regions used for Fake Factor estimation. For each, a pair $\ell_Z\ell_Z$ of Z-leptons is selected and a third ℓ_F lepton candidate from fake origin is selected.

To account for the p_{T} dependence of Fake Factors, each control region is additionally split in four bins of p_{T} of the fake lepton candidate. In each control region and in each p_{T} bin, the irreducible background is subtracted and a tight selection is applied, for W-lepton or Z-lepton, for muons or electrons. In each case, the proportion of fake leptons passing the tight selection allows to compute the Fake Factor. For example in Fig. 6.4, Fake Factors are estimated in data and Monte Carlo in the Z+jets control region. Furthermore, an $|\eta|$ dependence of the Fake Factors is also observed, as shown in Fig. 6.5. A parabolic fit of this dependence is used to correct event-by-event the Fake Factors.

Each control region emphasises a certain type of fake origin between photon conversion (PC), light-flavour jets (LF) and non-prompt lepton in heavy-flavour jets (HF). The proportion $f_{\text{fake origin}}^{\text{control region}}$ of each fake origin in each control region can be determined by Monte Carlo simulation. The control region specific Fake Factors can be transformed in fake origin specific Fake Factors by inverting the matrix

$$\begin{bmatrix} F_V^{Z+jets} \\ F_V^{t\bar{t}} \\ F_V^{V+\gamma} \end{bmatrix} = \begin{bmatrix} f_{\mathrm{HF}}^{Z+jets} & f_{\mathrm{LF}}^{Z+jets} & f_{\mathrm{PC}}^{Z+jets} \\ f_{\mathrm{HF}}^{t\bar{t}} & f_{\mathrm{LF}}^{t\bar{t}} & f_{\mathrm{PC}}^{t\bar{t}} \\ f_{\mathrm{HF}}^{V+\gamma} & f_{\mathrm{LF}}^{V+\gamma} & f_{\mathrm{PC}}^{V+\gamma} \end{bmatrix} \begin{bmatrix} F_V^{\mathrm{HF}} \\ F_V^{\mathrm{LF}} \\ F_V^{\mathrm{PC}} \end{bmatrix}, \tag{6.14}$$

with $V \in \{W, Z\}$. This procedure has to be performed for W-leptons and Z-leptons, per lepton flavour and per p_{T} bin to provide fake origin Fake Factors in all cases.

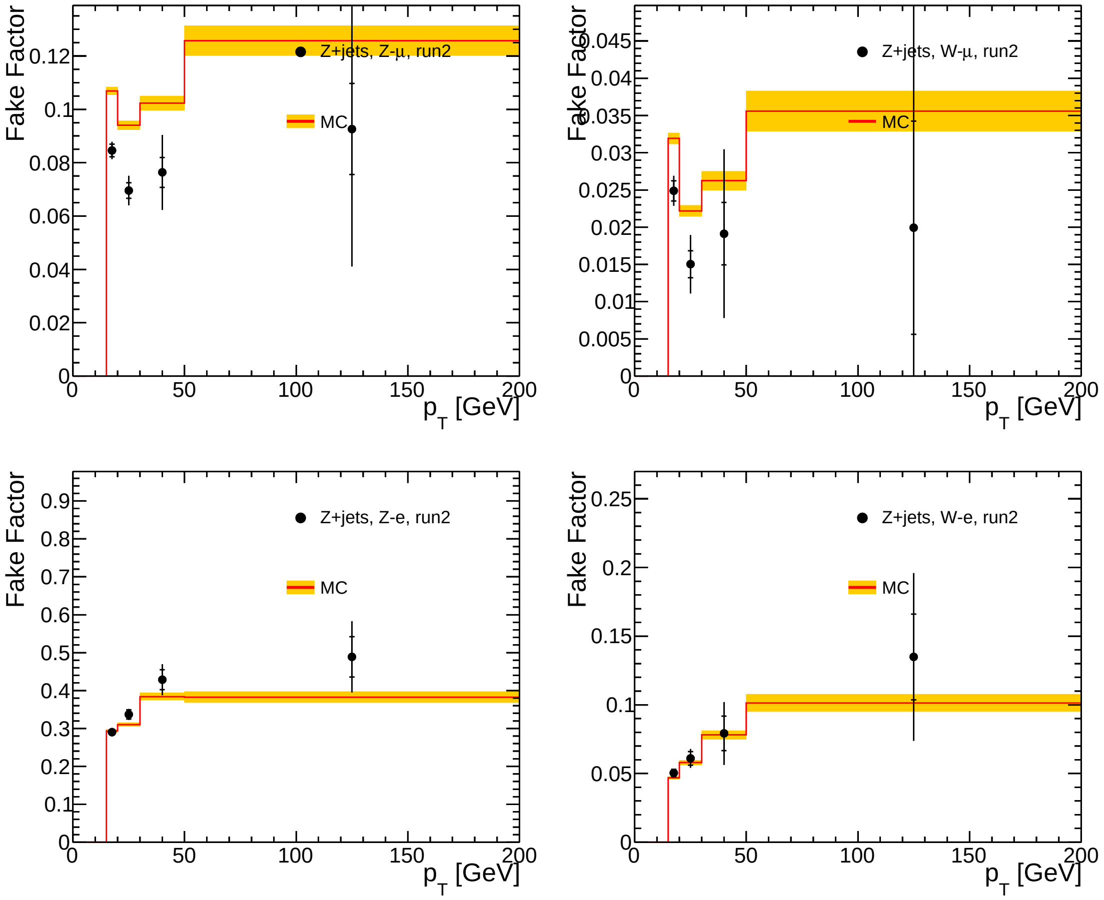

Figure 6.4 Fake Factor results in the Z+jets control region as a function of p_{T} for fake electrons (top) and fake muons (bottom) passing the Z-lepton (left) or W-lepton (right) selection. The results or represented for data (black dots) and Monte Carlo (red histogram). Uncertainties contain statistical uncertainties and systematic uncertainties originating from the subtraction of the irreducible background events from the control region.

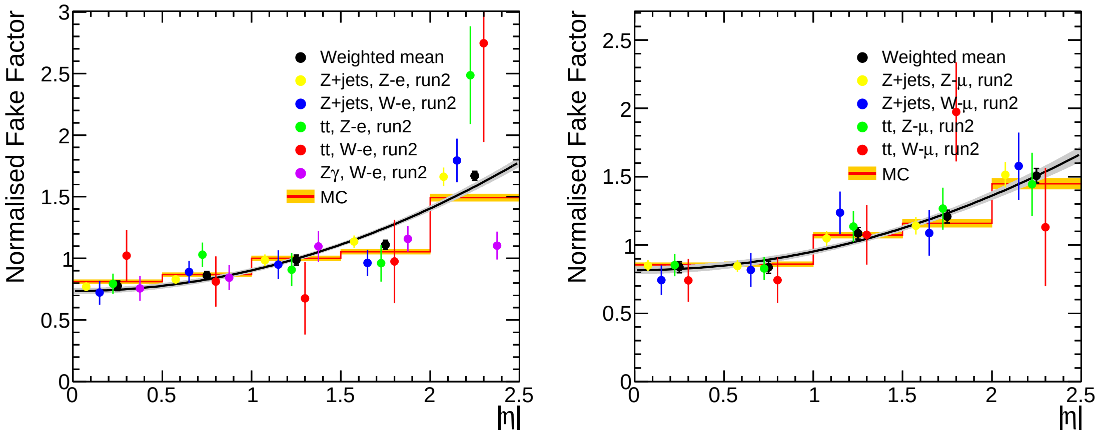

Figure 6.5 Fit of a parabolic function to the weighted mean (black dot) of normalised Fake Factors in bins of $|\eta|$ from the different control regions and for W-leptons and Z-leptons. Electrons and muons are treated separately and displayed on the left and right, respectively. For the representation, x-values of Fake Factors from different control regions (coloured dots) are displaced inside the bin. The shaded band around the fit result displays its 68 % confidence interval. Total uncertainties are displayed.

6.3.2.3 The Matrix Method background estimation

Finally, to apply Eq. (6.13), the fake origin proportion has to be estimated in all loose signal regions in a p_{T} dependent way. Then, for each event of each loose category, a Fake Factor from one fake origin is chosen randomly, reflecting the fake origin composition of this loose signal region. To summarise, in addition to a given fake origin, the chosen Fake Factor must also correspond to

- the lepton selection criteria failed (F_W or F_Z),
- the loose lepton candidate flavour (electron or muon),
- the loose lepton candidate p_{T} bin,
- and be corrected for the loose lepton candidate $|\eta|$ with the fitted parabolic function.

In the estimation of the misidentified leptons background with Eq. (6.13), uncertainties can affect the Fake Factors estimations or the $N^{red.}_{XXX}$ reducible loose signal region yields. The limited data in the loose signal regions translates in a statistical uncertainty on the estimated background. Then, systematic uncertainties are estimated, originating from:

- uncertainties on the estimation of the real leptons events (e.g. ZZ and WZ events) subtracted from the control regions. Their final contribution is labelled in the final fit `IrrSub`.
- statistical uncertainties in the control region samples affecting the determination of the fake factors F_V. They are labelled in the final fit `FFstat`.
- an uncertainty in the $F_V(|\eta|)$ parabolic correction labelled in the final fit `EtaCorr`.
- an uncertainty in the flavour composition of the loose signal regions labelled in the final fit `FlavorComp`.
- an uncertainty in the flavour Fake Factors due to uncertainty in the flavour composition of control regions labelled in the final fit `FFFlavorComp` .

Finally, the Matrix method can be compared to an independent alternative method, called MC scale factor method, where Monte Carlo samples for Z+jets, $Z\gamma$ and $t\bar{t}$ backgrounds are rescaled to data. The misidentified lepton background from the Matrix Method is compared to the sum of these rescaled Monte Carlo samples in bins of the variables m_{T}^{W} and m_Z in Fig. 6.6. The Matrix Method estimate is represented with its total uncertainty, including the systematic effect described above. The MC scale factor method estimate is found to agree with the Matrix Method estimate within its total uncertainty across all bins of both variables. The Matrix Method is therefore validated and will be used as baseline to estimate the background from misidentified leptons.

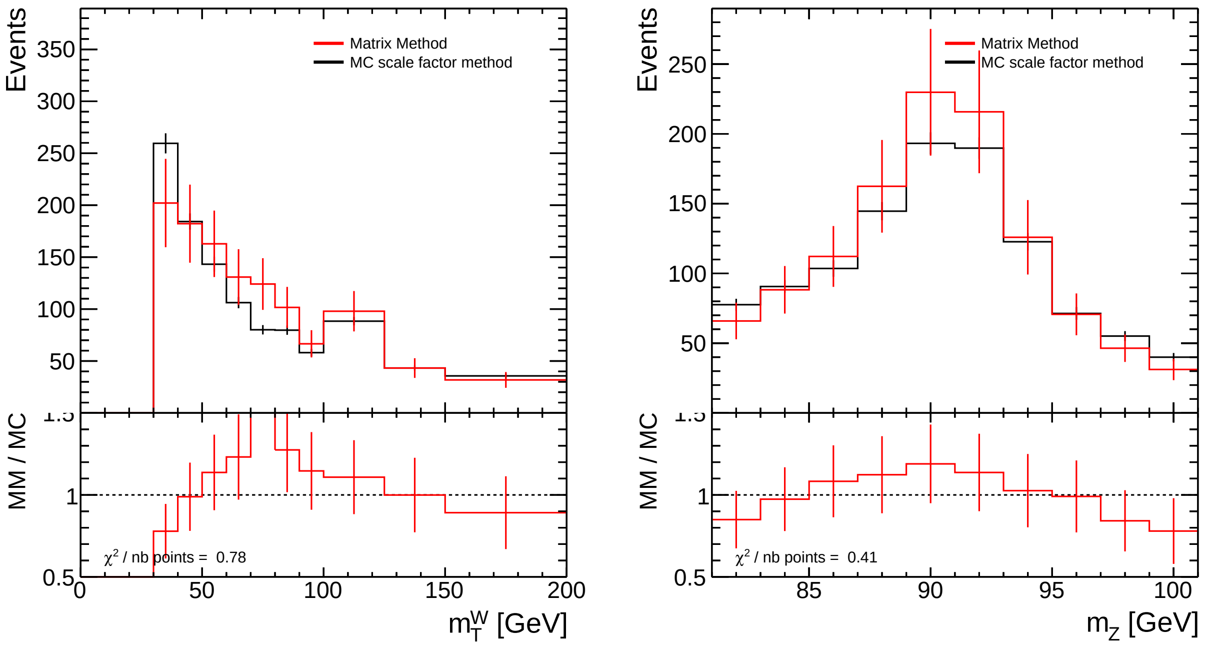

(a) (b)

Figure 6.6 Comparisons between distributions of the reducible background estimated by the MC scale factor method and by the Matrix Method, for the m_T^W (a) and m_Z (a) observables. Uncertainties are statistical only for the MC scale factor estimate, and from statistical and systematic origin for the Matrix Method estimate.

6.4 $W^{\pm}Z$ signal yield results

The selection on data presented in Section 6.1 and the estimation of signal and backgrounds presented in sections 5.3.1 and 6.3 respectively make it now possible to check the agreement of data to predictions. A cross section measurement was performed in Ref. [17] with a subset of the LHC Run 2 data, so no major discrepancies are expected; this is really a way to check the validity of the predictions.

In Table 6.6 the total event yields in both data and Monte Carlo are given for $W^{\pm}Z$ events per leptonic decay channel and in total. The uncertainties are only statistical. The row labelled WZ corresponds to the Powheg+Pythia prediction scaled to the NNLO prediction of [73] (see Section 5.3.1 for details) and including $W^{\pm}Z$ leptonic decays to electrons and muons, and the background from the decay to τ-leptons reconstructed as an electron or a muon. All reducible backgrounds are estimated with the Matrix Method and collectively labeled *Misidentified leptons*. The last two rows show a correct agreement of data to prediction within 5 % across all leptonic decay channels. The signal to background ratio is for all decay channel of 4.14. The same conclusion holds separating events by the charge of the $W^{\pm}$ boson, with a signal to background ratio of 4.64 and 3.55 for $W^{+}Z$ and $W^{-}Z$ events respectively.

Looking at event yields in bins of a kinematic variable produces a control distribution of this variable. This is done for the Z boson p_T, reconstructed from the four-momentum of the reconstructed decay Z-lepton pair, in Fig. 6.7(a). Similarly, this is done for the $W^{\pm}$ boson p_T in Fig. 6.7(b), with the extra step of reconstructing the p_z^{ν} with the DNN-based method presented in Section 6.2. Systematic uncertainties are from overall uncertainties

Channel	eee	$e\mu\mu$	μee	$\mu\mu\mu$	All
Data	3955	5895	4600	7486	21936
Total Expected	3843.8 ± 10.7	5618.0 ± 11.8	4693.1 ± 11.0	7310.1 ± 12.9	21464.9 ± 23.3
$W^{\pm}Z$	2991.0 ± 8.2	4431.3 ± 10.0	3874.5 ± 9.3	5993.6 ± 11.6	17290.4 ± 19.7
Total Bkg.	852.7 ± 7.0	1186.7 ± 6.4	818.6 ± 5.9	1316.5 ± 5.7	4174.6 ± 12.5
ZZ	274.1 ± 1.8	409.3 ± 2.2	277.4 ± 1.7	444.2 ± 2.3	1405.0 ± 4.0
Misid. leptons	289.3 ± 6.6	367.2 ± 5.8	182.9 ± 5.5	342.3 ± 4.9	1181.7 ± 11.5
$t\bar{t} + V$	160.7 ± 1.1	224.9 ± 1.3	196.9 ± 1.2	288.2 ± 1.5	870.7 ± 2.6
tZ	69.2 ± 0.4	100.7 ± 0.4	86.1 ± 0.4	131.7 ± 0.5	387.7 ± 0.9
$W^{\pm}Zjj$	51.0 ± 0.3	72.5 ± 0.4	64.8 ± 0.3	95.4 ± 0.4	283.6 ± 0.7
VVV	8.3 ± 0.1	12.2 ± 0.2	10.5 ± 0.2	14.8 ± 0.2	45.7 ± 0.3
(Data-MC)/MC [%]	2.89	4.93	−1.98	2.41	2.19
S/B	3.51	3.73	4.73	4.55	4.14

Table 6.6 Summary of observed and expected yields for $W^{\pm}Z$ in each leptonic decay channel of the analysis and for the sum of all channels. Only statistical uncertainties on the observed number of events and Monte Carlo samples are included. The ZZ contribution includes both ZZ inclusive and $ZZjj$−EW processes. The row labelled “S/B” corresponds to the signal over background ratio, as calculated using the expected number of events.

on irreducible background predictions (see Section 6.3.1) and systematic uncertainties of the Matrix Method for the misidentified lepton background (see Section 6.3.2). A good agreement between data and prediction is observed in the shapes of the distributions, as well as in the expected number of events.

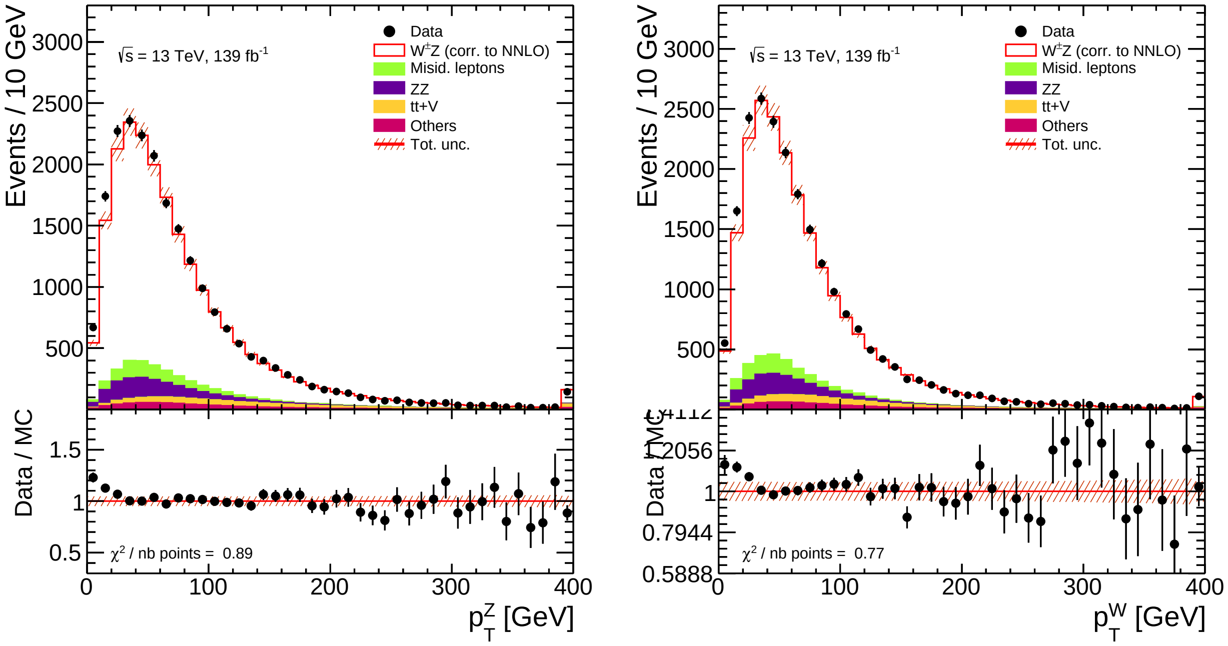

(a) **(b)**

Figure 6.7 Control distributions of the $W^{\pm}$ boson p_{T} (b) and of the Z boson p_{T} (a). All Monte Carlo expectations are scaled to the integrated luminosity of the data using the predicted Monte Carlo cross sections of each sample. The dashed red band represents the quadrature sum of all systematic uncertainties on the total Monte Carlo expectation (see text for details) and a 1.7 % systematic uncertainty on the luminosity [49].

Chapter 7

Polarisation measurement

From Run 2 data, $W^{\pm}Z$ events were selected and reconstructed as described in Chapter 6. In Section 6.4, the signal and background processes are found to be modelled correctly enough, as seen in the control distributions of Fig. 6.7 or the event yields in Table 6.6. It is now possible to target the final goal of the analysis described in this thesis: the study in data of polarisation in $W^{\pm}Z$ production. As detailed in Chapter 5, the parameters that will be measured, and of which theoretical predictions are available, are the single boson polarisation fractions and the joint-polarisation fractions. The latter two represent the primary goal as they have never been measured in diboson processes.

The main challenge is to measure the longitudinal-longitudinal 00 joint-polarisation fractions of $W^{\pm}Z$ bosons f_{00}, as this configuration is deemed to represent the smallest contribution in the inclusive $W^{\pm}Z$ events. Besides, f_{00} is of particular theoretical interest as many beyond the Standard Model effects can manifest themself in the 00 configuration. Another challenge will be to distinguish between the $f_{0\mathrm{T}}$ and the $f_{\mathrm{T}0}$ fractions, the first index corresponding to the $W^{\pm}$ boson polarisation, the second index to the Z boson polarisation.

In addition, the single boson polarisation fractions f_0, f_{L} and f_{R} will be measured on the full Run 2 data. This will improve the previous measurement [17] that used only a partial dataset recorded during the first two years of Run 2 with $36\,\mathrm{fb}^{-1}$ of integrated luminosity. More interestingly, it is possible from the joint-polarisation fractions to extract the single boson polarisation fractions allowing to test the consistency of both measurements. Furthermore, the correlation of the fractions between both bosons can be studied.

The polarisation and joint-polarisation fractions will be extracted from data through a binned maximum-likelihood template fit, described in Section 7.1. As a result, template distributions of a discriminating variable for all single boson polarisation or joint-polarisation states are needed at the detector level.

The template fit requires a good discriminating variable at the detector level. For joint-polarisation states, the angular variables mentioned in Chapter 5 are found to provide a moderate discriminating power. Therefore, a composite variable is designed in Section 7.2 using machine learning techniques to obtain an optimised discriminating variable.

The other critical point for the template fit is the accuracy of the detector level templates used. As presented in Section 5.1, direct theoretical calculations show the importance of having polarisation predictions at least at NLO in QCD. A first idea is to use the theoretical description in term of differential cross section described in Section 5.2 to obtain an analytical reweighting procedure. This method that I developed and adapted to joint-polarisation states, transforms inclusive Monte Carlo samples in samples for a given polarisation state, as described in Section 7.3. Using an inclusive Monte Carlo sample at NLO in QCD would therefore provide NLO accurate reconstructed level polarisation templates.

Other methods were developed using as starting point the polarised Monte Carlo generation MadGraph0,1j@LO described in Section 5.3.2. The polarised samples `MGgen` obtained this way are nevertheless not fully NLO accurate. Various methods described in Section 7.4 use the polarisation information of `MGgen` to generate NLO accurate polarised samples.

The choice of polarisation templates NLO in QCD accurate is a crucial step to avoid a biased measurement, as described in Section 7.5. In a study performed on NLO in QCD inclusive pseudo-datasets, one set of polarisation templates was found to be the least biased.

To finalise the template fit, uncertainties from various origins had to be implemented, as described in Section 7.6. In particular, modelling uncertainties associated to the generation and choice of NLO accurate polarisation templates constitute the main uncertainty and were the object of special care.

Finally, the result of the various template fits performed is presented in Section 7.7. The joint-polarisation fractions measured values in $W^{\pm}Z$ events, along with the separated $W^{+}Z$ and $W^{-}Z$ events, are presented. As side measurements, single boson polarisation fractions and the inclusive cross section of the $W^{\pm}Z$ production is obtained with improved uncertainty compared to Ref. [17]. The consistency of all fits is also checked and the impact of correlations between bosons polarisation is highlighted.

7.1 Binned Likelihood template fit

The stated goal of the measurement is to extract joint-polarisation and single boson polarisation fractions from data through a binned likelihood template fit [107]. In previous sections, two very distinct things have been studied. On the one hand, careful selection of events on Run 2 data provides a dataset designed to optimise the signal over background ratio. On the other hand, the signal and backgrounds are modelled from theoretical predictions. The template fit brings both together to measure polarisation fractions from data.

7.1.1 Principle of binned likelihood fit

In a simplified physics analysis with a designed measurement region, S signal and B background events are simulated, to be compared to the N data events obtained. Of course, it is impossible to know the exact repartition of the data events among signal and backgrounds. Besides, the N data events are subject to statistical fluctuations. In the context of particle physics at the LHC, as exemplified by Fig. 1, the physically interesting events represent at most one in ten millions of inelastic pp collisions. The selected data events thus qualify as very rare events and are modelled by a Poisson law. Consequently, the level of agreement between data and the simulated theoretical prediction is assessed by the Poisson probability

$$\mathcal{P}\left(N|S+B\right) = \frac{(S+B)^N}{N!}e^{-(S+B)} \ . \tag{7.1}$$

Then, a parameter of interest μ can be introduced to rescale the signal prediction, making the new theoretical prediction $\mu S + B$. The initial value of μ is one, but it is allowed to change to improve the agreement with data. Shifting the focus from the obtained data to the parameter μ, one can define the likelihood function for the N observed data events

$$L(\mu; N) = \mathcal{P}\left(N|\mu S+B\right) \ . \tag{7.2}$$

The idea of the fit is to find the value $\hat{\mu}$ that maximises this likelihood. However, in statistics, a value alone is worthless without an associated uncertainty. To obtain this, the probability distribution of the likelihood is necessary. In fact, a test statistic $t(\mu)$ can be designed as:

$$t(\mu; N) = -2\log\left(\frac{L(\mu; N)}{L(\hat{\mu}; N)}\right) \ . \tag{7.3}$$

By definition of $\hat{\mu}$, $t(\mu; N)$ is a positive function of μ that reaches zero only at $\mu = \hat{\mu}$. One could still by brute force estimate the distribution of this statistic with toy simulations. More interestingly, from Wilks approximation [107], this statistic follows asymptotically in N a χ^2 distribution with one degree of freedom. From there, the value of the test statistic t_{μ_0} for a chosen μ_0 becomes an estimate of how likely we were to observe N data events under the hypothesis $\mu = \mu_0$, with of course the hypothesis maximising the likelihood of the data being $\mu = \hat{\mu}$. More quantitatively, the p-value can be defined as

$$p = \int_{t_{\mu_0}}^{+\infty} \chi^2\left(t\right) dt \ , \tag{7.4}$$

integrating on the tail of the χ^2 distribution with one degree of freedom.

In a frequentist approach, no statement is ever made on the plausibility of an hypothesis against others. The likelihood of data under different hypothesis is what is studied using p-values, with the prescription that hypothesis with an associated p-value too low will be rejected. The threshold at which an hypothesis is rejected is an arbitrary value highly dependent on the scientific field. In particle physics, this threshold is traditionally set at a p-value of 2.87×10^{-7}. Below, it is possible to reject a null hypothesis, typically a background only hypothesis, and claim a discovery. This value corresponds to the probability of a gaussian random variable to be found at least five standard deviations σ above its mean. Symmetrically, a p-value can always be converted in this intuitive representation in term of number of standard deviations, called significance. Thus, a discovery requires a significance above $5\,\sigma$.

The simple description above, with one bin of N events described by one signal S and backgrounds B must be generalised to the actual template fit performed to extract polarisation and joint-polarisation fractions. For simplicity, the joint-polarisation measurement will be described here. First, there are in fact several signals each associated to a pure joint-polarisation state S^{00}, $S^{0\mathrm{T}}$, $S^{\mathrm{T}0}$ and S^{TT}, associated to their respective normalisation parameter μ. A single bin is not enough to evaluate simultaneously all four μ, as an infinite number of configurations for the μ values would allow fitting the N data events. This degeneracy is lifted using the histogram of a discriminating variable. The data yield in each bin b becomes n_b, and the signals and backgrounds are replaced by histograms S_b and B_b. The signal histograms are polarisation templates supposed to represent the event distribution of the discriminating variable for a given pure polarisation state. The likelihood becomes therefore

$$L(\mu_{00}, \mu_{0\mathrm{T}}, \mu_{\mathrm{T}0}, \mu_{\mathrm{TT}}) = \sum_b \mathcal{P}\left(n_b | \mu_{00} S_b^{00} + \mu_{0\mathrm{T}} S_b^{0\mathrm{T}} + \mu_{\mathrm{T}0} S_b^{\mathrm{T}0} + \mu_{\mathrm{TT}} S_b^{\mathrm{TT}} + B_b\right) \,. \tag{7.5}$$

It should be noted that the four μ are fully correlated across all bins of the histogram. A good discriminating variable, able to properly distinguish the four signal polarisation template, will therefore allow the extraction of the four μ simultaneously.

For now, no systematic uncertainty is considered; their treatment will be introduced in Section 7.6. The likelihood is thus solely a function of four parameters of interests. The template fit will maximise this likelihood yielding the maximum likelihood estimates $\hat{\mu}_{00}$, $\hat{\mu}_{0\mathrm{T}}$, $\hat{\mu}_{\mathrm{T}0}$ and $\hat{\mu}_{\mathrm{TT}}$. The test statistic adapted from Eq. (7.3) is thus a four parameter function that will asymptotically follow a χ^2 distribution with four degrees of freedom.

It is however possible to reduce the dimensionality of the likelihood by defining the *profiled* likelihood as $L\left(\mu, \hat{\hat{\theta}}(\mu)\right)$, where the $\hat{\hat{\theta}}(\mu_0)$ are the profiled values of the other parameters of the likelihood, that is their maximum likelihood estimate under the hypothesis that the non-profiled parameter $\mu = \mu_0$. The profiled likelihood is thus a single parameter function. The profiled likelihood ratio defined in analogy with Eq. (7.3) will then asymptotically follow a χ^2 distribution with one degree of freedom.

7.1.2 Parametrisation of the template fit

The binned likelihood template fit makes use of pure polarisation templates of a given discriminating variable. These templates are used to fit the event distribution in data of the discriminating variable. This is practically implemented using the `HistFactory` package [108] based on the `RooFit` statistical tools framework [109]. However, the simple description with four signals and their associated normalisation factor μ misses the specificity of polarisation fractions: their normalisation relation (1.48) and (1.53) for single boson polarisation and joint-polarisation respectively.

Therefore, the fit is parameterised such that the polarisation fractions can be extracted directly from the fit result taking into account this normalisation. For this, the simultaneous normalisation of all the templates will be absorbed by one parameter of interest, $N_{\mathrm{tot}}^{\mathrm{fit}}$ representing the total number of $W^{\pm}Z$ signal events. In parallel, the polarisation fractions, taking into account the normalisation relationship, will be affected by shape effects to adjust the proportion of each template. In single boson polarisation measurements, these fractions of interest are f_0, and the left and right polarisation difference $f_{\mathrm{L}} - f_{\mathrm{R}}$. The link between the parameters of interest and the normalisation factor μ_i with $i \in \{0, R, L\}$ is:

$$\mu_0 = \frac{f_0 \times N_{\mathrm{tot}}^{\mathrm{fit}}}{N_{\mathrm{Template}\ 0}^{\mathrm{MC}}} \,, \tag{7.6}$$

$$\mu_L = \frac{1 - f_0 + (f_{\mathrm{L}} - f_{\mathrm{R}})}{2} \times \frac{N_{\mathrm{tot}}^{\mathrm{fit}}}{N_{\mathrm{Template}\ L}^{\mathrm{MC}}} \,, \tag{7.7}$$

$$\mu_R = \frac{1 - f_0 - (f_{\mathrm{L}} - f_{\mathrm{R}})}{2} \times \frac{N_{\mathrm{tot}}^{\mathrm{fit}}}{N_{\mathrm{Template}\ R}^{\mathrm{MC}}} \,, \tag{7.8}$$

where $N^{\text{MC}}_{\text{Template } i}$, $i \in \{0, R, L\}$, is the integral over the Monte Carlo polarisation template at detector level.

The templates generated by Monte Carlo at particle level undergo several distortions when brought to detector level:

- Some events of the total phase space do not pass the fiducial cuts leading to a first distortion of the template. This acceptance is assessed for all templates by so-called *A-factors*.
- Some events in the fiducial phase space are not reconstructed because the detector is not perfectly efficient. Also, some events from outside the fiducial phase space can migrate into the measurement phase space. This overall effect called the efficiency of the detector is assessed by so-called *C-factors*.
- The template shape can be distorted due to migrations among the bins in the measurement phase space.

Shape effects on the template caused by event migration among the bins in the measurement phase space and from outside the fiducial phase space are taken into account by passing the templates with generated events in the total phase space through the detector simulation and by reconstructing them in the same way as the data. All shape distortions should therefore be propagated to the template if the modelling of the detector response is correct. This has been checked by independent measurements done by the ATLAS combined detector performance (CP) groups. Scale and correction factors make sure that the simulation describes the data well.

The template fit uses templates at detector level, as they must be comparable to the Run 2 data. Using Eq. (7.6)–(7.8) with the $N_{\text{Template } i}$ of the detector-level templates will then give the fractions at detector level. This is not very interesting as the values would depend heavily on the reconstruction done in the ATLAS detector. The goal is thus to measure the boson polarisation at particle level in the fiducial phase space.

The μ_i found (and thus the fractions associated) are brought to particle level in the fiducial phase space with the efficiency C-factor of the corresponding template

$$C_i = \frac{N^{\text{fiducial}}_{\text{Template } i}}{N^{\text{detector}}_{\text{Template } i}} \, . \tag{7.9}$$

This, as can be seen in Eq. (7.6)–(7.8), amounts to using for $N_{\text{Template } i}$ the value at particle level in the fiducial phase space of the Monte Carlo sample. The $N^{\text{fit}}_{\text{tot}}$ found will thus also correspond to the yield at particle level in the fiducial phase space, labelled more simply N_{tot} in the following. Similarly, the fractions f_0 and $f_{\text{L}} - f_{\text{R}}$ will be obtained directly at particle level in the fiducial phase space. Besides, for tests or theoretical predictions, the same template fit can be performed on pseudo data of Monte Carlo origin. This allows fitting with templates already at particle level in the fiducial phase space, or even in the total phase space. In any case, the described parametrisation will still yield parameters of interest at particle level in the fiducial phase space, allowing for comparisons. In the end, the parametrisation of Eq. (7.6)–(7.8) is in its final form:

$$\mu_0 = \frac{f_0 \times N_{\text{tot}}}{N^{\text{MC,fiducial}}_{\text{Template } 0}} , \tag{7.10}$$

$$\mu_L = \frac{1 - f_0 + (f_{\text{L}} - f_{\text{R}})}{2} \times \frac{N_{\text{tot}}}{N^{\text{MC,fiducial}}_{\text{Template } L}} , \tag{7.11}$$

$$\mu_R = \frac{1 - f_0 - (f_{\text{L}} - f_{\text{R}})}{2} \times \frac{N_{\text{tot}}}{N^{\text{MC,fiducial}}_{\text{Template } R}} . \tag{7.12}$$

Similarly, the joint-polarisation fractions f_{00}, $f_{0\text{T}}$, $f_{\text{T}0}$ and f_{TT} can be made the parameters of interest of the fit. With the normalisation relationship, the set of parameters of interest is $(f_{00}, f_{0\text{T}}, f_{\text{TT}}, N_{\text{tot}})$ with N_{tot} the total number of signal events. The fit scales the four input templates for polarisation configurations by the normalisation factors μ_i with $i \in \{00, 0T, T0, TT\}$ linked to the parameters of interest by:

$$\mu_{00} = \frac{f_{00} \times N_{\text{tot}}}{N^{\text{MC,fiducial}}_{\text{Template } 00}} , \tag{7.13}$$

$$\mu_{0T} = \frac{f_{0\text{T}} \times N_{\text{tot}}}{N^{\text{MC,fiducial}}_{\text{Template } 0T}} , \tag{7.14}$$

$$\mu_{T0} = \frac{(1 - f_{00} - f_{0\text{T}} - f_{\text{TT}}) \times N_{\text{tot}}}{N^{\text{MC,fiducial}}_{\text{Template } T0}} , \tag{7.15}$$

$$\mu_{TT} = \frac{f_{\text{TT}} \times N_{\text{tot}}}{N^{\text{MC,fiducial}}_{\text{Template } TT}} . \tag{7.16}$$

where $N^{\text{MC,fiducial}}_{\text{Template } i}$, $i \in \{00, 0T, T0, TT\}$, is the integral over the Monte Carlo template at particle level in the fiducial phase space.

Using the relationships described in Section 5.4.4, one can also use the set of parameters of interest $(R_c, f_0^W, f_0^Z, N_{\text{tot}})$. Then, Eq. (7.13)–(7.16) are adapted using Eq. (5.52)–(5.54). This change of parameters of interest of the fit does not affect its the behaviour. It is mostly a matter of internal calculation within the fitting framework to keep track of correlations between all parameters of the fit. This in particular means that the set of parameters of interest can be changed around the normalisation relationship, such as with $(f_{00}, f_{0\text{T}}, f_{\text{T}0}, N_{\text{tot}})$ to isolate $f_{\text{T}0}$. A fraction obtained with two different sets of parameters of interest is found in both cases at exactly the same value, within numerical precision of the computer, well below the statistical uncertainty from the fit.

7.1.3 Backgrounds in the parametrisation of the fit

At detector level, some $W^{\pm}Z$ events decaying to τ are reconstructed as signal, the τ subsequently decaying in an electron or a muon. The shape of this background is estimated from Monte Carlo as described in Section 6.3.1. However, its magnitude is directly linked to the cross section of $W^{\pm}Z$, and thus it must be linked to the parameter of interest of the fit N_{tot}. To establish this link, the fraction of τ event in reconstructed data f_{τ} is estimated from Monte Carlo

$$f_{\tau} = \frac{N^{\text{MC}}_{\tau}}{N^{\text{MC}}_{\tau} + N^{\text{MC}}_{\text{tot}}} \tag{7.17}$$

where N_τ^{MC} is the number of event in the τ background Monte Carlo sample and $N_{\text{tot}}^{\text{MC}}$ is the number of events in all signal polarised templates. As a result the normalisation factor μ_τ of this background is

$$\mu_\tau = \frac{N_\tau^{\text{fit}}}{N_\tau^{\text{MC}}} = N_{\text{tot}}^{\text{fit}} \times \frac{f_\tau^{\text{fit}}}{1 - f_\tau^{\text{fit}}} \times \frac{1}{N_\tau^{\text{MC}}} \, .$$

Finally, under the assumption that the fraction of τ is well described by the Monte Carlo and not affected by the fit, and adding a C-factor to account for the fact that the fitted N_{tot} is at particle level in the fiducial phase space, the normalisation factor μ_τ becomes background:

$$\mu_\tau = N_{\text{tot}} \times C_{\text{tot}} \times \frac{f_\tau}{1 - f_\tau} \times \frac{1}{N_\tau^{\text{MC}}} \, , \tag{7.18}$$

where C_{tot} is the global C-factor on the sum of the polarised templates making up the signal. In the template fit, the background from τ production will thus be rescaled by this normalisation factor μ_τ which is directly linked to the parameter of interest of the fit N_{tot}. The uncertainty on this τ background originates from the fraction f_τ. In order to quantify this uncertainty, an overall normalisation uncertainty of 10 % on this background is implemented in the fit.

7.2 Finding a discriminating variable

To be able to extract simultaneously all parameters of interest in a template fit, a variable giving very different shapes for the polarisation templates is needed. From theoretical considerations developed in Chapter 5, some angular variables characterising the topology of $W^\pm Z$ events can be used for that purpose. However, for joint-polarisation templates, an aggregated variable created using Deep Neural Networks is needed.

7.2.1 Angular variables

In single boson polarisation measurements, it was shown in Section 5.2 that the distribution of $q_W \cdot \cos\theta^*_{\ell W}$ or $\cos\theta^*_{\ell Z}$ have very distinct shapes in pure polarisation states. They will be used as discriminating variables to extract respectively the polarisation of the $W^\pm$ boson and the Z boson in a template fit. The shapes of the polarisation templates at particle level in the total phase space for these variables is simply given by the analytical functions summed in Eq. (5.28) and (5.29). They are visible in Fig. 5.4 fitting the inclusive $\cos\theta^*_\ell$ distribution. Using an analytical reweighting detailed ahead in Section 7.3, it is then possible to transfer these polarisation templates to detector level. As visible in Fig. 7.1, these variables keep their discriminating power at detector level, even though it is smeared by the reconstruction. The shapes suggest that the left and right polarisation will be better discriminated in the $W^\pm$ boson than in the Z boson. This is an impact of the parameter C_{w} defined in (5.25), originating from the electroweak mixing.

To extract joint-polarisation states however, there is no such clear choice from a theoretical point of view. The $|\cos\theta_V|$ was suspected in analogy with $\cos\theta^*_{\ell W}$ or $\cos\theta^*_{\ell Z}$ to have a discriminating shape for different joint-polarisation states. Thanks to a partial

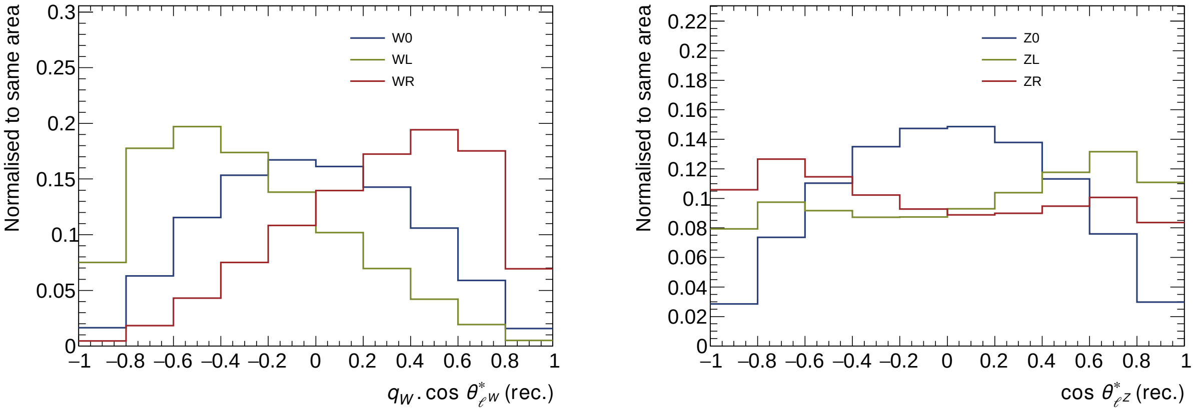

(a) $W^\pm$ **(b)** Z

Figure 7.1 All three single boson polarisation templates at detector level for $W^\pm$ boson using $q_W \cdot \cos\theta^*_{\ell W}$ (left) and for Z boson using $\cos\theta^*_{\ell Z}$ (right) in $W^\pm Z$ events. These templates were all rescaled to the same surface area.

amplitude zero effect [30], this variable has a very distinctive shape for the 00 joint-polarisation. This is verified using the polarised `MGgen` Monte Carlo samples defined in Section 5.3.2. The distribution of events for $|\cos\theta_V|$ presented in Fig. 7.2, both at particle level in the total phase space and at detector level, allow assessing its discriminating power by eye and see how reconstruction effects degrade it. The distinct shape of the 00 joint-polarisation template is clearly visible in Fig. 7.2(a) and reconstruction effect in Fig. 7.2(b) do not seem to modify much the discrimination of the 00 joint-polarisation against the others. However, already at particle level, the variable $|\cos\theta_V|$ almost does not discriminate between 0T, T0 and TT. To be able to extract all four joint-polarisation fractions, something more discriminant is needed.

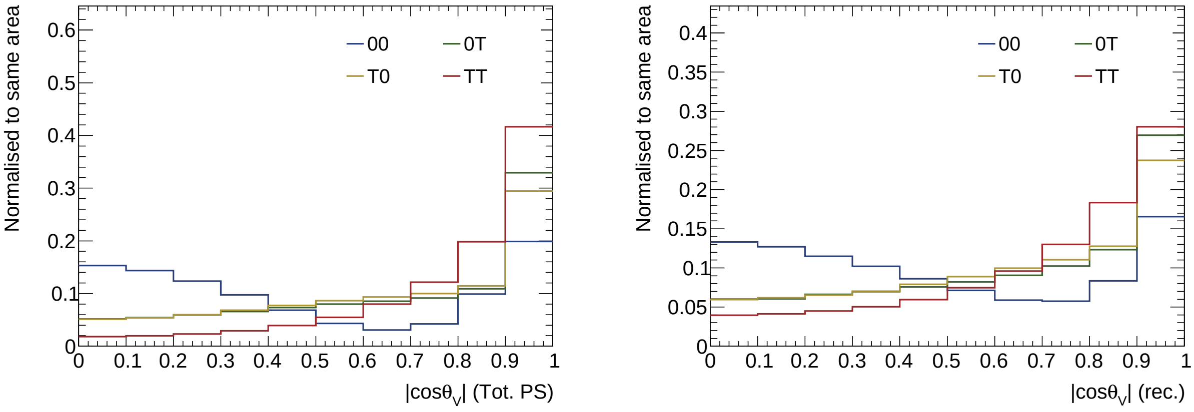

(a) **(b)**

Figure 7.2 All four `MGgen` joint-polarisation templates for $W^\pm Z$ events with $|\cos\theta_V|$ as discriminating variable are represented at particle level in the total phase space (a) and at reconstructed level (b). These templates were all rescaled to the same surface area.

7.2.2 The classification Deep Neural Network

A multiclass Deep Neural Network (DNN) was developed to discriminate among different polarisation states using Tensorflow v1.3 [102] with Keras v2.2.4-tf [103] back-end. The DNN was trained on the four pure joint-polarisation samples from MadGraph0,1j@LO generation (`MGgen` samples) at detector level. The input variables are listed in Table 7.1 ranked by their contribution to the discriminative power of the DNN. The main variable is $|y_Z - y_{\ell W}|$, the difference in rapidity between the Z boson and the decay lepton from the $W^{\pm}$ boson. It is a proxy for the $|\cos\theta_V|$ variable relying on readily accessible information with minimal reconstruction. The second variable is p_{T}^{WZ}, directly linked to additional jets from initial state radiations in NLO QCD real corrections. The differences in ϕ angle of the decay leptons, an incomplete angular description of the boson decay, are found to provide also a good improvement of the DNN. Finally, the p_{T} of all leptons and $E_{\mathrm{T}}^{\mathrm{miss}}$ are used, completing the kinematic description of the events. The choice was made to avoid the use of the neutrino longitudinal momentum p_z^{ν} to be independent of the choice and the performance of its reconstruction. Overall, the input variables are low level variables to provide a DNN with low theory dependence of which the detector level distribution in data can then be unfolded to particle level.

Table 7.1 DNN input variables ranked by their importance. It is defined by the drop in area under the ROC curve when they are the only one removed from the input list, one at a time.

$\|y_Z - y_{\ell W}\|$	0.080
p_{T}^{WZ}	0.024
$p_{\mathrm{T}}^{\ell W}$	0.012
$\Delta\phi(\ell^W, \ell^\nu)$	0.005
$\Delta\phi(\ell_1^Z, \ell_2^Z)$	0.005
$E_{\mathrm{T}}^{\mathrm{miss}}$	0.003
$p_{\mathrm{T}}^{\ell_2^Z}$	0.003
$p_{\mathrm{T}}^{\ell_1^Z}$	0.002

The classification DNN score p_{00}^{DNN} can be interpreted for each event as its probability to originate from a 00 joint-polarisation state. The 00 joint-polarisation is the most challenging to observe as from Table 5.3 it is expected to represent roughly 5 % of all $W^{\pm}Z$ events at particle level. Thus, p_{00}^{DNN} can be used as a discriminating variable. Nevertheless, the main challenge with such DNN score is to be able to separate the mixed (0T, T0) and TT joint-polarisation states that otherwise would both peak at zero. The best method was found to be to modify the target of the classification DNN during the training: instead of having each specialised joint-polarisation DNN score get a probability 1 for its associated joint-polarisation state and 0 for the three others, the mixed joint-polarisations also gets 0.5 probability in the p_{00}^{DNN} score. That way, 00 peaks at 1, TT peaks at 0 and the mixed modes 0T and T0 peak at 0.5 in the p_{00}^{DNN} distribution.

The DNN score p_{00}^{DNN} distribution at detector level for 00, TT and the mixed joint-polarisations is represented in Fig. 7.3. It is obtained from two disjoint sub-samples and a Kolmogorov-Smirnov test is performed between both sample distributions for each joint-polarisation state. The relatively low values of the Kolmogorov-Smirnov test results imply no sign of over-training. The performance of the DNN is evaluated through the integral of the receiver operating characteristic (ROC) curve, showing the background rejection as a function of the signal acceptance. The higher the area under the ROC curve is, the better

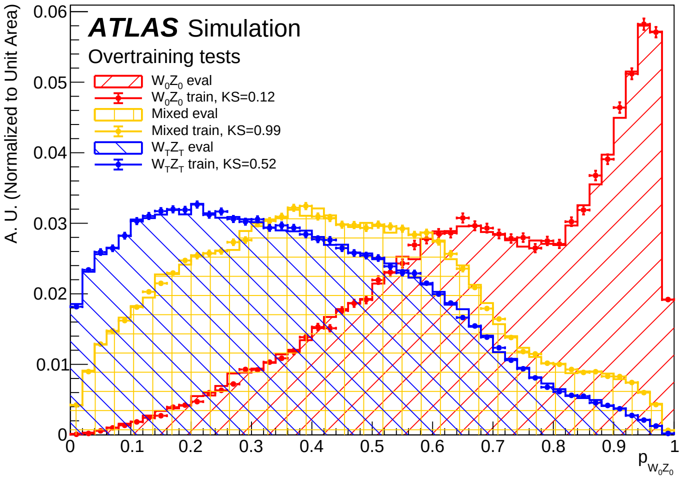

Figure 7.3 DNN score p_{00}^{DNN} distributions from a cross-training procedure on a training and an evaluation MadGraph0,1j@LO sample. Distributions computed on the evaluation (training) samples are represented with crosses (hatch filling). The results of the Kolmogorov-Smirnov test between the p_{00}^{DNN} distribution from the training and evaluation samples is presented in the legend for 00, TT and mixed joint-polarisations.

the discriminative power. This curve quantitatively shows that the DNN score p_{00}^{DNN} does discriminate very well the 00 joint-polarisation against all others, but that there is only a moderate discrimination between the mixed joint-polarisation states and TT.

Finally, while the classification DNN is trained at detector level, it is possible to obtain its distribution at particle level by using event-by-event the particle level values of the input variables. Passing through the same DNN architecture, these allow reconstructing a particle level DNN score identified as the particle level value associated to the detector level DNN score p_{00}^{DNN}.

7.2.3 Improving mixed states discrimination

The p_{00}^{DNN} score performs better than $|\cos\theta_V|$ as it allows separating 00, TT and mixed joint-polarisation states. By design, it nevertheless does not provide a good discriminating power between the mixed states. In such configurations, one boson is longitudinal while the other is not, yielding usually very different values for $\cos\theta^*_{\ell W}$ and $\cos\theta^*_{\ell Z}$, the longitudinal boson having $\cos\theta^*_\ell$ close to zero, and conversely the transversal boson having $\cos\theta^*_\ell$ close to one in absolute value. These variables not being used as inputs of the classification DNN, they can be combined with p_{00}^{DNN} to improve the separation between the mixed states.

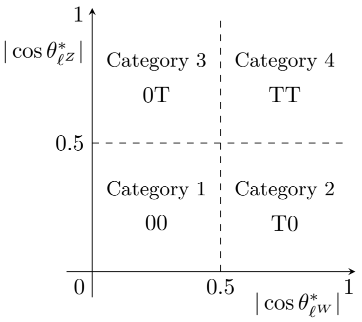

Figure 7.4 Scheme of categories as function of $\cos\theta^*_{\ell W}$ and $\cos\theta^*_{\ell Z}$.

Events are separated in four categories according to their $\cos\theta^*_{\ell W}$ and $\cos\theta^*_{\ell Z}$ values, according to the scheme represented in Fig. 7.4. Each event category is therefore dominated by 00, T0, 0T and TT joint-polarisation states, respectively. The p_{00}^{DNN} score is evaluated separately for events in the four categories and a one-dimensional distribution with twenty bins, that is five bins per category, is constructed, as presented in Fig. 7.5(a). This distribution will later be referred to as the 4-category p_{00}^{DNN}.

However, it should be noted that because the input variables to the classification DNN are not strictly independent of $\cos\theta^*_{\ell W}$ and $\cos\theta^*_{\ell Z}$, the variable p_{00}^{DNN}, let alone the 4-category p_{00}^{DNN}, cannot be used in an analytical reweighting as justified in Section 7.3.1. It is nonetheless possible to reweight $|\cos\theta_V|$ in the four aforementioned categories to obtain something able to discriminate between all joint-polarisation states. This is done in the same fashion as for the 4-category p_{00}^{DNN} creating a new variable labelled the 4-category $|\cos\theta_V|$ with the distribution of Fig 7.5(b).

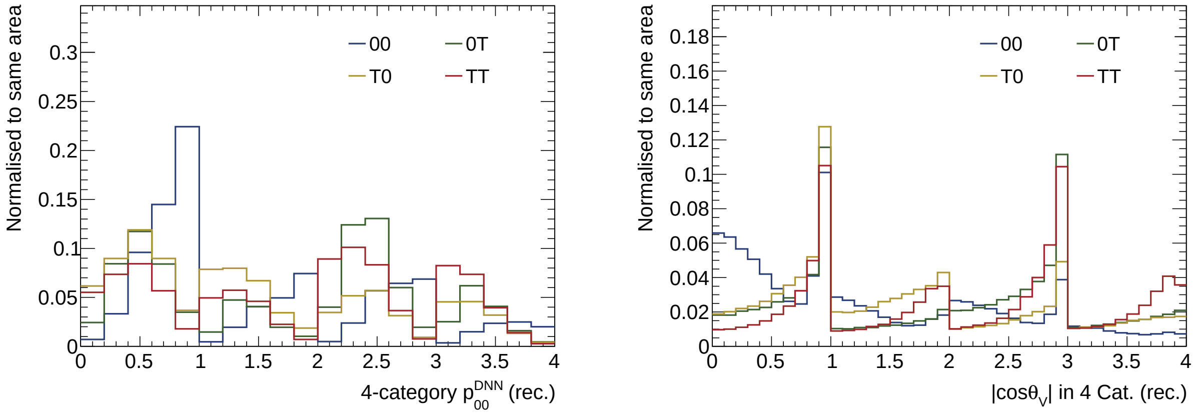

(a) **(b)**

Figure 7.5 All four `MGgen` joint-polarisation templates for $W^\pm Z$ events with the 4-category p_{00}^{DNN} (a) and the 4-category $|\cos\theta_V|$ (b) as discriminating variable are represented at detector level. These templates were all rescaled to the same surface area.

7.2.4 Choice of a discriminating variable

For joint-polarisation measurement, four discriminating variables have been identified, $|\cos\theta_V|$, p_{00}^{DNN} and their version in $\cos\theta^*_\ell$ categories, the 4-category $|\cos\theta_V|$ and the 4-category p_{00}^{DNN}. By eye, the p_{00}^{DNN} DNN score provides a better discriminating power and the splitting in $\cos\theta^*_\ell$ categories in all cases improves the separation of all joint-polarisation states. For a more quantitative estimation of the discriminating power of each variable, a simple binned maximum-likelihood template fit is performed using the inclusive POWHEG+PYTHIA sample as pseudo-dataset. To clearly distinguish the impact of changing the discriminating variable, no backgrounds[1] or systematic uncertainties is considered in this simple template fit. The template fit is performed at detector level with `MGgen` polarised samples. The templates and the pseudo-dataset are uncorrelated as they come from completely different Monte Carlo generations. What matters in this test is the change in the parameters of interest extracted values and uncertainties when the discriminating variable is changed.

First, it appears that using $|\cos\theta_V|$ or p_{00}^{DNN}, without the categories, the fit is not able to discriminate the mixed polarisation modes 0T and T0. As a result, the fit parameter of interest $f_{0\mathrm{T}}$ reaches its limit, set at 0 as should be for a fraction, and the fit does not converge.

---

[1] Backgrounds from τ decays and migrating γ^* are present in the inclusive POWHEG+PYTHIA sample and are therefore considered in this fit.

Using the 4-category $|\cos\theta_V|$, or the 4-category p_{00}^{DNN}, the fit is able to converge and the four parameters of interest extracted from these fits are shown in Table 7.2. Concerning the central value, it first should be noted that both variables give very similar result. This tends to validate the fact that the p_{00}^{DNN} does not hold any bias linked to the use of machine learning techniques, since it is consistent with a regular variable as $|\cos\theta_V|$. Concerning the uncertainties, another remarkable property is that they are similar for N_{tot}, as a sign of the decoupling between the overall normalisation and the polarisation content. However, looking at the fractions, the improved discriminating power of the 4-category p_{00}^{DNN} yields much smaller uncertainties. Looking at the inverse of the relative uncertainty $x/\delta x$ – a proxy for the significance – the 4-category $|\cos\theta_V|$ cannot reach the $5\,\sigma$ threshold for f_{00} and $f_{0\text{T}}$. This is before adding to the fit backgrounds and systematic uncertainty that will further degrade this significance. On the other hand, the lowest significance with the 4-category p_{00}^{DNN} is for f_{00} at around $7\,\sigma$, leaving good hopes that the $5\,\sigma$ threshold can be reached in the final fit for all joint-polarisation fractions.

	Central Value x	Uncertainty δx	$x/\delta x$
Fitting the 4-category $|\cos\theta_V|$ distribution			
N_{tot}	35400	300	120
f_{00}	0.039	0.013	2.9
$f_{0\text{T}}$	0.179	0.032	5.6
f_{TT}	0.655	0.033	20
Fitting the 4-category p_{00}^{DNN} distribution			
N_{tot}	35330	300	120
f_{00}	0.041	0.006	6.7
$f_{0\text{T}}$	0.226	0.020	12
f_{TT}	0.567	0.024	23

Table 7.2 Results of the fit for the parameters of interest N_{tot}, f_{00}, $f_{0\text{T}}$ and f_{TT}, fitting the distribution of the 4-category $|\cos\theta_V|$ (top) and of the 4-category p_{00}^{DNN} (bottom) from the inclusive POWHEG+PYTHIA sample in $W^\pm Z$ events at detector level.

In the end, using a classification DNN is more than an improvement compared to using a regular variable as $|\cos\theta_V|$; it is a crucial component of the analysis in order to reach the $5\,\sigma$ significance for the measured four joint-polarisation fractions. In the following, the 4-category p_{00}^{DNN} will be chosen as the discriminating variable for the joint-polarisation fraction measurement. In some cases, for clarity, the p_{00}^{DNN} distribution will be shown.

7.3 Templates from analytical reweighting

The diboson $W^\pm Z$ production process has been shown to be very sensitive to higher order corrections in perturbative QCD, as demonstrated by fixed-order theoretical calculations of the inclusive cross section in Section 5.1.1 or the joint-polarisation fractions in Section 5.2.3. In addition to having a good discriminating variable, it is thus important that the polarisation templates be NLO accurate in QCD. Not taking such effects into account can lead to distorted shapes for the polarisation templates leading to a biased measurement of fractions. The polarised samples `MGgen` obtained with the MADGRAPH0,1j@LO polarised generation are thus not enough, as they do not take fully into account NLO in QCD corrections.

From the analytical fit formulas of Section 5.4, an analytical reweighting at particle level of an inclusive Monte Carlo sample allows in principle the production of polarised sample. Using this method with a inclusive Monte Carlo generated at NLO in QCD will thus provide NLO accurate polarisation templates. Prior to version 2.7.3 of MadGraph5_aMC@NLO, it was impossible to generate directly polarised samples. This method was the only way to produce polarisation templates, as for example in Ref. [17]. It is in fact still the only method to provide templates for left or right polarisation of a vector boson, MadGraph being unable to generate the decay of the $W^{\pm}$ and Z bosons in these cases.

In this section, the founding principles and limitations of this analytical reweighting method are described. Its implementation in the case of single boson polarisation templates is then described and its principle is validated. Finally, its adaptation to joint-polarisation templates is discussed.

7.3.1 Single boson polarisation reweighting

Starting from an inclusive sample of $W^{\pm}Z$ events, it was shown in Section 5.4 that its built-in polarisation content can be estimated at particle level in the total phase space. Nevertheless, in data, acceptance cuts and inefficiencies of the detector do not allow to use the same techniques. The idea would be to generate sub-samples of pure polarisation states from inclusive Monte Carlo samples. This can be done reweighting the inclusive sample, event by event, by some probability that this event would be in a given polarisation state. Each event k can be described as the realisation $\vec{v}^k$ of a vector of random variables $\vec{\mathbf{V}}$ all independent following the law of

$$\vec{\mathbf{V}} = (\mathbf{V}_0, \mathbf{V}_1, ..., \mathbf{V}_N) \ ,$$

where the $\mathbf{V}_i$ are all the individual – and not necessarily continuous – variables describing the event. As a result, the marginal probability density functions of those $\mathbf{V}_i$ are estimated by their distribution histograms.

The goal will be to estimate the law of the vector $\vec{\mathbf{V}}$ in polarised cases from the estimation that we have of it in the inclusive case. This law lives in a N-dimensional space with some continuous dimensions, so the probability of a specific realisation of $\vec{\mathbf{V}}$ to be “closer” than some infinitesimal distance ε in this space to a given $\vec{v}$ will be written $\mathbb{P}\left(\vec{\mathbf{V}}\left(\vec{v}\right)\right)$.

The polarisation of a specific boson V is defined as a random discrete variable $\mathbf{H}$. The distribution of $\vec{\mathbf{V}}$ when the polarisation of the boson V is h_0 amounts to computing for all $\vec{v}$ the probability $\mathbb{P}\left(\vec{\mathbf{V}}\left(\vec{v}\right) \cap \mathbf{H} = h_0\right)$. Using conditional probabilities, this yields the fundamental relation

$$\mathbb{P}\left(\vec{\mathbf{V}}\left(\vec{v}\right) \cap \mathbf{H} = h_0\right) = \mathbb{P}\left(\mathbf{H} = h_0 | \vec{\mathbf{V}}\left(\vec{v}\right)\right) \mathbb{P}\left(\vec{\mathbf{V}}\left(\vec{v}\right)\right) \ . \tag{7.19}$$

The reweighting procedure amounts to applying to each event $\vec{v}$ the corresponding weight $\mathbb{P}\left(\mathbf{H} = h_0 | \vec{\mathbf{V}}\left(\vec{v}\right)\right)$ in order to go from the law of $\vec{\mathbf{V}}$ in the inclusive case to the polarised case. This weight is the probability for an event to originate from a boson of polarisation h_0 knowing its kinematic variables $\vec{v}$.

7.3.1.1 Polarising the distribution of one variable

For simplicity let us look at the case of only one variable $\mathbf{V}_1$. Going back to the N-dimensional case of $\vec{\mathbf{V}}$ is quite straight forward. The polarised distribution of $\mathbf{V}_1$ can be obtained from Eq. (7.19) knowing $\mathbb{P}\left(\mathbf{H}=h_0|\mathbf{V}_1\left(v_1\right)\right)$. This weight can in fact be estimated using a variable $\mathbf{V}_0$ independent of $\mathbf{V}_1$ and for which its distribution in the polarised cases is known from theory. Such variable is $q_W \cdot \cos\theta^*_{\ell W}$ for $W^\pm$ bosons and $\cos\theta^*_{\ell Z}$ for Z bosons. For a generic V boson, it will be noted $\mathbf{V}_0$ and the conditional probability $\mathbb{P}(\mathbf{V}_0\left(v_0\right)|\mathbf{H}=h)$ in all cases can be extracted from Eq. (5.28) and (5.29) as the various terms in $\cos\theta^*_\ell$ scaled by polarisation fractions:

$$\text{For } W^\pm \text{ bosons } (v_0 = q_W\cdot\cos\theta^*_{\ell W})\text{:}\ \begin{cases}\mathbb{P}(\mathbf{V}_0\left(v_0\right)|\mathbf{H}=0) &= \frac{3}{4}\left(1-v_0^2\right)\\ \mathbb{P}(\mathbf{V}_0\left(v_0\right)|\mathbf{H}=L) &= \frac{3}{8}\left(1-v_0\right)^2\\ \mathbb{P}(\mathbf{V}_0\left(v_0\right)|\mathbf{H}=R) &= \frac{3}{8}\left(1+v_0\right)^2\end{cases}, \tag{7.20}$$

$$\text{For } Z \text{ bosons } (v_0 = \cos\theta^*_{\ell Z})\text{:}\ \begin{cases}\mathbb{P}(\mathbf{V}_0\left(v_0\right)|\mathbf{H}=0) &= \frac{3}{4}\left(1-v_0^2\right)\\ \mathbb{P}(\mathbf{V}_0\left(v_0\right)|\mathbf{H}=L) &= \frac{3}{8}\left(1+v_0^2+2C_\mathrm{w}v_0\right)\\ \mathbb{P}(\mathbf{V}_0\left(v_0\right)|\mathbf{H}=R) &= \frac{3}{8}\left(1+v_0^2-2C_\mathrm{w}v_0\right)\end{cases}. \tag{7.21}$$

It is worth noting that the $\cos\theta^*_\ell$ variable characterises the decay of the boson V in its rest frame and is thus independent of all other bosonic variables, *e.g.* the p_T or $|\eta|$ of V. Of course, the polarisation can affect the distribution of bosonic variables meaning $\mathbf{V}_0$ is not strictly independent of other variables. Nevertheless, the conditional law of $\mathbf{V}_0$ with the polarisation holds all the information and adding any other bosonic variable in the conditional part will not change this conditional law.

From there, the factor $\mathbb{P}\left(\mathbf{H}=h_0|\mathbf{V}_1\left(v_1\right)\right)$ needed to reweight the distribution of the variable $\mathbf{V}_1$ in the polarisation h_0 can be obtained looking at the conditional distribution of $\mathbf{V}_0$ with $\mathbf{V}_1$:

$$\mathbb{P}\left(\mathbf{V}_0\left(v_0\right)|\mathbf{V}_1(v_1)\right) = \sum_{h=0,L,R}\mathbb{P}\left(\mathbf{H}=h|\mathbf{V}_1(v_1)\right)\mathbb{P}\left(\mathbf{V}_0\left(v_0\right)|\mathbf{H}=h\cap\mathbf{V}_1(v_1)\right). \tag{7.22}$$

Crucially, $\mathbf{V}_1$ must be a bosonic variable, independent of the leptonic decay. This allows to consider that $\mathbf{V}_0$ only depends on $\mathbf{H}$ hence the simplification

$$\mathbb{P}\left(\mathbf{V}_0\left(v_0\right)|\mathbf{V}_1(v_1)\right) = \sum_{h=0,L,R}\mathbb{P}\left(\mathbf{H}=h|\mathbf{V}_1(v_1)\right)\mathbb{P}\left(\mathbf{V}_0\left(v_0\right)|\mathbf{H}=h\right). \tag{7.23}$$

The left part can be estimated by plotting the inclusive distribution of $\mathbf{V}_0$ in bins of v_1. Then, Eq. (7.23) is analogous to the differential cross section of Eq. (5.28) and (5.29), with the addition of cuts defining bins of v_1. That way, the requested weight $\mathbb{P}\left(\mathbf{H}=h|\mathbf{V}_1(v_1)\right)$ can be identified as $f_h(v_1)$ the polarisation fraction in that v_1 bin. It can thus be extracted from techniques described in Section 5.4 and then used to polarise the distribution of $\mathbf{V}_1$.

$$\mathbb{P}\left(\mathbf{V}_1\left(v_1\right)\cap\mathbf{H}=h\right) = f_h(v_1)\mathbb{P}\left(\mathbf{V}_1\left(v_1\right)\right). \tag{7.24}$$

7.3.1.2 Polarising the distribution of multiple variables

The same procedure can be extended to any amount of conditional variables using in Eq. (7.24) the fraction $f_h(v_1, v_2, ..., v_N)$ as long as neither v_0 nor a leptonic variable directly dependent on v_0 is used. Of course, the more conditional variables are added, the less events will be found in the multi-dimensional bin of all these variables, and the less accurate the extracted fraction from the distribution of $\mathbf{V}_0$ will be. On the other hand, a variable that is not in the conditional part of the polarisation fraction is not guaranteed to have its distribution properly reweighted to the polarised distribution. Then, one may ask what is the result of this reweighting on the distribution of such a variable. The distribution obtained for variable $\mathbf{V}_2$ with the reweighting of only $\mathbf{V}_1$ to polarisation h is called $F^h(v_2)$. Then, summing on all values of v_1 (practically all the bins of v_1), it can be expressed as

$$\begin{aligned} F^h(v_2) &= \sum_{v_1} f_h(v_1)\mathbb{P}\left(\mathbf{V}_2(v_2) \cap \mathbf{V}_1(v_1)\right) && (7.25)\\ &= \sum_{v_1} \mathbb{P}\left(\mathbf{V}_1(v_1) \cap \mathbf{H} = h\right) \mathbb{P}\left(\mathbf{V}_2(v_2) | \mathbf{V}_1(v_1)\right) \ . && (7.26) \end{aligned}$$

It is clear from this expression that the difference of $F^h(v_2)$ with the true distribution will come from the dependence of $\mathbf{V}_2$ with $\mathbf{V}_1$. Let us consider first the case of $\mathbf{V}_2$ and $\mathbf{V}_1$ independent. Then,

$$\begin{aligned} F^h(v_2) &= \sum_{v_1} \mathbb{P}\left(\mathbf{V}_1(v_1) \cap \mathbf{H} = h\right) \mathbb{P}\left(\mathbf{V}_2(v_2)\right) && (7.27)\\ &= \mathbb{P}\left(\mathbf{H} = h\right) \mathbb{P}\left(\mathbf{V}_2(v_2)\right) \ , && (7.28) \end{aligned}$$

with $\mathbb{P}\left(H = h\right)$ actually being the total phase space fraction for polarisation h. Thus, the distribution is only affected by an overall factor. In this case, the analytical reweighting fails maximally for $\mathbf{V}_2$. Now, if $\mathbf{V}_2$ is completely dependent of $\mathbf{V}_1$, meaning that there is a function g such that $\mathbf{V}_2 = g(\mathbf{V}_1)$, then

$$\begin{aligned} F^h(v_2) &= \sum_{v_1} \mathbb{P}\left(\mathbf{V}_1(v_1) \cap \mathbf{H} = h\right) \mathbb{1}_{v_2 = g(v_1)} && (7.29)\\ &= \mathbb{P}\left(\mathbf{V}_2(v_2) \cap \mathbf{H} = h\right) \ . && (7.30) \end{aligned}$$

This time, the obtained distribution is exactly the polarised one that would have come from reweighting conditionally to $\mathbf{V}_2$. The same conclusion holds replacing $\mathbf{V}_1$ by an arbitrary number of variables. As a result, reweighting conditionally to a basis of independent variables would be enough to generate the distribution of any variable for a given polarisation. Typically, this can be done with one or two conditional variables only, for lack of statistical power in the inclusive Monte Carlo sample.

Even though the variable $\mathbf{V}_0$ cannot be used as a conditional variable of the reweighting, its distribution can be polarised for free using the theoretical knowledge on its polarised distribution. Using Bayes theorem,

$$\mathbb{P}\left(\mathbf{H} = h_0 | \mathbf{V}_0\left(v_0\right)\right) = \frac{\mathbb{P}\left(\mathbf{H} = h_0\right) \mathbb{P}\left(\mathbf{V}_0\left(v_0\right) | \mathbf{H} = h_0\right)}{\sum\limits_{h=0,L,R} \mathbb{P}\left(\mathbf{H} = h\right) \mathbb{P}\left(\mathbf{V}_0\left(v_0\right) | \mathbf{H} = h\right)} \ . \qquad (7.31)$$

Here, the denominator is actually, depending on the case, exactly the differential cross section of Eq. (5.28) or (5.29). It acts as a flattener of the $\mathbf{V}_0$ distribution. Then the numerator reshapes it along the requested polarisation. Replacing $\mathbb{P}\left(\mathbf{H} = h\right) = f_h$ by the polarisation fraction in bins of conditional variables $f_h(v_1, v_2, ..., v_N)$, provides the weight $\mathbb{P}\left(\mathbf{H} = h_0 | \mathbf{V}_0\left(v_0\right), \mathbf{V}_1\left(v_1\right) ...\right)$ that will polarise the distribution of all the variables in its conditional part.

7.3.1.3 Practical implementation

Practically, each event of the Monte Carlo sample is attributed a polarising weight. To compute this weight, the polarisation fraction in the bin associated to the values of the conditional variables for this event are chosen. Then these fractions are used in Eq. (7.31) and the $\mathbb{P}\left(\mathbf{V}_0\left(v_0\right)|\mathbf{H}=h\right)$ are taken depending on the boson from Eq. (7.20) or (7.21), using for $q_W \cdot \cos\theta^*_{\ell W}$ or $\cos\theta^*_{\ell Z}$ the values in the considered event. For example, the weight to get a W^+ boson with longitudinal polarisation, considering only one conditional variable v_1 is

$$w_{W_0^+}(\cos\theta^*_{\ell W}, v_1) = \frac{f_0(v_1)\frac{3}{4}\left(1-\cos^2\theta^*_{\ell W}\right)}{f_0(v_1)\frac{3}{4}\left(1-\cos^2\theta^*_{\ell W}\right) + f_\mathrm{L}(v_1)\frac{3}{8}\left(1-\cos\theta^*_{\ell W}\right)^2 + f_\mathrm{R}(v_1)\frac{3}{8}\left(1+\cos\theta^*_{\ell W}\right)^2}\,. \tag{7.32}$$

For the Z boson, a technical complication arises. The functions of $\cos\theta^*_{\ell Z}$ in the numerator and denominator of the polarising weight will contain the C_w parameter which is directly linked to the weak mixing angle $\sin^2(\theta_\mathrm{w})$, a fundamental parameter of the Standard Model. This parameter will enter the analysis in two places:

- In the extraction of the polarisation fractions from the Monte Carlo inclusive distribution.
- In the data or pseudo-data used in the final fit, internally driving the shape of the fitted distribution.

The first point concerns the denominator of the polarising weight. To properly extract the polarisation information built in the inclusive Monte Carlo prediction, the same $\sin^2(\theta_\mathrm{w})$ value as used internally by the Monte Carlo generator must be used in the fitting function. Similarly, the denominator acting as a flattener of the $\cos\theta^*_{\ell Z}$ distribution, the internal C_w value is also used there. The second point concerns the numerator which drives the shape of the $\cos\theta^*_{\ell Z}$ distribution. In the final fit, the normalisation of the polarised distributions of $\cos\theta^*_{\ell Z}$ is adjusted in order to fit the $\cos\theta^*_{\ell Z}$ distribution in data. The sum of the polarised $\cos\theta^*_{\ell Z}$ distributions will properly reproduce the shape of the fitted data if the C_w value used in the Left and Right polarised distributions matches the C_w value of what is being fitted. For test fits with pseudo-data, the C_w value used for the generated Monte Carlo events of that pseudo-dataset must be used. For the final fit on data however, an effective C_w must be used, derived from the effective value of $\sin^2(\theta_\mathrm{w})$ as reported in Ref. [70].

7.3.2 Choice of conditional variables

The goal of the analytical reweighting is to generate polarised samples, of which one discriminating variable will be used as a template. Naively, correctly modifying the distribution of the discriminating variable should be enough for this purpose. Conveniently, for single boson polarisation this discriminating variable is $\cos\theta^*_\ell$ which by construction of the method is always correctly reweighted. Nevertheless, the Monte Carlo events go in the analysis chain through a detector simulation to obtain their detector-level equivalent. In this process, it keeps its polarising weight acquired from particle level information, but the variables describing it are modified. This results in reconstructed distributions of variables distorted by acceptance cuts and reconstruction inefficiencies.

Consequently, the discriminating variable distribution at reconstructed level relies on other variables. This is especially the case for $\cos\theta^*_{\ell W}$ where the p_z^ν reconstruction relies on many variables and is in turn necessary to determine the detector level value of $\cos\theta^*_{\ell W}$. As a result, it is important to identify which variables have a strong dependence with the polarisation to determine if they need to be added as conditional variables. The analytical reweighting will then generate a correctly modified distribution of these conditional variables if the polarisation fractions are extracted in bins of this variable.

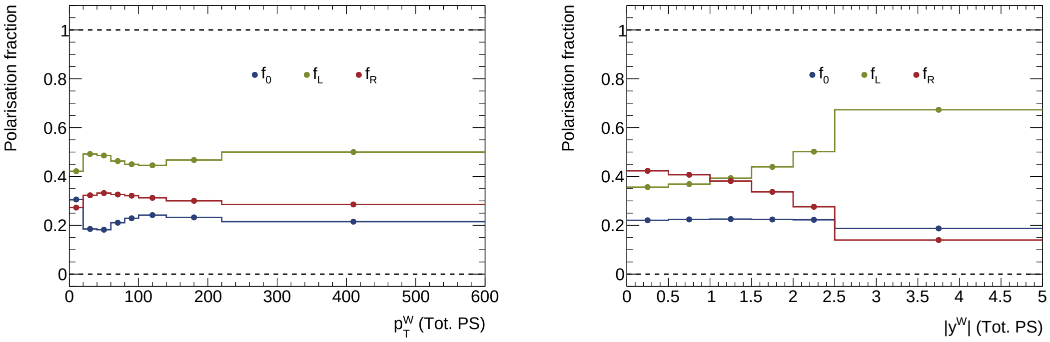

(a) with p_{T}^W **(b)** with $|y^W|$

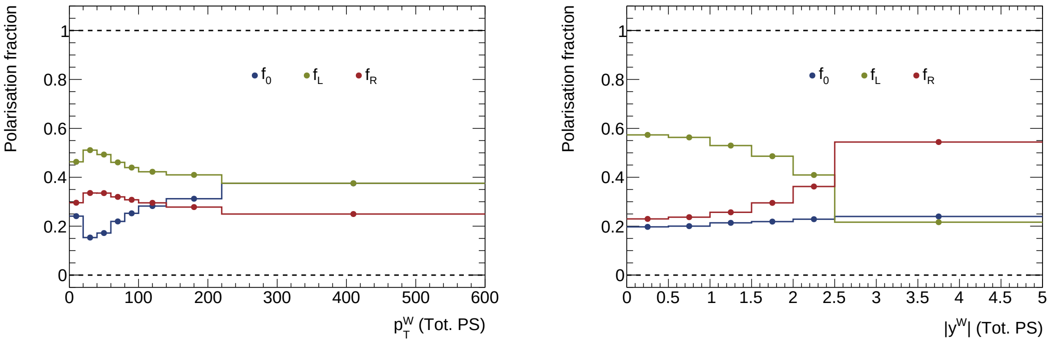

(c) with p_{T}^Z **(d)** with $|y^Z|$

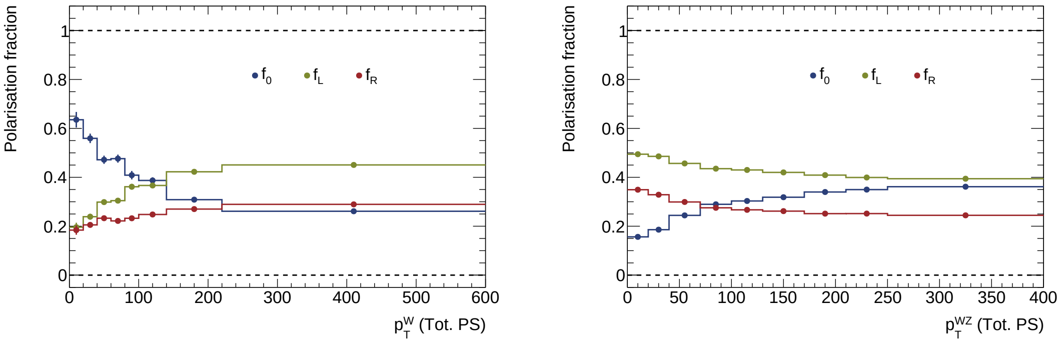

(e) with p_{T}^W, with cut $p_{\mathrm{T}}^Z > 200\,\mathrm{GeV}$ **(f)** with $p_{\mathrm{T}WZ}$

Figure 7.6 Evolution of the three polarisation fractions f_0, f_{L} and f_{R} of a W^+ boson with respect to different kinematic variables, extracted from Powheg+Pythia in the total phase space with the moments method.

Similarly to what was done in Section 5.4.2, it is possible to plot the evolutions of all polarisation fractions as a function of any variable eligible to be a conditional variable (necessarily bosonic variables as explained in Section 7.3.1). In Fig. 7.6 this is done with inclusive W^+Z particle-level events in the total phase space generated by Powheg+Pythia.

The evolution of all three polarisation fractions of the $W^{\pm}$ boson is presented, but similar effects are observed on the fractions of the Z boson or with $W^{-}Z$ events.

From Fig. 7.6(a) and 7.6(b), it is visible that as expected, the fractions depend on the transverse momentum and rapidity of the considered boson. Additionally , it appears that the p_{T} plays a bigger role in the evolution of f_0 while the f_{L} and f_{R} have a dependency mainly with the rapidity $|\eta|$. Looking at Fig. 7.6(c), the dependence with the p_{T} of the second boson, here the Z boson, is visible. This is a sign that the polarisation fractions of the two bosons are not independent: at high p_{T}^{Z}, f_0^{W} is enhanced. Also, the rapidity of the second boson has opposite trends of f_{L} and f_{R} as the considered boson (Fig. 7.6(d)).

Moreover, it is also possible to identify how cuts on a given variable affect the polarisation content of the sample at particle level in order to define a phase space enhanced for a particular polarisation. Adding a cut to select $p_{\mathrm{T}}^{Z} > 200\,\mathrm{GeV}$ changes completely the picture of the evolution of f_0 with p_{T}^{W} as can be seen in Fig. 7.6(e). Suddenly, low p_{T}^{W} favours f_0. This can be explained by looking at Fig. 7.6(f) showing that the longitudinal polarisation is favoured by unbalanced p_{T} between the $W^{\pm}$ and Z bosons. This is ultimately linked to NLO effects, as an additional jet seems to add flexibility to the angular momentum conservation allowing for more longitudinal bosons.

The number of conditional variables used in the reweighting cannot be too high as we need to divide the phase space in bins of each of these variables simultaneously. The number of events available in each bin is therefore reduced according to the number of variables. To generate samples with a single boson polarised, only two conditional variables are considered: p_{T} and $|\eta|$ of the polarised boson. That way, the kinematic variables of the leptons produced by the decay, being determined by $\cos\theta_{\ell}^{*}$, p_{T} and $|\eta|$, will be correctly modified. And as a result, cuts on these variables will not degrade the quality of the polarised templates.

Yet as this section shows, correlations between the polarisation of the bosons imply that kinematic variables of the other boson will also be affected. Cuts there will in turn degrade the polarised template, as these variables would not be correctly reweighted. Thus, a study on the validity of the reweighting at the reconstructed level must be performed.

7.3.3 Validation of the analytical reweighting

Three polarised samples are generated for each boson from the inclusive Powheg+Pythia sample, using $\cos\theta_{\ell}^{*}$ as the discriminating variable and (p_{T},$|\eta|$) as the conditional variables. In principle, the set of events at reconstructed level is the same in all three polarised samples, only their polarising weights are different. From Eq. (7.31), it is clear that the sum of the three polarising weights for a same event will give exactly one. Consequently, summing the distribution of any variable from all three polarised samples produces exactly the inclusive Powheg+Pythia distribution.

To check the overall validity of the method, each polarisation template should originate from a different subset of the inclusive sample. This way the event-by-event automatic sum to one disappears and it is the overall shape of the templates whose sum should give back the inclusive sample, within statistical fluctuations. For this, polarised samples *0, L, R* are obtained reweighting the inclusive Powheg+Pythia sample corresponding respectively to run periods 2015-2016, 2017 and 2018, subdivisions of Run 2. These are effectively three independent subsets of events. The sum of these polarised samples is then compared to the full Run 2 inclusive sample. To match the full Run 2 inclusive sample overall normalisation, the templates are rescaled using a template fit. The interesting part in this test is not the post-fit values of the fractions, but simply the capability of the polarised templates to recover together the shape of the inclusive distribution. The rescaled polarised templates are summed and compared to the inclusive sample, with the supplementary technicality that backgrounds from τ decay and γ^* migration described in Section 6.3.1 are present in the Powheg+Pythia sample and must be subtracted.

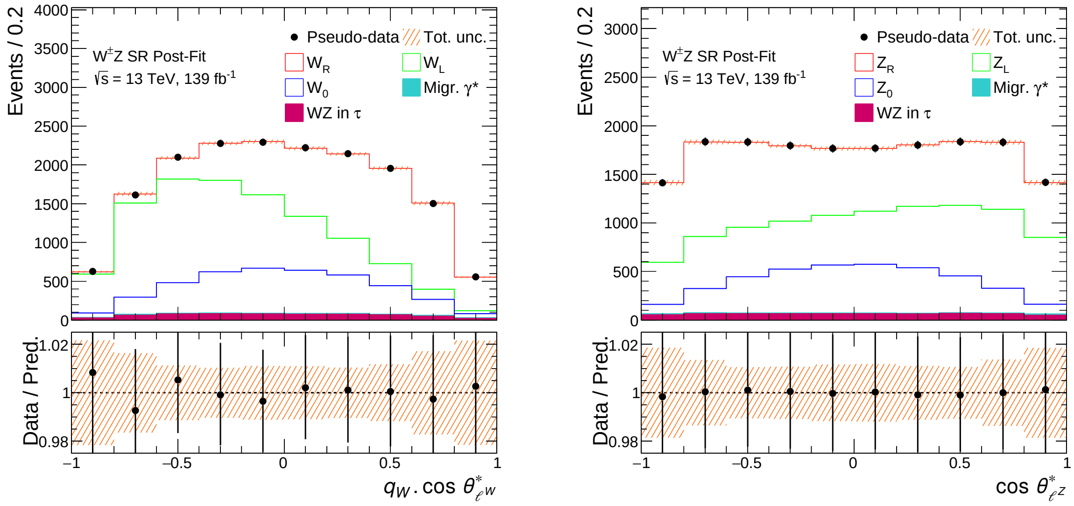

(a) $W^\pm$ boson **(b)** Z boson

Figure 7.7 Independent closure test at reconstructed level for the $W^\pm$ boson (a) and the Z boson (b). The polarisation templates were generated with the reweighting each of a different subset of the Powheg+Pythia sample. The τ decay and migrating γ^* background contributions in the inclusive sample have their templates included but left unaffected by the template fit.

The result in Fig. 7.7 shows that bin-by-bin, the non-closure is always well bellow the range of statistical fluctuations represented by the orange hatches in the ratio panel. As a result the closure test is passed and the concept of the reweighting method is validated in single boson polarisation.

7.3.4 Reweighting for joint-polarisation

So far, the reweighting formula of Eq. (7.19) allows reweighting a variable distribution to represent a state with a single polarised boson. It must be adapted to represent states with both boson polarised, the so-called joint-polarisation states. This is naturally done by

$$\mathbb{P}\left(\vec{\mathbf{V}}(\vec{v})\ \cap\ \mathbf{H}^W = h\ \cap\ \mathbf{H}^Z = h'\right) = \mathbb{P}\left(\mathbf{H}^W = h\ \cap\ \mathbf{H}^Z = h' \mid \vec{\mathbf{V}}(\vec{v})\right)\mathbb{P}\left(\vec{\mathbf{V}}(\vec{v})\right)\ . \quad (7.33)$$

Here, the $\mathbb{P}\left(\mathbf{H}^W = h \cap \mathbf{H}^Z = h' \mid \vec{\mathbf{V}}(\vec{v})\right)$ can be noted $f_{h^W \cap h^Z}(\vec{v})$ the joint-polarisation fraction conditionally to all the variables of the events being $\vec{v}$. In practice, only one variable v_1 is used. These fractions are extracted with a 2D fit as described in Section 5.4.3, but in bins of the conditional variable v_1. In the case of joint-polarisation, the variables $q_W \cdot \cos\theta^*_{\ell W}$ or $\cos\theta^*_{\ell Z}$ cannot be used as discriminating variables as they only affect the polarisation of one boson. The variable v_1 must be sensitive to both boson polarisation and therefore, as hinted in Section 5.2.1, $|\cos\theta_V|$ is chosen. To improve the behaviour of the reweighted sample at detector level, $\cos\theta^*_{\ell W}$ and $\cos\theta^*_{\ell Z}$ are also modified, since it can be done for free in the same fashion as in Eq. (7.31).

As was done in Section 7.3.2, the joint-polarisation fractions evolution with $|\cos\theta_V|$ is represented in Fig. 7.8 separately for W^+Z and W^-Z events. From there, f_{00} shows a very distinctive evolution compared to f_{TT}. The mixed fractions $f_{0\mathrm{T}}$ and $f_{\mathrm{T}0}$ on the other hand stay roughly constant along $|\cos\theta_V|$. This demonstrates that $|\cos\theta_V|$ is still a good discriminating variable at NLO in QCD for the 00 and TT joint-polarisation state, but still lacks discriminative power to disentangle the mixed polarisation states.

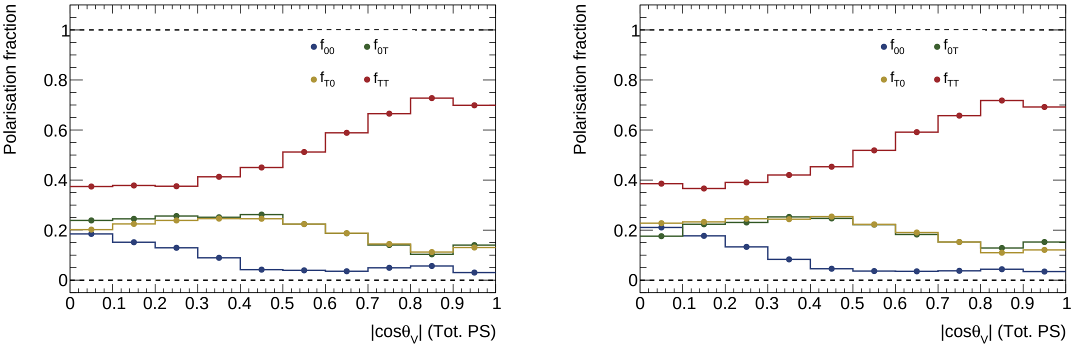

(a) W^+Z **(b)** W^-Z

Figure 7.8 Joint-polarisation fractions of an inclusive Powheg+Pythia sample at particle level in the total phase space in bins of $|\cos\theta_V|$ in W^+Z events (a) and in W^-Z events (b).

However, as found in Section 7.2, the $|\cos\theta_V|$ and even the 4-category $|\cos\theta_V|$ variables do not provide sufficient discriminative power to ensure enough precision in the measurement of all the joint-polarisation fractions. The discriminating variable chosen, however, is based on a classification DNN using as input fermionic variables that are not independent of $\cos\theta^*_{\ell W}$ or $\cos\theta^*_{\ell Z}$. As a result, the 4-category p_{00}^{DNN} cannot be reweighted with this method. The analytical reweighting will therefore be used in the following to generate the single boson polarisation templates. Using the 4-category $|\cos\theta_V|$ variable, joint-polarisation templates can also be produced at the particle level in the fiducial phase space. In this case, the discriminating power is enough to extract from the inclusive Powheg+Pythia sample joint-polarisation fractions predictions in the fiducial phase space. Collectively, all the polarisation templates obtained with this method applied to the inclusive Powheg+Pythia sample will be labelled `PHPrw`. Similarly, if the reweighting is applied to the inclusive MadGraph0,1j@LO sample, they will be labelled `MGrw`.

7.4 Templates from polarised Monte Carlo generation

The analytical reweighting described in Section 7.3 cannot produce joint-polarisation templates based on the 4-category p_{00}^{DNN} as discriminating variable. Consequently, two approaches making use of the LO polarised `MGgen` samples were developed to produce NLO accurate polarisation templates. The simplest one is to use some kind of reweighting of the polarisation templates from `MGgen` samples to bring them to NLO accuracy. This can be done using the fixed order polarised theoretical calculation at NLO in QCD described in

Section 5.2.3. For the same purpose, a method involving Deep Neural Networks trained to learn the difference between LO and NLO samples can be used. Symmetrically, this new method can polarise an NLO inclusive sample to obtain NLO accurate polarisation templates. It uses DNNs trained to learn the differences between the different joint-polarisation states using the `MGgen` samples. All these methods will provide ultimately four different sets of polarisation templates.

7.4.1 Reweighting polarised LO Monte Carlo samples to NLO predictions

Differently from the MadGraph0,1j@LO generation, calculations using MoCaNLO only give cross sections in predefined phase spaces. It is possible to go beyond the overall fraction prediction by computing differential cross sections, bin-by-bin of a given variable, but the full kinematic description of $W^{\pm}Z$ events as obtained in Monte Carlo generation is out of reach. However, computing NLO theoretical differential cross sections for key variables can be a way to assess the effect of each correction on its distribution, and ultimately correct distributions from Monte Carlo samples. The theoretical prediction for the distribution of the DNN score p_{00}^{DNN}, presented in Section 7.2 and specifically designed for this analysis, was estimated as well by Ansgar Denner and Giovanni Pelliccioli the authors of Ref. [77] in collaboration with my analysis team. The differential cross sections for $|\cos\theta_V|$ and p_{00}^{DNN} are given in Fig. 7.9. Looking at the grey, pink and black line, the non-resonant background and interference contributions look negligible. It is also visible in the ratio from LO to NLO panel of $|\cos\theta_V|$ that in the low $|\cos\theta_V|$ region where the discrimination between TT and 00 joint-polarisation is the best, very strong NLO contribution affect the TT joint-polarisation spoiling the discrimination. It should thus be expected that

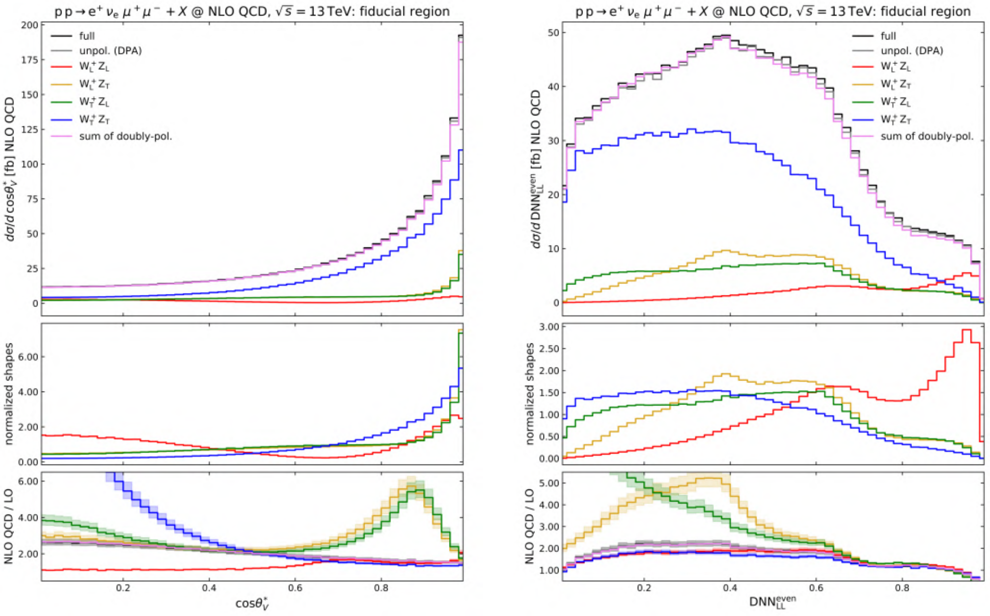

(a) **(b)**

Figure 7.9 Particle-level in the fiducial phase space distribution of $|\cos\theta_V|$ (a) and p_{00}^{DNN} (b) in $pp \to e^+\nu_e\mu^+\mu^-$ events. From top down: NLO QCD differential cross-sections, NLO QCD normalised distribution shapes (integral equal to 1), K-factors (NLO QCD/ LO).

$|\cos\theta_V|$ would loose its discriminative power from higher order in QCD corrections. On the other hand the high $p_{00}^{\rm DNN}$ region critical for the discrimination of 00 against other joint-polarisations is not subject to strong NLO corrections. From there, it is possible to account for the missing virtual NLO corrections in the $p_{00}^{\rm DNN}$ distribution obtained from MadGraph0,1j@LO generation.

Nevertheless, distributions from MoCaNLO are computed at fixed-order in QCD at parton level, as opposed to Monte Carlo generations that include real corrections in parton showers and soft physics effects. As a result, the particle level distributions in `MGgen` samples are not fully comparable to the parton level distributions computed with MoCaNLO. In order to reweight the reference `MGgen` distributions for a given polarisation, labeled $\textsc{MadGraph}_{ref,\rm pol.}$, the following K-factor evaluated in each bin can be used:

$$K_{\rm MG\,p.s.} = \frac{\textsc{MoCaNLO}^{parton}_{\rm pol.}}{\textsc{MadGraph}^{parton}_{ref,\rm pol.}} = \frac{\textsc{MoCaNLO}^{parton}_{\rm pol.}}{\textsc{MadGraph}^{particle}_{ref,\rm pol.}} \cdot \frac{\textsc{MadGraph}^{particle}_{ref,\rm pol.}}{\textsc{MadGraph}^{parton}_{ref,\rm pol.}} \,. \tag{7.34}$$

This factor reweights the `MGgen` samples prediction at parton level to the parton level MoCaNLO prediction, which is similar to reweighting directly the particle level `MGgen` predictions and correcting by a parton shower factor extracted directly from the `MGgen` samples.

This K-factor can be modified by replacing the parton shower term, extracted solely from MadGraph, by a parton shower term making use of the Powheg+Pythia sample:

$$K_{\rm PHP\,p.s.} = \frac{\textsc{MoCaNLO}^{parton}_{\rm pol.}}{\textsc{MadGraph}^{particle}_{ref,\rm pol.}} \cdot \frac{\textsc{Powheg+Pythia}^{particle}_{\rm incl.}}{\textsc{MoCaNLO}^{parton}_{\rm incl.}} \,. \tag{7.35}$$

This time the parton shower correcting factor compares the Powheg+Pythia inclusive prediction to the MoCaNLO inclusive prediction. This factor made visible in Fig. 7.10, is sizeable.

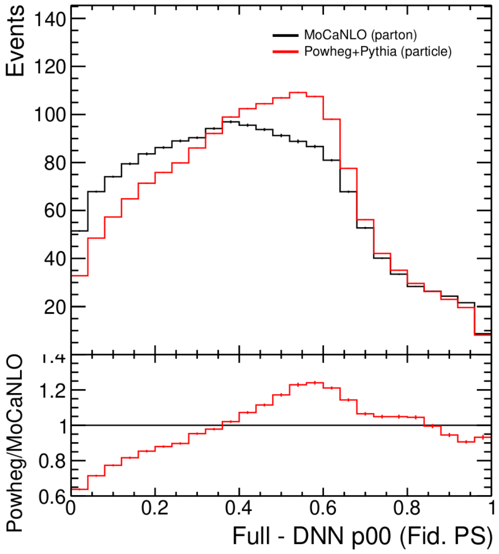

Figure 7.10 Comparison of Powheg+Pythia and MoCaNLO predictions in the fiducial phase space at particle and parton level respectively, for the $p_{00}^{\rm DNN}$ distribution.

Using the factor $K_{\rm PHP\,p.s.}$ assumes similar parton shower corrections for all pure joint-polarisation states. On the other hand, the factor $K_{\rm MG\,p.s.}$ uses parton estimated from a

LO sample corrected for real corrections, while the factor $K_{\mathrm{PHP\,p.s.}}$ uses directly parton showers from NLO samples. Though in both cases the parton shower is generated by PYTHIA, its merging with the original Monte Carlo generation is here not the same. For now, both methods are considered to provide polarised NLO accurate templates of p_{00}^{DNN}. The polarised samples obtained reweighting with the factor $K_{\mathrm{MG\,p.s.}}$ will in the following be collectively labelled `MoCmps` samples. On the other hand, those obtained reweighting with the factor $K_{\mathrm{PHP\,p.s.}}$ will in the following be collectively labelled `MoCpps` samples.

7.4.2 Reweighting with a DNN

A completely different method based on reweighting with a DNN score was developed to obtain NLO accurate templates. This will amount to a multidimensional reweighting.

7.4.2.1 Principle

Let us consider two samples S_A and S_B each associated to the distinct distributions $p_A(x)$ and $p_B(x)$ for a same variable, where x is a vector of observables fully describing a generated event. To morph the distribution of S_A into the distribution of S_B, event by event, the weight $p_B(x)/p_A(x)$ must be used. As described in [110], such weight can be approximated using a classification DNN trained to classify events between S_A, with target one, and S_B, with target zero. Then, for an event x with the score DNN(x), the approximation

$$w(x) = \frac{\mathrm{DNN}(x)}{1 - \mathrm{DNN}(x)} \approx \frac{p_B(x)}{p_A(x)} \,, \tag{7.36}$$

provides the needed weight. This approximation will be tested in the following.

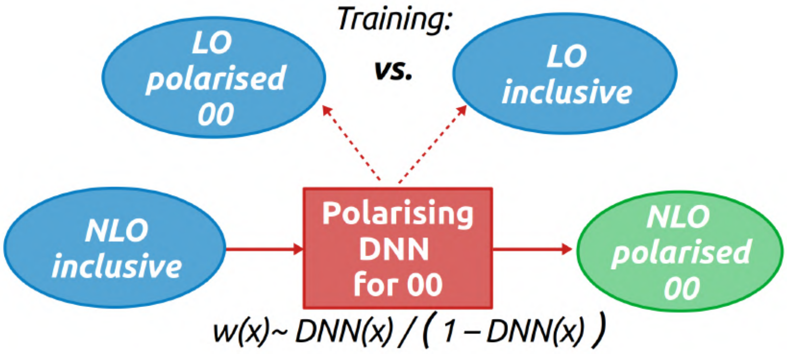

Figure 7.11 Sketch of the DNN-based reweighting of an inclusive NLO sample to a polarised NLO sample for the 00 joint-polarisation state. In blue are the samples used as input, and in green is the newly obtained sample. The DNN represented in red, applying to each event x the weight $w(x) = \mathrm{DNN}(x)/\,(1 - \mathrm{DNN}(x))$, classifies event between the 00 joint-polarisation with target 1 and the inclusive sample with target 0.

In the case of joint-polarisation templates, the distribution of the discriminating variable p_{00}^{DNN} is available at LO polarised from `MGgen` samples and at NLO from the inclusive POWHEG+PYTHIA sample. The goal would be to obtain it at NLO polarised, either reweighting the LO polarised distribution to morph them from LO to NLO, or reweighting the NLO inclusive distribution to morph it into all four joint-polarisation distributions. The latter method is sketched in Fig. 7.11 for the 00 joint-polarisation state.

However, this method relies on the assumption that the polarisation information in the shape of the p_{00}^{DNN} distribution is independent of the generation order in QCD. In other words, the p_{00}^{DNN} distribution $p_{NLO}^{hh'}(x)$ of events x for joint-polarisation hh' at NLO QCD can be factorised as:

$$p_{NLO}^{hh'}(x) \propto p_{LO}(x) \times f_{hh'}(x) \times g_{LO\to NLO}(x) \;, \tag{7.37}$$

with p_{LO} the inclusive distribution at LO, $f_{hh'}$ a polarising factor and $g_{LO\to NLO}$ a polarisation independent factor bringing the LO distribution to NLO QCD. Under such assumption, the polarised `MGgen` samples provide the distribution $p_{LO}(x) \times f_{hh'}(x)$ while the POWHEG+PYTHIA sample provides the distribution $p_{LO}(x) \times g_{LO\to NLO}(x)$.

Consequently, the DNN reweighting to obtain NLO polarised templates relies on the assumptions of Eq. (7.36) and (7.37). Validating these two DNN reweighting assumptions is necessary to ensure that this reweighting really provides a reliable improvement of the polarised `MGgen` samples.

7.4.2.2 Validation of the DNN output to weight approximation

The approximation of Eq. (7.36), that a distribution can be reweighted with a DNN score, is tested in two ways. First, five reweighting DNNs are trained.

- Four DNNs, labelled $\mathrm{DNN}_{hh'}$ are trained on the four polarised `MGgen` samples to classify each between one pure joint-polarisation state hh' and the inclusive MADGRAPH0,1j@LO sample, obtained from the sum of the polarised `MGgen` samples. Under both DNN reweighting assumptions, the $\mathrm{DNN}_{hh'}$ will provide a weight which should approximate the $f_{hh'}$ of Eq. (7.37).

- One DNN labelled $\mathrm{DNN}_{LO\to NLO}$ is trained on the inclusive MADGRAPH0,1j@LO sample and the POWHEG+PYTHIA sample to classify events between LO and NLO. Under both DNN reweighting assumptions, the $\mathrm{DNN}_{hh'}$ will provide a weight which should approximate the $g_{LO\to NLO}$ of Eq. (7.37).

All DNNs needed for the reweighting and its validation were trained using Tensorflow v1.3 [102] with Keras v2.2.4-tf [103] back-end. The training was performed in the total phase space with particle-level samples `MGgen` and POWHEG+PYTHIA. The latter is split in two (training/evaluation samples for $\mathrm{DNN}_{LO\to NLO}$) to avoid biases in the cross-checks. Similarly, each `MGgen` polarised sample is split in four: the first half is split in training and evaluation samples for the $\mathrm{DNN}_{hh'}$, the second half is summed to get an inclusive MADGRAPH0,1j@LO split again in training (for $\mathrm{DNN}_{LO\to NLO}$) and evaluation samples (input to the $\mathrm{DNN}_{hh'}$). This way, each event is only used once in all the validation procedure.

All reweighting DNNs share the same architecture, loss function, and training hyperparameters as the classification DNN defined in Section 7.2. They also share the same input variables which are the inputs used for the classification DNN listed in Table 7.1 extended by four variables. These additional variables hold information about neutrino longitudinal momentum and variables sensitive to NLO effects: the invariant mass of the $W^{\pm}Z$ system m_{WZ}, $|\cos\theta_V|$, $\cos\theta^*_{\ell W}$, and $\cos\left(\theta^*_{\ell Z_{ss}}\right)$, defined as $\cos\theta^*_{\ell Z}$, only considering the decay angle with the lepton of same sign as the $W^{\pm}$ boson charged decay lepton instead of always the negatively charged one.

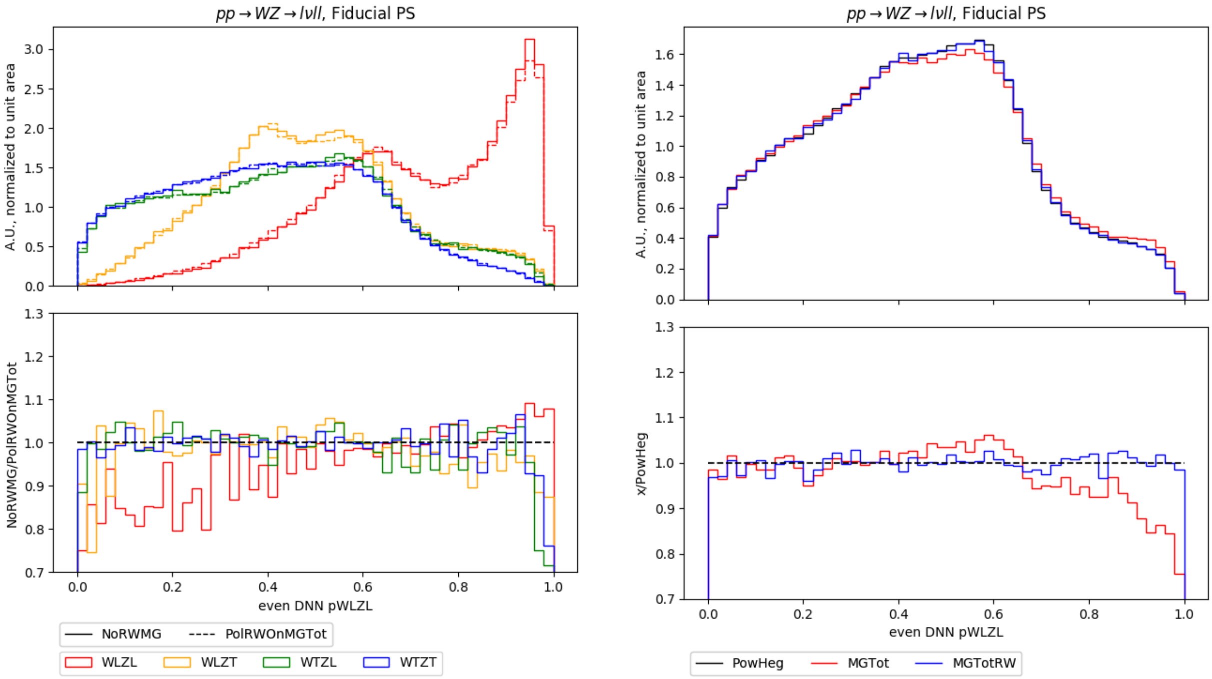

(a) (b)

Figure 7.12 Distributions of p_{00}^{DNN} in the fiducial phase space in $W^{\pm}Z$ events. All distributions were rescaled to the same surface area. In (a), the `MGgen` distributions in solid lines are compared one to one to the reweighted inclusive MadGraph0,1j@LO distributions in dashed lines for all four joint-polarisation states. In (b), the Powheg+Pythia distribution in black is compared to the reweighted inclusive MadGraph0,1j@LO distribution in blue and the original MadGraph0,1j@LO distribution in red. In both cases, the bottom panels provide ratios between the compared distributions.

The first test assesses the validity of the weight approximation for the output of the $\mathrm{DNN}_{hh'}$. The summed MadGraph0,1j@LO samples form an inclusive LO sample. This sample is applied the reweighting from $\mathrm{DNN}_{hh'}$ to obtain a hh' joint-polarisation state sample. This is repeated for all joint-polarisation states creating four reweighted polarised samples. They are then compared one to one to the original `MGgen` polarised samples. In Fig. 7.12(a), the two distributions of p_{00}^{DNN} are found to agree within 10 % for all joint-polarisation states, except for low yield bins where the ratio gets large more easily. Considering that the initial inclusive sample is the same for all joint-polarisation reweighted samples this result is already a good performance. The weights obtained from these $\mathrm{DNN}_{hh'}$ are thus found to approximate correctly $f_{hh'}$.

Symmetrically, the sum of polarised MadGraph0,1j@LO samples is reweighted by $\mathrm{DNN}_{LO\to NLO}$ to obtain an inclusive NLO sample. This sample can then be compared to the Powheg+Pythia sample. In Fig. 7.12(b) the two distributions of p_{00}^{DNN} are found to agree within a few percents. As visible with the representation of the original LO inclusive MadGraph0,1j@LO distribution, the reweighting does make up for the original 10 % to 15 % difference with the NLO Powheg+Pythia. The weight obtained from $\mathrm{DNN}_{LO\to NLO}$ is thus found to approximate correctly $g_{LO\to NLO}$.

7.4.2.3 Validation of the factorisation assumption

The factorisation assumption in Eq. (7.37) can be assessed with a large cross-check using all five reweighting DNNs. Using the reweighting from the $\mathrm{DNN}_{hh'}$ on the NLO inclusive Powheg+Pythia sample should create four polarised samples at NLO with the application of the $f_{hh'}$ factor to the distributions. The polarised samples obtained this way will in the following be collectively labelled `PHPdnn` samples. Alternatively, using the reweighting from $\mathrm{DNN}_{LO\rightarrow NLO}$ on the four polarised LO MadGraph0,1j@LO samples should create four polarised samples at NLO with the application of the $g_{LO\rightarrow NLO}$ factor to the distributions. The polarised samples obtained this way will in the following be collectively labelled `MGdnn` samples.

Comparing the `PHPdnn` and `MGdnn` samples provides a test of the factorisation assumption. In Fig. 7.13(a), the two distributions of p_{00}^{DNN} are found to agree within 10 % for all joint-polarisation states, except for low yield bins where the ratio gets large more easily. This moderate difference has to be compared to the difference between the NLO `PHPdnn` polarised samples and the LO `MGgen` polarised samples visible in Fig. 7.13(b). The differences there reach 20 % and is almost never below 10 % for the 00 joint-polarisation. As a result, the factorisation assumption is considered to be verified.

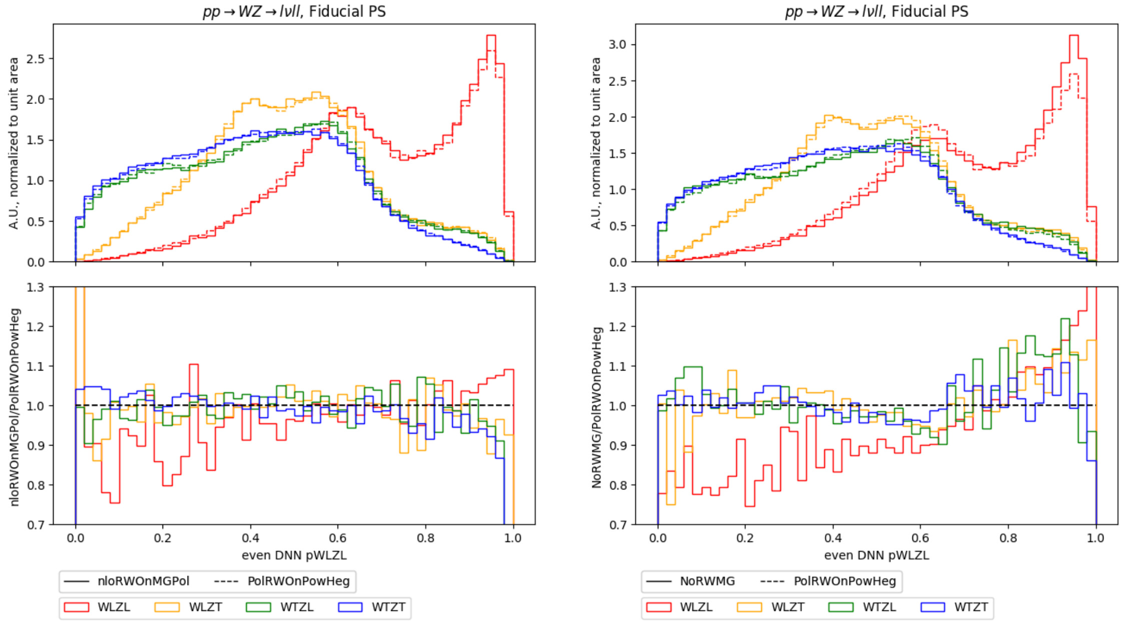

(a) (b)

Figure 7.13 Distributions of p_{00}^{DNN} in the fiducial phase space in $W^{\pm}Z$ events. All distributions were rescaled to the same surface area. In (a), the `MGdnn` distributions in solid line are compared one to one to the `PHPdnn` distributions in dashed lines for all four joint-polarisation states. In (a), the `MGgen` distributions in solid line are compared one to one to the `PHPdnn` distributions in dashed lines for all four joint-polarisation states. In both cases, the bottom panels provide ratios between the compared distributions.

Consequently, the idea of a DNN-based reweighting is validated. It is found to provide two comparable ways to obtain polarised samples at NLO. Additionally, the difference between LO and NLO polarised samples is found to be sizeable, justifying the necessity of such reweighting.

7.5 Need for NLO accurate templates

In the previous sections, many different methods to obtain NLO accurate templates were described and one must be chosen for the final template fit on Run 2 data. To assess their performances, each set of templates is used to fit an NLO inclusive sample at the detector level. The result is compared to the Monte Carlo particle-level expectation. A set of polarisation templates truly NLO accurate should then show no bias.

7.5.1 Summary of polarisation templates sets

Several ways to produce joint-polarisation templates at detector level of the 4-category p_{00}^{DNN} have been presented. The following two methods can already be discarded as fatally flawed in the context of joint-polarisation states:

- The direct Monte Carlo generation with MadGraph0,1j@LO described in Section 5.3.2 produces four joint-polarisation templates labelled `MGgen`. They are generated at LO, but the merging with an additional jet allows to emulate real NLO corrections. They are nevertheless far from being NLO accurate.
- The analytical reweighting described in Section 7.3 performs well in generating polarisation templates for the discriminating variables $q_W \cdot \cos\theta^*_{\ell W}$ or $\cos\theta^*_{\ell Z}$. This allows for single boson polarisation measurement. However, this method cannot use the classification DNN score p_{00}^{DNN} because it uses leptonic variables as input. This reweighting is applied to the inclusive Powheg+Pythia sample to get templates labelled `PHPrw` with as discriminating variable the 4-category $|\cos\theta_V|$. As shown in Section 7.2, this variable is not discriminative enough to allow for the measurement of joint-polarisation fractions.

Theoretical calculations at parton level described in Section 5.2.3 provide the NLO prediction for the distribution of p_{00}^{DNN}. These theoretical distributions can be used to obtain K-factors to bring the `MGgen` distribution of p_{00}^{DNN} to NLO as described in Section 7.4.1. These calculations being at parton level, a procedure has to be defined to get to particle-level NLO samples. Two ways to do this were presented:

- Using factor $K_{\text{MG p.s.}}$ of Eq. (7.34) to reweight the p_{00}^{DNN} distribution from polarised `MGgen` samples – that is using some kind of MadGraph parton shower effect – provides templates labelled `MoCmps`.
- Using factor $K_{\text{PHP p.s.}}$ of Eq. (7.35) to reweight the p_{00}^{DNN} distribution from polarised `MGgen` samples – that is using some kind of Powheg+Pythia parton shower – provides templates labelled `MoCpps`.

A method of reweighting using a classification DNN score is described in Section 7.4.2. This can be used either to reweight a polarised sample from LO to NLO, or to reweight an inclusive NLO sample in order to polarise it. These produces two sets of templates:

- A DNN is trained to discriminate one polarisation state against their inclusive sum, using in the training the polarised `MGgen` samples. This is repeated for each of the four polarisation states creating four polarising DNNs. Each is used to reweight the inclusive NLO Powheg+Pythia sample to obtain the four polarisation templates labelled `PHPdnn`.

- A DNN is trained to classify between LO and NLO inclusive samples, using in the training the inclusive NLO Powheg+Pythia sample and the inclusive MadGraph0,1j@LO sample. It is used to reweight distributions from LO to NLO. Applied on the polarised `MGgen` samples, polarisation templates labelled `MGdnn` are obtained.

These six different ways of generating polarised templates are summarised in Table 7.3. They are all shown in Fig. 7.14 for the distribution of p_{00}^{DNN} at detector level in all polarisation states. The templates `MGgen` being at LO, they will only be used as point of comparison to assess the change in templates emulating NLO in QCD. Strong deviations from it are visible, of up to 25 % depending on the alternative template. Deviations among the other templates are also clearly visible, indicating that they do not all emulate correctly NLO corrections. The set of templates `PHPrw` are unable to get a polarised distribution of the p_{00}^{DNN} as is clear on the figure. These templates will still be used to get the expected value of polarisation fractions at particle level from the inclusive Powheg+Pythia sample as is described in the next section.

Table 7.3 The six different ways to obtain polarisation templates. The original Monte Carlo sample designates the sample used as input of the method, either to polarise it or bring it to NLO accuracy.

Name	**Original Monte Carlo sample**	**Method used**	**LO/NLO**
`MGgen`	Polarised MadGraph0,1j@LO	Polarised Monte Carlo generation (Section 5.3.2)	LO
`PHPrw`	Powheg+Pythia	Analytical reweighting (Section 7.3)	NLO
`MoCmps`	Polarised MadGraph0,1j@LO	Reweighting to NLO QCD calculation using $K_{\mathrm{MG\,p.s.}}$ (Section 7.4.1)	NLO
`MoCpps`	Polarised MadGraph0,1j@LO	Reweighting to NLO QCD calculation using $K_{\mathrm{PHP\,p.s.}}$ (Section 7.4.1)	NLO
`MGdnn`	Polarised MadGraph0,1j@LO	DNN reweighting LO→NLO (Section 7.4.2) Trained on: MadGraph0,1j@LO and Powheg+Pythia	NLO
`PHPdnn`	Powheg+Pythia	Polarising DNN reweighting (Section 7.4.2) Trained on: Polarised MadGraph0,1j@LO	NLO

7.5.2 Particle level expectation for fractions

To select the most accurate set of polarisation templates, a bias study is performed. This requires to have an idea of what are the expected values for the fractions extracted from inclusive Monte Carlo samples.

Polarisation fractions were extracted from the inclusive Powheg+Pythia sample at particle level in the total phase space thanks to analytical fits or the moments method described in Section 5.4. However, the Monte Carlo expectations for fractions obtained in Tables 5.2 and 5.3 are not comparable to the measured fractions which are obtained at the particle level in the fiducial phase space. To extract the particle-level expectation in this phase space, such analytical methods do not work, the fiducial cuts distorting the shape of the $q_W \cdot \cos\theta^*_{\ell W}$ and $\cos\theta^*_{\ell Z}$ variables.

Therefore, a template fit is used, just as described in Section 7.1, but using polarised templates at particle level in the fiducial phase space. Additionally, being at particle level, no backgrounds or systematic uncertainties appear. The `PHPrw` set of templates obtained from the analytical reweighting of the inclusive Powheg+Pythia sample is used for this fit. For single boson polarisation, $q_W \cdot \cos\theta^*_{\ell W}$ and $\cos\theta^*_{\ell Z}$ are used as discriminating

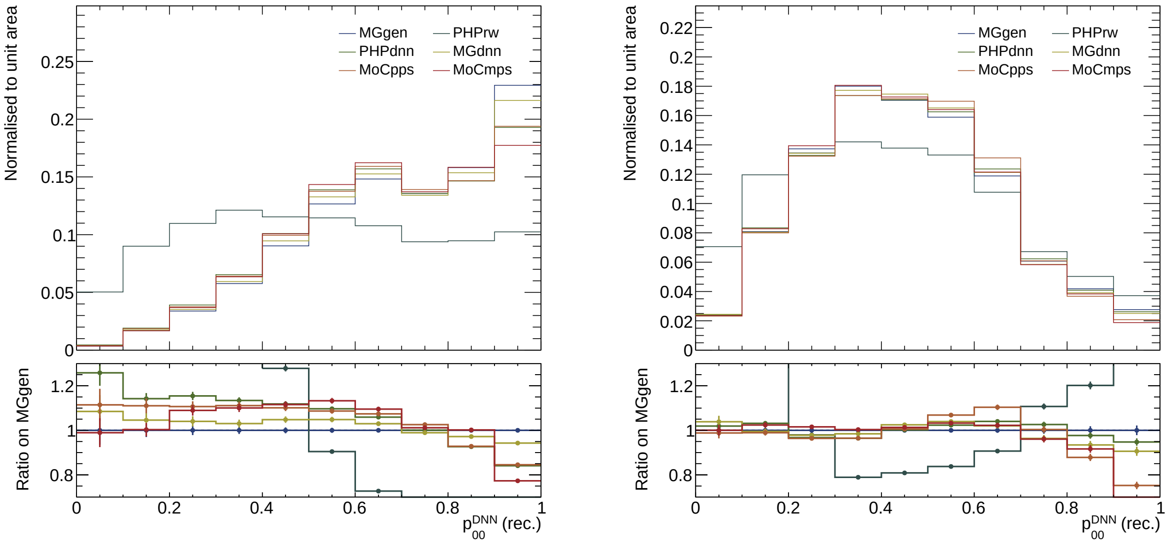

(a) 00 **(b)** $0T$

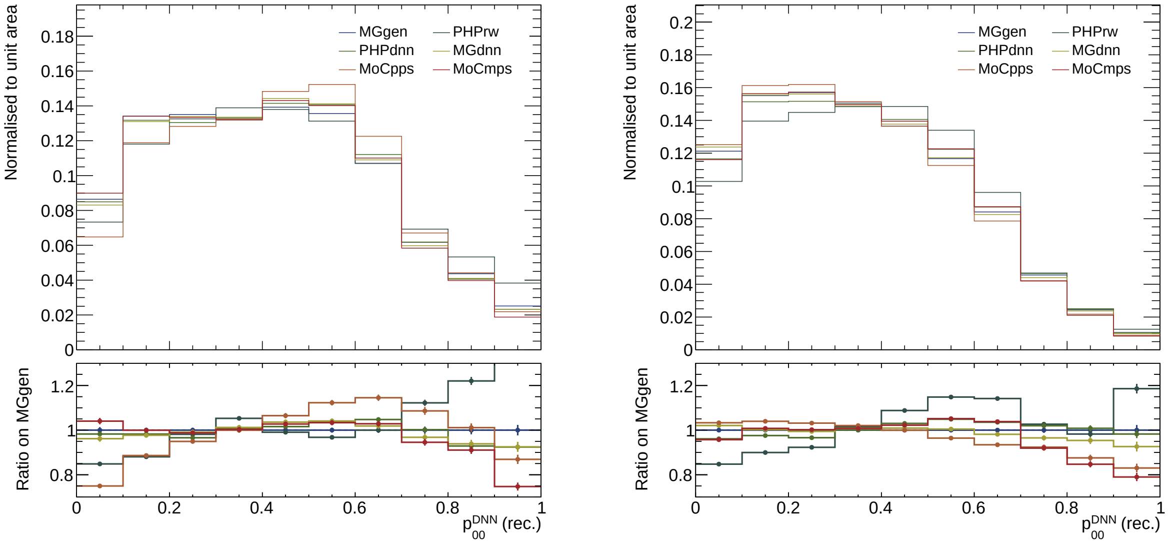

(c) $T0$ **(d)** TT

Figure 7.14 Distributions at detector level of p_{00}^{DNN} for the six sets of polarisation templates at hand `MGgen`, `PHPrw`, `MGdnn`, `PHPdnn`, `MoCmps` and `MoCpps`, for $W^{\pm}Z$ events and for polarisations 00 (a), 0T (b), T0 (c) and TT (d). These templates were all rescaled to the same surface area.

variables respectively for the $W^{\pm}$ boson and the Z boson. For joint-polarisation, the 4-category $|\cos\theta_V|$ is used as discriminating variable. Simultaneously, the Powheg+Pythia sample is the pseudo-dataset fitted. This template fit is therefore what is called an Asimov fit, since it was shown that one expects perfect closure in this case in Section 7.3.3. The pre-fit proportions of the polarised template would give the same fractions as the fit, but using the fit framework also provides the associated uncertainty from statistical origin. This allows considering the results of such fit of the inclusive Powheg+Pythia sample as close as possible to the true polarisation fractions content in the fiducial phase space that are built in the Powheg+Pythia Monte Carlo generation. The values extracted this way for the joint-polarisation fractions are used as the reference in the bias study performed in the next section, and visible in Fig. 7.15.

7.5.3 Bias study on all sets of polarisation templates

Among the five possible ways to generate polarisation templates of the discriminating variable 4-category p_{00}^{DNN} described in Section 7.5.1, that is `MGgen`, `MGdnn`, `PHPdnn`, `MoCmps` and `MoCpps`, one is chosen to perform the final template fit while the others will be used to assess modelling uncertainties, as described ahead in Section 7.6.2. All the following fits will be signal only without any systematic uncertainty implemented, to isolate the differences between the five methods.

To find how well the sets of templates reach NLO accuracy, they are all made to fit the inclusive Powheg+Pythia sample at detector level. The reference truth value is obtained as described in Section 7.5.2. The results are presented in Fig. 7.15. Here, the fits are performed in $W^{\pm}Z$ events, but also on the two subsets defined by the charge of the $W^{\pm}$ boson, $W^{+}Z$ and $W^{-}Z$ events.

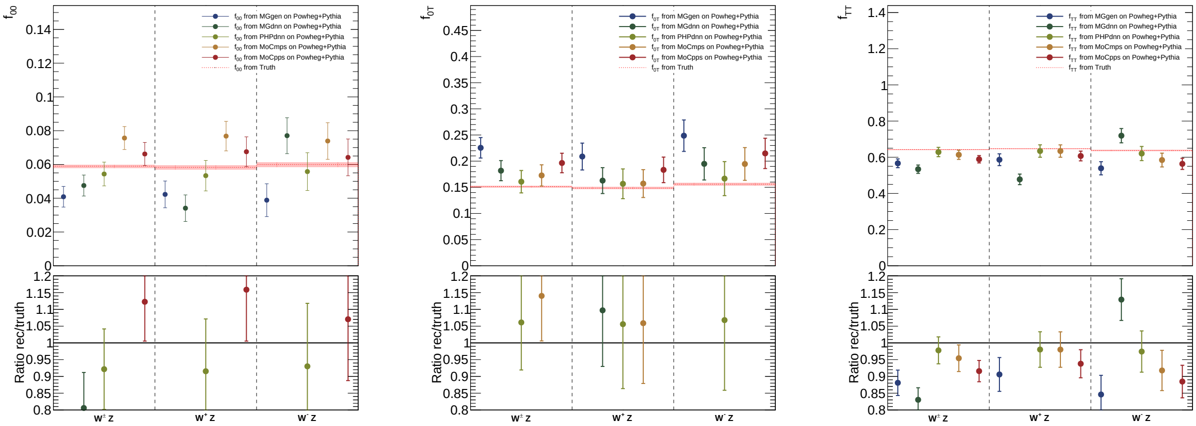

(a) f_{00} **(b)** $f_{0\mathrm{T}}$ **(c)** f_{TT}

Figure 7.15 Results of signal only fits of Powheg+Pythia at detector level for the parameters of interest f_{00} (a), $f_{0\mathrm{T}}$ (b) and f_{TT} (c) for all five templates `MGgen`, `MGdnn`, `PHPdnn`, `MoCmps` and `MoCpps` in all charge configurations. Uncertainties are from statistical origin only.

Some bias clearly appears in these results for all templates. The true value should be in 68 % of cases within the uncertainty bar (*i.e.* one sigma interval) of the fit result, so perfect closure is not expected. It is visible that `MGgen` has a big bias that some kind of reweighting to the NLO corrects. The template `PHPdnn` is found to have the smallest bias by far. Templates originating from MadGraph all have a significant bias as well, the various corrections to NLO helping to reduce it. Among them, `MoCpps` performs better for f_{00} while `MoCmps` is better in $f_{0\mathrm{T}}$ and f_{TT}, but the bias is always much bigger than for `PHPdnn`. To validate this, the same test is performed but fitting this time the MadGraph@NLO inclusive sample described in Section 5.3.1. The reference values are kept the same as the one extracted from Powheg+Pythia, as no major differences in polarisation content are found between the two NLO inclusive samples. Again, as visible in Fig. 7.16, `PHPdnn` clearly is the least biased sample. This indicates that this property is not originating from some link between the derivation of `PHPdnn` templates and the Powheg+Pythia sample. Consequently, `PHPdnn` is chosen as the baseline set of polarisation templates for the final fit.

The `MGgen` templates are not NLO accurate. They cannot be used to extract polarisation fractions, as NLO effects (among which virtual corrections) on the shape of polarisation templates are not negligible and need to be taken into account to avoid biases. From this

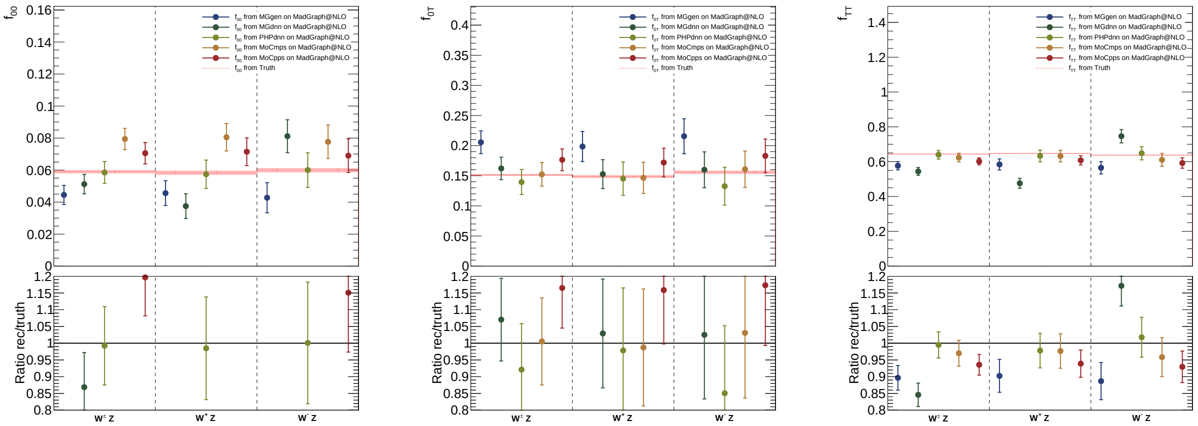

(a) f_{00} **(b)** $f_{0\mathrm{T}}$ **(c)** f_{TT}

Figure 7.16 Results of signal only fits of MadGraph@NLO at detector level for the parameters of interest f_{00} (a), $f_{0\mathrm{T}}$ (b) and f_{TT} (c) for all five templates `MGgen`, `MGdnn`, `PHPdnn`, `MoCmps` and `MoCpps` in all charge configurations. Uncertainties are from statistical origin only.

study, the reweighting to NLO of a single variable at generated level, as done in the `MoCpps` and `MoCmps` sets of templates, is found to be less efficient than the more general DNN reweighting which acts as some sort of multi-dimensional reweighting.

For single boson polarisation templates, only the `PHPrw` set is available to extract f_0, f_{L} and f_{R}, and is expected to be NLO accurate. Still, similar bias study are performed comparing its performance to the `MGrw` templates obtained by reweighting the inclusive MadGraph0,1j@LO sample with the analytical reweighting. A sizeable bias of at most more than one standard deviation is found for the values of the parameters of interest f_0 and $f_{\mathrm{L}} - f_{\mathrm{R}}$ extracted using the `MGrw` templates. On the other hand, the `PHPrw` templates extract fractions with almost no bias, even when fitting the alternative inclusive NLO sample MadGraph@NLO. This shows that some NLO accuracy is transmitted from the original inclusive Monte Carlo sample to the polarisation templates through the analytical reweighting.

7.6 Uncertainties

With the 4-category p_{00}^{DNN} as discriminating variable and the set of polarisation templates `PHPdnn` identified as NLO accurate, everything is ready to perform the template fit. This fit should incorporate systematic uncertainties from backgrounds, particle reconstructions, Parton Distribution Functions (PDF) or the QCD renormalisation scale μ_R and factorisation scale μ_F used in the Monte Carlo generation. The main uncertainty in this analysis will arise from modelling uncertainties, estimating the remaining inaccuracies in the shape of the polarisation templates.

7.6.1 The treatment of systematic uncertainties

Systematic uncertainties are taken into account in a binned maximum-likelihood template fit using nuisance parameters α_{NP}. Considering a systematic uncertainty applying to backgrounds, for example an overall normalisation uncertainty as in Section 6.3.1, the associated nuisance parameter is incorporated in the likelihood in two places:

$$L(\mu; N) = \mathcal{P}\left(N|\mu S + f(\alpha_{\mathrm{NP}})B\right)\ \mathcal{G}(\alpha_{\mathrm{NP}})\ , \tag{7.38}$$

where $f(\alpha_{\mathrm{NP}})$ is the response function and $\mathcal{G}(\alpha_{\mathrm{NP}})$ is the constraint term. The response function encodes how the nuisance parameter acts on the background or signal model. The constraint term reflects additional knowledge available on this nuisance parameter. Typically, the nuisance parameter is a random variable centred on zero, with a standard deviation of one and the constraint term acts as its probability density function.

In this analysis, the response function of systematic uncertainties are implemented in two ways:

Overall normalisation uncertainties : Typically of $x\,\%$ on a background, they are modeled with a response function $f(\alpha_{\mathrm{NP}}) = (1 + \alpha_{\mathrm{NP}} \times x/100)$ applied across all bins on the background template.

Shape uncertainties : the nuisance parameters has a response function based on *Up* and *Down* variations. By a procedure depending on the underlying physical systematic uncertainty, bin by bin, the template for a background or signal is modified by the nuisance parameter. The obtained modified shapes for the nuisance parameter, up or down by one standard deviation, creates histograms for *Up* and *Down* variations. With a variety of possible procedures, the template is morphed continuously from the *Down* variation to the *Up* variation through the nominal histogram. If the *Up* and *Down* variations are normalised to the nominal template normalisation, the effect of the uncertainty is purely on shape. Otherwise, it can also have a normalisation effect.

In `HistFactory`, by default, all the constraint terms are standardised gaussian distributions and the morphing is based on a piecewise linear interpolation between the three known histograms [108].

Then, from a statistical point of view, the nuisance parameter is treated as any other variable of the likelihood. As a result, just like parameters of interests, after the fit (*post-fit* as opposed to *pre-fit*, before the fit), its value can deviate from zero if it is found to help maximise the likelihood. In this case, the nuisance parameter is said to be pulled. The uncertainty on this parameter can also be extracted similarly as for a parameter of interest. If the uncertainty is below one, the parameter is said to be over-constrained by the fit. This means that the fit allowed to improve the understanding of the value of the nuisance parameter. Depending on the nature of the underlying systematic uncertainty, pulls or over-constraints can be legitimate or indicate a mismodelling or a wrong parametrisation of the fit.

7.6.2 Modelling uncertainties

7.6.2.1 Principle of modelling uncertainty

Modelling uncertainties for polarisation templates are extracted using alternative template sets. A procedure to be detailed further will use these alternative templates to produce two variation templates labelled *Up* and *Down*. Yet, these labels are somewhat arbitrary and do not imply anything about the position of these variations compared to the nominal one. One can represent in the most formal way these variations for a bin i and a polarisation h, by

$$U_i^h = T_i^h + \Delta_i^h \ , \tag{7.39}$$

$$D_i^h = T_i^h - \Delta_i^h \ , \tag{7.40}$$

where U (resp. D) is the *Up* (resp. *Down*) variation and T is the nominal template. The deviation Δ is chosen the same for both variations for reasons of symmetry. The procedure to extract the Δ should be such that bin-to-bin correlations are kept, and as a consequence this Δ can be positive or negative.

In the case of single boson polarisation templates, an additional property arises from the way the polarisation templates are generated. They are obtained from the analytical reweighting and therefore all sum up to the inclusive distribution as demonstrated in Section 7.3.3. This happens because the weights used to polarise all sum up to one by construction. This means that their sum should give back the inclusive distribution $(\sigma_i)_{1\leq i\leq n}$ and N_{tot} is extracted independently of the fractions. As a result, one desirable property for modelling variations is that they would respect this. This is achieved in two ways. First, a single nuisance parameter is associated to all polarisation templates to parametrise their joint modelling uncertainty (and not one per template). Secondly, the normalisation relationship

$$\forall i, \ \sum_h T_i^h = \sigma_i \ ,$$

is enforced on the variations, yielding the following property of Δ:

Property 1 (Reweighting normalisation)

$$\forall i, \ \sum_h \left(T_i^h + \Delta_i^h\right) = \sigma_i \Leftrightarrow \forall i, \ \sum_h \Delta_i^h = 0 \ .$$

Finally, the templates will be fitted and their overall integral will change. The modelling uncertainty accounts for our imperfect knowledge of the shape of the polarisation templates, but not for overall scale uncertainties. At the generated level in the fiducial phase space, where the fraction and overall normalisation N_{tot} are extracted, the variation templates should have the same integral as the nominal one. Then, at the detector level some overall normalisation differences can arise from different reconstruction efficiency in bins of the template distribution. As a result, it is desirable that the *Up* and *Down* variations have the same integral as the nominal template at particle level in the fiducial phase space. This entails, for the variation Δ the property:

Property 2 (Shape-only variation)

$$\forall h, \ \sum_i U_i^{h,\text{Fid}} = \sum_i T_i^{h,\text{Fid}} \Leftrightarrow \sum_i \Delta_i^{h,\text{Fid}} = 0 \ .$$

7.6.2.2 The reweighting uncertainty

For the single boson polarisation measurement, we have at hand three different sets of templates: `PHPrw`, `MGrw` and `MGgen`. The main one, used in the template fit is `PHPrw`. The two others will be used to extract a modelling uncertainty assessing how the analytical reweighting procedure degrades a polarisation template. To simplify the notations, bin i of a template of polarisation h is noted P_i^h if it comes from the `PHPrw` set, G_i^h if it comes from the `MGgen` set and R_i^h if it comes from the `MGrw` set.

The templates `MGrw` come from the reweighting of the sum of the `MGgen` samples and consequently, any differences with the `MGgen` templates is directly a sign of mismodelling by the analytical reweighting. The `MGgen` sample only exist for the longitudinal 0 and transverse T polarisations for both boson, so the comparison can only be done for these two polarisation templates. It is worth noticing that the normalisation relationship of the analytical reweighting translates in the following formula:

$$\forall i,\ R_i^0 - G_i^0 = -\left(R_i^T - G_i^T\right)\ . \tag{7.41}$$

To have the generated *true* template to be within the uncertainty bands of the reweighted template:

$$\forall h, \forall i,\ R_i^h + \Delta_i^h \geq G_i^h \geq R_i^h - \Delta_i^h\ .$$

Choosing one of the cases of equality brings

$$\forall h, \forall i,\ \Delta_i^{h\ \mathrm{MG}} = G_i^h - R_i^h\ ,$$

and of course with Eq. (7.41) ensues $\forall i,\ \Delta_i^{0\ \mathrm{MG}} = -\Delta_i^{T\ \mathrm{MG}}$.

This difference is used to create a modelling uncertainty for the longitudinal polarisation template by rescaling it to the fiducial cross section σ^{Fid} of the `PHPrw` template. For the left-handed L and right-handed R polarisation templates, the same difference Δ^0 is used with appropriate factors to enforce Property 1 of reweighting normalisation. This gives

$$\forall i, \left\{ \begin{array}{lcl} \Delta_i^0 & = & \left(G_i^0 - R_i^0\right) \frac{\sigma^{\mathrm{Fid}}_{P^0}}{\sigma^{\mathrm{Fid}}_{R^0}} \\ \Delta_i^L & = & -\frac{1}{2}\Delta_i^0 \\ \Delta_i^R & = & -\frac{1}{2}\Delta_i^0 \end{array} \right. \ , \tag{7.42}$$

where $\sigma^{\mathrm{Fid}}_{P^0}$ (resp. $\sigma^{\mathrm{Fid}}_{R^0}$) is the fiducial cross section of the `PHPrw` (resp. `MGrw`) template.

This modelling uncertainty enforces by default Property 1 of reweighting normalisation. Additionally, it still works in the case of MadGraph as again $\Delta_i^T = -\Delta_i^0$. Additionally, though the templates `MGgen` and `MGrw` do not have exactly the same normalisation, they are very close. As such, Property 2 of shape only variation is not verified, but the impact on the overall normalisation will be very small. This difference can be considered as an additional degradation of the analytical reweighting method which is covered by the modelling uncertainty.

The resulting *Up* and *Down* variations for this modelling uncertainty are represented for the polarisation templates of the $W^{\pm}$ boson in Fig. 7.17 for the distributions used as inputs to the template fits. The opposite directions of one variation from the 0 template to the L and R template, a sign of Property 1, is clearly visible.

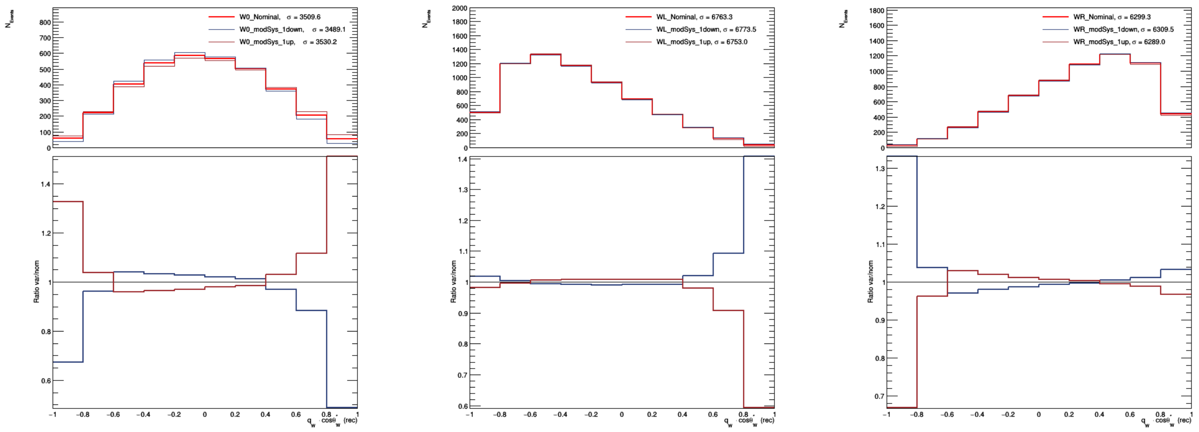

(a) W_0 **(b)** W_L **(c)** W_R

Figure 7.17 Modelling uncertainty *Up* and *Down* variations on the distributions of $q_W \cdot \cos\theta^*_{\ell W}$ in $W^\pm$ template 0 (a) template L (b) and template R (c). The bottom panels provide ratios of the variations to the nominal distribution.

For joint-polarisation templates, a similar systematic uncertainty is developed to account for uncertainties from the DNN reweighting. As described in Section 7.4.2, the principle of this method is validated by the closure of Fig 7.12(a). This closure compares the `MGgen` samples to their sum reweighted by the DNN in the same fashion as `PHPdnn`. This is exactly equivalent to the comparison between the `MGgen` and `MGrw` templates described above.

A similar modelling uncertainty is thus implemented using the small non-closure of figure 7.12(a). Property 1 of reweighting normalisation, can be relaxed here as the four polarisation templates arise from four different MadGraph generations. Thus changes in the shape of one template has no reason to affect the shapes of the others. Noting for polarisation h, G^h the `MGgen` template, R^h the template obtained by re-polarising with the DNN reweighting the inclusive MadGraph0,1j@LO sample from the sum of the `MGgen` templates, and P^h the `PHPdnn` template, the variations Δ_i for bin i are

$$\forall i,\ \forall h \in \{00, 0T, T0, TT\}\,,\ \Delta_i^h = \left(G_i^h - R_i^h\right) \frac{\sigma^{\text{Fid}}_{P^h}}{\sigma^{\text{Fid}}_{R^h}}\ . \tag{7.43}$$

There, $\sigma^{\text{Fid}}_{P^h}$ (resp. $\sigma^{\text{Fid}}_{R^h}$) is the fiducial cross section of the `PHPdnn` (resp. the MadGraph0,1j@LO re-polarised by the DNN template). They are used to rescale the non-closure to the fiducial cross section of `PHPdnn` and thus extract a variation used for the uncertainty.

This provides a modelling uncertainty targeting the remaining non-closure of the DNN-based reweighting. This uncertainty of the method is associated to a single nuisance parameter just as in the single boson polarisation case , labelled α`_theo_ModSys_DNNrw` . This one nuisance parameter is correlated to all polarisations as it is an uncertainty on the DNN reweighting method, which uses DNNs with the same structure, with the same input variables and trained on different combinations of the same four `MGgen` polarised samples.

7.6.2.3 Alternative polarisation templates uncertainty

In joint-polarisation measurement many sets of templates were developed. As detailed in Section 7.5, templates from `PHPdnn` are chosen as baseline for the final template fit.

However, as visible in Fig. 7.15 the choice of a set of template can have big repercussions on the measured value of the joint-polarisation fraction. An uncertainty associated to this choice of template set is derived considering one alternative set.

The initial variation Δ is taken to be the difference between the nominal `PHPdnn` sample and the second least biased one. This is the template `MoCpps` for f_{00}, and `MoCmps` for $f_{0\mathrm{T}}$ and f_{TT} as can be seen in Fig. 7.15 and 7.16. These two other templates have additionally the advantage of originating from a method that is completely independent of the one used for `PHPdnn`. The choice between `MoCmps` and `MoCpps` amounts to choosing between a low bias on f_{00} and a low bias on the two other fractions. Due to the large correlations between the fractions, `MoCmps` is chosen.

To enforce Property 2, the template `MoCmps` is first rescaled to the `PHPdnn` particle-level in the fiducial phase space cross section. This yields for a template of polarisation $h \in \{00, 0T, T0, TT\}$ the difference Δ_i^h in bin i,

$$\Delta_i^h = \mathtt{MoCmps}_i^h \frac{\sigma^{\mathrm{Fid}}_{\mathtt{PHPdnn}^h}}{\sigma^{\mathrm{Fid}}_{\mathtt{MoCmps}^h}} - \mathtt{PHPdnn}_i^h \ , \tag{7.44}$$

with σ^{Fid} the cross section of the templates at the particle level in the fiducial phase space.

With such an implementation, the *Up* variation, that is "nominal+Δ" corresponds to a rescaled version of the `MoCmps` template while the nominal variation is the `PHPdnn` template. There is no physical meaning in having a *Down* variation, "nominal-Δ", as this does not correspond to an alternative polarisation template. The *Down* variation is thus chosen equal to the nominal. These are associated to one nuisance parameter labelled α`_theo_ModSys_MoCmps` . It parametrises the global choice between the two main template sets, hence why the same one parameter is applied to all polarisations at once. Because of how its response function is implemented, it might get pulled from 0 to around 1, implying a more "`MoCmps` shape" than expected, but should not be pulled much more outside $[0, 1]$ as this would lead the fit to use shapes that are too far from an actual template and thus have no physical meaning. The specificities of this modelling uncertainty imply that the default gaussian constraint used for other systematics cannot be used here. The constraint term of this uncertainty is designed to be flat between 0 and 1, reflecting indifference between `PHPdnn` and `MoCmps`, and should avoid pulling much further than 1. This modelling uncertainty ultimately is not allowed to give shapes other than `PHPdnn`, `MoCmps` or in between. A fitting constraint term is implemented thanks to a double Fermi distribution

$$f_{\text{Double Fermi}}(x) = \frac{1}{1+\exp\left(-\frac{x-0.5}{0.1}\right)} \times \frac{1}{1+\exp\left(\frac{x-1.5}{0.1}\right)} \ . \tag{7.45}$$

The parameters of the probability distribution are chosen to have a flat curve between 0 and 1, and steep dives from 1 to 2 and symmetrically from 0 to -1. This distribution is visible in Fig. 7.18.

For single boson polarisation templates, a similar uncertainty is derived from an alternative set of polarisation template: the inclusive NLO SHERPA sample described in Section 5.3 is reweighted with the analytical reweighting to provide a set of polarisation templates labelled `SHrw`. An important feature of the SHERPA sample is that it relies on its own parton shower algorithm, as opposed to the MADGRAPH or POWHEG samples that are all interfaced with PYTHIA for this purpose. Comparing the baseline `PHPrw` templates

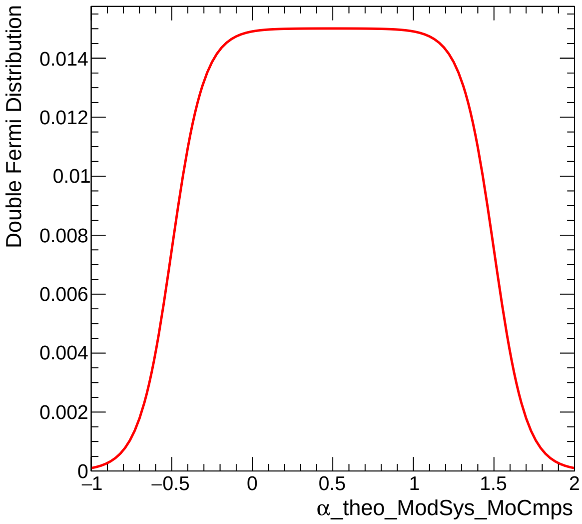

Figure 7.18 The double Fermi probability density function used as constraint term in the fit.

to the alternative `SHrw` templates provides a conservative uncertainty covering for parton shower uncertainties.

For each polarisation, the template `SHrw` is rescaled to the same integral as the nominal `PHPrw`. Then the difference Δ_i is extracted in each bin i. The obtained histogram of Δ is then smoothed. Then, the statistical fluctuations on Δ are removed in each bin i using the following procedure

$$\forall i,\ \Delta_i^{'} = \begin{cases} 0 & \text{if} |\Delta_i| < |Stat_i| \\ sign(\Delta_i)\left(|\Delta_i| - |Stat_i|\right) & \text{else} \end{cases} \tag{7.46}$$

where $Stat_i$ is the statistical uncertainty on Δ_i propagated from the uncorrelated statistical uncertainties of `PHPrw` and `SHrw` in bin i. The modified $\Delta^{'}$ difference is then used to get *Up* and *Down* variations.

7.6.3 Other systematic uncertainties

In the final fit, in addition to all the polarisation templates, the contribution from irreducible backgrounds as described in Section 6.3.1 along with the Matrix Method estimate for all reducible backgrounds, described in Section 6.3.2 are considered in the signal region. In addition to the modelling uncertainties described in Section 7.6.2 that are specific to this polarisation measurement, various other more usual systematic uncertainties are considered.

Systematic uncertainties originating from physics object reconstruction and calibration in the detector are propagated to the shape of the final fit templates. They arise from dedicated algorithms developed by the combined detector performance groups of ATLAS:

- The uncertainties due to electrons and muons reconstruction, identification, isolation requirements and trigger efficiencies as well as in the lepton momentum scale and resolution are assessed using tag-and-probe methods in $Z \to \ell\ell$ events [94, 95, 111]. For the measurements of fractions in the $W^{\pm}$ charge-dependent subsets of $W^{+}Z$ and $W^{-}Z$ events, an uncertainty arising from the charge misidentification of electrons is also considered.

- The uncertainties on the jet energy scale and resolution are based on their respective measurements in data [112].
- The uncertainties on $E_{\mathrm{T}}^{\mathrm{miss}}$ are estimated by propagating the uncertainties on the transverse momenta of reconstructed objects and by applying momentum scale and resolution uncertainties to the track-based soft term [100].
- A variation in the pile-up reweighting of Monte Carlo samples is included under the name `PRW_DATASF` to cover the uncertainty on the ratio between the predicted and measured inelastic cross-Section [113].

They are implemented as shape uncertainties on the polarisation templates and main backgrounds ZZ and $t\bar{t}+V$, but can have an effect on normalisation *e.g.* for lepton isolation efficiency uncertainty. The associated nuisance parameters have names of the form α`_obj_`* and are labelled physics object systematic uncertainties.

Theory systematic uncertainties from the Parton Distributions Functions (PDF) and the QCD renormalisation scale μ_R and factorisation scale μ_F impact the shape of the signal and background templates in the signal region. The QCD scale and PDF uncertainties are implemented as shape uncertainties on the signal polarisation templates.

- The QCD scale uncertainty is evaluated with the 7-point scale variation that is varying independently μ_R and μ_F at half or double of their nominal value, with the constraint $0.5 \leq \mu_R/\mu_F \leq 2$, in the POWHEG+PYTHIA sample. The extreme variations among the seven are taken as *Up* and *Down* variations.
- The uncertainties due to the PDF and the α_{s} value used in the PDF determination are evaluated using the PDF4LHC prescription [114].

Here, the *Up* and *Down* variations are rescaled to the generator level in the fiducial phase space normalisation of the nominal template to only take into account effects in the reconstruction efficiency and in the shape of distributions, without acceptance effects. The associated nuisance parameters have names of the form α`_theo_`* and are labelled theory systematic uncertainties, together with the modelling uncertainties.

Shape and normalisation uncertainties on the ZZ background process, the dominant background in the signal, are implemented in the fit with theory systematics from QCD scale and PDF obtained exactly as for the signal, barring the normalisation at generator level in the fiducial phase space step. A ZZ control region is added in the final fit to constrain the nuisance parameters associated to each of these uncertainties in both regions. This control region, as already described in Section 6.3.1, is obtained by inverting the fourth lepton veto in Table 6.3. The total number of events in this control region is fitted simultaneously with the signal region in the final fit. The yields in this region are estimated with the same background samples as in the signal region. The $W^{\pm}Z$ signal events, here treated as an additional background with an overall uncertainty of 5 %, is estimated by the POWHEG+PYTHIA sample. The rescaling of the Monte Carlo samples to the data yield in this region will constrain and possibly pull the nuisance parameters associated to the theory uncertainties of the ZZ background process. The associated nuisance parameters have names of the form α`_theo_ZZ_`* and are grouped with theory systematic uncertainties.

Irreducible background processes implemented are the ZZ background, the $t\bar{t}+V$ background, the τ decay background, and grouped in the *Others* category, the tZ, VVV, $WZjj$–EW and migrating γ^* subdominant background processes. Barring the ZZ background process, each is associated with an overall normalisation uncertainty devised in

Section 6.3.1. The τ decay background is treated as described in Section 7.1.3. The associated nuisance parameters have names of the form α`_norm_*` and are labelled normalisation systematic uncertainties.

The reducible backgrounds originating from fake leptons is estimated with the matrix method of Section 6.3.1 fit under the label *Misid. leptons*. Different systematic uncertainties, described in Section 6.3.2.3, are implemented in the fit as shape uncertainties. The associated nuisance parameters have names of the form α`_norm_MM_*` and are grouped with normalisation systematic uncertainties.

The 1.7 % relative uncertainty on the luminosity [49] is implemented as an overall normalisation uncertainty applied to all non fitted Monte Carlo samples barring the ZZ sample whose normalisation is already constrained by the ZZ control region. It is associated to a nuisance parameter `Lumi` grouped with the normalisation systematic uncertainties.

7.6.4 Behaviour of the systematic uncertainties in the fit

Pulls of nuisance parameters and correlations between fit parameters provide information about the stability of the fit. The mismodelling of a distribution or a fit template can be absorbed by a parameter of interest or a nuisance parameter. In that case, the fit result of the parameters of interest could be biased. This would manifest itself in a strong correlation between parameters and pulls which deviate from zero. Over-constrained nuisance parameters can be a sign of mismodelling for certain uncertainties: it indicates that the associated uncertainty is better constrained by the fit than by the dedicated procedure from which it was derived. This can happen for theory or modelling uncertainties, defined somewhat loosely for lack of a better procedure. However, this should not happen for physics object uncertainties estimated by the work of combined detector performance group.

A template fit is performed to extract joint-polarisation fractions, replacing the data by a pseudo-dataset from the inclusive POWHEG+PYTHIA Monte Carlo sample in $W^{\pm}Z$ events selection. The goal is to check the correct behaviour of all systematic uncertainties implemented. A single boson polarisation template fit behaves similarly regarding the uncertainties. The pulls and constraints of all systematic uncertainties are represented in the pull plots of Fig. 7.19, classed by their type. This serves also as a complete list of all systematic uncertainties considered in the fit.

No significantly pulled or over constrained systematic is found within physics object uncertainties and normalisation uncertainties. However, two theory uncertainties from Fig. 7.19(c) stand out. On one side, the QCD scale uncertainty on the ZZ background template is over-constrained. This is expected as it is exactly the purpose of the ZZ control region to constrain the theory systematics of the ZZ background. Then comes the alternative set of polarisation templates uncertainty whose nuisance parameter α`_theo_ModSys_MoCmps` is very constrained. This is an indication that this two points uncertainty is too conservative, the pseudo-dataset used having already shown a preference for `PHPdnn` over `MoCmps` as was shown in Section 7.5. Besides, using a single nuisance parameter for all polarisation templates, a reflection of the normalisation relationship between fractions, forces the parametrisation of the uncertainty to be unidimensional, contributing to the constraining of this uncertainty.

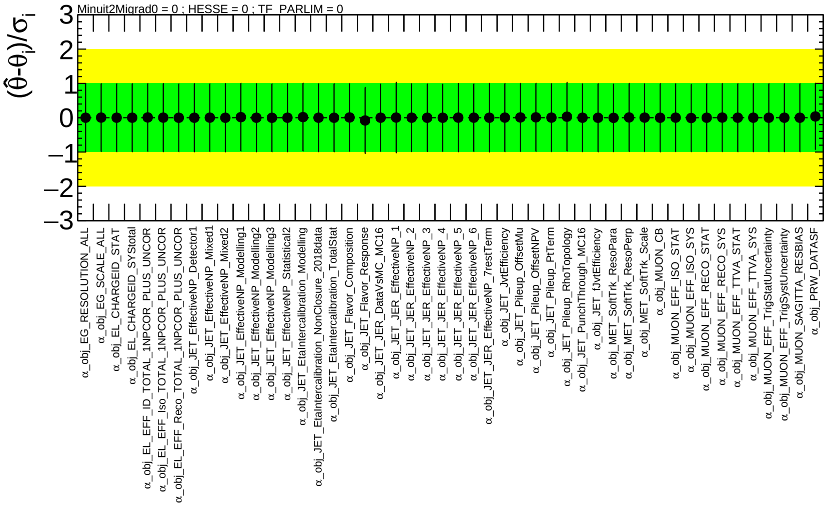

(a) Physics object

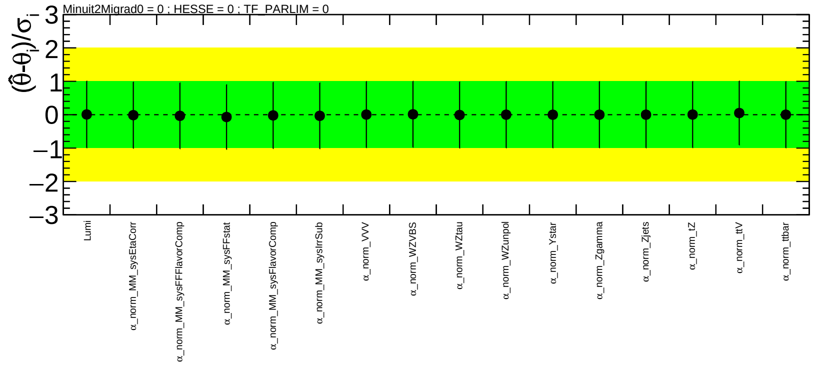

(b) Normalisation

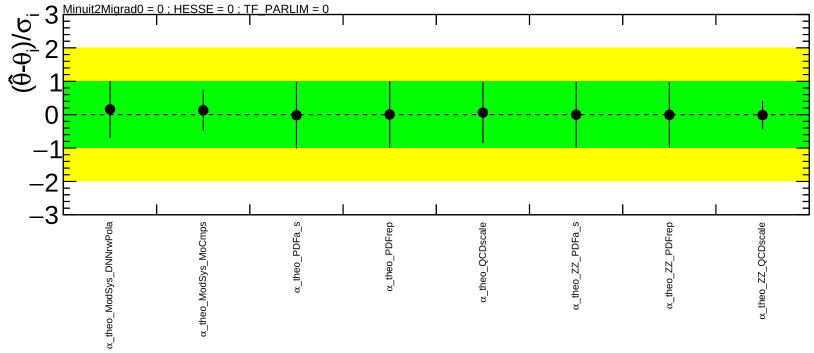

(c) Theory

Figure 7.19 Pull plots for the three types of systematic uncertainties in a template fit of Powheg+Pythia pseudo-dataset, in $W^{\pm}Z$ events selection: physics object (a), normalisation (b) and theory (c).

The correlation matrix between all the fit parameters is represented in Fig. 7.20 for parameters that have at least some sizeable correlations with others. The luminosity, pile-up and background uncertainties are strongly correlated with N_{tot} and almost not to the fractions, in a show of the decorrelation between the fractions and overall normalisation in the template fit. On the other hand, the polarisation fractions are mainly correlated to the modelling uncertainties, showing the importance of studies on the choice of the set of polarisation template of Section 7.5. Finally, some correlations are observed between the nuisance parameters of the ZZ theory uncertainties. These correlations of around -0.3 between the ZZ QCD scale and the ZZ PDF uncertainties is directly linked to the ZZ control region: there being only one bin, for the total number of events, a small degeneracy between these nuisance parameters appears. This explains also the correlation of ZZ QCD scale with the $t\bar{t}+V$ background normalisation, the second background in magnitude in the ZZ control region. Other correlations between nuisance parameters are negligible.

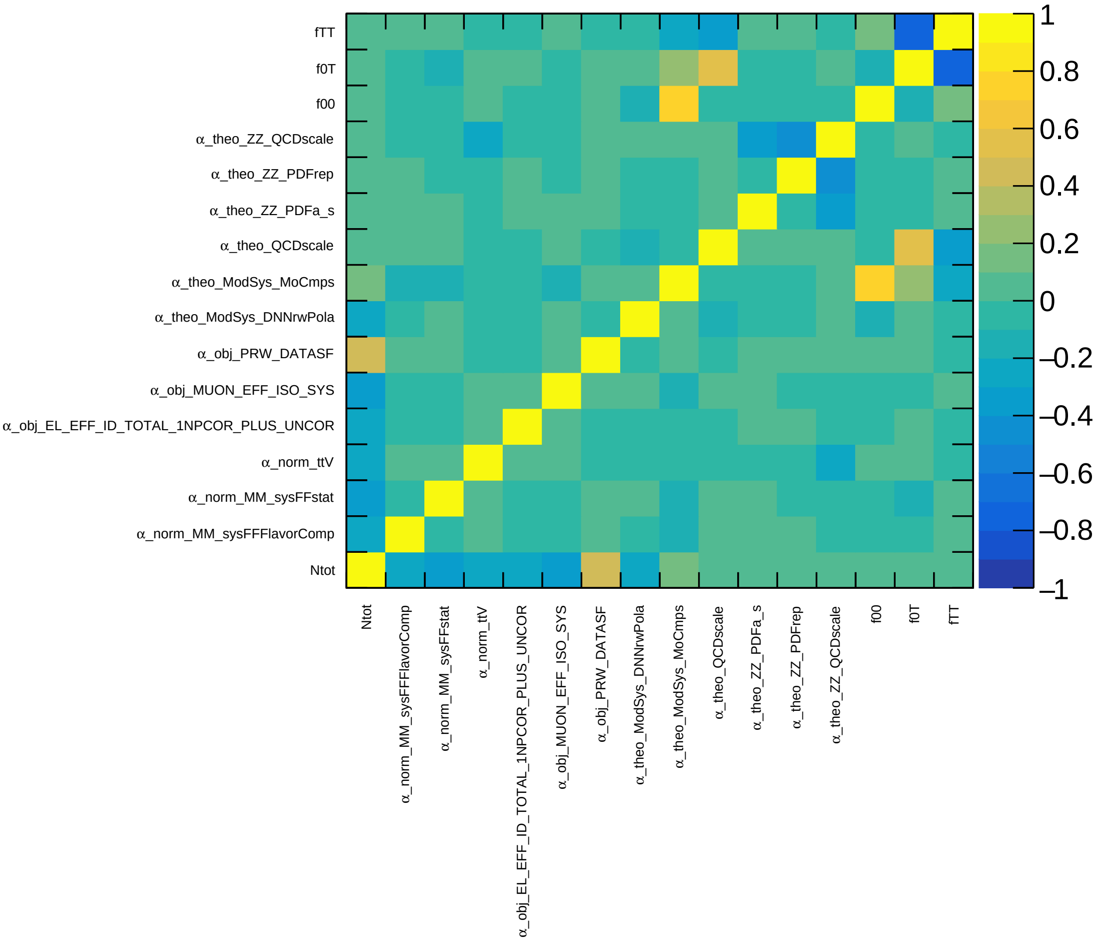

Figure 7.20 Correlation matrix between all fit parameters in a template fit of Powheg+Pythia pseudo-dataset, in $W^{\pm}Z$ events selection. Only parameters that have at least one correlation coefficient above 0.2 are kept.

7.7 Fit results

7.7.1 Joint-polarisation fraction results

The measurement of joint-polarisation fractions is performed with a binned maximum-likelihood template fit on the Run 2 dataset in the $W^{\pm}Z$ events selection, but also separating by the charge of the $W^{\pm}$ boson in the $W^{+}Z$ and $W^{-}Z$ events selection. The pre-fit and post-fit distribution of the 4-category p_{00}^{DNN} in the $W^{\pm}Z$ events selection are shown in Fig. 7.21. The corresponding post-fit yields in the signal region and the ZZ control region are detailed in Table 7.4. The rescaling of the ZZ background contribution is clearly visible, along with the associated constraining of its contribution uncertainty. The strong correlations between the four signal polarisation templates, fitted simultaneously, creates increased uncertainties on their individual post-fit yields.

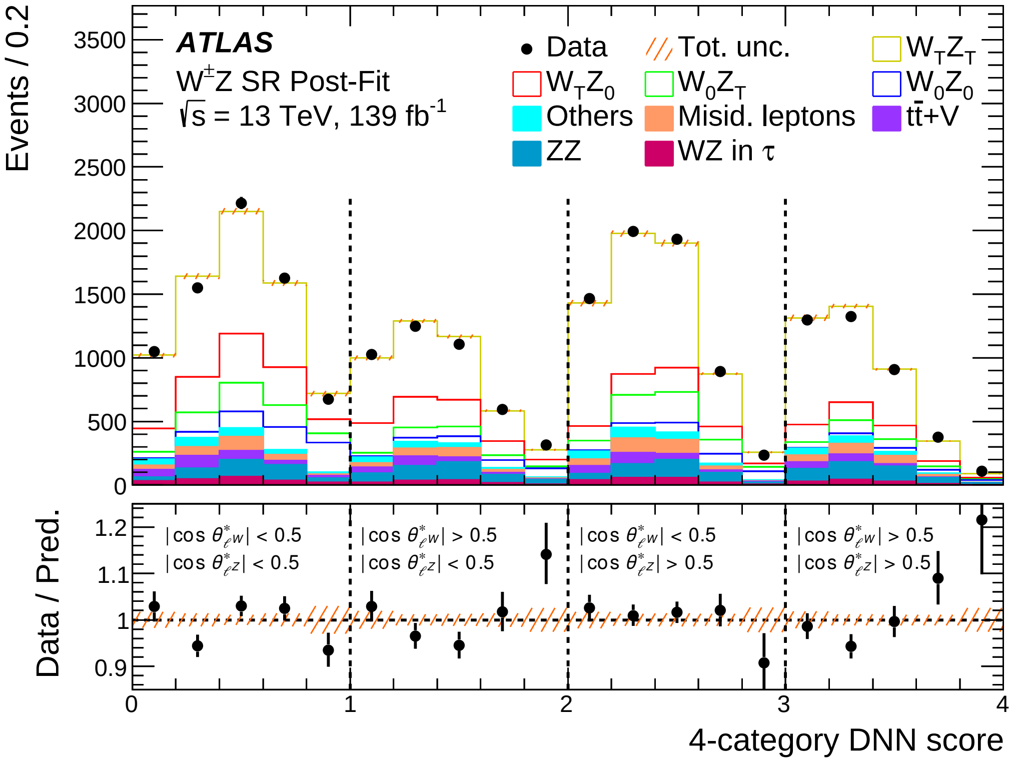

Figure 7.21 Post-fit distribution of the 4-category p_{00}^{DNN} in the $W^{\pm}Z$ events selection at detector level. In the top panel, respective contributions of the $W^{\pm}Z$ joint-polarisation templates 00, 0T, T0 and TT and backgrounds are stacked on top of each other in the same order as in the legend. The uncertainty band around the expectation includes all systematic uncertainties as obtained from the fit. The ratio of data to prediction is represented in the bottom panel.

The measured values of f_{00}, $f_{0\mathrm{T}}$, $f_{\mathrm{T}0}$ and f_{TT} are presented in Table 7.5 along with theoretical predictions. The fit only extracts three fractions at a time, the fourth being constrained by the normalisation uncertainty. Practically, reparametrising the fit allows directly extracting the fourth fraction with its uncertainty. The Powheg+Pythia theoretical predictions are extracted through a fit at particle level in the fiducial phase space as explained in Section 7.5.2, with the addition of theory uncertainties from PDF and QCD scales. The NLO QCD predictions arise from Ref. [77], with the quoted uncertainty from QCD scale uncertainty obtained with a 7-point scale variation.

Table 7.4 Expected and observed number of events in the $W^{\pm}Z$ signal region (left) and in the ZZ control region (right). Numbers are presented before and after a fit to the 4-category p_{00}^{DNN} distribution in the $W^{\pm}Z$ events selection. The pre-fit uncertainties quoted are from statistical and systematic origin but do not take into account correlations between parameters of the fit. The post-fit uncertainties quoted are from statistical and systematic origin and take into account the correlations between the various parameters of the fit. These correlations explain the larger post-fit uncertainties compared to pre-fit ones for $W^{\pm}Z$ signal templates.

	Signal Region	
	Pre-fit	Post-fit
WZ in τ	620 ± 60	630 ± 60
ZZ	1420 ± 120	1630 ± 50
$t\bar{t}+V$	870 ± 130	830 ± 120
Misid. leptons	1170 ± 230	1010 ± 220
Others	800 ± 90	790 ± 90
W_0Z_0	920 ± 40	1190 ± 160
W_0Z_T	2670 ± 50	1900 ± 500
$W_\mathrm{T}Z_0$	2670 ± 60	3100 ± 400
$W_\mathrm{T}Z_\mathrm{T}$	10200 ± 230	10900 ± 600
Total MC	21400 ± 600	21950 ± 170
Data	—	21936

	ZZ Control Region	
	Pre-fit	Post-fit
WZ unpol.	35.6 ± 1.9	35.9 ± 1.9
ZZ	2030 ± 150	2290 ± 50
$t\bar{t}+V$	153 ± 23	144 ± 22
Z+jets	8.5 ± 3.4	8.7 ± 3.4
Others	38 ± 8	39 ± 8
Total MC	2260 ± 160	2510 ± 50
Data	—	2554

Table 7.5 Measured joint-polarisation fractions f_{00}, $f_{0\mathrm{T}}$, $f_{\mathrm{T}0}$ and f_{TT} in the fiducial phase space, for $W^{\pm}Z$, $W^{+}Z$ and $W^{-}Z$ events. The total uncertainties in the measurements are reported. The measurements are compared with predictions from Powheg+Pythia and from NLO QCD fixed-order calculations [77]. The uncertainties on the Powheg+Pythia predictions include statistical, PDF and QCD scale uncertainties; the uncertainties in the NLO QCD fixed-order predictions include QCD scale uncertainties.

	Data	Powheg+Pythia	NLO QCD
	$W^{\pm}Z$		
f_{00}	0.067 ± 0.010	0.0590 ± 0.0009	0.058 ± 0.002
$f_{0\mathrm{T}}$	0.110 ± 0.029	0.1515 ± 0.0017	0.159 ± 0.003
$f_{\mathrm{T}0}$	0.179 ± 0.023	0.1465 ± 0.0017	0.149 ± 0.003
f_{TT}	0.644 ± 0.032	0.6431 ± 0.0021	0.628 ± 0.004
	$W^{+}Z$		
f_{00}	0.072 ± 0.016	0.0583 ± 0.0012	0.057 ± 0.002
$f_{0\mathrm{T}}$	0.119 ± 0.034	0.1484 ± 0.0022	0.155 ± 0.003
$f_{\mathrm{T}0}$	0.152 ± 0.033	0.1461 ± 0.0022	0.147 ± 0.003
f_{TT}	0.66 ± 0.04	0.6472 ± 0.0026	0.635 ± 0.004
	$W^{-}Z$		
f_{00}	0.063 ± 0.016	0.0600 ± 0.0014	0.059 ± 0.002
$f_{0\mathrm{T}}$	0.11 ± 0.04	0.1560 ± 0.0027	0.166 ± 0.003
$f_{\mathrm{T}0}$	0.21 ± 0.04	0.1470 ± 0.0027	0.152 ± 0.003
f_{TT}	0.62 ± 0.05	0.6370 ± 0.0033	0.618 ± 0.004

The overall uncertainty on the polarisation fractions can be broken down depending on the origin of the uncertainty as in Table 7.6. Statistical and modelling uncertainties have similar contributions to the precision of the measurements. Other important uncertainties come from the QCD scale uncertainties and jets reconstruction and calibration uncertainties. All these are ultimately linked to higher order in QCD corrections, affecting the shape of the polarisation templates.

Table 7.6 Summary of the absolute uncertainties in the joint-polarisation fractions f_{00}, $f_{0\mathrm{T}}$, $f_{\mathrm{T}0}$, and f_{TT} measured in $W^{\pm}Z$ events.

	f_{00}	$f_{0\mathrm{T}}$	$f_{\mathrm{T}0}$	f_{TT}
e energy scale and id. efficiency	0.00018	0.0009	0.0012	0.0019
μ energy scale and id. efficiency	0.0004	0.0004	0.0004	0.0008
$E_{\mathrm{T}}^{\mathrm{miss}}$ and jets	0.0017	0.0021	0.0020	0.0023
Pile-up	0.00031	0.00027	0.0007	0.0010
Misidentified lepton background	0.0012	0.0026	0.0013	0.0016
ZZ background	0.0005	0.00028	0.0005	0.0004
Other backgrounds	0.0016	0.0025	0.0021	0.0025
Parton Distribution Function	0.00025	0.0029	0.00014	0.0028
QCD scale	0.00010	0.014	0.0014	0.012
Modelling	0.005	0.007	0.005	0.008
Total systematic uncertainty	0.006	0.017	0.006	0.016
Luminosity	0.00019	0.0004	0.0004	0.00034
Statistical uncertainty	0.007	0.016	0.019	0.019
Total	0.010	0.029	0.023	0.032

The binned likelihood is profiled as described in Section 7.1.1 in order to depend on only one fraction at a time. Using the likelihood ratio of Eq. (7.3) provides the uncertainty on each fractions. In particular, evaluating this ratio under the hypothesis that the fraction is zero, meaning that no event for the joint-polarisation state considered is observed, provides the significance of each extracted fractions. The expected significance obtained from a fit on POWHEG+PYTHIA pseudo-dataset can be compared to the observed significance in data. In $W^{\pm}Z$ events, the presence of a pair of W and Z bosons with a simultaneous longitudinal polarisation (f_{00}) is observed with a significance of $7.1\,\sigma$, compared to $6.2\,\sigma$ expected. The other joint-polarisation fractions $f_{0\mathrm{T}}$, $f_{\mathrm{T}0}$ and f_{TT} are also measured with observed (expected) significances of $3.4\,\sigma$ ($5.4\,\sigma$), $7.1\,\sigma$ ($6.6\,\sigma$) and $11\,\sigma$ ($9.7\,\sigma$), respectively. In conclusion, all joint-polarisation states are observed, the 0T state being simply the complementary of the three others observed with a significance above $5\,\sigma$.

Profiling the likelihood keeping two parameters of interest not-profiled provides a two parameter function. The likelihood ratio of Eq. (7.3) provides a test statistic following a χ^2 distribution with two degrees of freedom. Finding the values where this two dimension test statistic is at the $1\,\sigma$ and $2\,\sigma$ significance threshold provides the contour to respectively the 68 % and 95.5 % confidence level regions. This is done for all the fractions two by two in $W^{\pm}Z$ events in Fig. 7.22. The corresponding results in $W^{+}Z$ and $W^{-}Z$ events are shown in Appendix D. The separation by the $W^{\pm}$ boson charge yields similar results only with bigger regions due to the reduced number of events in these subsets. A better than $2\,\sigma$

agreement of the measured joint-polarisation fractions with the predictions at NLO QCD from Ref. [77] and from POWHEG+PYTHIA is observed.

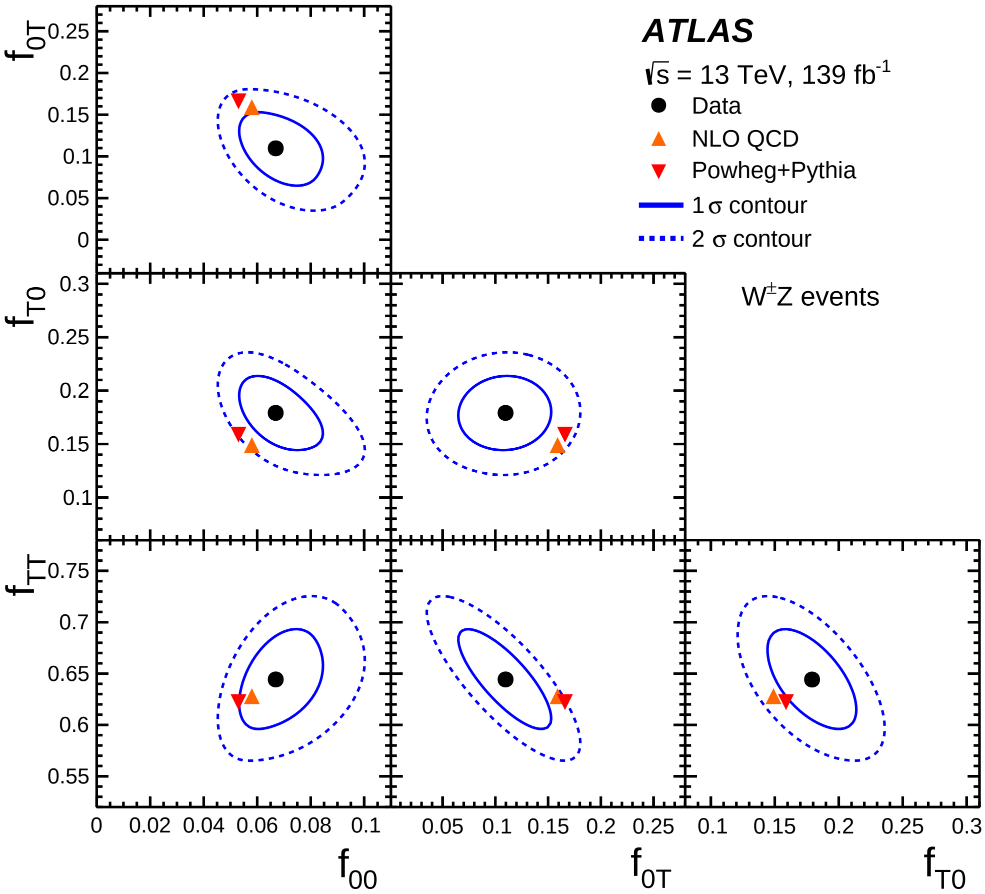

Figure 7.22 Measured joint-polarisation fractions f_{00}, $f_{0\mathrm{T}}$, $f_{\mathrm{T}0}$ and f_{TT} of the $W^{\pm}$ and Z bosons in $W^{\pm}Z$ events, compared to NLO QCD fixed-order predictions [77] (orange triangle) and to Monte Carlo predictions from POWHEG+PYTHIA (red triangle). The effect of PDF and QCD scale uncertainties on the POWHEG+PYTHIA and NLO QCD fixed-order predictions are of the same size as the respective markers. The solid and dashed ellipses around the data points correspond to one and two standard deviations, respectively.

7.7.2 Single boson polarisation results and independence

Similarly, the single boson polarisation fractions are extracted for the $W^{\pm}$ boson and the Z boson separately with a template fit on Run 2 data in $W^{\pm}Z$ events, but also separating by the charge of the $W^{\pm}$ boson in $W^{+}Z$ and $W^{-}Z$ events. This measurements supersedes the previous similar measurement on the partial Run 2 dataset of Ref. [17]. The values of the fractions extracted in this previous analysis are not comparable to the present measurement because of an inconsistency in the definition of the $\cos\theta^{*}_{\ell}$ variables that was corrected in the present measurement. This change in the definition of the $\cos\theta^{*}_{\ell}$ is further explained in Appendix E. For the $W^{\pm}$ boson polarisation fractions, the post-fit distribution of $q_W \cdot \cos\theta^{*}_{\ell W}$ in the $W^{\pm}Z$ events selection is shown in Fig. 7.23(a). For the Z boson polarisation fractions, the post-fit distribution of $\cos\theta^{*}_{\ell Z}$ in the $W^{\pm}Z$ events selection is shown in Fig. 7.23(b). The post-fit yields are comparable to those obtained in Table 7.4.

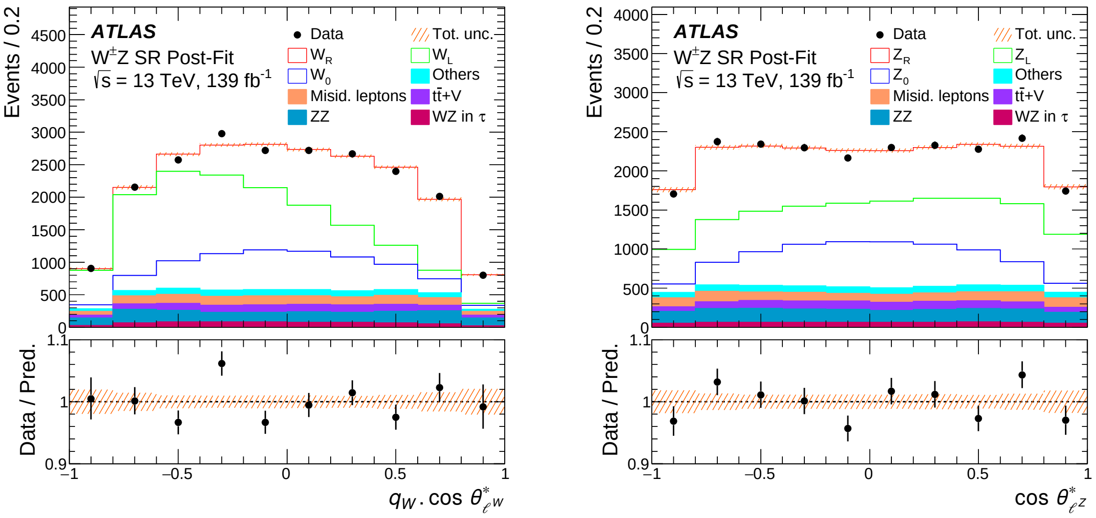

(a) (b)

Figure 7.23 Post-fit distribution of $q_W \cdot \cos\theta^*_{\ell W}$ (a) and $\cos\theta^*_{\ell Z}$ (b) in the $W^{\pm}Z$ events selection at detector level. In the top panel, respective contributions of the $W^{\pm}Z$ single polarisation templates 0, L and R of the $W^{\pm}$ boson or the Z boson and backgrounds are stacked on top of each other in the same order as in the legend. The uncertainty band around the expectation includes all systematic uncertainties as obtained from the fit. The ratio of data to prediction is represented in the bottom panel.

The measured values of f_0 and $f_{\rm L} - f_{\rm R}$ are presented in Table 7.7 along with theoretical predictions from Powheg+Pythia. The NLO QCD calculation of Ref. [77] only provides a prediction on f_0. Good agreement is observed, always within $1\,\sigma$ for f_0 and within $1.5\,\sigma$ for $f_{\rm L} - f_{\rm R}$, except in W^-Z where a small tension at $2.3\,\sigma$ is observed. The breakdown of the uncertainty depending on the origin is presented in Table 7.8. For f_0 of the $W^{\pm}$ boson, the modelling uncertainty is of the same order as the statistical uncertainty. All other parameters are statistically dominated.

Table 7.7 Single boson polarisation fractions f_0 and $f_{\rm L} - f_{\rm R}$ of the $W^{\pm}$ boson and Z boson measured in the fiducial phase space, for $W^{\pm}Z$, W^+Z and W^-Z events. The total uncertainties in the measurements are reported. The measurements are compared with predictions from Powheg+Pythia and for f_0, from NLO QCD fixed-order calculations [77]. The uncertainties on the Powheg+Pythia predictions include statistical, PDF and QCD scale uncertainties; the uncertainties in the NLO QCD fixed-order predictions include QCD scale uncertainties.

	f_0			$f_{\rm L} - f_{\rm R}$	
	Data	Powheg+Pythia	NLO QCD	Data	Powheg+Pythia
W in W^+Z	0.23 ± 0.05	0.2044 ± 0.0024	0.211 ± 0.002	0.071 ± 0.023	0.0990 ± 0.0015
W in W^-Z	0.19 ± 0.05	0.217 ± 0.004	0.225 ± 0.001	0.026 ± 0.027	-0.0491 ± 0.0020
W in $W^{\pm}Z$	0.21 ± 0.04	0.2094 ± 0.0016	0.217 ± 0.001	0.059 ± 0.016	0.0390 ± 0.0011
Z in W^+Z	0.223 ± 0.025	0.1971 ± 0.0019	0.206 ± 0.002	-0.20 ± 0.10	-0.217 ± 0.006
Z in W^-Z	0.241 ± 0.029	0.2065 ± 0.0023	0.211 ± 0.001	0.10 ± 0.13	0.092 ± 0.007
Z in $W^{\pm}Z$	0.231 ± 0.019	0.2009 ± 0.0014	0.208 ± 0.001	-0.10 ± 0.08	-0.092 ± 0.005

Finally, the $1\,\sigma$ and $2\,\sigma$ contours for the pair of parameters (f_0,$f_{\rm L} - f_{\rm R}$) are presented for the $W^{\pm}$ boson and Z boson in Fig. 7.24, showing agreement of the measured f_0 and $f_{\rm L} - f_{\rm R}$ with Powheg+Pythia predictions. The corresponding results in W^+Z and W^-Z events are shown in Appendix D.

Table 7.8 Summary of the absolute uncertainties in the polarisation fractions f_0 and $f_{\mathrm{L}} - f_{\mathrm{R}}$ measured in $W^{\pm}Z$ events for $W^{\pm}$ and Z bosons.

	$W^{\pm}$ in $W^{\pm}Z$		Z in $W^{\pm}Z$	
	f_0	$f_{\mathrm{L}} - f_{\mathrm{R}}$	f_0	$f_{\mathrm{L}} - f_{\mathrm{R}}$
e energy scale and id. efficiency	0.0029	0.00030	0.0027	0.0007
μ energy scale and id. efficiency	0.004	0.0018	0.0015	0.0005
$E_{\mathrm{T}}^{\mathrm{miss}}$ and jets	0.004	0.0011	0.0006	0.0028
Pile-up	0.0028	0.0015	0.0024	0.0029
Misidentified lepton background	0.007	0.00032	0.0033	0.0011
ZZ background	0.0015	0.00025	0.0012	0.0023
Other backgrounds	0.0020	0.0005	0.0013	0.0012
Parton Distribution Function	0.0011	0.0011	0.00011	0.0005
QCD scale	0.012	0.0025	0.0004	0.005
Modelling	0.025	0.0012	0.004	0.018
Total systematic uncertainty	0.030	0.004	0.007	0.019
Luminosity	0.0005	0.00004	0.00012	0.00018
Statistical uncertainty	0.028	0.015	0.018	0.08
Total	0.04	0.016	0.019	0.08

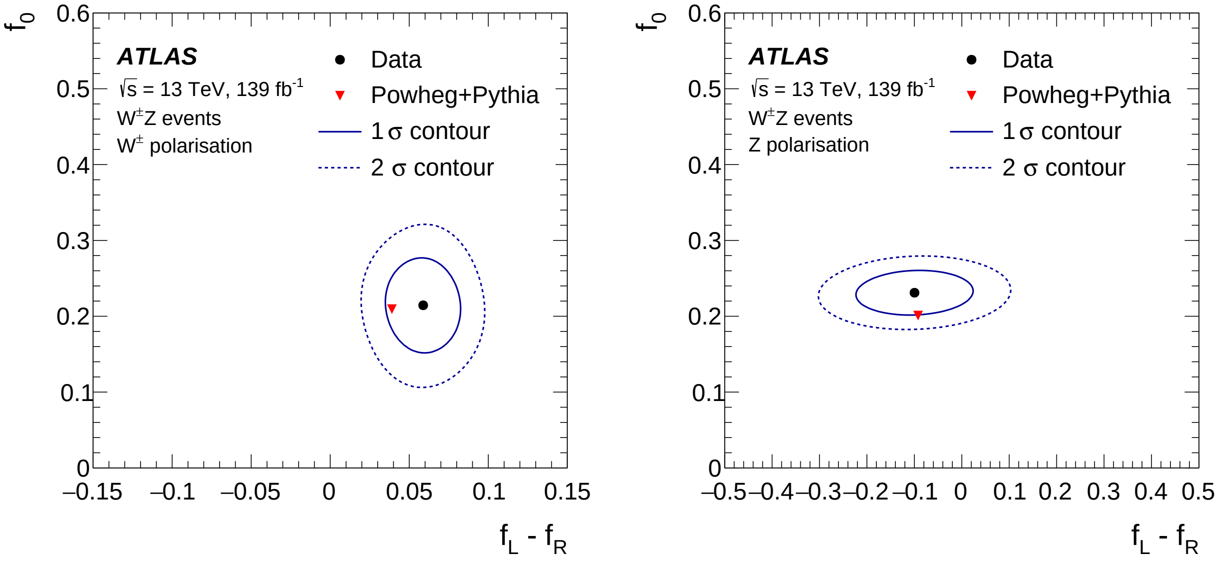

(a) (b)

Figure 7.24 Single boson polarisation fractions f_0 and $f_{\mathrm{L}} - f_{\mathrm{R}}$ measured for the $W^{\pm}$ boson (a) and Z boson (b) in $W^{\pm}Z$ events, compared with predictions from Powheg+Pythia with $\sin^2\theta_{\mathrm{w}} = 0.23152$ (red triangle). The effect of PDF and QCD scale uncertainties on the Powheg+Pythia predictions are of the same size as the triangle marker. The solid and dashed ellipses around the data points correspond to one and two standard deviations, respectively.

Finally, the $W^{\pm}Z$ production cross section can be extracted dividing the N_{tot} parameter, extracted in the fits simultaneously with the fractions, by the luminosity and four, the number of leptonic decay channels considered in the measurement. The smallest uncertainty on this parameter is obtained with the fit of the $q_W \cdot \cos\theta^{*}_{\ell W}$ distribution. The observed cross sections, inclusively and splitting by the charge of the $W^{\pm}$ boson, are presented in Eq. (7.47)–(7.49). With respect to the MATRIX predictions of Ref. [73] summarised in

Eq. (5.12)–(5.14), very good agreement is observed and with similar precision:

$$\sigma^{\text{Fid.}}_{W^{\pm}Z\to\ell^{\pm}\nu\ell'\bar{\ell}'} = 64.6 \pm 0.5\ (\text{stat.}) \pm 1.8\ (\text{syst.}) \pm 1.1\ (\text{lumi.})\ \text{fb}\ , \tag{7.47}$$

$$\sigma^{\text{Fid.}}_{W^{+}Z\to\ell^{+}\nu\ell'\bar{\ell}'} = 38.2 \pm 0.4\ (\text{stat.}) \pm 0.9\ (\text{syst.}) \pm 0.6\ (\text{lumi.})\ \text{fb}\ , \tag{7.48}$$

$$\sigma^{\text{Fid.}}_{W^{-}Z\to\ell^{-}\nu\ell'\bar{\ell}'} = 26.2 \pm 0.3\ (\text{stat.}) \pm 0.8\ (\text{syst.}) \pm 0.4\ (\text{lumi.})\ \text{fb}\ . \tag{7.49}$$

These inclusive cross sections were also measured in Ref. [17] and agreed with the MATRIX prediction as well, but with a precision roughly twice that of the theory. However, these cross sections were extracted using dressed leptons and compared to a MATRIX prediction rescaled to be at the dressed level as well. They are thus not fully comparable to the present measurement performed with Born leptons.

7.7.3 Test of the independence of the fractions

The link between joint-polarisation and single boson polarisation was tested in Section 5.4.4 at particle level in the total phase space. It is possible to test it at detector level as a check of the consistency of the joint-polarisation fit and the single boson polarisation fits. Using Eq. (5.56)–(5.59) to reparametrise the joint-polarisation fit to the 4-category p_{00}^{DNN} variable, fractions f_0^W, f_0^Z and the parameter R_c defined in Eq. (5.55) are extracted.

The obtained f_0^W and f_0^Z are compared to the single boson polarisation fit in Fig. 7.25 for $W^{\pm}Z$ events. Results for $W^{+}Z$ and $W^{-}Z$ events are presented in Appendix D. Overall, good consistency between the fits is observed, as the single boson polarisation measurement is always well within the 68 % confidence level region. For reference, the Powheg+Pythia

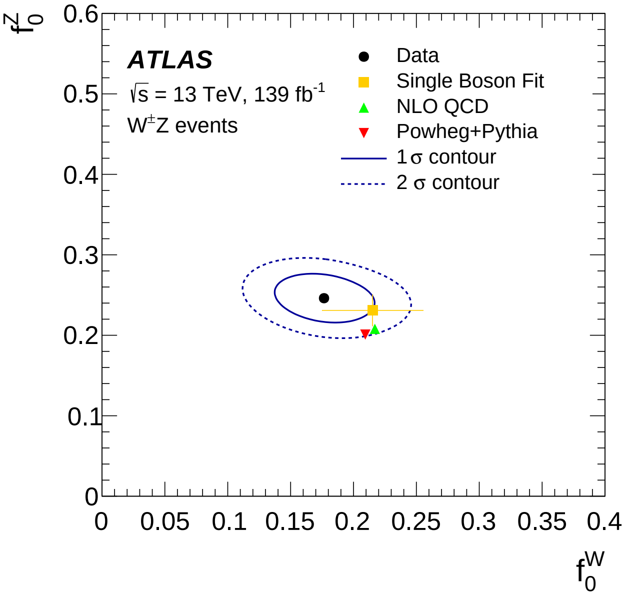

Figure 7.25 Measured polarisation fractions f_0^W and f_0^Z in $W^{\pm}Z$ events. The black point is the simultaneously measured values from the template fit on the 4-category DNN score distribution. The orange square with uncertainty bars is the measured value from two single boson polarisation template fits to $q_W \cdot \cos\theta^*_{\ell W}$ and $\cos\theta^*_{\ell Z}$ distributions. The red triangle is the theoretical predictions at NLO in QCD and LO for the electroweak interaction from Powheg+Pythia. The solid and dashed ellipses around the data points correspond to one and two standard deviations to the joint measurement of f_0^W and f_0^Z, respectively.

prediction is also plotted and shown to be yet closer to the single boson polarisation measurement. This reflects the greater complexity of the simultaneous joint-polarisation measurement and limits of the assumption that interferences can be ignored.

The parameter $R_c = f_{00}/(f_0^W f_0^Z)$ is expected to be exactly one if the single boson polarisations are independent. A value of $R_c = 1.3$ is predicted in $W^\pm Z$ events by NLO QCD fixed-order calculations [77], indicating the presence of correlation between polarisation states of the bosons. It is measured in $W^\pm Z$ events to be $R_c = 1.54 \pm 0.35$ in the fit to the 4-category p_{00}^{DNN}. The observed significance with respect to the independence hypothesis, i.e. $R_c = 1$, is $1.6\,\sigma$ in $W^\pm Z$ events. The profiled likelihood for R_c is represented in Fig. 7.26. This absence of independence shows the importance of extracting joint-polarisation fractions directly, instead of simply multiplying single boson polarisation fractions.

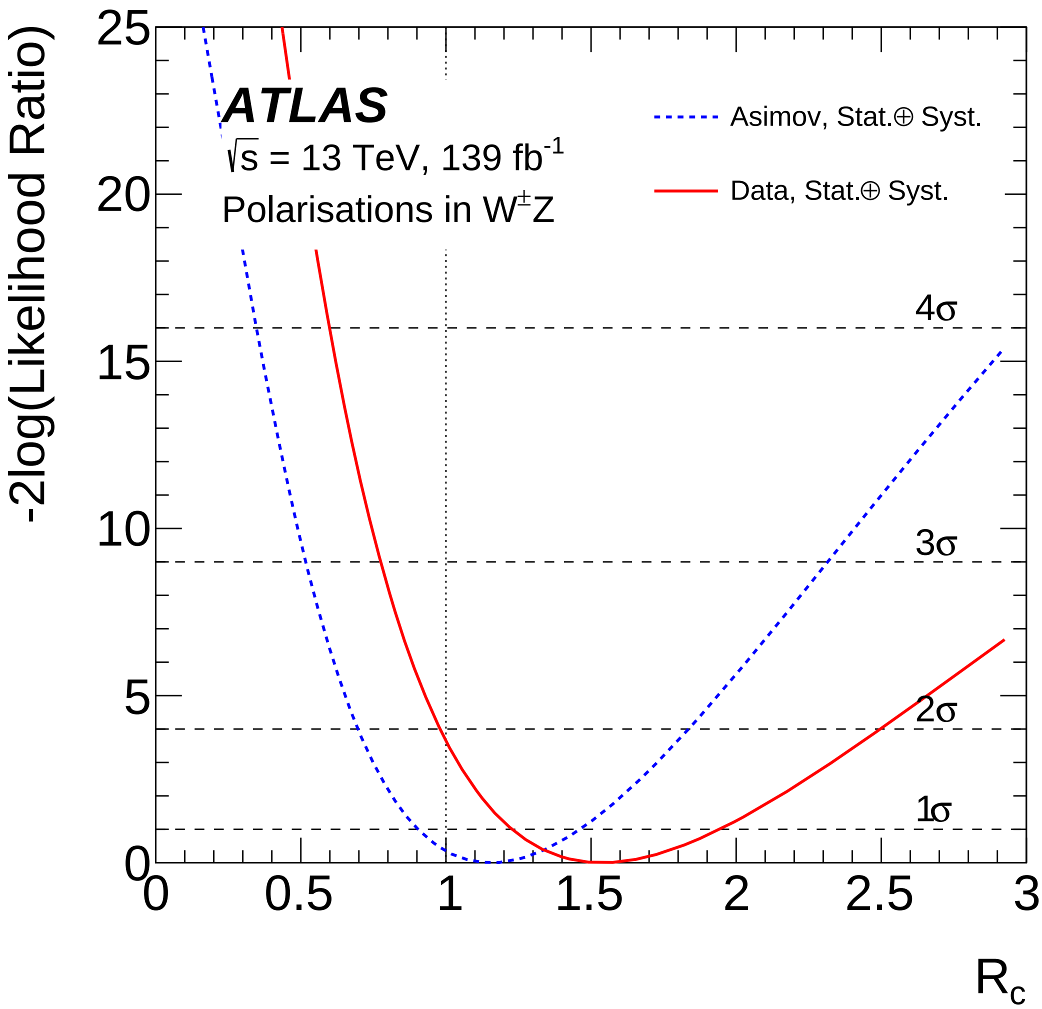

Figure 7.26 Curve of the test statistic $-2\log(\text{Likelihood Ratio})$ along the ratio R_c in $W^\pm Z$ events. The likelihood ratio is profiled for all systematic uncertainties. Its width at the $1\,\sigma$ horizontal line gives the total statistical and systematic asymmetrical uncertainty on R_c. The blue dashed curve represent the expected result, from an Asimov fit at reconstructed level. The red curve represents the result on Run 2 data. The vertical line at 1 corresponds to the absence of spin correlation hypothesis.

Appendices

Appendix A

Direct computation of polarised boson decay

In this appendix, the explicit calculation of the Feynamn diagram of a vector boson decay is presented. The vector boson, a $W^\pm$ or Z boson decays in two leptons:

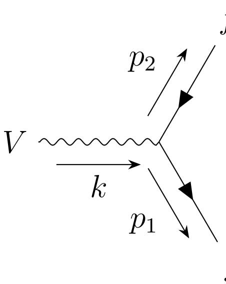

Figure A.1 Feynman diagram of the decay of a vector boson with momentum k and polarisation vector ε^μ in a fermion of momentum p_1 and an anti-fermion of momentum p_2.

The rest frame of the decaying boson is considered for this calculation. The z-axis definition has no impact in this calculation, so the result will be valid in both the *Helicity* frame and the *Modified Helicity* frame described in Section 5.2.1. Therefore, the polarisation four-vector are given by Eq. (1.42). For simplicity, the x-axis and y-axis are chosen so that the leptons decay in the xOz plane. Then, their four-momenta are:

$$p_1^\mu = (E_1^*, p^* \sin\theta_\ell^*, 0, p^*\cos\theta_\ell^*)\ , \qquad p_2^\mu = (E_2^*, -p^* \sin\theta_\ell^*, 0, -p^*\cos\theta_\ell^*)\ ,$$

with the E and p^* being respectively the energy and the norm of the momentum in the rest frame of the decaying boson. The angle θ_ℓ^* is the decay angle of the fermion with respect to the z-axis.

The interaction between the vector boson V and the leptons is described by the charged current Lagrangian $\mathcal{L}_{CC}$ for the $W^\pm$ boson, and the neutral current Lagrangian $\mathcal{L}_{NC}$ for the Z boson, as defined in Eq. (1.25) and (1.26). Both cases are considered using the parametrisation $\gamma^\mu(c_v - c_a\gamma_5)$ where for the $W^\pm$ boson, $c_v = c_a = 1/2$. Finally, in the following, the mass of leptons is neglected, being several orders of magnitude below the typical energy of the decay at the mass of the $W^\pm$ or Z boson. It ensues the simplification $E_1 = E_2 = p^* = m_V/2$, with m_V the mass of the decaying boson. The matrix element computation for a vector boson V with polarisation h gives:

$$\begin{aligned}
&i\mathcal{M}_h \propto \varepsilon_h^{\mu}\ \bar{u}_s(p_1)\ \gamma_\mu(c_v - c_a\gamma_5)\ v_{s'}(p_2) \\
&|\mathcal{M}_h|^2 \propto \sum_{s,s'} \varepsilon_h^{\mu}\ \bar{u}_s(p_1)\ \gamma_\mu(c_v - c_a\gamma_5)\ v_{s'}(p_2)\ \varepsilon_h^{*\ \nu}\ \bar{v}_{s'}(p_2)\ \gamma_\nu(c_v - c_a\gamma_5)\ u_s(p_1) \\
&|\mathcal{M}_h|^2 \propto \varepsilon_h^{\mu}\varepsilon_h^{*\ \nu}\ \mathrm{Tr}\left[(\not{p}_1 + m_1)\ \gamma_\mu(c_v - c_a\gamma_5)\ (\not{p}_2 + m_2)\ \gamma_\nu(c_v - c_a\gamma_5)\right]\ .
\end{aligned}$$

Neglecting the mass of fermions, developing and using γ_5 properties,

$$\begin{aligned}
&|\mathcal{M}_h|^2 \propto \varepsilon_h^{\mu}\varepsilon_h^{*\ \nu}\ \left[(c_v^2 + c_a^2)\mathrm{Tr}\left(\not{p}_1\gamma_\mu\not{p}_2\gamma_\nu\right) - 2c_vc_a\mathrm{Tr}\left(\not{p}_1\gamma_\mu\not{p}_2\gamma_\nu\gamma_5\right)\right] \\
&|\mathcal{M}_h|^2 \propto (c_v^2 + c_a^2)\varepsilon_h^{\mu}\varepsilon_h^{*\ \nu}\ 4p_1^{\alpha}p_2^{\beta}\left(g_{\alpha\mu}g_{\beta\nu} + g_{\alpha\nu}g_{\beta\mu} - g_{\alpha\beta}g_{\mu\nu}\right) - 2c_vc_a\varepsilon_h^{\mu}\varepsilon_h^{*\ \nu}p_1^{\alpha}p_2^{\beta}\ 4i\epsilon_{\mu\alpha\nu\beta} \\
&|\mathcal{M}_h|^2 \propto 4(c_v^2 + c_a^2)\left((\varepsilon_h \cdot p_1)(\varepsilon_h^* \cdot p_2) + (\varepsilon_h \cdot p_2)(\varepsilon_h^* \cdot p_1) - (\varepsilon_h \cdot \varepsilon_h^*)(p_2 \cdot p_1)\right) - 8ic_vc_a\varepsilon_h^{\mu}\varepsilon_h^{*\ \nu}p_1^{\alpha}p_2^{\beta}\ \epsilon_{\mu\alpha\nu\beta}\ .
\end{aligned}$$

With the explicit polarisation and momenta four-vectors, we get

$$\begin{aligned}
(\varepsilon_0 \cdot p_1)(\varepsilon_0^* \cdot p_2) + (\varepsilon_0 \cdot p_2)(\varepsilon_0^* \cdot p_1) - (\varepsilon_0 \cdot \varepsilon_0^*)(p_2 \cdot p_1) &= -2p^{*2}\cos^2\theta_\ell^* + 2p^{*2} \\
(\varepsilon_\pm \cdot p_1)(\varepsilon_\pm^* \cdot p_2) + (\varepsilon_\pm \cdot p_2)(\varepsilon_\pm^* \cdot p_1) - (\varepsilon_\pm \cdot \varepsilon_\pm^*)(p_2 \cdot p_1) &= -p^{*2}\sin^2\theta_\ell^* + 2p^{*2} \\
&= p^{*2}(1 + \cos^2\theta_\ell^*)\ ,
\end{aligned}$$

and

$$\begin{aligned}
i\varepsilon_0^{\mu}\varepsilon_0^{*\ \nu}p_1^{\alpha}p_2^{\beta}\ \epsilon_{\mu\alpha\nu\beta} &= 0 \\
i\varepsilon_\pm^{\mu}\varepsilon_\pm^{*\ \nu}p_1^{\alpha}p_2^{\beta}\ \epsilon_{\mu\alpha\nu\beta} &= \frac{i}{2}\left[\epsilon_{1\alpha2\beta}(\mp i)p_1^{\alpha}p_2^{\beta} + \epsilon_{2\alpha1\beta}(\pm i)p_1^{\alpha}p_2^{\beta}\right] \\
&= \frac{i}{2}\left[-(\mp i)(p_1^0p_2^3 - p_1^3p_2^0) + (\pm i)(p_1^0p_2^3 - p_1^3p_2^0)\right] \\
&= \frac{i}{2}\left(\mp 4ip^{*2}\cos\theta_\ell^*\right) = \pm 2p^{*2}\cos\theta_\ell^*\ .
\end{aligned}$$

It then follows that

$$\begin{aligned}
|\mathcal{M}_0|^2 &\propto 4(c_v^2 + c_a^2)2p^{*2}\left(1 - \cos^2\theta_\ell^*\right)\ , \\
|\mathcal{M}_\pm|^2 &\propto 4(c_v^2 + c_a^2)p^{*2}\left(1 + \cos^2\theta_\ell^* \mp 2\frac{2c_vc_a}{c_v^2 + c_a^2}\cos\theta_\ell^*\right)\ .
\end{aligned}$$

Integrating on θ_ℓ^* between zero and π yields the same result for all polarisation states. In other words, the total cross section is independent of the polarisation, and can be used to normalise the differential cross section associated to $\cos\theta_\ell^*$. With the C_{w} defined in Eq. (5.25), it becomes:

$$\begin{aligned}
\frac{1}{\sigma}\frac{d\sigma_0}{d\cos\theta_\ell^*} &= \frac{3}{4}\left(1 - \cos^2\theta_\ell^*\right)\ , \\
\frac{1}{\sigma}\frac{d\sigma_\pm}{d\cos\theta_\ell^*} &= \frac{3}{8}\left(1 + \cos^2\theta_\ell^* \mp 2C_{\mathrm{w}}\cos\theta_\ell^*\right)\ .
\end{aligned}$$

For the $W^\pm$ boson, C_{w} is precisely one whereas for the Z boson, it is a function of $\sin^2(\theta_{\mathrm{w}})$. This formula can be adapted to the W^+ case noting that there, the change of definition for θ_ℓ^* makes every $\cos\theta_\ell^*$ pick up a minus sign. Thus, the three terms of Eq. (5.28) and (5.29) are found back through this direct calculation.

Appendix B

Comparison of extraction methods for single boson polarisation fractions

The three methods developed to extract single boson polarisation fractions described in Section 5.4.1 are the fit with three parameters (FIT3), the fit with two parameters (FIT2) and the moments method (MOM).

These three methods were compared by applying them on particle-level distributions of events from the Powheg+Pythia Monte Carlo sample in the total phase space and separating W^+Z events and W^-Z events. As explained in Section 7.3.2, these fractions are needed in bins of the p_T and $|\eta|$ of the studied boson. It is in this more stringent context with reduced statistics compared to the full phase space, that the comparisons are performed. In Fig. B.2, the relative difference on fractions of the W^+ boson, obtained with different methods, is shown to be very small, below or of the order of the statistical uncertainties, as can be checked on Fig. B.1 which gives results using the moments method for reference. In Fig. B.3, the relative difference between the statistical uncertainties on the fractions obtained with two different methods is plotted. For f_0 in all cases, the difference is negligible, of the order of 1 %. However, for f_L and f_R, there is a consistent difference of around 10 % across the 2D plot when comparing the fit with three parameters to the others. The fit with two parameters and the moments method stay comparable. In the end these differences – concerning only the uncertainty, not the central value – are considered negligible. Similar results are found for W^- boson and Z boson in W^+Z and W^-Z events.

The moments method is chosen to extract the polarisation fractions of a single boson as it provides more flexibility than the fits. The previous single boson polarisation measurement [17] used the fit with three parameters.

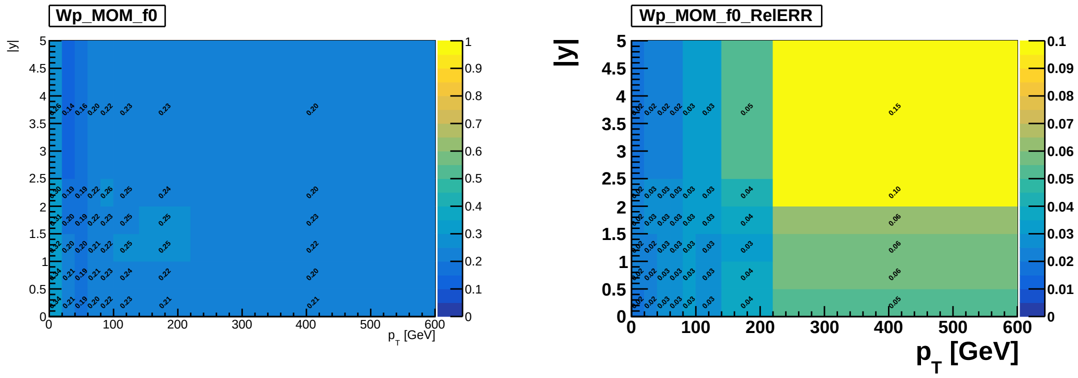

(a) f_0 **(b)** Δf_0

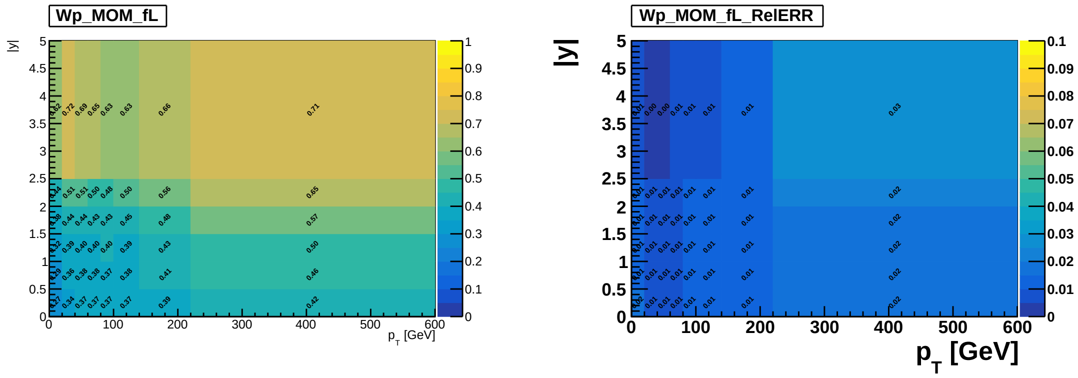

(c) f_{L} **(d)** Δf_{L}

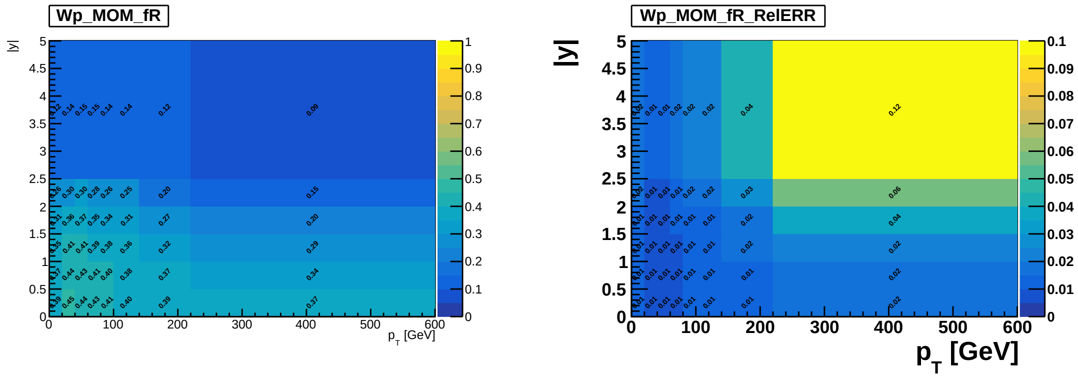

(e) f_{R} **(f)** Δf_{R}

Figure B.1 W^+ boson polarisation fractions at particle level in the total phase space, extracted from POWHEG+PYTHIA with the moments method. The fractions, from top to bottom f_0, f_{L}, f_{R}, are shown in the left column in bins of p_{T} and $|y|$ of the W^+ boson, along with their associated statistical uncertainties in the right column.

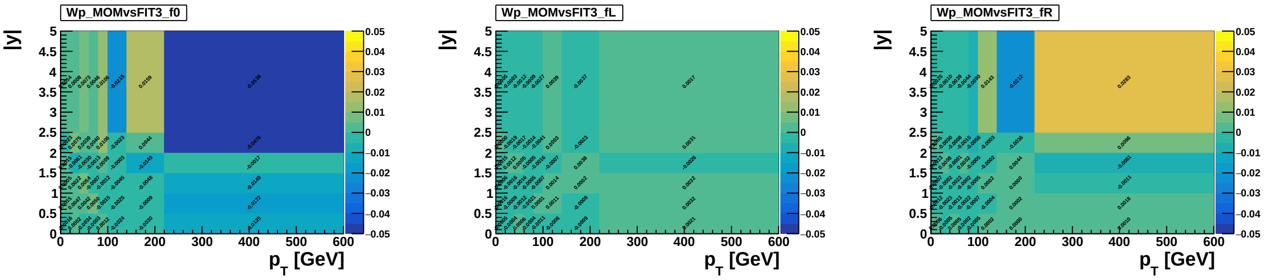

(a) $\frac{f_0^{MOM} - f_0^{FIT3}}{f_0^{MOM}}$ **(b)** $\frac{f_L^{MOM} - f_L^{FIT3}}{f_L^{MOM}}$ **(c)** $\frac{f_R^{MOM} - f_R^{FIT3}}{f_R^{MOM}}$

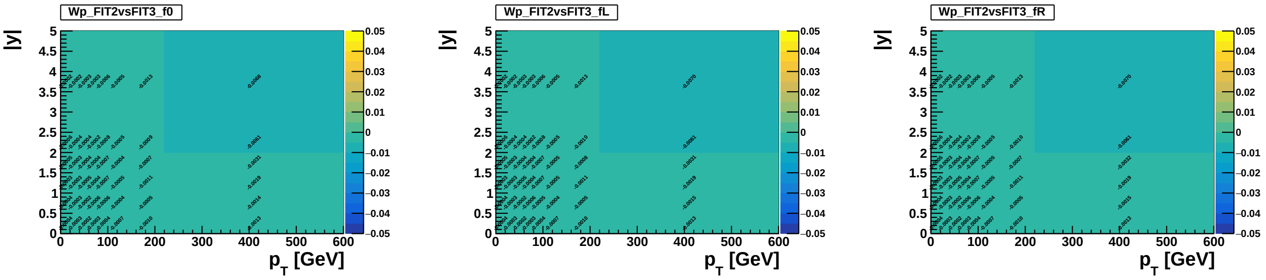

(d) $\frac{f_0^{FIT2} - f_0^{FIT3}}{f_0^{FIT2}}$ **(e)** $\frac{f_L^{FIT2} - f_L^{FIT3}}{f_L^{FIT2}}$ **(f)** $\frac{f_R^{FIT2} - f_R^{FIT3}}{f_R^{FIT2}}$

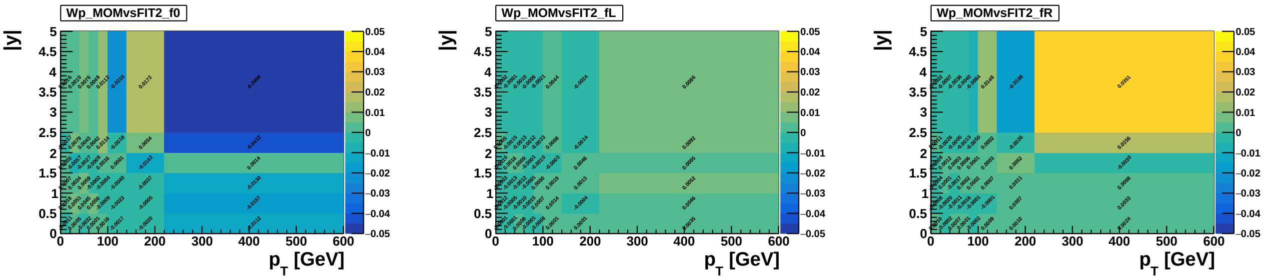

(g) $\frac{f_0^{MOM} - f_0^{FIT2}}{f_0^{MOM}}$ **(h)** $\frac{f_L^{MOM} - f_L^{FIT2}}{f_L^{MOM}}$ **(i)** $\frac{f_R^{MOM} - f_R^{FIT2}}{f_R^{MOM}}$

Figure B.2 Relative difference on fractions obtained by two different methods, extracted from Powheg+Pythia in the total phase space, in bins of p_{T} and $|y|$, for the W^+ boson. From left to right are shown f_0, f_{L} and f_{R}.
(a)–(c) Comparing moments method to the fit with three parameters.
(d)–(f) Comparing the fit with two and three parameters.
(g)–(i) Comparing moments method to the fit with two parameters.

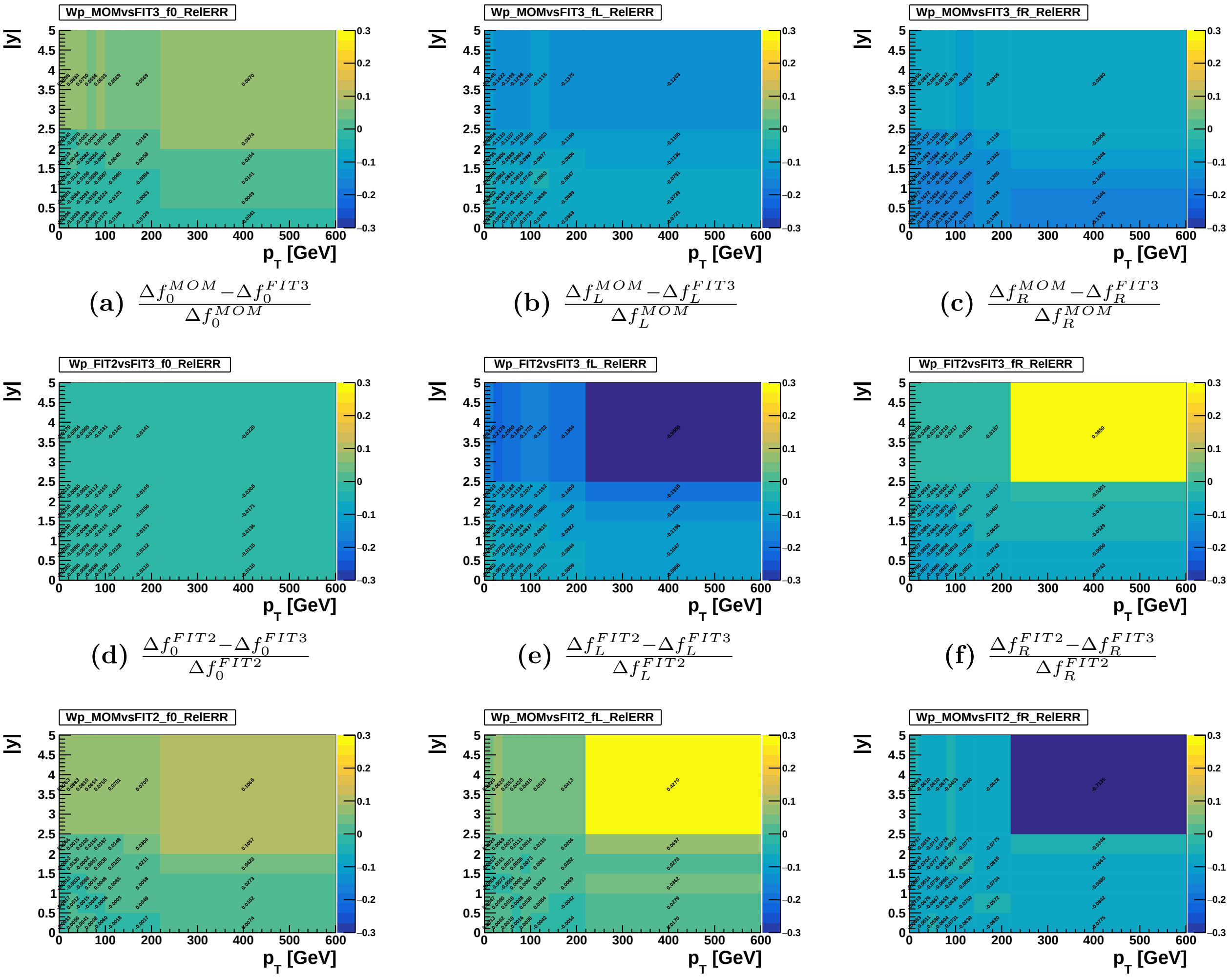

(a) $\frac{\Delta f_0^{MOM} - \Delta f_0^{FIT3}}{\Delta f_0^{MOM}}$ **(b)** $\frac{\Delta f_L^{MOM} - \Delta f_L^{FIT3}}{\Delta f_L^{MOM}}$ **(c)** $\frac{\Delta f_R^{MOM} - \Delta f_R^{FIT3}}{\Delta f_R^{MOM}}$

(d) $\frac{\Delta f_0^{FIT2} - \Delta f_0^{FIT3}}{\Delta f_0^{FIT2}}$ **(e)** $\frac{\Delta f_L^{FIT2} - \Delta f_L^{FIT3}}{\Delta f_L^{FIT2}}$ **(f)** $\frac{\Delta f_R^{FIT2} - \Delta f_R^{FIT3}}{\Delta f_R^{FIT2}}$

(g) $\frac{\Delta f_0^{MOM} - \Delta f_0^{FIT2}}{\Delta f_0^{MOM}}$ **(h)** $\frac{\Delta f_L^{MOM} - \Delta f_L^{FIT2}}{\Delta f_L^{MOM}}$ **(i)** $\frac{\Delta f_R^{MOM} - \Delta f_R^{FIT2}}{\Delta f_R^{MOM}}$

Figure B.3 Relative statistical uncertainty difference on fractions obtained by two different methods, extracted from Powheg+Pythia in the total phase space, in bins of p_{T} and $|y|$, for the W^+ boson. From left to right are shown f_0, f_{L} and f_{R}.
(a)–(c) Comparing moments method to the fit with three parameters.
(d)–(f) Comparing the fit with two and three parameters.
(g)–(i) Comparing moments method to the fit with two parameters.

Appendix C

Choice of the p_z^ν reconstruction method

The study detailed in this appendix compares fractions extracted from a template fit using the analytical p_z^ν reconstruction and the DNN-based p_z^ν reconstruction. Both methods are detailed in Section 6.2. The comparison is only performed for single boson polarisation fractions, as a similar result is expected for joint-polarisation fractions. The sets of polarisation templates `MGgen`, `MGrw` and `PHPrw` are all generated in two versions, one with the analytical p_z^ν reconstruction, and one with the DNN-based p_z^ν reconstruction. The shapes of the templates are affected by the change of neutrino reconstruction. This obviously affects more the W templates, but the Z templates are also slightly affected because $\cos\theta^*_{\ell Z}$ is modified by the boost in the WZ rest frame. These differences can be seen in Fig. C.1.

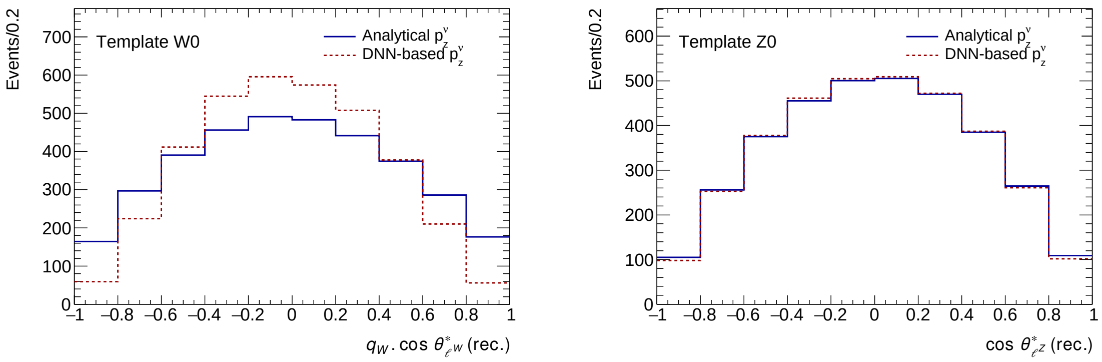

(a) $q_W \cdot \cos\theta^*_{\ell W}$ **(b)** $\cos\theta^*_{\ell Z}$

Figure C.1 Comparisons of $q_W \cdot \cos\theta^*_{\ell W}$ (a) and $\cos\theta^*_{\ell Z}$ (b) distributions at detector level using analytical and DNN-based reconstruction of p_z^ν in $W^\pm Z$ events, for longitudinal `PHPrw` polarisation templates.

Fits are performed for the `MGrw` and `PHPrw` polarisation template sets in both configurations as shown in Fig. C.2 and C.3. The template sets fit at detector level the inclusive Monte Carlo sample they come from, that is the inclusive MadGraph0,1j@LO sample for `MGrw` and the inclusive Powheg+Pythia sample for `PHPrw`. Such fits are Asimov fits as Section 7.3.3 showed that the sum of analytically reweighted templates gives back exactly the original inclusive template. This time, the fits are performed with both signal and backgrounds templates as the addition of backgrounds processes might affect how templates with different shapes fit the pseudo-data. All the systematic uncertainties are included as well, and especially the modelling uncertainty. Here, the reference represented by a line is the analytical p_z^ν reconstruction result and the points represent the DNN-based p_z^ν reconstruction result, for each set of templates and each boson. The central values of the parameters of interest stay within statistical uncertainties at the same value as is visible in Fig. C.2. However, the uncertainty is found to be slightly lower using the DNN-based p_z^ν reconstruction as shown in Fig. C.3. In the end, the difference between the two p_z^ν reconstruction methods is very small. But the DNN-based one being found to be slightly better, it is the one that will be used as baseline.

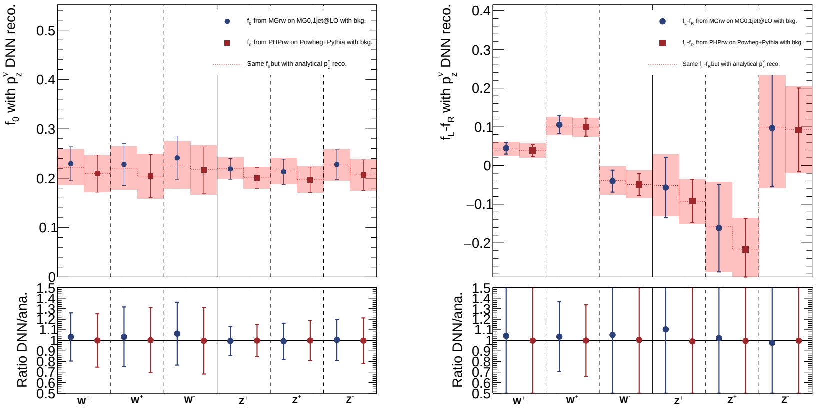

(a) f_0 **(b)** $f_L - f_R$

Figure C.2 Central value of parameters of interest from an Asimov fit of signal and backgrounds. f_0 (a) and $f_\mathrm{L} - f_\mathrm{R}$ (b) central values are shown using analytical (red dotted line) and DNN-based (points) p_z^ν reconstruction, for templates `MGrw` and `PHPrw` and for $W^\pm$ and Z boson in all charge configurations. The bottom plot shows the ratio between the uncertainty values for both methods of p_z^ν reconstruction.

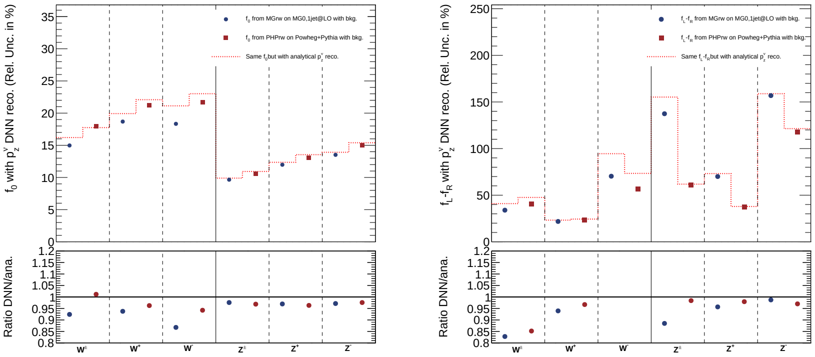

(a) f_0 **(b)** $f_\mathrm{L} - f_\mathrm{R}$

Figure C.3 Relative uncertainties on parameters of interest from an Asimov fit of signal and backgrounds. f_0 (a) and $f_\mathrm{L} - f_\mathrm{R}$ (b) uncertainties are shown using analytical (red dotted line) and DNN-based (points) p_z^ν reconstruction, for templates `MGrw` and `PHPrw` and for $W^\pm$ and Z boson in all charge configurations. The bottom plot shows the ratio between the uncertainty values for both methods of p_z^ν reconstruction.

Appendix D

Polarisation with $W^{\pm}$ charge separation

In this appendix are presented the results of Section 7.7 separating by the $W^{\pm}$ boson charge between $W^{+}Z$ events and $W^{-}Z$ events. The main impact is in increased uncertainties as expected from the reduced statistical power of these subsets of events. Overall, no major difference is visible from the inclusive $W^{\pm}Z$ events regarding joint-polarisation fractions.

In single boson polarisation fractions, differences are mainly visible looking at the two transverse polarisation fractions f_{L} and f_{R}. The small tension at $2.3\,\sigma$ on $f_{\mathrm{L}} - f_{\mathrm{R}}$ in $W^{-}Z$ events appears clearly in Fig. D.6.

The consistency check between single boson fraction measurement and joint-polarisation fraction measurement yields similar results. Finally, the R_c parameter profiled likelihood is simply wider in these subsets. In $W^{-}Z$ events, the independence assumption is still within $1\,\sigma$ of the measured value.

D.1 In W^+Z events

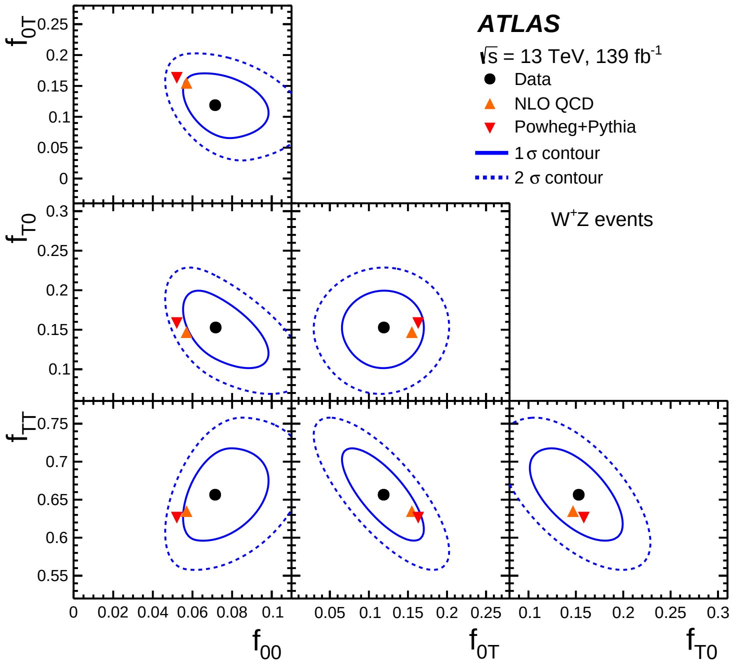

Figure D.1 Measured joint-polarisation fractions f_{00}, $f_{0\mathrm{T}}$, $f_{\mathrm{T}0}$ and f_{TT} of the $W^\pm$ and Z bosons in W^+Z events, compared to NLO QCD fixed-order predictions [77] (orange triangle) and to Monte Carlo predictions from Powheg+Pythia (red triangle). The effect of PDF and QCD scale uncertainties on the Powheg+Pythia and NLO QCD fixed-order predictions are of the same size as the respective markers. The solid and dashed ellipses around the data points correspond to one and two standard deviations, respectively.

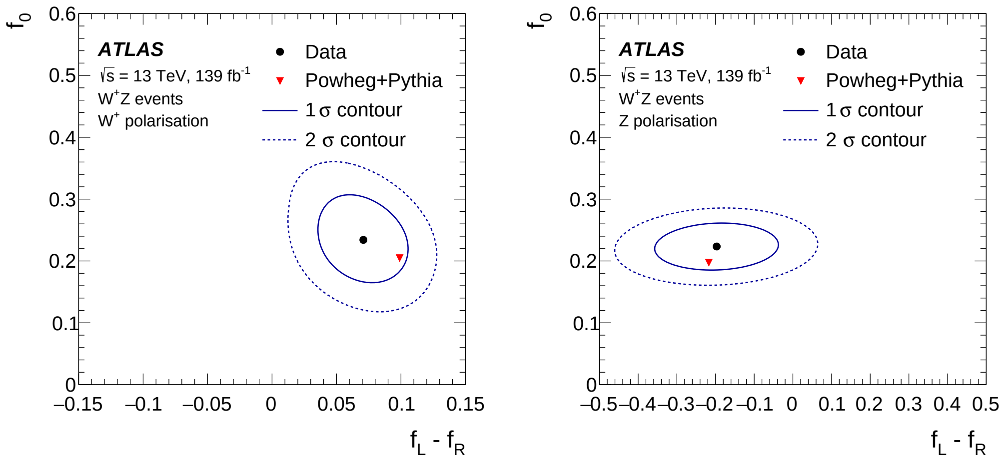

(a) **(b)**

Figure D.2 Single boson polarisation fractions f_0 and $f_\mathrm{L}-f_\mathrm{R}$ measured for the W^+ boson (a) and Z boson (b) in W^+Z events, compared with predictions from Powheg+Pythia with $\sin^2\theta_\mathrm{w} = 0.23152$ (red triangle). The effect of PDF and QCD scale uncertainties on the Powheg+Pythia predictions are of the same size as the triangle marker. The solid and dashed ellipses around the data points correspond to one and two standard deviations, respectively.

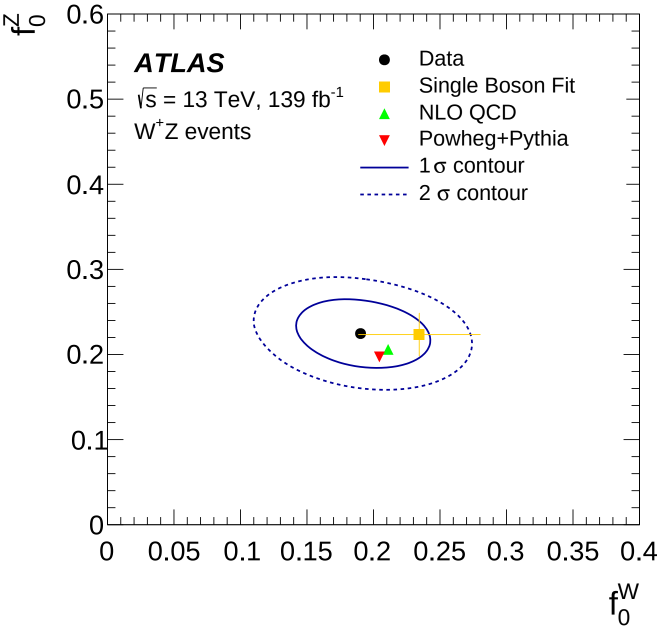

Figure D.3 Measured polarisation fractions f_0^W and f_0^Z in W^+Z events. The black point is the simultaneously measured values from the template fit on the 4-category DNN score distribution. The orange square with uncertainty bars is the measured value from two single boson polarisation template fits to $q_W \cdot \cos\theta^*_{\ell W}$ and $\cos\theta^*_{\ell Z}$ distributions. The red triangle is the theoretical predictions at NLO in QCD and LO for the electroweak interaction from Powheg+Pythia. The solid and dashed ellipses around the data points correspond to one and two standard deviations to the joint measurement of f_0^W and f_0^Z, respectively.

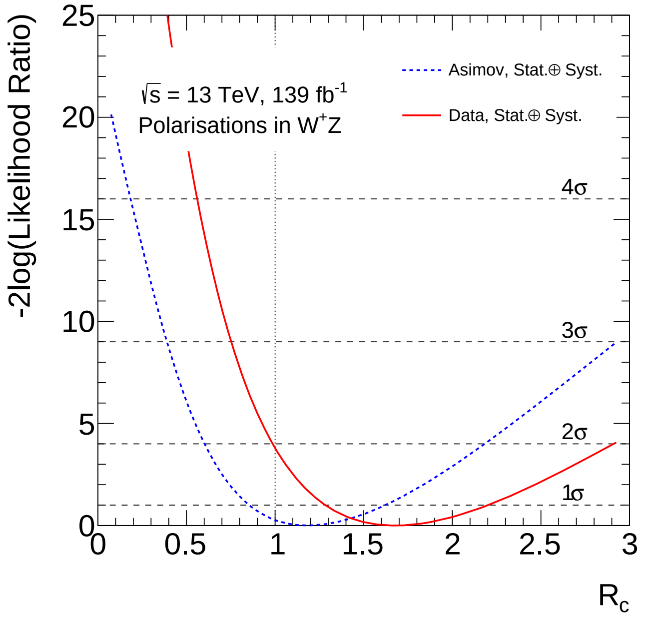

Figure D.4 Curve of the test statistic $-2\log(\text{Likelihood Ratio})$ along the ratio R_c in W^+Z events. The likelihood ratio is profiled for all systematic uncertainties. Its width at the 1σ horizontal line gives the total statistical and systematic asymmetrical uncertainty on R_c. The blue dashed curve represent the expected result, from an Asimov fit at reconstructed level. The red curve represents the result on Run-2 data. The vertical line at 1 corresponds to the absence of spin correlation hypothesis.

D.2 In W^-Z events

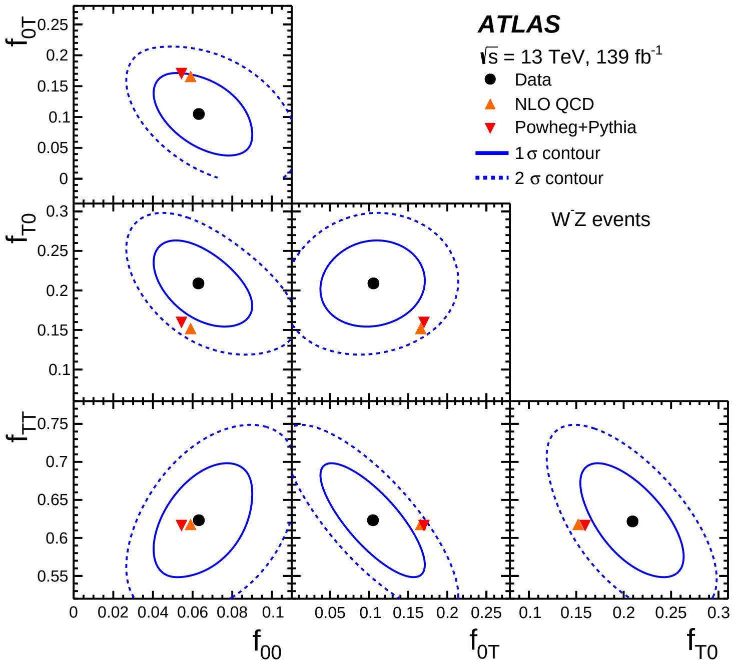

Figure D.5 Measured joint-polarisation fractions f_{00}, $f_{0\mathrm{T}}$, $f_{\mathrm{T}0}$ and f_{TT} of the W^- and Z bosons in W^-Z events, compared to NLO QCD fixed-order predictions [77] (orange triangle) and to Monte Carlo predictions from Powheg+Pythia (red triangle). The effect of PDF and QCD scale uncertainties on the Powheg+Pythia and NLO QCD fixed-order predictions are of the same size as the respective markers. The solid and dashed ellipses around the data points correspond to one and two standard deviations, respectively.

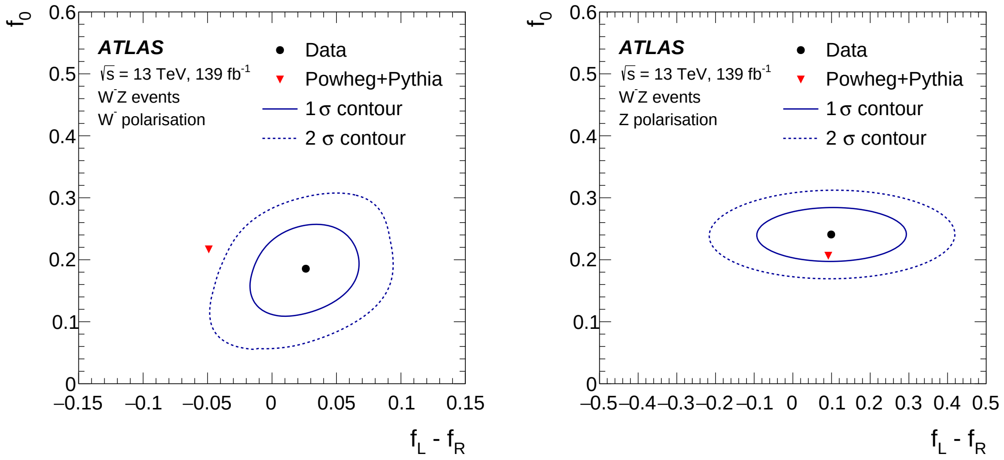

(a) **(b)**

Figure D.6 Single boson polarisation fractions f_0 and $f_{\mathrm{L}} - f_{\mathrm{R}}$ measured for the W^- boson (a) and Z boson (b) in W^-Z events, compared with predictions from Powheg+Pythia with $\sin^2\theta_{\mathrm{w}} = 0.23152$ (red triangle). The effect of PDF and QCD scale uncertainties on the Powheg+Pythia predictions are of the same size as the triangle marker. The solid and dashed ellipses around the data points correspond to one and two standard deviations, respectively.

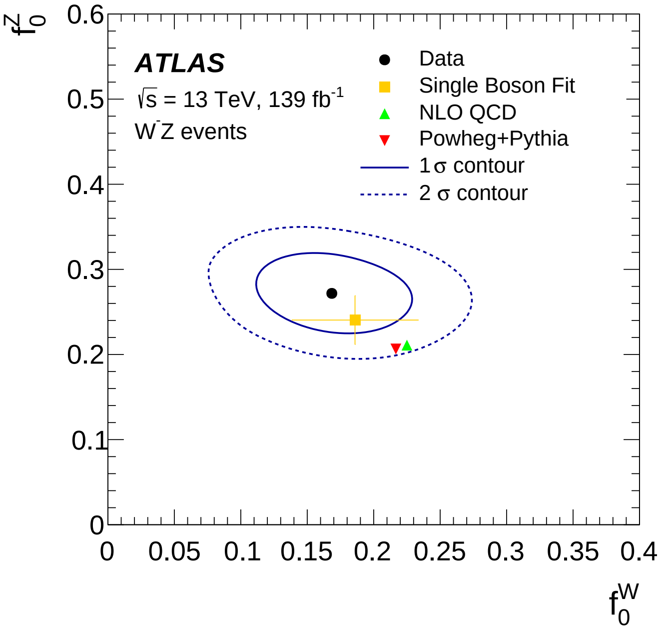

Figure D.7 Measured polarisation fractions f_0^W and f_0^Z in W^-Z events. The black point is the simultaneously measured values from the template fit on the 4-category DNN score distribution. The orange square with uncertainty bars is the measured value from two single boson polarisation template fits to $q_W \cdot \cos\theta^*_{\ell W}$ and $\cos\theta^*_{\ell Z}$ distributions. The red triangle is the theoretical predictions at NLO in QCD and LO for the electroweak interaction from POWHEG+PYTHIA. The solid and dashed ellipses around the data points correspond to one and two standard deviations to the joint measurement of f_0^W and f_0^Z, respectively.

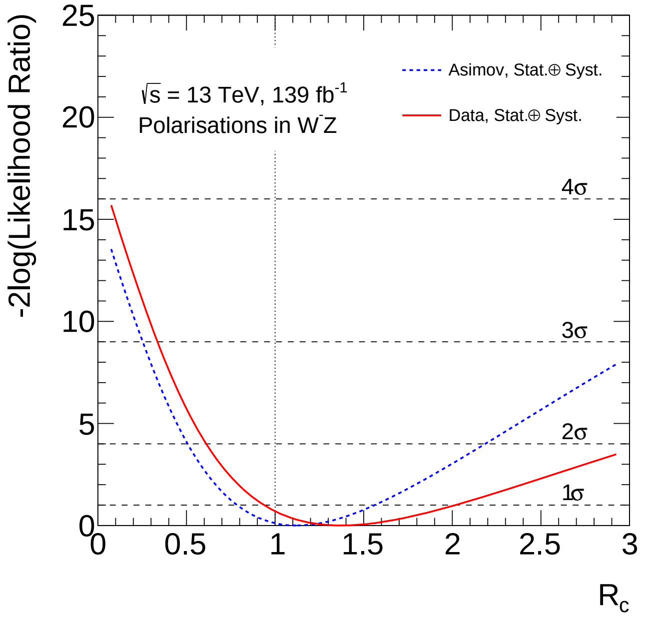

Figure D.8 Curve of the test statistic $-2\log$ (Likelihood Ratio) along the ratio R_c in W^-Z events. The likelihood ratio is profiled for all systematic uncertainties. Its width at the horizontal $1\,\sigma$ line gives the total statistical and systematic asymmetrical uncertainty on R_c. The blue dashed curve represent the expected result, from an Asimov fit at reconstructed level. The red curve represents the result on Run-2 data. The vertical line at 1 corresponds to the absence of spin correlation hypothesis.

Appendix E

Definition of $\cos\theta^*_\ell$ in the previous single boson polarisation fraction measurement

In the previous measurement of single boson polarisation fractions of Ref. [17], the $\cos\theta^*_\ell$ definition was ill-defined. To compute it for a boson V, one needs a four-vector of the boson V and a four-vector of the associated decay lepton. The $\cos\theta^*_\ell$ will be obtained from the scalar product of both vectors. Experimentally, one starts with kinematic variables in the laboratory frame $\mathfrak{R}_{lab}$. In the *Modified Helicity* frame, the boson four-vector is obtained by boosting its four-vector from the laboratory frame to the $W^\pm Z$ rest frame $\mathfrak{R}_{WZ}$. On the other hand, the decay lepton four-vector must be boosted in the V boson rest frame $\mathfrak{R}_V$ and there are two ways to do that :

Previous measurement [17]: Take the four-vector of the boson in the laboratory frame $\mathfrak{R}_{lab}$ and boost it directly in the V rest frame $\mathfrak{R}_V$ with the Lorentz transform $\Lambda_{\mathfrak{R}_{lab}\to\mathfrak{R}'_V}$.

Present measurement: Take the four-vector of the boson in the laboratory frame $\mathfrak{R}_{lab}$ and boost it first in the $W^\pm Z$ rest frame $\mathfrak{R}_{WZ}$ with $\Lambda_{\mathfrak{R}_{lab}\to\mathfrak{R}_{WZ}}$, and then boost it again in the V rest frame $\mathfrak{R}_V$ with $\Lambda_{\mathfrak{R}_{WZ}\to\mathfrak{R}_V}$.

It is well known that the composition of non-collinear boosts do not necessarily give a new boost: an additional rotation will appear. Here, to transform the four-vector of the lepton from the previous analysis way to the current way, one must use the transition matrix

$$R_{\mathfrak{R}'_V\to\mathfrak{R}_V} = \Lambda_{\mathfrak{R}_{WZ}\to\mathfrak{R}_V}\Lambda_{\mathfrak{R}_{lab}\to\mathfrak{R}_{WZ}}\Lambda^{-1}_{\mathfrak{R}_{lab}\to\mathfrak{R}_V} , \tag{E.1}$$

which is a rotation. The problem with the previous way of computing $\cos\theta^*_\ell$ is that the lepton four-vector used had its coordinates in $\mathfrak{R}'_V$ with its axes not aligned to the axes of $\mathfrak{R}_{WZ}$. As a result the angle between the lepton direction and the V boson direction was systematically off by an additional rotation angle. Additionally, this rotation angle changes event by event, as it depends on the direction of the boost $\Lambda_{\mathfrak{R}_{WZ}\to\mathfrak{R}_V}$ given by the angle θ_V defined in figure 5.2(b).

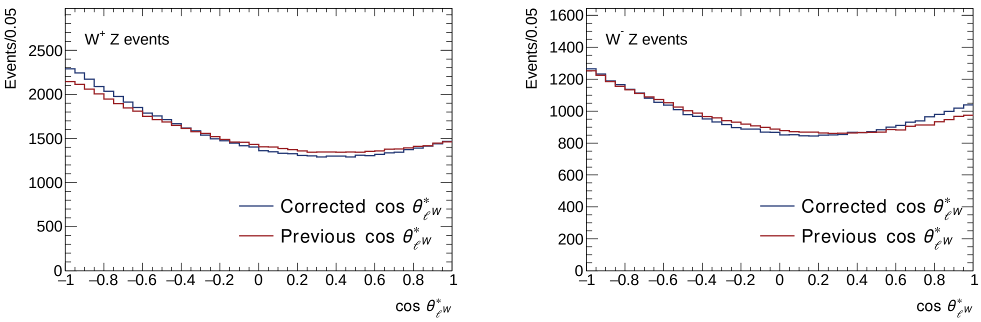

(a) W^+ **(b)** W^-

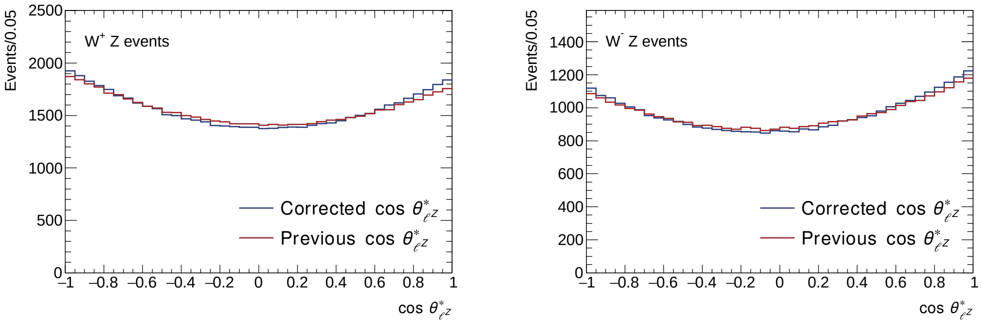

(c) Z in W^+Z **(d)** Z in W^-Z

Figure E.1 Comparing previous to current $\cos\theta^*_\ell$ definition at particle level in the total phase space for all bosons in all charge configurations, using the inclusive POWHEG+PYTHIA sample.

Yet, even though the previous $\cos\theta^*_\ell$ was wrong, the difference with the correct $\cos\theta^*_\ell$ used here is in the end rather small, as can be seen in Fig. E.1. This small difference still has an impact on the values of the fractions at truth level in the total phase space as can be seen in Table E.1. Of course, the uncertainties are not affected as this correction only amounts to a small change in the shape of the fitted distribution.

In W^+Z events

	W^+ boson polarisation		Z boson polarisation	
	Corrected $\cos\theta^*_{\ell W}$	Previous $\cos\theta^*_{\ell W}$	Corrected $\cos\theta^*_{\ell Z}$	Previous $\cos\theta^*_{\ell Z}$
f_0	0.1821 ± 0.0009	0.2151 ± 0.0009	0.1807 ± 0.0009	0.2100 ± 0.0009
f_L	0.5006 ± 0.0006	0.4687 ± 0.0006	0.3612 ± 0.0017	0.3314 ± 0.0017
f_R	0.3172 ± 0.0005	0.3162 ± 0.0005	0.4580 ± 0.0018	0.4585 ± 0.0017

In W^-Z events

	W^- boson polarisation		Z boson polarisation	
	Corrected $\cos\theta^*_{\ell W}$	Previous $\cos\theta^*_{\ell W}$	Corrected $\cos\theta^*_{\ell Z}$	Previous $\cos\theta^*_{\ell Z}$
f_0	0.1901 ± 0.0011	0.2218 ± 0.0012	0.1822 ± 0.0012	0.2086 ± 0.0012
f_L	0.3652 ± 0.0007	0.3404 ± 0.0007	0.5053 ± 0.0022	0.4774 ± 0.0022
f_R	0.4447 ± 0.0008	0.4378 ± 0.0008	0.3125 ± 0.0022	0.3139 ± 0.0022

Table E.1 Fraction results at particle level in the total phase space with previous and current corrected $\cos\theta^*_\ell$ extracted from the inclusive POWHEG+PYTHIA sample.

Conclusion

Within the scope of this thesis, the joint-polarisation fractions in a diboson process are measured for the first time. It constitutes the first ever observation of two bosons produced simultaneously in a longitudinal polarisation state. This thesis also details my personal contribution to the upgrade of the ATLAS detector before the start of the Run 3 of the LHC.

The trigger system of the liquid Argon-based calorimeters of ATLAS was improved to prepare for higher pile-up conditions in Run 3 and particularly for the High-Luminosity LHC runs that will follow. The trigger-level information from the calorimeter cells was increased in spatial granularity by a factor ten, from Trigger Towers to Super Cells. This required a complete overhaul of the trigger electronic chain to cope with a largely increased amount of data to manage within the strict latency criteria required by the trigger system. In particular, I contributed to configuration software of the LATOME boards responsible for the energy deposit computation. I developed the proper loading of calibration coefficients in registers of the LATOME, used by the User Code block to compute energies. I then participated to the commissioning of this User Code block.

On the analysis side, the measurement of vector boson polarisation states in $W^{\pm}Z$ production was detailed. This measurement used the full Run 2 dataset collected by the ATLAS detector at the LHC, in *pp* collisions at a centre-of-mass energy of 13 TeV between 2015 and 2018, corresponding to an integrated luminosity of $139\,\mathrm{fb}^{-1}$. Among the collected data, events corresponding to a $W^{\pm}Z$ production were selected, using the leptonic decay mode. The corresponding experimental signature in the detector is

$$pp \to \ell\nu\ell'\bar{\ell}' + X \ ,$$

with each lepton ℓ being either an electron or a muon. A fiducial phase space closely matching the event selection was defined. All measurements were then performed in this phase space.

The theoretical description of polarisation implies a strong dependence on the frame chosen for the measurements. In order to meaningfully measure joint-polarisation fractions simultaneously with single boson polarisation fractions, the centre-of-mass frame of the $W^{\pm}Z$ system is chosen, leading to the *Modified Helicity* frame used for single boson polarisation measurements.

The polarisation fractions were measured through binned maximum-likelihood template fits. As a first step, a discriminating variable was needed to extract simultaneously all polarisation fractions. For single boson polarisation, simple analytical variables can be used, namely $q_W \cdot \cos\theta^*_{\ell W}$ for the $W^{\pm}$ boson polarisation measurement, and $\cos\theta^*_{\ell Z}$ for the Z boson polarisation measurement. However, for joint-polarisation fractions, an aggregated variable using a Deep Neural Network (DNN) output had to be used to obtain enough sensitivity in the measurement. Combined with the $\cos\theta^*_{\ell W}$ and $\cos\theta^*_{\ell Z}$ variables, this 4-category p_{00}^{DNN} DNN output allowed for the separation between longitudinal-longitudinal 00, longitudinal-transverse 0T, transverse-longitudinal T0 and transverse-transverse TT joint-polarisation states.

The next challenge was to develop templates of pure polarisation states for the discriminating variable. In single boson polarisation measurement, an analytical reweighting method provides such template with NLO in QCD accuracy for the three polarisation states longitudinal 0, left L and right R. However, this method cannot be used with the aggregated 4-category p_{00}^{DNN} variable. Other ideas implied the use of LO Monte Carlo polarised generation. These samples were brought to NLO in QCD accuracy using a reweighting to fixed-order polarised calculation at NLO in QCD. Another idea made use of classification DNNs to provide a multi-dimensional reweighting bringing the polarised samples to NLO in QCD accuracy, or symmetrically, polarising an inclusive NLO in QCD accurate sample. This latter method was found to provide templates with the least bias on NLO in QCD pseudo-datasets.

The binned maximum-likelihood template fit provided the first ever observation of pair-produced vector bosons simultaneously polarised longitudinally, with observed and expected significance of $7.1\,\sigma$ and $6.2\,\sigma$ respectively. In the fiducial phase space of this analysis, for $W^{\pm}Z$ production, the fraction of longitudinal-longitudinal joint-polarisation is measured to be $f_{00} = 0.067 \pm 0.010$. Other joint-polarisation measured are $f_{0\mathrm{T}} = 0.110 \pm 0.029$, $f_{\mathrm{T}0} = 0.179 \pm 0.023$ and $f_{\mathrm{TT}} = 0.644 \pm 0.032$. The same measurement was also performed separating by the charge of the $W^{\pm}$ boson, in $W^{+}Z$ and $W^{-}Z$ events. No major differences were observed with the inclusive $W^{\pm}Z$ results. All measured values are found to be consistent with Standard Model predictions within two standard deviations.

Single boson polarisation fractions was measured in $W^{\pm}Z$ production as well, extending the previous measurement of Ref. [17] to the full Run 2 dataset. The measured f_0 and $f_{\mathrm{L}} - f_{\mathrm{R}}$ are found to agree with the Standard Model prediction. Moreover, their measurement is consistent with the joint-polarisation fractions measured, neglecting the effect of interferences which are expected from calculations to be well below the precision of the present measurements.

Finally, it was checked that the polarisation fractions of the two bosons cannot be considered to be independent of each other. The joint-polarisation fraction f_{00} was found to be more than 50 % higher than the multiplication of single boson f_0 polarisation fractions. This demonstrates the need for a direct measurement of joint-polarisation fractions, rejecting the independence assumption at more than $1\,\sigma$.

This measurement was approved by the ATLAS Collaboration and published in Ref. [115]. It constitutes a pioneering work for further joint-polarisation studies. Other diboson processes could be studied, or alternatively, the measurement could be performed in a more restricted phase space where new physics might manifest itself more clearly. The ultimate goal, for now inaccessible for lack of statistical power, would be the observation of the very delicate process of vector boson scattering with both bosons polarised longitudinally.

Remerciements

Ces trois années de thèses n'auront pas été sans épreuves, avec en vrac la pire pandémie vécue par l'humanité depuis près d'un siècle, `HistFactory` et sa (non) documentation, les ping-pongs administratifs entre Collège et École doctorale, un écran d'ordinateur qui casse à deux semaines du rendu de thèse aux rapporteurs ou encore l'envoie d'un colocataire indélicat vers d'autres formes de logement collectif aux portes particulièrement malaimables. Je n'aurais jamais pu traverser toutes ces difficultés seul. Je tiens donc à remercier toutes les personnes qui m'ont permis de mener à bien cette thèse et même de m'y épanouir !

En premier lieu, je ne remercierai jamais assez mon directeur de thèse Emmanuel Sauvan pour m'avoir guidé à travers toutes ces années. Au delà de la physique, je lui dois aussi beaucoup en méthodes de travail, en compréhension du monde d'ATLAS et de la recherche en général et en savoir-être pour faire avancer ma carrière. J'ai bien conscience de la chance que j'ai eu d'avoir un niveau d'encadrement si élevé et je tâcherai de suivre cette exemple si l'occasion m'en est donnée.

Je tiens également à remercier Guillaume Unal, Elzbieta Richter-Wass et Gilles Maurin d'avoir accepté d'être membres de mon jury. Je remercie tout particulièrement mes rapporteurs Philippe Schwemling et Vincent Tisserand pour leurs retours complets sur mes histoires de LATOME et de bosons.

Sur le front des LATOMEs, je remercie Thibault Guillemin pour m'avoir initié au monde de LAr Online et de l'EMF, des serveurs UDP à lancement manuel et des LArC restés sur la mauvaise version. Merci également à Fatih Bellacchia pour m'avoir tant appris sur les rigueurs du C++, Sylvain Lafrasse pour m'avoir si souvent débloqué quand je n'arrivais simplement pas à compiler mes packages LAr Online et Nicolas Chevillot pour ses explications toujours limpides du fonctionnement du firmware de la LATOME.

Merci à l'équipe LAr du CERN, en particulier pour ces semaines d'intégration du firmware qui m'ont souvent permis d'échapper au confinement. Merci donc à mon vaillant petit proximètre qui apparemment était une condition de survie nécessaire dans un CERN pandémisé. Merci surtout à Georges Aad pour ces longues journées à essayer de faire cracher des énergies aux LATOME. Merci à Yuji Enari pour m'avoir vaillamment expliqué pourquoi il allait me falloir plusieurs jours pour faire fonctionner trois additions et quatre multiplications avec des bits. Merci à Pavol Strizenec pour m'avoir expliqué les raisons plus ou moins philosophiques d'avoir quatre ou cinq identifiants différents pour les Super Cellules. Merci à Adriana Milic pour sa bonne humeur en integration room. Merci enfin à Emmanuel Monnier pour avoir accepté de me recommander dans mes candidatures à des post-doctorats.

Côté bosons, je remercie particulièrement Francesco Costanza pour son expertise DNN qui aura été décisive pour l'analyse: sans DNN il n'y a plus grand chose qui aurait fonctionné !

Je remercie également Lucia Di Ciaccio, Narei Lorenzo Martinez et Iro Koletsou pour leurs remarques et conseils toujours pertinents. Merci à Nicolas Berger pour son aide sur toute question de statistique et tout particulièrement pour sa très élégante fonction de double-fermi. Merci également à Marco Delmastro pour sa relecture experte de ma description du Calorimètre LAr. Merci à Claire Adam-Bourdarios pour m'avoir offert la possibilité de donner une présentation grand public de Fête de la Science. Merci plus généralement à tout le reste de l'équipe ATLAS du LAPP.

Je remercie également les membres de mon bureau éditorial Evelin Meoni, Michel Lefebvre et Chilufya Mwewa qui ont eu fort à faire pour permettre la validation de notre analyse dans les temps. Je remercie particulièrement sa présidente Evelin Meoni pour ses retours constructifs (même si je ne suis toujours pas convaincu par cette histoire de changement de couleur de courbes) et pour m'avoir recommandé dans mes candidatures de post-doctorats.

Je remercie plus généralement les collègues du LAPP qui ont tenté de maintenir de la vie dans ce labo malgré les aléas pandémiques. Merci à Corinne Feullar et au reste de l'équipe administrative pour avoir su endurer ma phobie paperassière.

Tout spécialement, je tiens à remercier Isabelle Debonis pour m'avoir offert la possibilité d'enseigner à l'IUT d'Annecy. La façon dont elle l'avait organisé m'a permis de m'épanouir pleinement dans cette activité d'abord intimidant. J'ai beaucoup aimé (dé)régler des goniomètres et expliquer la mécanique newtonienne avec des skieurs fous.

Bien sûr, si j'avais dû partager ma vie intégralement entre Argon et boson, je n'aurais pas gardé ma santé mentale très longtemps. Je remercie donc tous les autres doctorants du LAPP d'avoir su faire renaître une belle ambiance de laboratoire post-covid, à coup d'afterworks pré-couvre-feu et de concours de pétanque.

Je remercie particulièrement ma voisine de bureau Gitu qui s'est bien assurée que je ne travaille pas trop ! Merci aussi Léo, co-bureau sur le tard qui a accompagné mes dernières intenses semaines de rédaction.

Je dois aussi remercier ceux qui ont par la force des choses joué les collègues de bureau en ces temps de confinements : mes colocataires ! Merci donc Ursule et Emma pour m'avoir laissé transformer le meuble télé en open-space, et merci d'avoir transformé mon quotidien confiné en mini télé-réalité !

Un merci spécial aux *anciens du 80*: Guillaume au mille capots et qui réussit mieux les tomates que les boutures, Nadège, "la petite dame" partenaire de rock confiné et de poulet frites du dimanche midi. Merci aussi Eva pour ta bonne humeur irradiante de bon matin et ton acharnement à me faire gravir tous les sommets de Haute-Savoie. Au fil du temps, on a finit par former un petit foyer entre nos deux appartements, c'était bon de rentrer à la maison. Avec tous les autres, Mickaël, Fabio, Yann, Julie, Victor, Zoé, Julien, on n'était pas loin de recréer des épisodes de *Friends* (avec parfois un peu trop de policiers à mon goût).

Merci également Sylvain, bien souvent la voix de la raison à qui je dois surement de ne pas être encore mort au fond d'une grotte du Parmelan. En tout cas sois tranquille, tu gardes le record du nombre de visites sur Annecy.

Enfin, je ne serais peut-être pas rendu si loin sans ma famille : mon papa, ma maman qui m'ont toujours soutenu dans ma passion pour les sciences, même si ça commence à faire un petit bout de temps qu'ils n'y comprennent plus rien ; mon adorablement agaçante petite sœur ; mon petit frère le kéké des plages.

Merci aussi à mes grands-parents : mamie Rosette qui m'a hébergé pendant mes trois années de classes prépa, papi Pierre et mamie Cot' notamment pour m'avoir recueilli pendant mes révisons de Master, fuyant ma passoire thermique de banlieue parisienne.

Et pour finir, je reconnais ce que je dois aux nombreuses canettes d'Orangina sans lesquelles je n'aurais jamais pu finir cette thèse dans les temps !

Merci Léo pour le mème !

Bibliography

[1] ATLAS Collaboration, *Observation of a new particle in the search for the Standard Model Higgs boson with the ATLAS detector at the LHC*, Phys. Lett. B **716** (2012) 1, arXiv: `1207.7214 [hep-ex]` (cit. on pp. xi, 3).

[2] CMS Collaboration, *Observation of a New Boson at a Mass of 125 GeV with the CMS Experiment at the LHC*, Phys. Lett. B **716** (2012) 30, arXiv: `1207.7235 [hep-ex]` (cit. on pp. xi, 3).

[3] T. Aaltonen et al., *High-precision measurement of the W boson mass with the CDF II detector*, Science **376** (2022) 170 (cit. on p. xi).

[4] ATLAS Collaboration, *Standard Model Summary Plots February 2022*, tech. rep., All figures including auxiliary figures are available at https://atlas.web.cern.ch/Atlas/GROUPS/PHYSICS/PUBNOTES/ATL-PHYS-PUB-2022-009: CERN, 2022, URL: `http://cds.cern.ch/record/2804061` (cit. on p. xii).

[5] OPAL Collaboration, *W boson polarisation at LEP2*, Phys. Lett. B **585** (2004) 223, arXiv: `hep-ex/0312047 [hep-ex]` (cit. on p. xii).

[6] P. Achard et al., *Measurement of W polarisation at LEP*, Phys. Lett. B **557** (2003) 147, arXiv: `hep-ex/0301027` (cit. on p. xii).

[7] J. Abdallah et al., *Study of W boson polarisations and Triple Gauge boson Couplings in the reaction e+e- —> W+W- at LEP 2*, Eur. Phys. J. C **54** (2008) 345, arXiv: `0801.1235 [hep-ex]` (cit. on p. xii).

[8] F. D. Aaron et al., *Events with Isolated Leptons and Missing Transverse Momentum and Measurement of W Production at HERA*, Eur. Phys. J. C **64** (2009) 251, arXiv: `0901.0488 [hep-ex]` (cit. on p. xii).

[9] CDF and D0 Collaborations, *Combination of CDF and D0 measurements of the W boson helicity in top quark decays*, Phys. Rev. D **85** (2012) 071106, arXiv: `1202.5272 [hep-ex]` (cit. on p. xii).

[10] CDF Collaboration, *Measurement of W-Boson Polarization in Top-Quark Decay in $p\bar{p}$ Collisions at $\sqrt{s} = 1.96$ TeV*, Phys. Rev. Lett. **105** (2010) 042002, arXiv: `1003.0224 [hep-ex]` (cit. on p. xii).

[11] D0 Collaboration, *Measurement of the W boson helicity in top quark decays using 5.4 fb^{-1} of $p\bar{p}$ collision data*, Phys. Rev. D **83** (2011) 032009, arXiv: `1011.6549 [hep-ex]` (cit. on p. xii).

[12] ATLAS Collaboration, *Measurement of the polarisation of W bosons produced with large transverse momentum in pp collisions at $\sqrt{s} = 7$ TeV with the ATLAS experiment*, Eur. Phys. J. C **72** (2012) 2001, arXiv: `1203.2165 [hep-ex]` (cit. on p. xii).

[13] CMS Collaboration, *Measurement of the Polarization of W Bosons with Large Transverse Momenta in W+jets Events at the LHC*, Phys. Rev. Lett. **107** (2011) 021802, arXiv: `1104.3829 [hep-ex]` (cit. on p. xii).

[14] CDF Collaboration, *First Measurement of the Angular Coefficients of Drell-Yan e^+e^- Pairs in the Z Mass Region from $p\bar{p}$ Collisions at $\sqrt{s}$ = 1.96 TeV*, Phys. Rev. Lett. **106** (2011) 241801, arXiv: `1103.5699 [hep-ex]` (cit. on p. xii).

[15] ATLAS Collaboration, *Measurement of the angular coefficients in Z-boson events using electron and muon pairs from data taken at $\sqrt{s} = 8$ TeV with the ATLAS detector*, JHEP **08** (2016) 159, arXiv: `1606.00689 [hep-ex]` (cit. on pp. xii, 76).

[16] CMS Collaboration, *Angular coefficients of Z bosons produced in pp collisions at $\sqrt{s}$ = 8 TeV and decaying to $\mu^+\mu^-$ as a function of transverse momentum and rapidity*, Phys. Lett. B **750** (2015) 154, arXiv: `1504.03512 [hep-ex]` (cit. on p. xii).

[17] ATLAS Collaboration, *Measurement of $W^{\pm}Z$ production cross sections and gauge boson polarisation in pp collisions at $\sqrt{s} = 13$ TeV with the ATLAS detector*, Eur. Phys. J. C **79** (2019) 535, arXiv: `1902.05759 [hep-ex]` (cit. on pp. xii, xiii, 91, 95, 100, 103, 104, 115, 147, 150, 157, 169, 172).

[18] CMS Collaboration, *Measurement of the inclusive and differential WZ production cross sections, polarization angles, and triple gauge couplings in pp collisions at $\sqrt{s}$ = 13 TeV*, (2021), arXiv: `2110.11231 [hep-ex]` (cit. on p. xii).

[19] P. Achard et al., *Study of spin and decay-plane correlations of W bosons in the $e^+e^- \to W^+W^-$ process at LEP*, Eur. Phys. J. C **40** (2005) 333, arXiv: `hep-ex/0501036` (cit. on p. xiii).

[20] G. Abbiendi et al., *Measurement of W boson polarizations and CP violating triple gauge couplings from W^+W^- production at LEP*, Eur. Phys. J. C **19** (2001) 229, arXiv: `hep-ex/0009021` (cit. on p. xiii).

[21] J. Abdallah et al., *Correlations between Polarisation States of W Particles in the Reaction $e^-e^+ \to W^-W^+$ at LEP2 Energies 189-GeV - 209-GeV*, Eur. Phys. J. C **63** (2009) 611, arXiv: `0908.1023 [hep-ex]` (cit. on pp. xiii, 81).

[22] ATLAS Collaboration, *Measurement of the $W^{\pm}Z$ boson pair-production cross section in pp collisions at $\sqrt{s} = 13$ TeV with the ATLAS Detector*, arXiv e-prints, arXiv:1606.04017 (2016) arXiv:1606.04017, arXiv: `1606.04017 [hep-ex]` (cit. on p. xiii).

[23] A. Burger, 'Measurement of Vector Boson polarisation in WZ production at the LHC with the ATLAS detector', PhD thesis: École doctorale de Physique de Grenoble, 2018 (cit. on p. xiii).

[24] F. Englert and R. Brout, *Broken Symmetry and the Mass of Gauge Vector Mesons*, Phys. Rev. Lett. **13** (1964) 321, ed. by J. C. Taylor (cit. on pp. 1, 3, 6).

[25] P. W. Higgs, *Broken Symmetries and the Masses of Gauge Bosons*, Phys. Rev. Lett. **13** (1964) 508, ed. by J. C. Taylor (cit. on pp. 1, 3, 6).

[26] F. Gelis, *Quantum Field Theory: From Basics to Modern Topics*, Cambridge University Press, 2019 (cit. on p. 1).

[27] H. Lehmann, K. Symanzik and W. Zimmermann, *On the formulation of quantized field theories*, Nuovo Cim. **1** (1955) 205 (cit. on p. 2).

[28] M. S. Chanowitz and M. K. Gaillard, *The TeV Physics of Strongly Interacting W's and Z's*, Nucl. Phys. B **261** (1985) 379 (cit. on p. 10).

[29] M. Aaboud et al., *Observation of electroweak $W^{\pm}Z$ boson pair production in association with two jets in pp collisions at $\sqrt{s} =$ 13 TeV with the ATLAS detector*, Phys. Lett. B **793** (2019) 469, arXiv: `1812.09740 [hep-ex]` (cit. on p. 10).

[30] U. Baur, T. Han and J. Ohnemus, *Amplitude zeros in $W^{+/-}$ Z production*, Phys. Rev. Lett. **72** (1994) 3941, arXiv: `hep-ph/9403248` (cit. on pp. 10, 110).

[31] G. Panico, F. Riva and A. Wulzer, *Diboson interference resurrection*, Phys. Lett. B **776** (2018) 473, arXiv: `1708.07823 [hep-ph]` (cit. on p. 10).

[32] C. Bourrely, E. Leader and J. Soffer, *Polarization phenomena in hadronic reactions*, Physics Reports **59** (1980) 95, ISSN: 0370-1573, URL: `https://www.sciencedirect.com/science/article/pii/0370157380900174` (cit. on pp. 11, 69).

[33] H.-L. Lai et al., *New parton distributions for collider physics*, Physical Review D **82** (2010), URL: `https://doi.org/10.1103%2Fphysrevd.82.074024` (cit. on p. 14).

[34] S. Höche, *Introduction to parton-shower event generators*, arXiv e-prints, arXiv:1411.4085 (2014) arXiv:1411.4085, arXiv: `1411.4085 [hep-ph]` (cit. on pp. 15, 16).

[35] J. Alwall et al., *The automated computation of tree-level and next-to-leading order differential cross sections, and their matching to parton shower simulations*, JHEP **07** (2014) 079, arXiv: `1405.0301 [hep-ph]` (cit. on pp. 16, 74).

[36] S. Alioli, P. Nason, C. Oleari and E. Re, *A general framework for implementing NLO calculations in shower Monte Carlo programs: the POWHEG BOX*, JHEP **06** (2010) 043, arXiv: `1002.2581 [hep-ph]` (cit. on pp. 16, 74).

[37] T. Sjöstrand et al., *An introduction to PYTHIA 8.2*, Comput. Phys. Commun. **191** (2015) 159, arXiv: `1410.3012 [hep-ph]` (cit. on pp. 16, 74).

[38] P. Nason, *A New method for combining NLO QCD with shower Monte Carlo algorithms*, JHEP **11** (2004) 040, arXiv: `hep-ph/0409146` (cit. on pp. 16, 74).

[39] S. Frixione, P. Nason and C. Oleari, *Matching NLO QCD computations with parton shower simulations: the POWHEG method*, JHEP **11** (2007) 070, arXiv: `0709.2092 [hep-ph]` (cit. on pp. 16, 74).

[40] E. Bothmann et al., *Event generation with Sherpa 2.2*, SciPost Physics **7** (2019), URL: `https://doi.org/10.21468%2Fscipostphys.7.3.034` (cit. on pp. 16, 74).

[41] L. Evans and P. Bryant, *LHC Machine*, Journal of Instrumentation **3** (2008) S08001, URL: `https://doi.org/10.1088/1748-0221/3/08/s08001` (cit. on pp. 17, 19).

[42] ATLAS Collaboration, *The ATLAS Experiment at the CERN Large Hadron Collider*, Journal of Instrumentation **3** (2008) S08003, URL: `https://doi.org/10.1088/1748-0221/3/08/s08003` (cit. on pp. 17, 25, 27, 28, 31).

[43] R. W. Assmann, M. Lamont and S. Myers, *A Brief History of the LEP Collider*, Nucl. Phys. B, Proc. Suppl. **109** (2002) 17, URL: `https://cds.cern.ch/record/549223` (cit. on p. 18).

[44] *The Tevatron legacy: a luminosity story*, CERN Courier **56** (2016) 25, URL: `https://cds.cern.ch/record/2232578` (cit. on p. 18).

[45] H. Damerau et al., *LHC Injectors Upgrade, Technical Design Report*, 2014, URL: `https://cds.cern.ch/record/1976692` (cit. on pp. 19, 23, 24).

[46] F. Marcastel, *CERN's Accelerator Complex. La chaîne des accélérateurs du CERN*, (2013), General Photo, URL: `http://cds.cern.ch/record/1621583` (cit. on p. 20).

[47] R. Steerenberg, *Hadron Accelerators*, CERN-Fermilab HCP Summer School, 2017, URL: `https://indico.cern.ch/event/598530/contributions/2547206/attachments/1516215/2366657/HadronAcc-1_2017.pdf` (cit. on p. 20).

[48] G. Avoni et al., *The new LUCID-2 detector for luminosity measurement and monitoring in ATLAS*, Journal of Instrumentation **13** (2018) P07017, URL: `https://doi.org/10.1088/1748-0221/13/07/p07017` (cit. on p. 21).

[49] ATLAS Collaboration, *Luminosity determination in pp collisions at* $\sqrt{s} = 13$ *TeV using the ATLAS detector at the LHC*, tech. rep., CERN, 2019, URL: `https://cds.cern.ch/record/2677054` (cit. on pp. 21, 94, 101, 141).

[50] ATLAS Collaboration, *Luminosity Public Results Run-2*, URL: `https://twiki.cern.ch/twiki/bin/view/AtlasPublic/LuminosityPublicResultsRun2#Publications_and_Conference_Resu` (cit. on pp. 21, 22).

[51] HL-LHC Collaboration, *The HL-LHC project*, URL: `https://hilumilhc.web.cern.ch/content/hl-lhc-project` (cit. on p. 23).

[52] O. Aberle et al., *High-Luminosity Large Hadron Collider (HL-LHC): Technical design report*, CERN Yellow Reports: Monographs, CERN, 2020, URL: `https://cds.cern.ch/record/2749422` (cit. on p. 23).

[53] S. Fartoukh et al., *LHC Configuration and Operational Scenario for Run 3*, tech. rep., CERN, 2021, URL: `https://cds.cern.ch/record/2790409` (cit. on p. 24).

[54] M. Chalmers, *LHC Run 3: the final countdown*, CERN Courier (2022), URL: `https://cerncourier.com/a/lhc-run3-th-final-countdown/` (cit. on p. 24).

[55] J. T. Boyd, 'LHC Run-2 and Future Prospects', *2019 European School of High-Energy Physics*, 2020, arXiv: `2001.04370 [hep-ex]` (cit. on p. 24).

[56] ATLAS Collaboration, *Drift Time Measurement in the ATLAS Liquid Argon Electromagnetic Calorimeter using Cosmic Muons*, Eur. Phys. J. C **70** (2010) 755, arXiv: `1002.4189 [physics.ins-det]` (cit. on p. 29).

[57] ATLAS Collaboration, *ATLAS Liquid Argon Calorimeter Phase-I Upgrade: Technical Design Report*, tech. rep., CERN-LHCC-2013-017, ATLAS-TDR-022, https://cds.cern.ch/record/1602230, 2013, URL: `https://cds.cern.ch/record/1602230` (cit. on pp. 30, 35, 36, 42–46).

[58] ATLAS Collaboration, *ATLAS liquid-argon calorimeter: Technical Design Report*, Technical design report. ATLAS, CERN, 1996, URL: `https://cds.cern.ch/record/331061` (cit. on pp. 30, 35, 37, 38).

[59] ATLAS Collaboration, *Technical Design Report for the Phase-I Upgrade of the ATLAS TDAQ System*, tech. rep., Final version presented to December 2013 LHCC, 2013, URL: `https://cds.cern.ch/record/1602235` (cit. on p. 33).

[60] W. Cleland and E. Stern, *Signal processing considerations for liquid ionization calorimeters in a high rate environment*, Nucl. Inst. Meth. A **338** (1994) 467, ISSN: 0168-9002, URL: `https://www.sciencedirect.com/science/article/pii/0168900294913323` (cit. on pp. 38, 39).

[61] M. Aleksa et al., *ATLAS Combined Testbeam: Computation and Validation of the Electronic Calibration Constants for the Electromagnetic Calorimeter*, tech. rep., CERN, 2006, URL: `https://cds.cern.ch/record/942528` (cit. on pp. 39, 40).

[62] L. Di Ciaccio, D. Fournier and F. Hubaut, *High Voltage corrections for electromagnetic calorimeter*, tech. rep., CERN, 2005, URL: `https://cds.cern.ch/record/830849` (cit. on p. 40).

[63] L. Courneyea et al., *Computation and validation of the electronic calibration constants for the ATLAS Liquid Argon Calorimeters*, tech. rep., CERN, 2010, URL: `https://cds.cern.ch/record/1278462` (cit. on pp. 40–42).

[64] G. Aad et al., *The Phase-I trigger readout electronics upgrade of the ATLAS Liquid Argon calorimeters*, JINST **17** (2022) P05024, arXiv: `2202.07384 [physics.ins-det]` (cit. on pp. 44, 47, 50, 51).

[65] R. Jones, L. Mapelli, Y. Ryabov and I. Soloviev, *The OKS persistent in-memory object manager*, IEEE Transactions on Nuclear Science **45** (1998) 1958 (cit. on p. 52).

[66] I. Soloviev, *The version control service for the ATLAS data acquisition configuration files*, Journal of Physics: Conference Series **396** (2012) 012047, URL: `https://doi.org/10.1088/1742-6596/396/1/012047` (cit. on p. 52).

[67] ATLAS Collaboration, *ATLAS Computing: technical design report*, Technical design report. ATLAS, CERN, 2005, URL: `https://cds.cern.ch/record/837738` (cit. on p. 52).

[68] M. Verducci, *ATLAS conditions database experience with the LCG COOL conditions database project*, Journal of Physics: Conference Series **119** (2008) 042031, URL: `https://doi.org/10.1088/1742-6596/119/4/042031` (cit. on p. 52).

[69] ATLAS Collaboration, *LArCalo Public Pilot Beam 2021*, URL: `https://twiki.cern.ch/twiki/bin/view/AtlasPublic/LArCaloPublicPilotBeam2021` (cit. on p. 59).

[70] P. A. Zyla et al., *Review of Particle Physics*, PTEP **2020** (2020) 083C01 (cit. on pp. 64, 85, 89, 91, 118).

[71] ATLAS Collaboration, *Measurement of the $W \to \ell\nu$ and $Z/\gamma^* \to \ell\ell$ Production Cross Sections in Proton-Proton Collisions at $\sqrt{s} = 7$ TeV with the ATLAS Detector*, JHEP **12** (2010) 060, arXiv: `1010.2130 [hep-ex]` (cit. on p. 64).

[72] M. Grazzini, S. Kallweit, D. Rathlev and M. Wiesemann, *$W^{\pm}Z$ production at hadron colliders in NNLO QCD*, Phys. Lett. B **761** (2016) 179, arXiv: `1604.08576 [hep-ph]` (cit. on pp. 64, 73).

[73] M. Grazzini, S. Kallweit, D. Rathlev and M. Wiesemann, *$W^{\pm}Z$ production at the LHC: fiducial cross sections and distributions in NNLO QCD*, JHEP **05** (2017) 139, arXiv: `1703.09065 [hep-ph]` (cit. on pp. 66, 73, 100, 149).

[74] M. Jacob and G. Wick, *On the General Theory of Collisions for Particles with Spin*, Annals of Physics **281** (2000) 774, ISSN: 0003-4916, URL: `http://www.sciencedirect.com/science/article/pii/S0003491600960226` (cit. on pp. 69, 70).

[75] J. A. Aguilar-Saavedra and J. Bernabéu, *Breaking down the entire W boson spin observables from its decay*, Phys. Rev. **D93**, 011301 (2016) 011301, arXiv: `1508.04592 [hep-ph]` (cit. on p. 69).

[76] J. A. Aguilar-Saavedra, J. Bernabéu, V. A. Mitsou and A. Segarra, *The Z boson spin observables as messengers of new physics*, European Physical Journal C **77**, 234 (2017) 234, arXiv: `1701.03115 [hep-ph]` (cit. on p. 69).

[77] A. Denner and G. Pelliccioli, *NLO QCD predictions for doubly-polarized WZ production at the LHC*, Phys. Lett. B **814** (2021) 136107, arXiv: `2010.07149 [hep-ph]` (cit. on pp. 72, 73, 82, 123, 144, 145, 147, 148, 151, 164, 166).

[78] A. Denner and G. Pelliccioli, *Polarized electroweak bosons in W^+W^- production at the LHC including NLO QCD effects*, JHEP **09** (2020) 164, arXiv: `2006.14867 [hep-ph]` (cit. on p. 72).

[79] D. N. Le and J. Baglio, *Doubly-polarized WZ hadronic cross sections at NLO QCD+EW accuracy*, (2022), arXiv: `2203.01470 [hep-ph]` (cit. on p. 73).

[80] ATLAS Collaboration, *The ATLAS Simulation Infrastructure*, Eur. Phys. J. C **70** (2010) 823, arXiv: `1005.4568 [physics.ins-det]` (cit. on p. 74).

[81] S. Agostinelli et al., *GEANT4 – a simulation toolkit*, Nucl. Instrum. Meth. A **506** (2003) 250 (cit. on p. 74).

[82] Melia, Tom and Nason, Paolo and Röntsch, Raoul and Zanderighi, Giulia, *W^+W^-, WZ and ZZ production in the POWHEG BOX*, JHEP **11** (2011) 078, arXiv: `1107.5051 [hep-ph]` (cit. on p. 74).

[83] R. Frederix and S. Frixione, *Merging meets matching in MC@NLO*, JHEP **12** (2012) 061, arXiv: `1209.6215 [hep-ph]` (cit. on p. 74).

[84] F. Cascioli, P. Maierhofer and S. Pozzorini, *Scattering Amplitudes with Open Loops*, Phys. Rev. Lett. **108** (2012) 111601, arXiv: `1111.5206 [hep-ph]` (cit. on p. 74).

[85] T. Gleisberg and S. Hoeche, *Comix, a new matrix element generator*, JHEP **12** (2008) 039, arXiv: `0808.3674 [hep-ph]` (cit. on p. 74).

[86] S. Schumann and F. Krauss, *A parton shower algorithm based on Catani-Seymour dipole factorisation*, JHEP **03** (2008) 038, arXiv: `0709.1027 [hep-ph]` (cit. on p. 74).

[87] S. Höche, F. Krauss, M. Schönherr and F. Siegert, *QCD matrix elements + parton showers. The NLO case*, JHEP **04** (2013) 027, arXiv: `1207.5030 [hep-ph]` (cit. on p. 74).

[88] D. B. Franzosi, O. Mattelaer, R. Ruiz and S. Shil, *Automated predictions from polarized matrix elements*, Journal of High Energy Physics **2020** (2020), URL: `https://doi.org/10.1007%2Fjhep04%282020%29082` (cit. on p. 74).

[89] P. Artoisenet, R. Frederix, O. Mattelaer and R. Rietkerk, *Automatic spin-entangled decays of heavy resonances in Monte Carlo simulations*, JHEP **03** (2013) 015, arXiv: `1212.3460 [hep-ph]` (cit. on p. 74).

[90] L. Lonnblad, *Correcting the color dipole cascade model with fixed order matrix elements*, JHEP **05** (2002) 046, arXiv: `hep-ph/0112284` (cit. on p. 75).

[91] L. Lonnblad and S. Prestel, *Matching Tree-Level Matrix Elements with Interleaved Showers*, JHEP **03** (2012) 019, arXiv: `1109.4829 [hep-ph]` (cit. on p. 75).

[92] ATLAS Collaboration, *The ATLAS Collaboration Software and Firmware*, ATL-SOFT-PUB-2021-001, 2021, URL: `https://cds.cern.ch/record/2767187` (cit. on p. 86).

[93] ATLAS Collaboration, *Electron reconstruction and identification in the ATLAS experiment using the 2015 and 2016 LHC proton-proton collision data at $\sqrt{s}$ = 13 TeV*, Eur. Phys. J. C **79** (2019) 639, arXiv: `1902.04655 [physics.ins-det]` (cit. on p. 86).

[94] ATLAS Collaboration, *Electron and photon performance measurements with the ATLAS detector using the 2015-2017 LHC proton-proton collision data*, JINST **14** (2019) P12006, arXiv: `1908.00005 [hep-ex]` (cit. on pp. 86, 89, 139).

[95] ATLAS Collaboration, *Muon reconstruction and identification efficiency in ATLAS using the full Run 2 pp collision data set at* $\sqrt{s} = 13$ *TeV*, Eur. Phys. J. C **81** (2021) 578, arXiv: `2012.00578 [hep-ex]` (cit. on pp. 87, 139).

[96] ATLAS Collaboration, *Jet energy scale and resolution measured in protonproton collisions at* $\sqrt{s} = 13$ *TeV with the ATLAS detector*, Eur. Phys. J. C **81** (2021) 689, arXiv: `2007.02645 [hep-ex]` (cit. on p. 87).

[97] M. Cacciari, G. P. Salam and G. Soyez, *The anti-*k_t *jet clustering algorithm*, JHEP **04** (2008) 063, arXiv: `0802.1189 [hep-ph]` (cit. on p. 87).

[98] ATLAS Collaboration, *Jet reconstruction and performance using particle flow with the ATLAS Detector*, Eur. Phys. J. C **77** (2017) 466, arXiv: `1703.10485 [hep-ex]` (cit. on p. 87).

[99] ATLAS Collaboration, *Performance of pile-up mitigation techniques for jets in pp collisions at* $\sqrt{s} = 8$ *TeV using the ATLAS detector*, Eur. Phys. J. C **76** (2016) 581, arXiv: `1510.03823 [hep-ex]` (cit. on p. 87).

[100] ATLAS Collaboration, *Performance of missing transverse momentum reconstruction with the ATLAS detector using proton-proton collisions at* $\sqrt{s}$ *= 13 TeV*, Eur. Phys. J. C **78** (2018) 903. 66 p, arXiv: `1802.08168`, URL: `https://cds.cern.ch/record/2305380` (cit. on pp. 87, 140).

[101] A. Ballestrero, E. Maina and G. Pelliccioli, *Polarized vector boson scattering in the fully leptonic WZ and ZZ channels at the LHC*, JHEP **09** (2019) 087, arXiv: `1907.04722 [hep-ph]` (cit. on p. 91).

[102] Martin Abadi et al., *TensorFlow: Large-Scale Machine Learning on Heterogeneous Systems*, Software available from tensorflow.org, 2015, URL: `https://www.tensorflow.org/` (cit. on pp. 91, 111, 126).

[103] F. Chollet et al., *Keras*, 2015, URL: `https://github.com/fchollet/keras` (cit. on pp. 91, 111, 126).

[104] ATLAS Collaboration, *Observation of the associated production of a top quark and a Z boson in pp collisions at* $\sqrt{s} = 13$ *TeV with the ATLAS detector*, JHEP **07** (2020) 124, arXiv: `2002.07546 [hep-ex]` (cit. on p. 94).

[105] ATLAS Collaboration, *Measurements of* $W^{\pm}Z$ *production cross sections in pp collisions at* $\sqrt{s} = 8$ *TeV with the ATLAS detector and limits on anomalous gauge boson self-couplings*, Phys. Rev. D **93** (2016) 092004, arXiv: `1603.02151 [hep-ex]` (cit. on p. 95).

[106] ATLAS Collaboration, *Search for supersymmetry at* $\sqrt{s}$*=8 TeV in final states with jets and two same-sign leptons or three leptons with the ATLAS detector*, JHEP **06** (2014) 035, arXiv: `1404.2500 [hep-ex]` (cit. on p. 95).

[107] G. Cowan, K. Cranmer, E. Gross and O. Vitells, *Asymptotic formulae for likelihood-based tests of new physics*, Eur. Phys. J. C **71** (2011) 1554, [Erratum: Eur.Phys.J.C 73, 2501 (2013)], arXiv: `1007.1727 [physics.data-an]` (cit. on pp. 104, 105).

[108] K. Cranmer, G. Lewis, L. Moneta, A. Shibata and W. Verkerke, *HistFactory: A tool for creating statistical models for use with RooFit and RooStats*, tech. rep., New York U., 2012, URL: `https://cds.cern.ch/record/1456844` (cit. on pp. 106, 134).

[109] W. Verkerke and D. P. Kirkby, *The RooFit toolkit for data modeling*, eConf **C0303241** (2003) MOLT007, ed. by L. Lyons and M. Karagoz, arXiv: `physics/0306116` (cit. on p. 106).

[110] A. Andreassen and B. Nachman, *Neural networks for full phase-space reweighting and parameter tuning*, Phys. Rev. **D101** (9 2020) 091901, URL: `https://link.aps.org/doi/10.1103/PhysRevD.101.091901` (cit. on p. 125).

[111] ATLAS Collaboration, *Muon reconstruction performance of the ATLAS detector in proton-proton collision data at* $\sqrt{s} = 13$ *TeV*, The European Physical Journal C **76** (2016), URL: `https://doi.org/10.1140%2Fepjc%2Fs10052-016-4120-y` (cit. on p. 139).

[112] ATLAS Collaboration, *Jet energy scale measurements and their systematic uncertainties in proton-proton collisions at* $\sqrt{s} = 13$ *TeV with the ATLAS detector*, Phys. Rev. D **96** (2017) 072002, arXiv: `1703.09665 [hep-ex]` (cit. on p. 140).

[113] ATLAS Collaboration, *Measurement of the Inelastic Proton-Proton Cross Section at* $\sqrt{s} = 13$ *TeV with the ATLAS Detector at the LHC*, Phys. Rev. Lett. **117** (2016) 182002, arXiv: `1606.02625 [hep-ex]` (cit. on p. 140).

[114] J. Butterworth et al., *PDF4LHC recommendations for LHC Run II*, J. Phys. G **43** (2016) 023001, arXiv: `1510.03865 [hep-ph]` (cit. on p. 140).

[115] ATLAS Collaboration, *Observation of gauge boson joint-polarisation states in* $W^{\pm}Z$ *production from pp collisions at* $\sqrt{s} = 13$ *TeV with the ATLAS detector*, 2022, URL: `https://arxiv.org/abs/2211.09435` (cit. on p. 172).

Résumé

Dans le cadre du Modèle Standard de la physique des particules, le mécanisme de brisure spontanée de symétrie électrofaible est responsable de l'apparition d'un état de polarisation longitudinale dans les bosons vecteurs massifs $W^{\pm}$ et Z. L'étude des états de co-polarisation dans les processus dibosons, correspondant à la production de paire de deux de ces bosons vecteurs, constitue un test précis du Modèle Standard car elle permet de sonder indirectement ce mécanisme de brisure de symétrie. Cette thèse étudie le processus diboson $W^{\pm}Z$ en utilisant les données enregistrées par le détecteur ATLAS pendant le Run 2 du LHC, correspondant à une luminosité intégrée de $139\,\mathrm{fb}^{-1}$ de collisions proton–proton à une énergie de centre de masse de 13 TeV. Le détecteur ATLAS s'appuie sur un système de déclenchement pour gérer la grande quantité de données produites au LHC et être capable de conserver les événements rares tels que ceux provenant des processus dibosons. La mise à niveau de ce système de déclenchement en vue du Run 3 du LHC est également présentée dans cette thèse, en se concentrant sur le nouveau ňăDigital Triggerăž des calorimètres à argon liquide. Dans le jeu de données du Run 2, les événements de production inclusive $W^{\pm}Z$ avec désintégration leptonique des deux bosons de jauge en électrons ou muons sont sélectionnés. Dans ces événements, les quatre fractions de co-polarisation, en considérant les états de polarisation longitudinale ou transversale pour chaque boson, sont extraites à l'aide de techniques dajustements de modèles à maximum de vraisemblance. Les fractions de polarisation n'étant pas des quantités invariantes de Lorentz, elles sont obtenues dans le référentiel du centre de masse $W^{\pm}Z$. Un soin particulier est apporté au choix d'une variable discriminante pour l'ajustement des modèles et au développement de modèles de polarisation corrects, en s'appuyant notamment sur des techniques avancées de réseaux de neurones profonds. La production simultanée de paires de bosons vecteurs polarisés longitudinalement est mesurée pour la première fois avec une significance de 7,1 écarts-types. Les fractions de co-polarisation mesurées et intégrées sur la région fiducielle sont $f_{00} = 0.067 \pm 0.010$, $f_{0\mathrm{T}} = 0.110 \pm 0.029$, $f_{\mathrm{T}0} = 0.179 \pm 0.023$ et $f_{\mathrm{TT}} = 0.644 \pm 0.032$, en accord avec les prédictions du Modèle Standard les plus précises disponibles. Les fractions de polarisation individuelles des bosons $W^{\pm}$ et Z sont également mesurées séparément et s'avèrent cohérentes avec les fractions de co-polarisation dans la limite des corrélations attendues. Les fractions de polarisation et co-polarisation des bosons sont également mesurées séparément dans les événements $W^{+}Z$ et $W^{-}Z$.

Abstract

Within the Standard Model of particle physics, the electroweak spontaneous symmetry breaking mechanism is responsible for the appearance of a longitudinal polarisation state in the massive $W^{\pm}$ and Z vector bosons. The study of joint-polarisation states in diboson processes, corresponding to the pair production of two such vector bosons, constitutes a detailed test of the Standard Model as it allows to probe indirectly this symmetry breaking mechanism. This thesis studies the $W^{\pm}Z$ diboson process using the data recorded by the ATLAS detector during Run 2 of the LHC, corresponding to an integrated luminosity of $139\,\mathrm{fb}^{-1}$ of proton–proton collisions at a centre-of-mass energy of 13 TeV. The ATLAS detector relies on a trigger system to manage the large amount of data produced at the LHC and be able to keep rare events such as those from diboson processes. The upgrade of this trigger system in preparation for the Run 3 of the LHC is also presented in this thesis, focusing on the new Digital Trigger of the Liquid Argon calorimeters. In the Run 2 dataset, events of $W^{\pm}Z$ inclusive production with leptonic decay of the two gauge bosons into electrons or muons are selected. In such events, the four joint-polarisation fractions, considering longitudinal or transverse polarisation states for each boson, are extracted through a binned maximum-likelihood template fits. Polarisation fractions not being Lorentz invariant quantities, they are obtained in the $W^{\pm}Z$ centre-of-mass frame. Special care is taken in the choice of a discriminating variable for the template fit and the development of accurate polarisation templates, relying in particular on advanced Deep Neural Networks techniques. The simultaneous pair-production of longitudinally polarised vector bosons is measured for the first time with a significance of 7.1 standard deviations. The measured joint-polarisation fractions integrated over the fiducial region are $f_{00} = 0.067 \pm 0.010$, $f_{0\mathrm{T}} = 0.110 \pm 0.029$, $f_{\mathrm{T}0} = 0.179 \pm 0.023$ and $f_{\mathrm{TT}} = 0.644 \pm 0.032$, in agreement with the next-to-leading-order Standard Model predictions. Single boson polarisation fractions of the $W^{\pm}$ and Z bosons are also measured and found to be consistent with joint-polarisation fractions within the expected amount of correlations. Both the joint and single boson polarisation fractions are also measured separately in $W^{+}Z$ and $W^{-}Z$ events.